

Thèse présenté pour obtenir le grade de

DOCTEUR EN SCIENCES
Roko Pleština

Evidence for a Standard Model Higgs boson like particle decaying into four leptons with the CMS detector

Evidence pour une nouvelle particule semblable au boson de Higgs du modèle standard et se désintégrant en quatre leptons dans l'expérience CMS

Soutenue devant du jury:

Président du jury M. JEAN-CLAUDE BRIENT, *LLR, Palaiseau*

Rapporteurs M. PHILIPPE BLOCH, *CERN, Genève*

MME. ANNE-ISABELLE ETIENVRE, *CEA, Saclay*

Examinateurs M. ABDELHAK DJOUADI, *LPTHE, Orsay*

M. IVICA PULJAK, *FESB, Split (Co-directeur de thèse)*

M. YVES SIROIS, *LLR, Palaiseau (Directeur de thèse)*

Palaiseau, 21 février 2013

To my wife Jelena, of course..... and to our Father

Acknowledgements

Don't worry - you will not find "secret treasure tests" here. These are normally put somewhere in the middle of a chapter in the middle of a thesis in order to see if the thesis has been thoroughly read. I know this is the part that everybody taking this thesis into hands will read. Thus, writing acknowledgements makes my hands shake knowing how forgetful and ungrateful I am.

So, I first want to thank to all people and institutions I don't mention here. To all those, whose help and presence I took for granted, or who helped me in different ways, but always staying hidden behind the scenes.

Now, to those of whom I am aware of...

To Yves Sirois, my thesis advisor...

for your patience, support, encouragement, knowledge and last minute interventions. I am sorry for all the white hair I have caused. I add also all the wonderful conversations and moments spent with you and Louise around the table in Anthony. It's not that I want to, but I cannot get rid of the "Queen Elisabeth cake" ever since my wife tasted it at your home.

To Ivica Puljak, my thesis co-advisor...

for your patience, fruitful discussions, support, diplomatic solutions, peacefulness in hard moments. Thank you for not letting me quit the night before the thesis defence.

To Jean-Claude Brient, Philippe Bloch, Anne-Isabelle Etievre, Abdelhak Djouadi, Ivica Puljak and Yves Sirois, my thesis jury members...

for your devotion, time, careful reading of my thesis, encouragement and a very pleasant defence. I am particularly grateful to Anne-Isabelle Etievre and Philippe Bloch—writers of the thesis report—for their incredible effort to read 300 pages of thesis and provide corrections, helpful comments and hints to improve this thesis.

To the Laboratoire Leprince-Ringuet (LLR), Palaiseau, France, my host lab...

for its support in various ways throughout my PhD time, for its friendly, productive and supportive environment.

Acknowledgements

To the Faculty of Electrical Engineering, Mechanical Engineering and Naval Architecture (FESB), Split, Croatia, my home university... for its supportive environment, for enabling multiple travels to CERN, Paris and conferences. I must not forget all the pain I have caused to our secretaries when resolving complicated travel budget.

To the Croatian Ministry of Science and Education...

for providing financial support, enabling our groups frequent travels to conferences and CERN.

To the French Embassy in Croatia...

for their constant engagement to improve the scientific communication between Croatia and France, financial support, and specifically for providing the scholarship enabling my long stay in France.

To the CMS Collaboration at CERN...

for its collaborative, creative and productive environment. This thesis has been made by “standing on the shoulders of giants” who devoted their lives to design, construct and run our experiment. Taking part in the Higgs Physics Analysis Group (Higgs PAG) and Electron Photon Physics Object Group (Egamma POG) has been a pleasure. Thank you for your many fruitful discussions, hints and a terrific analysis which made the Higgs boson show up! I owe a special gratitude to the administration of our collaboration for making physicist’s life “easier”.

To Jelena, my wife...

for being my wife. It’s been a hard time for you. So many absences, diners that got cold, holidays spent working... Thank you for your patience, encouragement, advices, discussions and much more. Thank you for raising Ruder Karlo. Thank you for your love.

To Zdravka and Andrija, my parents...

for helping me out through out all my life, for putting me in the right places at the right moments, for your support in difficult moments.

To Andreja and Frane, my sisters family...

for your constant help, encouragement, prayer.

To Stephanie, Clementine, Christophe, Roberto, Michal, Florian, Claude, Alex, Andrea, David, Misha and Nadir, my LLR colleagues ...

for helpful discussions, sharing the knowledge and many technicalities that made life easier. The team work that I have experienced at LLR will remain as a team work model to me.

Acknowledgements

To Ludwik Dobrzynski...

for your generosity, advices, support and lively discussions. You have been like a father to me and your home like a home to me through all these years.

To Marko Kovač...

for all the help during the final stages of my PhD, for the long nights spent together adjusting parameters of fits for tag-and-probe.

To Karlo Lelas...

for a lot of physics discussions, showing me the beauty and quirk of details in physics and for helping me fulfil my teaching duties.

To Anita, Dunja, Mirjana, Bojan, Damir, Nikola, Srećko, Stipe, Suri, my FESB colleagues...

for being friends, enabling this work in various ways. I owe special gratitude to Anita who was always there with her readiness to solve problems of any kind.

To Vuko, Senka, Srećko, Alberto, Orso...

for many helpful discussions, technical solutions while writing this thesis.

Oh my God! I always forget You ... and many others ...

Preface

I started to work on my PhD thesis in fall 2009, at a time where we were intensively preparing for the first collisions at the LHC collider. I began with contributions to the commissioning of the electrons with early data in 2010 and 2011. The reconstruction of electrons in CMS relies on rather elaborate techniques combining information from the electromagnetic calorimeter and the tracker detectors. We first validated the reconstruction of all individual observables and verified the agreement with Monte Carlo (MC) simulation. We then used the very first data with single Z (and W) production and deployed tag-and-probe (T&P) techniques. I co-signed six analysis notes on the topic of electron measurements during that phase.

In the $H \rightarrow ZZ^{(*)} \rightarrow 4\ell$ analysis my contributions include work on definition and implementation of the overall analysis strategy (from the analysis with first data to the most recent results on properties measurements), definition and development of the lepton isolation algorithm, measurements of electrons reconstruction efficiencies, data-to-Monte-Carlo ratios and systematics with the specifically developed T&P method, integration of analysis tools in the software framework, processing and maintaining analysis data samples. In what follows these contributions are explained in more details.

The search for the Higgs boson through its decay to four leptons is known as the “golden channel”. It has been considered as one of the flagship channels for analysis in the CMS experiment since the origin of the LHC project. This channel provides the main motivation for high efficiency and precision of lepton reconstruction down to the lowest possible momenta. Such high efficiencies must be achieved while providing powerful lepton identification and isolation observables for the signal to background discrimination, and allowing for performance and background control from data. The main strategy of the analysis has been developed during many years and I was privileged to start my thesis project in the group which was one of the main actors in this analysis since the beginning. The main emphasis of the analysis with first data was the lepton reconstruction and background control. The work was first focused on the deployment of the high efficiency lepton reconstruction algorithm down to low momenta, with the full control of systematic uncertainties. I have participated in the commissioning of electrons with early data, from the overall electron reconstruction to the specific parts, such as charge determination, track seeding, reconstruction efficiency and momentum determination. My work, together with other colleagues from the group, resulted in the fully functional official software for electron reconstruction, which has been used for many analyses in the CMS experiment, and in particular for the Higgs boson search in the four lepton channel.

The framework for the $H \rightarrow ZZ^{(*)} \rightarrow 4\ell$ analysis has been established when my thesis project

started. My initial contribution consisted of implementing of the final layer of the analysis workflow and testing the full analysis chain, including data processing, skimming and maintenance. This part of my contribution has continued until the final published results. The analysis strategy has evolved with the amount of data collected and has been influenced by our better understanding and control of the detector and the underlying physics. First results of the analysis have been presented in the European Physics Society conference (EPS) in Grenoble in 2011, where we demonstrated excellent control of the lepton reconstruction, understanding of the background processes and robustness of the full analysis chain, including the statistical interpretation of results. The further natural evolution of analysis included opening of the phase space to accept more signal events (developing and deploying more involved tools for background control in constantly increasing hostile environment of more and more pile-up events) and to explore full event kinematics and sophisticated analysis methods. My contribution to this process was in developing, deploying and testing the analysis tools, integrating the full analysis chain and optimizing the selection steps, documenting and presenting the results in internal and external meetings.

A particular emphasis throughout all my PhD has been put on lepton isolation as a key ingredient in our Higgs boson search. The lepton isolation is one of the key observables for the Higgs search in 4 lepton channel. Nevertheless, it has to be carefully designed to take into account the kinematics of the Higgs decay (spin 0) to Zs (spin 1) and further on to leptons (spin 1/2). In many cases ($\sim 5\%$) leptons from either Z are quasi-collinear, thus entering into each others isolation cone. This happens for Higgs boson at low mass since Zs are produced at rest but also for Higgs boson at significantly high masses when Zs acquire boost. Part of my work was dedicated to properly exclude the nearby lepton energy deposit when computing isolation to avoid loosing the efficiency of selection. Continuing to work with lepton isolation, I participated in pile-up study task force in 2011 to check the impact of the multiple interactions on isolation observables. Isolation is, of course, susceptible to pile-up, when calorimetry is considered because the information on vertex is not available. I worked on establishing an isolation calculation method immune to additional energy flow from pile-up interactions. The method is known across CMS as the “effective area” correction (EA). It uses the information of the average energy density in detector obtained via FastJet calculation to estimate the pile-up. Using calorimeter instead of simple vertex multiplicity information gives a handle also to out-of-time pile-up. Since one of the 4 leptons in the final state typically has a transverse momentum of less than 10 GeV, we had to push the lepton acceptances to values as low as 5 (7) GeV for muons (electrons). In this low p_T region, the data-to-MC discrepancies are expected to be larger, therefore a solid data driven control of efficiencies had to be established. I was directly working on this issue using tag-and-probe technique which profits from leptonic Z decays to evaluate selection efficiencies directly from data. These measurements were used in the analysis in the form of per-lepton scale factors and its uncertainties propagate through the analysis.

Abstract

This thesis reports the discovery of the new boson recently observed at a mass near 125 GeV in the CMS experiment at CERN. The measurements of the properties of the new boson are reviewed. The results are obtained from a comprehensive search for the standard model Higgs boson in the $H \rightarrow ZZ$ decay channel, where both Z bosons decay to electron or muon lepton pairs. The search covers Higgs boson mass hypotheses in the range $110 < m_H < 1000$ GeV. The analysis uses proton-proton collision data recorded by the CMS detector at the LHC, corresponding to integrated luminosities of 5.1 fb^{-1} at $\sqrt{s} = 7 \text{ TeV}$ and 12.2 fb^{-1} at $\sqrt{s} = 8 \text{ TeV}$. The new boson is observed with a local significance above the expected background of 4.5 standard deviations. The signal strength μ , relative to the expectation for the standard model Higgs boson, is measured to be $\mu = 0.80^{+0.35}_{-0.28}$ at 126 GeV. A precise measurement of its mass has been performed and gives $126.2 \pm 0.6 \text{ (stat)} \pm 0.2 \text{ (syst)} \text{ GeV}$. The hypothesis 0^+ of the standard model for the spin $J = 0$ and parity $P = +1$ quantum numbers is found to be consistent with the observation. The data disfavour the pseudoscalar hypothesis 0^- with a CL_s value of 2.4%. No other significant excess is found, and upper limits at 95% confidence level exclude the ranges 113–116 GeV and 129–720 GeV while the expected exclusion range for the standard model Higgs boson is 118–670 GeV.

A special emphasis throughout the thesis has been put on lepton isolation. Lepton isolation being one of the key observables for the discovery is highly susceptible to pile-up conditions of the LHC machine. This thesis establishes a robust method to marginalize the effect of pile-up on isolation. The method is now used across different analysis in CMS. A special attention has also been put on measurements of the efficiencies of lepton identification, isolation and impact parameter requirements directly from data using leptonic decays of Z boson. The measurements were used to produce final per lepton scale factors when calculating the significance of excess of four lepton events.

Résumé

Cette thèse présente la mise en évidence dans l'expérience CMS d'un nouveau boson dans la voie $H \rightarrow ZZ$ et la contribution à la découverte de ce nouveau boson à une masse proche de 125 GeV dans l'expérience CMS au CERN. La mesure des propriétés est passée en revue. Les résultats sont obtenus par une analyse inclusive du canal $H \rightarrow ZZ \rightarrow 4\ell$, i.e. où chacun des bosons Z se désintègre en une paire de leptons (ℓ), électrons ou muons. La recherche du boson de Higgs couvre toutes les hypothèses de masse dans le domaine $110 < m_H < 1000$ GeV. L'analyse utilise les données de collisions proton-proton enregistrées par le détecteur CMS au collisionneur LHC, correspondants à des luminosités intégrées de 5.1 fb^{-1} à $\sqrt{s} = 7$ TeV et 12.2 fb^{-1} à $\sqrt{s} = 8$ TeV. Le nouveau boson est observé avec une signification statistique au-dessus du bruit de fond attendu de 4.5 écarts standards. L'intensité du signal μ , normalisé à l'attendu pour le boson de Higgs du modèle standard, est mesuré à une valeur de $\mu = 0.80^{+0.35}_{-0.28}$ à 126 GeV. Une mesure précise de la masse du nouveau boson a été effectué et donne 126.2 ± 0.6 (stat) ± 0.2 (syst) GeV. L'hypothèse d'un boson scalaire 0^+ est en accord avec l'observation. Les données expérimentales défavorisent l'hypothèse pseudoscalaire 0^- avec CL_s de 2.4%. Aucun autre excès significatif n'est observé, et des limites supérieures d'exclusions sont obtenues à 95% de niveau de confiance pour les domaines 113–116 GeV et 129–720 GeV, alors que la domaine d'exclusion attendue en absence du boson de Higgs est de 118–670 GeV.

Pour cette thèse, une emphase particulière a été mis sur l'isolation des leptons. L'isolation des leptons fait parties des observables clefs sur le chemin de la découverte. En même temps, l'isolation est très sensible aux conditions pile-up de la machine LHC. Cette thèse établit une méthode robuste qui permet de marginaliser l'effet de pile-up sur l'isolation. La méthode est maintenant utilisée à travers les différentes analyses de CMS. Une attention particulière a également été mis sur les mesures de l'efficacité de l'identification des leptons, l'isolation et le paramètre d'impact directement à partir de données à l'aide désintégrations leptoniques de boson Z . Les mesures ont été utilisées pour les corrections finales appliquées aux leptons lors du calcul de la signification statistique de l'excès des événements à quatre leptons.

Contents

Acknowledgements	v
Preface	ix
Abstract / Résumé	xi
Introduction	1
I Breaking the Symmetry	5
1 The Standard Model	7
1.1 The Standard Model of Elementary Particles	7
1.2 The Electroweak Theory	8
1.3 The Brout-Englert-Higgs Mechanism	11
1.3.1 Vector Boson Masses and Couplings	14
1.3.2 Fermion Masses and Couplings	14
1.3.3 Higgs Boson Mass	16
2 Higgs Boson Search at the LHC	19
2.1 Higgs Production	19
2.1.1 Gluon-gluon Fusion	20
2.1.2 Vector Boson Fusion	20
2.1.3 Higgsstrahlung and Associated Production	21
2.2 Higgs Decay	22
2.2.1 Low Mass Region	23
2.2.2 Intermediate Mass Region	23
2.2.3 High Mass Region	23
2.2.4 Higgs total Decay Width	24
II Accelerate and Collide	27
3 Large Hadron Collider	29
3.1 Performance Goals	29
3.2 Nominal Centre of Mass Energy and Magnet Systems	31

Contents

3.3	Nominal Luminosity and Beam Parameters	32
3.4	Lattice Layout	33
3.5	LHC Collision Detectors	34
3.5.1	Pile-up Events	34
3.5.2	Collision Rate	35
3.5.3	High Radiation	35
3.6	Operation from 2010 to 2012	35
4	Compact Muon Solenoid	37
4.1	CMS Detector and its Magnet	37
4.2	Coordinate System	38
4.3	Inner Tracking System	40
4.4	Electromagnetic Calorimeter	42
4.4.1	ECAL Crystals and Geometry	43
4.4.2	Photodetectors	45
4.4.3	Preshower	46
4.4.4	Laser Monitoring	46
4.4.5	Detector Calibration	47
4.4.6	Energy Resolution	47
4.4.7	Position Resolution and Alignment	49
4.5	Hadron Calorimeter	49
4.6	Muon System	51
4.6.1	Drift Tube Chambers	51
4.6.2	Cathode Strip Chambers	52
4.6.3	Resistive Plate Chambers	52
4.6.4	Muon Momentum Resolution	53
4.7	Trigger and Data Acquisition	53
4.7.1	Level-1 Trigger Architecture	54
4.7.2	High-Level Trigger Architecture	57
4.7.3	The Data Acquisition System	58
4.8	Leptons Signature in CMS	59
4.8.1	Electrons	59
4.8.2	Muons	60
III	Choose Building Blocks	63
5	Datasets and Triggers	65
5.1	Collision Data	65
5.2	Simulated Samples	67
5.2.1	Signal: $H \rightarrow ZZ^{(*)} \rightarrow 4\ell$	69
5.2.2	Background: $q\bar{q} \rightarrow ZZ^{(*)} \rightarrow 4\ell$	71
5.2.3	Background: $gg \rightarrow ZZ^{(*)} \rightarrow 4\ell$	71

Contents

5.2.4	Background: $Z + \text{jets} \rightarrow 2\ell + \text{jets}$	72
5.2.5	Background: $t\bar{t} \rightarrow 2\ell 2\nu 2b$	72
6	Leptons and Photons	73
6.1	Electrons	74
6.1.1	Reconstruction	74
6.1.2	Identification	84
6.2	Muons	91
6.2.1	Reconstruction	91
6.2.2	Identification	92
6.3	Lepton Isolation	94
6.3.1	Pile-up Subtraction	98
6.3.2	Working Point Optimization	102
6.4	Leptons common Vertex	104
6.5	Photons	104
6.5.1	Photon Observables and FSR Recovery	104
6.5.2	Photon Reconstruction, Identification and Isolation	105
6.5.3	Building Z bosons with FSR Photon Recovery	106
6.5.4	Performance of FSR Photon Recovery	107
7	Lepton Selection Validation from Data	111
7.1	Tag-and-probe Method	111
7.2	Electron measurements	113
7.2.1	Reconstruction	114
7.2.2	Identification	116
7.2.3	Isolation and Impact Parameter	116
7.2.4	Trigger	122
7.2.5	Electron Scale Factors	124
7.3	Muon Measurements	130
7.3.1	Reconstruction and Identification	130
7.3.2	Impact Parameter	131
7.3.3	Isolation	131
7.3.4	Trigger	131
IV	Come Together	133
8	Analysis Strategy and Event Selection	135
8.1	General Analysis Strategy	136
8.2	Event Selection	138
8.2.1	Trigger Selection	139
8.2.2	Lepton Selection	139
8.2.3	Final Selection and Combinatorics	140
8.2.4	Event Selection Performances and Control	141

Contents

9 Signal Modelling and Uncertainties	147
9.1 Signal Model at Low Masses	148
9.2 Signal Model at High Masses	150
9.2.1 Lineshape with Complex Pole Scheme	150
9.2.2 Evaluation of the High-mass Corrections Systematic Uncertainties	152
9.2.3 High Higgs Boson Mass Signal Model	152
9.3 Signal Model Uncertainties	154
9.3.1 Theoretical Uncertainties	154
9.3.2 Data-to-MC Scale Factors from Efficiencies	157
9.3.3 Four-lepton mass Scale and Resolution	160
9.4 Event-by-event Mass Errors	166
9.4.1 Calibration of Per-event Mass Errors	167
9.4.2 Expectations from Simulation	168
9.4.3 Validation of Per-event Mass Errors from Data	170
9.5 Event-by-event Mass Errors Model	175
10 Reducible Background Modelling and Uncertainties	177
10.1 Reducible Background Estimation	177
10.2 Methodology	178
10.2.1 Results on Data	183
10.2.2 Alternative Method	183
10.3 Reducible Background Uncertainties	184
10.3.1 Statistics in 4ℓ control sample	185
10.3.2 Functional form for $\mathbf{m}_{4\ell}$ shape	185
10.3.3 Closure Test with Z and Opposite Flavor Leptons	186
10.4 Reducible Background Summary	186
11 Irreducible Background Modelling and Uncertainties	189
11.1 ZZ ^(*) Background Model	190
11.2 ZZ ^(*) Background Model Uncertainties	193
11.2.1 Theoretical Uncertainties	193
12 Kinematic Discriminant	197
12.1 Methodology	197
12.2 Construction of MELA Discriminant	199
12.3 Parametrization of MELA Discriminant	203
12.4 MELA for Spin-Parity Properties Measurements	205
13 Statistical Analysis	211
13.1 Methodology of using 2D Distributions	211
13.2 Methodology of using 3D Distributions	215
13.3 Methodology for Spin and Parity Measurements	219

V Bingo!	223
14 Final Results	225
14.1 Summary of Selection and Systematic Uncertainties	225
14.1.1 Event Yields	225
14.1.2 Event Distributions	228
14.1.3 Systematic Uncertainties	234
14.2 Exclusion Limits	236
14.3 Significance of Excesses	238
14.4 Mass Measurement	240
14.5 Spin and Parity Measurements	242
Conclusions	245
Appendix	247
A ECAL Energy Measurement with Multivariate Regression	249
B Tag-and-probe Measurements	253
References	273
Curriculum Vitae	275

Introduction

To express the complexity of the Universe with a handful of fundamental laws is absolutely essential if one wishes to understand the phenomena within the matter and the space enclosing us. While the trial of formulating these relations must be as old as the spoken word, it needed the formalism of natural science in general and mathematics in particular to reward these trials with success—success in a twofold manner. First, only the mathematical formulation of phenomena allows a quantification and thus a verification against measured observations, second, it can in general be understood and tested by anyone.

Together with the deployment of the scientific method, the idea that matter is built up from a limited set of elementary components was developed. The idea that the profound constituents are the elements water, fire, earth and air was stated by the Greek philosopher Empedocles five centuries B.C.. Shortly after Leucippus and Democritus established the principle that all matter is formed by extremely small, fundamental and indestructible particles, that they called atoms. The idea of the atoms was picked up by scientists in the 19th century, but only in the year 1909, with the experiment of Ernest Rutherford, it became clear that the atoms have structure. Furthermore, with the discovery of the neutron by James Chadwick in 1932 it was established that the nucleus itself is composed of smaller particles.

In the 50's and 60's of the 20th century several particle physics experiments showed that there are many more particles with characteristics similar to the protons and neutrons. It was believed that they themselves are not fundamental, but formed by even smaller particles, the *quarks*. The *quark model*, whose convincing confirmation was the discovery of point-like constituents of the protons in 1969, allowed to classify all the known *hadrons* as compound objects of two or three quarks.

In parallel to the search for the elements of matter, the question on their interaction was posed. The work of James Clerk Maxwell was pioneering in this regard. He discovered unique fundamental mechanism behind the electricity and magnetism phenomena—the *electromagnetism*. This observation was formed in a set of equations—the *Maxwell equations*, which, together with the discovery of the quantum nature of physics and special relativity, formed later the extremely successful theory of Quantum Electrodynamics (QED).

Inspired by the success of the field theoretical formulation of the electromagnetism, taking it

Introduction

as a template, the endeavor was set to describe the other forces, the *weak force* responsible for the decay of nuclei and the *strong force*, responsible for the formation of discovered hadrons. It was found that the strong interaction can be formulated as a relativistic field-theory of colour charged quarks and gluons, known as Quantum Chromodynamics (QCD). The weak force could be combined with QED into the so called *electroweak interaction*, also known as Glashow-Weinberg-Salam (GWS) model. The GWS theory together with QCD form the current most successful theory for the interaction of elementary particles, referred to as the Standard Model (SM) of Particle Physics.

In general in such theories, known as *Gauge Theories*, the particles responsible for the action of the force, the *gauge* or *vector* bosons, as well as elementary fermions, have to be massless. However, experiments showed that the particles responsible for the weak interaction are very massive. Elementary matter particles also have masses. A mechanism, the so-called Brout-Englert-Higgs (BEH) mechanism has been proposed to remedy the theory deficiency. This mechanism, developed and published in 1964 by Peter Higgs, Robert Brout and Francois Englert, postulates the existence of a new scalar field responsible for electroweak symmetry breaking (EWSB), the Higgs field. The gauge bosons acquire mass. The fermions become massive by interacting via Yukawa interactions with the Higgs field. The theory predicts the existence of a physical scalar boson, the Higgs boson.

A variety of tests and precision measurements over the last decades gave very strong confidence in the Standard Model, in particular the prediction and discovery of particles like Z boson and top quark. The discovery of the Higgs boson, the only missing piece, would be (is) the unprecedented achievement of the Standard Model.

The mass of the Higgs boson, the quanta of the Higgs field is not predicted by the mechanism, thus it has to be experimentally deduced. The existence of an elementary particle such as the Higgs boson is tested at colliders. High energy collisions are aimed to create the searched particle, and detectors embedded around collision points allow to seek for a typical signature. After the exclusions from the Large Electron Positron Collider (LEP) and the Tevatron experiments, the Large Hadron Collider (LHC) became the major actor for the Higgs hunting and possibly taming in the full mass range allowed by the theory.

The development and construction of the LHC machine took over two decades. It was built to provide proton-proton collisions with a nominal centre of mass energy of 14 TeV (7 TeV and 8 TeV during the first years) and a very high luminosity. In parallel, detectors were designed and built, responding to the LHC characteristics and the physics goals. In particular the Compact Muon Solenoid (CMS) and A Toroidal LHC Apparatus (ATLAS) experiments were primarily set to search for the Higgs boson in a wide variety of production and decay channels. The response of the detectors has been simulated with great care, facilitating the development of physics object reconstruction and research analysis.

This thesis work started with the very first collisions at the LHC at the end of 2009. By spring 2010, the LHC reached working conditions for the physics with an energy in the centre of mass

of the proton-proton collisions of 7 TeV. I was involved in the commissioning of basic objects for the reconstruction of the collision events, and in particular of the electrons.

At that time, I also took part in the deployment of the analysis strategy for the search of the Higgs boson, specifically in the determination of the discriminating observables as well as definition of Higgs boson mass-dependent search phase space. The search relies solely on the measurement of leptons achieving high reconstruction, identification and isolation efficiency for a $ZZ \rightarrow 4\ell$ system. The ZZ system is composed of two same-flavour and opposite-charge isolated leptons, e^+e^- and $\mu^+\mu^-$ in the mass range $m_{4\ell} > 100$ GeV. One or both of the Z bosons can be off-shell. The background sources include an irreducible four-lepton contribution from direct ZZ (or $Z\gamma$) production via $q\bar{q}$ annihilation and gg fusion. Reducible contributions arise from $Zb\bar{b}$ and $t\bar{t}$ where the final states contain two isolated leptons and two b jets producing secondary leptons. Additional background of instrumental nature arises from $Z + \text{jets}$ events where jets are misidentified as leptons.

In the following months, LHC was constantly increasing luminosity accelerating the collection of data. The increase of luminosity resulted in multiple collisions in a single bunch crossing, the so-called *pile-up*. To ensure the robustness of measured quantities, especially lepton isolation, a correction method using the average energy density deposited by the emerging particles has been deployed. The method is known as *effective area correction* and is currently used across many analysis in CMS. By the international conferences of the summer 2011, enough data had been collected to produce the first comprehensive search for the Higgs boson at the LHC and it was becoming clear that this simple and robust analysis had to be expanded to better cover the very low mass range.

This thesis describes the analysis as it was developed and deployed starting in fall 2011 with increased acceptance for Higgs boson in the low mass range. This implied even more demanding conditions on low p_T leptons, which presupposes a good control of lepton measurements. This work was carried out using the tag-and-probe method which uses Z decays as a handle to extract the possible differences between collision data and simulation. In addition, an effort was made to extract the maximum amount of information from events, using per-event mass uncertainties and, starting from spring 2012, exploiting the discriminating power from the full decay kinematics.

The thesis is divided into five parts. Part one, “Breaking the Symmetry”, is dedicated to theoretical aspects of Higgs boson phenomenology at hadron colliders. After a brief introduction to Standard Model in chapter 1, with focus on the BEH mechanism, we turn in chapter 2 to the relevant Higgs production processes and decay modes at LHC.

Part two, “Accelerate and collide”, gives a short overview of the experimental apparatus, the CMS detector at the LHC. A slight accent has been put on the electromagnetic calorimetry as it is one of the key components in the electron reconstruction and measurements.

In the third part we concentrate to “Choose building Blocks” for the analysis. After a brief

discussion on simulation and collision data choice for the analysis in the chapter 5, we quickly move to a detailed overview of physics objects—electrons, muons and photons—in chapter 6. An emphasis is put on electron reconstruction, identification and particularly isolation being one of the main topics I have been working on. In this very chapter, we also define the final state radiation (FSR) recovery strategy which has been put in place for the 2012 analysis. Bearing in mind that we have four leptons in final state, it is hard to overemphasize the importance of lepton selection efficiency measurements using *data-driven* techniques. These are presented in chapter 7.

Having chosen the building blocks, we try to make them “Come together” in part four. We start in chapter 8 by carefully defining the analysis strategy which would allow for a graduate decent into the signal phase space and a good control of background rates. Since the search for a Higgs boson in four-lepton channel is a hunt for a resonance in the four-lepton invariant mass parameter space, it is beneficial to model the signal yields, shapes and efficiencies, as well as background ones with respect to mass. These models are then used as inputs for the final statistical analysis. A detailed discussion of signal and background models is presented in chapters 9, 10 and 11. In chapter 12 we shed light on the full kinematic discriminant which complements the four-lepton mass measurement and increase the sensitivity of the search.

“Bingo!”—the title says it all. In this part we present the final statistical analysis and results for the exclusion limits and significances of event excesses in the four-lepton invariant mass spectrum. In addition, we bring a strategy to measure the Higgs boson spin-parity properties. The boson discovery at mass around 125 GeV—although in this channel only observation—was announced on a memorable CERN seminar in Geneva on 4th July 2012 by CMS spokesperson Joseph Incandela. Quickly afterwards, the analysis was published in a prestigious journal—Physics Letters B [1].

“Bingo!”—the title says it all. In this part we present the final statistical analysis and results for the exclusion limits and significances of event excesses in the four-lepton invariant mass spectrum. Evidence was found for the existence of a new boson around 125 GeV from the $H \rightarrow ZZ^{(*)} \rightarrow 4\ell$ channel, and, combined with the $H \rightarrow \gamma\gamma$ channel, led to the observation by CMS. Similar observations were obtained simultaneously by the ATLAS experiment. The discovery of a new boson was announced on a memorable CERN seminar in Geneva on the 4th of July 2012 by the CMS spokesperson, Joe Incandela, and the ATLAS spokesperson, Fabiola Gianotti. Quickly afterwards, the analysis was published in a prestigious journal—Physics Letters B [1]. More data was analysed in the $H \rightarrow ZZ^{(*)} \rightarrow 4\ell$ in fall 2012 and the first spin-parity measurements performed by the CMS experiment have been published in another prestigious journal, Physics Review Letters. All these results are described in this thesis.

Breaking the Symmetry Part I

1 The Standard Model

The fundamental components of matter and their interactions are nowadays best described by the Standard Model of Particle Physics (SM), which is based on two complementary quantum field theories, describing the *electroweak interaction* (Glashow-Weinberg-Salam model or GWS) and the *strong interaction* (Quantum Chromodynamics or QCD). The gauge group of the Standard Model is $SU(3)_C \otimes SU(2)_L \otimes U(1)_Y$, where $SU(2)_L \otimes U(1)_Y$ are related to the couplings of the electroweak interaction, whilst $SU(3)_C$ is related to gauge couplings in quantum chromodynamics. In this chapter, a short overview of the electroweak theory (Sec. 1.2) is given, focusing the attention on the EWSB, the Higgs mechanism and the Higgs boson (Sec. 1.3). In subsequent chapter we will set the theoretical landscape for the Higgs boson searches performed at the LHC by introducing the relevant production and decay modes of the boson.

Note that *natural units* will be used, i.e. $\hbar = c = 1$, unless otherwise specified.

1.1 The Standard Model of Elementary Particles

The SM describes the matter at the physical level as composed by 3 families of 4 elementary particles, which are *fermions* with spin 1/2. Ordinary matter is composed only of the 1st family members, and other two families can be regarded as the replicas of the first one. The corresponding particles belonging to separate families are said to have different *flavours*, with same coupling constants but with different masses. The fermions can be divided into two main groups, *leptons* and *quarks*, whose classification is given in Table 1.1. Quarks are subject to both strong and electroweak interactions and do not exist as free states, but only as constituents of a wide class of particles, the *hadrons*, such as protons and neutrons. Leptons, instead, only interact by electromagnetic and weak forces.

In the SM, the interactions between particles are described in terms of the exchange of *bosons*, integer-spin particles which are carriers of the fundamental interactions. The main characteristics of bosons and corresponding interactions are summarized in Table 1.2 (the *gravitational* interaction is not taken into account, as it is not relevant at the scales of mass and distance

Chapter 1: The Standard Model

Fermions	1 st fam.	2 nd fam.	3 rd fam.	Charge	Interactions
Quarks	u	c	t	$+\frac{2}{3}$	all
	d	s	b	$-\frac{1}{3}$	
Leptons	e	μ	τ	-1	weak, electromagnetic
	ν_e	ν_μ	ν_τ	0	weak

Table 1.1: Classification of the three families of fundamental fermions.

typical of the particle physics).

Quantum	Electromagnetic	Weak	Strong
	Photon (γ)	W^\pm, Z	Gluons
Mass [GeV]	0	80–90	0
Coupling constant	$\alpha(Q^2 = 0) \approx \frac{1}{137}$	$G_F \approx 1.2 \cdot 10^{-5} \text{ GeV}^{-2}$	$\alpha_s(m_Z) \approx 0.1$
Range [cm]	∞	10^{-16}	10^{-13}

Table 1.2: Fundamental interactions relevant in particle physics and corresponding carriers.

As previously mentioned, the SM describes these interactions by means of two gauge theories: the Quantum Chromodynamics and the theory of the electroweak interaction (Glashow-Weinberg-Salam model), which unifies the electromagnetic and weak interactions. Since the present work deals with a purely electroweak decay, in the next sections only the latter theory will be described in some detail.

1.2 The Electroweak Theory

From a historical point of view, the starting point for the study of electroweak interactions is Fermi's theory of muon decay [2], which is based on an effective four-fermion Lagrangian¹:

$$\mathcal{L} = -\frac{4G_F}{\sqrt{2}} \bar{\nu}_\mu \gamma^\alpha \frac{1-\gamma_5}{2} \mu \bar{e} \gamma_\alpha \frac{1-\gamma_5}{2} \nu_e, \quad (1.1)$$

with $G_F \approx 1.16639 \times 10^{-5} \text{ GeV}^{-2}$. Eq. 1.1 represents a “point like” interaction, with only one vertex and without any intermediate boson exchanged. It is usually referred to as a $V - A$ interaction, being formed by a *vectorial* and an *axial* component. The term $\frac{1}{2}(1 - \gamma_5)$ that appears in it is the negative chirality projector. Only the left-handed components of fermions takes part to this effective interaction.

Fermi's Lagrangian is not normalizable and it results in a non-unitary \mathcal{S} matrix. Both renor-

¹The same formalism can also be used to treat β decays, starting from a Lagrangian similar to Eq. 1.1.

malizability and unitarity problems can be overcome by describing the weak interaction with a *gauge* theory, i.e. requiring its Lagrangian to be invariant under local transformations generated by the elements of some Lie group (*gauge transformations*). The specific group of local invariance (*gauge group*) is to be determined by the phenomenological properties of the interaction and of the particles involved. In particular, the resulting Lagrangian must reduce to Eq. 1.1 in the low energy limit. A detailed derivation of this Lagrangian is not provided here, but the results are summarized in the following (for details about the GWS model, see Refs. [3, 4, 5]).

A gauge theory for weak interactions is conceived as an extension of the theory of electromagnetic interaction, the QED, which is based on the gauge group $U(1)_{EM}$, associated to the conserved quantum number Q (*electric charge*). In this case, the condition of local invariance under the $U(1)_{EM}$ group leads to the existence of a massless vector field, the *photon*.

A theory reproducing both the electromagnetic and weak interaction phenomenology is achieved by extending the gauge symmetry to the group $SU(2)_I \otimes U(1)_Y$. In this sense, the weak and electromagnetic interactions are said to be partially unified. The generators of $SU(2)_I$ are the three components of the *weak isospin* operator, $t^a = \frac{1}{2}\tau^a$, where τ^a are the Pauli matrices. The generator of $U(1)_Y$ is the *weak hypercharge* Y operator. The corresponding quantum numbers satisfy

$$Q = I_3 + \frac{Y}{2},$$

where I_3 is the third component of the weak isospin (eigenvalue of t^3).

Fermions can be divided in doublets of negative chirality (*left-handed*) particles and singlets of positive chirality (*right-handed*) particles, as follows:

$$L_L = \begin{pmatrix} v_{\ell,L} \\ \ell_L \end{pmatrix}, \quad \ell_R \quad \quad Q_L = \begin{pmatrix} u_L \\ d_L \end{pmatrix}, \quad u_R, \quad d_R, \quad (1.2)$$

where $\ell = e, \mu, \tau$, $u = u, c, t$ and $d = d, s, b$. Chirality is not to be confused with helicity. Helicity coincides with chirality only for massless particles (e.g. the neutrino²), since it is not possible to make Lorentz transformation which would result with reversing the orientation of the momentum vector, since their velocity always equals c . For massive particles, one can change helicity by changing the Lorentz frame—chirality however is the intrinsic property of the particle, independent of the frame of reference.

In Table 1.3, I_3 , Y and Q quantum numbers of all fermions are reported.

The requirement of local gauge invariance is one of the most fascinating concepts in quantum field theories as it implies the very existence of the fundamental interactions. Inspired by QED, imposing the requirement of local gauge invariance with respect to the $SU(2)_I \times U(1)_Y$ group *alone* introduces four massless vector fields, $W_\mu^{1,2,3}$ and B_μ , which couple to fermions with

²existence of neutrino mixing implies that the GWS has to be extended or that there is Beyond SM physics.

Chapter 1: The Standard Model

I₃	Y	Q
$\begin{pmatrix} u_L \\ d_L \end{pmatrix}$	$\begin{pmatrix} \frac{1}{2} \\ -\frac{1}{2} \end{pmatrix}$	$\begin{pmatrix} \frac{1}{3} \\ \frac{1}{3} \end{pmatrix}$
u_R, d_R	$0, 0$	$\frac{4}{3}, -\frac{2}{3}$
$\begin{pmatrix} \nu_{\ell,L} \\ \ell_L \end{pmatrix}$	$\begin{pmatrix} \frac{1}{2} \\ -\frac{1}{2} \end{pmatrix}$	$\begin{pmatrix} -1 \\ -1 \end{pmatrix}$
ℓ_R	0	-2
		-1

Table 1.3: Isospin (I_3), hypercharge (Y) and electric charge (Q) of the fermions in the 1st family. Other two families are exact replicas of the first one.

two different coupling constants, g and g' .

Notice that B_μ does not represent the photon field, because it arises from the $U(1)_Y$ group of hypercharge, instead of $U(1)_{EM}$ group of electric charge. The gauge-invariant Lagrangian for fermion fields can be written as follows:

$$\mathcal{L} = \overline{\Psi}_L \gamma^\mu \left(i\partial_\mu + g t_a W_\mu^a - \frac{1}{2} g' Y B_\mu \right) \Psi_L + \overline{\psi}_R \gamma^\mu \left(i\partial_\mu - \frac{1}{2} g' Y B_\mu \right) \psi_R \quad (1.3)$$

where

$$\Psi_L = \begin{pmatrix} \psi_L^1 \\ \psi_L^2 \end{pmatrix}$$

and where Ψ_L and ψ_R are summed over all the possibilities in Eq. 1.2.

As already stated, $W_\mu^{1,2,3}$ and B_μ do not represent physical fields, which are given instead by linear combinations of the four mentioned fields: the charged bosons W^+ and W^- correspond to³

$$W_\mu^\pm = \sqrt{\frac{1}{2}} (W_\mu^1 \mp i W_\mu^2), \quad (1.4)$$

while the neutral bosons γ and Z correspond to

$$A_\mu = B_\mu \cos \theta_W + W_\mu^3 \sin \theta_W \quad (1.5)$$

$$Z_\mu = -B_\mu \sin \theta_W + W_\mu^3 \cos \theta_W, \quad (1.6)$$

obtained by mixing the neutral fields W_μ^3 and B_μ with a rotation defined by the *Weinberg angle* θ_W . In terms of the fields in Eqs. 1.4 and 1.6, the interaction term between gauge fields and fermions, taken from the Lagrangian in Eq. 1.3, becomes

$$\mathcal{L}_{int} = \frac{1}{2\sqrt{2}} g (J_\alpha^+ W^{(+)\alpha} + J_\alpha^- W^{(-)\alpha}) + \frac{1}{2} \sqrt{g'^2 + g^2} J_\alpha^Z Z^\alpha - e J_\alpha^{EM} A^\alpha, \quad (1.7)$$

³ $W_\mu^{(-)}$ is sometimes denoted simply as W_μ . In that case one can note that $W_\mu^{(+)}$ equals W_μ^\dagger .

where J^{EM} is the electromagnetic current coupling to the photon field, while J^+, J^- and J^Z are the three weak isospin currents. It is found that

$$J_\alpha^Z = J_\alpha^3 - 2 \sin^2 \theta_W \cdot J_\alpha^{EM}.$$

A_μ can then be identified with the photon field and, requiring the coupling terms to be equal, one obtains

$$g \sin \theta_W = g' \cos \theta_W = e \quad (1.8)$$

which represents the electroweak unification. The GWS model thus predicts the existence of two charged gauge fields, which only couple to left-handed fermions, and two neutral gauge fields, which interact with both left- and right-handed components.

1.3 The Brout-Englert-Higgs Mechanism

In order to correctly reproduce the phenomenology of weak interactions, both fermion and gauge boson fields must acquire mass, in agreement with experimental results. Up to this point, however, all particles are considered massless: in the electroweak Lagrangian, in fact, a mass term for the gauge bosons would violate gauge invariance⁴, which is needed to ensure the renormalizability of the theory.

There must be something *external* to the fundamental fields fermions and gauge boson fields of the theory to generate the mass of the particle while preserving the local gauge symmetry which is at the very origin of the existence of interactions. In the Standard Model this is achieved by postulating the existence of a new field, a scalar field—the so-called Higgs field, which is needed to ensure the renormalizability of the theory. Masses are thus introduced with the so-called *BEH mechanism* [6, 7, 8, 9, 10, 11], which allows fermions and W^\pm, Z bosons to be massive⁵, while keeping the photon massless. Such mechanism is accomplished by means of a doublet of complex scalar fields

$$\phi = \begin{pmatrix} \phi^+ \\ \phi^0 \end{pmatrix} = \frac{1}{\sqrt{2}} \begin{pmatrix} \phi^1 + i\phi^2 \\ \phi^3 + i\phi^4 \end{pmatrix}, \quad (1.9)$$

which is introduced in the electroweak Lagrangian within the term

$$\mathcal{L}_{EWSB} = (D^\mu \phi)^\dagger (D_\mu \phi) + V(\phi^\dagger \phi), \quad (1.10)$$

where $D_\mu = \partial_\mu - ig t_a W_\mu^a + \frac{i}{2} g' Y B_\mu$ is the covariant derivative. The Lagrangian in Eq. 1.10 is invariant under $SU(2)_I \otimes U(1)_Y$ transformations, since the kinetic part is written in terms of

⁴Explicit mass terms for fermions would not violate gauge invariance, but in the GWS model the Lagrangian is also required to preserve invariance under *chirality* transformations, and this is achieved only with massless fermions.

⁵Rigorously speaking, the BEH mechanism is only needed to explain how W^\pm and Z acquire their mass. A *fermiophobic* Higgs boson, i.e. not coupling to fermions, is also looked for at the LHC [12].

covariant derivatives and the potential V only depends on the product $\phi^\dagger \phi$. The ϕ field is characterized by the following quantum numbers:

	I₃	Y	Q
$\begin{pmatrix} \phi^+ \\ \phi^0 \end{pmatrix}$	$\begin{pmatrix} \frac{1}{2} \\ -\frac{1}{2} \end{pmatrix}$	$\begin{pmatrix} 1 \\ 1 \end{pmatrix}$	$\begin{pmatrix} 1 \\ 0 \end{pmatrix}$

Writing the potential term as follows (see also Fig. 1.1)

$$V(\phi^\dagger \phi) = -\mu^2 \phi^\dagger \phi - \lambda(\phi^\dagger \phi)^2, \quad (1.11)$$

where the choice of $\mu^2 > 0$ and $\lambda > 0$ leads to a very interesting shape of the potential, crucial for the BEH mechanism. Such a choice of the potential, shown in Fig. 1.1, has a minimum for

$$\phi^\dagger \phi = \frac{1}{2}(\phi_1^2 + \phi_2^2 + \phi_3^2 + \phi_4^2) = -\frac{\mu^2}{2\lambda} \equiv \frac{v^2}{2}. \quad (1.12)$$

This minimum is not found for a single value of ϕ , but for a manifold of non-zero values. The choice of (ϕ^+, ϕ^0) corresponding to the ground state (i.e. the lowest energy state, or vacuum) is arbitrary and the chosen point is not invariant under rotations in the (ϕ^+, ϕ^0) plane: this is referred to as *spontaneous symmetry breaking*. If one chooses to fix the ground state on the ϕ^0 axis, the vacuum expectation value of the ϕ field is

$$\langle \phi \rangle = \frac{1}{\sqrt{2}} \begin{pmatrix} 0 \\ v \end{pmatrix}, \quad v^2 = -\frac{\mu^2}{\lambda}. \quad (1.13)$$

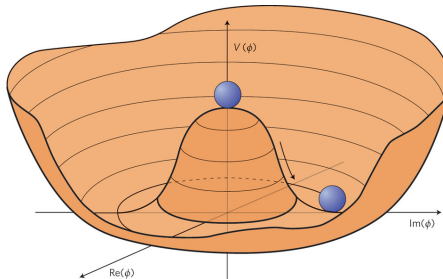


Figure 1.1: Shape of the Higgs potential of Eq. 1.11.

The ϕ field can thus be rewritten in a generic gauge, in terms of its vacuum expectation value:

$$\phi = \frac{1}{\sqrt{2}} e^{\frac{i}{v} \phi^a t_a} \begin{pmatrix} 0 \\ H + v \end{pmatrix}, \quad a = 1, 2, 3$$

where the three fields ϕ^a and the fourth $\phi^4 = H + v$ are called *Goldstone fields*. Being scalar and massless, they introduce four new degrees of freedom, in addition to the six degrees due to the transverse polarizations of the massless vector bosons W^\pm and Z . The unitary gauge is

fixed by the transformation

$$\phi' = e^{-\frac{i}{v}\phi^a t_a} \phi = \frac{1}{\sqrt{2}} \begin{pmatrix} 0 \\ H + v \end{pmatrix} = \frac{1}{\sqrt{2}} \begin{pmatrix} 0 \\ \phi^4 \end{pmatrix}.$$

The remaining field, the *Higgs field*, has now a zero expectation value.

Rewriting the Lagrangian in Eq. 1.10 with the ϕ field in the unitary gauge, \mathcal{L}_{EWSB} results from the sum of three terms:

$$\mathcal{L}_{EWSB} = \mathcal{L}_H + \mathcal{L}_{HW} + \mathcal{L}_{HZ}, \quad (1.14)$$

where the three terms can be written as follows, using the approximation $V \sim \mu^2 H^2 + \text{const}$ and neglecting higher order terms:

$$\begin{aligned} \mathcal{L}_H &= \frac{1}{2} \partial_\alpha H \partial^\alpha H + \mu^2 H^2 \\ \mathcal{L}_{HW} &= \frac{1}{4} v^2 g^2 W_\alpha W^{\dagger\alpha} + \frac{1}{2} v g^2 H W_\alpha W^{\dagger\alpha} \end{aligned} \quad (1.15)$$

$$\begin{aligned} \mathcal{L}_{HZ} &= \frac{1}{8} v^2 (g^2 + g'^2) Z_\alpha Z^\alpha + \frac{1}{4} v (g^2 + g'^2) H Z_\alpha Z^\alpha \\ &= \frac{1}{2} m_Z^2 Z_\alpha Z^\alpha + \frac{1}{2} g_{HZ} H Z_\alpha Z^\alpha. \end{aligned} \quad (1.16)$$

Eqs. 1.15 and 1.16 now contain mass terms for W^\pm and Z : each of the three gauge bosons has acquired mass and an additional degree of freedom, corresponding to the longitudinal polarization. At the same time, three of the four Goldstone bosons have disappeared from the Lagrangian \mathcal{L}_{EWSB} , thus preserving the total number of degrees of freedom: the degrees linked to the missing Goldstone bosons have become the longitudinal degrees of the vector bosons. A scalar boson, the so-called Higgs boson associated to the Higgs field is present as a new massive particle in the theory. The mass of the Higgs boson which is presumed to be related to self-interactions of the field is not predicted by the theory.

In summary, the BEH mechanism is used to introduce the weak boson masses without explicitly breaking the gauge invariance and thus preserving the renormalizability of the theory. When a symmetry is “spontaneously” broken, in fact, it is not properly eliminated—it is rather “hidden” by the choice of the ground state. In practice, this means that physical bosons can now be massive despite the fact that the fundamental gauge bosons of the theory remain massless. In addition, not only bosons, but all other particles acquire their mass through the interaction with Higgs field. It can be shown that the minimum for the Higgs field is still invariant for the $U(1)_{EM}$ group: the electromagnetic symmetry is therefore unbroken and the photon remains massless.

1.3.1 Vector Boson Masses and Couplings

Equations 1.15 and 1.16 show that the masses of vector bosons W^\pm and Z are related to the parameter v , the vacuum expectation value (VEV) which sets a characteristic mass scale for the EWSB, and to the electroweak coupling constants:

$$\begin{cases} m_W = \frac{1}{2} v g \\ m_Z = \frac{1}{2} v \sqrt{g^2 + g'^2} \end{cases} \rightarrow \frac{m_W}{m_Z} = \frac{g}{\sqrt{g^2 + g'^2}} = \cos \theta_W. \quad (1.17)$$

Also the couplings of vector bosons to the Higgs can be obtained from Eqs. 1.15 and 1.16 and are found to depend on the square of m_W and m_Z :

$$g_{HW} = \frac{1}{2} v g^2 = \frac{2}{v} m_W^2 \quad (1.18)$$

$$g_{HZ} = \frac{1}{2} v (g^2 + g'^2) = \frac{2}{v} m_Z^2. \quad (1.19)$$

A relation between decay ratios of Higgs boson to a W pair and to a Z pair can be derived from Eqs. 1.18 and 1.19:

$$\frac{BR(H \rightarrow W^+ W^-)}{BR(H \rightarrow ZZ)} = \left(\frac{g_{HW}}{\frac{1}{2} g_{HZ}} \right)^2 = 4 \left(\frac{m_W^2}{m_Z^2} \right)^2 \sim 2.4.$$

Finally, the characteristic mass scale for EWSB can be determined from the relation between the v parameter and the Fermi constant G_F :

$$v = \left(\frac{1}{\sqrt{2} G_F} \right)^{\frac{1}{2}} \simeq 246 \text{ GeV}. \quad (1.20)$$

1.3.2 Fermion Masses and Couplings

The Higgs mechanism is also used to generate the fermion masses, by introducing in the SM Lagrangian a $SU(2)_I \otimes U(1)_Y$ invariant term (called *Yukawa term*) that represents the interaction between the Higgs and the fermion fields. Since ϕ is an isodoublet, while the fermions are divided in left-handed doublet and right-handed singlet, the Yukawa terms (one for each fermion generation) must have the following expression for leptons:

$$\mathcal{L}_\ell = -G_{H\ell} \cdot \bar{l}_\ell \phi \ell_R + \bar{\ell}_R \phi^\dagger l_\ell.$$

In the unitary gauge, the first component of ϕ is zero, therefore a mass term will arise from the Yukawa Lagrangian only for the second component of l_ℓ : this correctly reproduces the fact that neutrino is (approximately) massless.

$$\mathcal{L}_\ell = -\frac{G_{H\ell}}{\sqrt{2}} v \bar{\ell} \ell - \frac{G_{H\ell}}{\sqrt{2}} H \bar{\ell} \ell. \quad (1.21)$$

1.3. The Brout-Englert-Higgs Mechanism

For what concerns the quark fields, the *down* quarks (d, s, b) are treated in the same way as leptons; *up* quarks (u, c, t), instead, must couple to the charge-conjugate of ϕ

$$\phi^c = -i\tau_2\phi^* = \frac{1}{\sqrt{2}} \begin{pmatrix} \phi^3 - i\phi^4 \\ -\phi^1 + i\phi^4 \end{pmatrix},$$

which becomes in the unitary gauge

$$\phi^c = \frac{1}{\sqrt{2}} \begin{pmatrix} \eta + v \\ 0 \end{pmatrix}.$$

The Yukawa Lagrangian will be therefore

$$\mathcal{L}_Y = -G_{H\ell}\bar{L}_L\phi\ell_R - G_{Hd}\bar{Q}_L\phi d_R - G_{Hu}\bar{Q}_L\phi^c u_R + h.c.. \quad (1.22)$$

From Eq. 1.21, the mass of a fermion (apart from neutrinos) and its coupling constant to the Higgs boson are found to be

$$m_f = \frac{G_{Hf}}{\sqrt{2}}v \quad (1.23)$$

$$g_{Hf} = \frac{G_{Hf}}{\sqrt{2}} = \frac{m_f}{v}. \quad (1.24)$$

Being the G_{Hf} free parameters, the mass of the fermions cannot be predicted by the theory.

At this point we can understand more deeply what the fermion mass terms in the Lagrangian really means. The interaction with the Higgs field transform a right-handed chirality in a left-handed chirality (and vice versa) such that the physical object becomes a massive particle. The mass term is therefore only measure of the strength of the interaction of particle with Higgs field.

This analysis is somewhat illustrative, since it does not take account of the fact that in reality there are three families of quarks and leptons. Complete analysis would be more complicated, since the weak mass eigenstates are not the same as the physical mass eigenstates. If one wants to deal with the physical particles, one needs to make transformation from the weak mass basis to physical mass bases. This is accomplished by the usual unitary transformation matrices, Cabibbo–Kobayashi–Maskawa (CKM) and Pontecorvo–Maki–Nakagawa–Sakata (PMNS) matrices, for quark and lepton sectors respectively.

1.3.3 Higgs Boson Mass

Among the 18 free parameters of the SM⁶, the Higgs boson mass is the only still undetermined one. Although the Higgs boson mass is not predicted by the theory, the assumption that the Higgs boson acquires a mass, e.g. via self-interactions of the Higgs field, is essential for the EWSB mechanism, i.e. without the mass of the Higgs, there would be no "Mexican hat" potential. Its mass depends on the parameters v and λ , but while the former can be estimated by its relation with the G_F constant of Fermi's theory, the latter is characteristic of the field ϕ and cannot be determined other than measuring the Higgs mass itself. However, both theoretical and experimental constraints exist, including those from direct search at colliders, in particular LEP.

Theoretical Constraints

Theoretical constraints to the Higgs mass value [13] can be found by imposing the energy scale Λ up to which the SM is valid, before the perturbation theory breaks down and non-SM phenomena emerge. The upper limit is obtained by requiring that the running quartic coupling of Higgs potential λ remains finite up to the scale Λ (*triviality*). A lower limit is found instead by requiring that λ remains positive after the inclusion of radiative corrections, at least up to Λ : this implies that the Higgs potential is bounded from below, i.e. the minimum of such potential is an absolute minimum (*vacuum stability*). A looser constraint is found by requiring such minimum to be local, instead of absolute (*metastability*). These theoretical bounds on the Higgs mass as a function of Λ are shown in Fig. 1.2.

If the validity of the SM is assumed up to the Planck scale ($\Lambda \sim 10^{19}$ GeV), the allowed Higgs mass range is between 130 and 190 GeV, while for $\Lambda \sim 1$ TeV the Higgs mass can be up to 700 GeV. On the basis of these results, however, colliders should look for the Higgs boson up to masses of ~ 1 TeV. If the Higgs particle is not found in this mass range, then a more sophisticated explanation for the EWSB mechanism will be needed.

Very important limits come from the requirement of the unitarity of S-matrix, which basically can be reduced to the claim that scattering probability cannot exceed the value of 100%. In order to avoid violation of unitarity, the Higgs boson plays crucial role, since this very concept allows us to regulate the unitarity of S-matrix as Λ increases.

Experimental Constraints

Bounds on the Higgs mass are also provided by electroweak precision measurements at LEP, SLC and Tevatron [14] (updated in 2010). Direct searches at LEP-II have set the limit $m_H > 114.4$ GeV (95% C.L.) [15] and those performed at Tevatron have excluded the mass

⁶ 9 fermion masses (+ 3 neutrino masses, if $m_\nu \neq 0$), 3 CKM mixing angles + 1 phase (+ 3 more angles + 1 additional phase for neutrinos), the electromagnetic coupling constant α_{EM} , the strong coupling constant α_S , the weak coupling constant G_F , the Z boson mass and the Higgs boson mass.

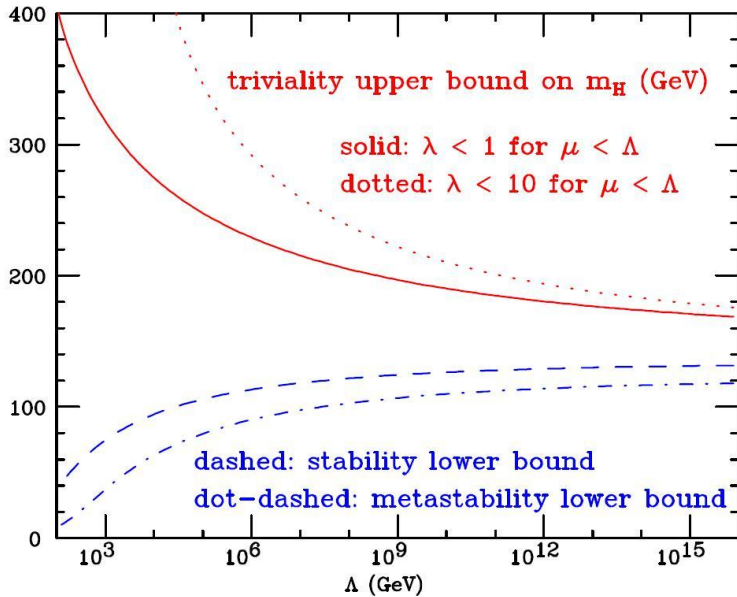


Figure 1.2: Red line: triviality bound (for different upper limits to λ); blue line: vacuum stability (or metastability) bound on the Higgs boson mass as a function of the new physics (or cut-off) scale Λ [13].

range $158 < m_H < 175$ GeV also at 95% C.L. [16] (see Fig. 1.3 left). Moreover, since the Higgs boson contributes to radiative corrections, many electroweak observables are logarithmically sensitive to m_H and can thus be used to constrain its mass. All the precision electroweak measurements performed by the four LEP experiments and by SLD, CDF and D \emptyset have been combined together and fitted [17], assuming the SM as the correct theory and using the Higgs mass as free parameter. The result of this procedure is summarized in Fig. 1.3 (b), where $\Delta\chi^2 = \chi^2 - \chi^2_{min}$ is plotted as a function of m_H .

The solid curve is the result of the fit, while the shaded band represents the theoretical uncertainty due to unknown higher order corrections. The indirectly measured value of the Higgs boson mass, corresponding to the minimum of the curve, is $m_H = 91^{+30}_{-23}$ GeV at 68% confidence level (CL). This value corresponds to the black line in Fig. 1.3 and does not take the theoretical uncertainties into account. The indirect constraints thus favour a low mass value for the Higgs boson. But the dependence on the Higgs boson mass of the indirect constraints is only logarithmic such that the central value must be interpreted with care. It remains essential to search for a SM Higgs boson over the full mass range allowed by the theory.

Such results are model-dependent, as the loop corrections take into account only contributions from known physics. This result is thus well-grounded only within the SM theory and has always to be confirmed by the direct observation of the Higgs boson.

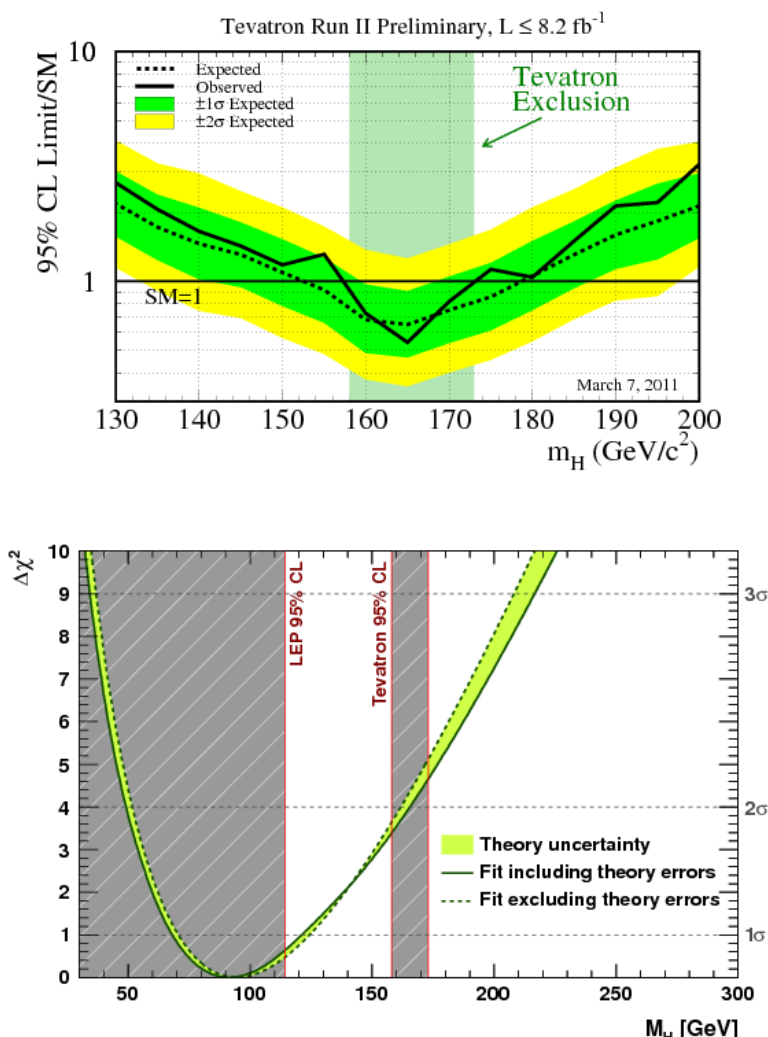


Figure 1.3: (a) 2011 Tevatron exclusion at 95% C.L. in Higgs boson mass range from 158 to 172 GeV. (b) $\Delta\chi^2$ of the fit to the electroweak precision measurements of LEP, SLC, and Tevatron as a function of the Higgs mass (2012). The solid (dashed) lines give the results when including (ignoring) theoretical errors. The gray area represents the region excluded by direct searches at LEP and Tevatron.

2 Higgs Boson Search at the LHC

The experiments at the LHC are searching for the SM Higgs boson within the full mass range allowed by the theory given unitary and above LEP constraints, i.e. from 114 up to about 800 GeV to 1 TeV. In the work described by this thesis, the analysis has been performed up to 800 GeV. In this chapter, the main Higgs production and decay processes are described. This will allow to identify the most promising channels in the perspective of a Higgs boson discovery.

While the Higgs mass is not predicted by the theory, the Higgs couplings to the fermions or bosons are predicted to be proportional to the corresponding particle masses for fermions or squared masses for bosons, as in Eqs. 1.18, 1.19 and 1.24. For this reason, the Higgs production and decay processes are dominated by channels involving the coupling of Higgs to heavy particles, mainly to W^\pm and Z bosons and to the third generation fermions. For what concerns the remaining gauge bosons, the Higgs does not couple to photons and gluons at tree level, but only by one-loop graphs where the main contribution is given by $q\bar{q}$ and by W^+W^- loops.

2.1 Higgs Production

The main processes contributing to the Higgs production at a hadron collider are represented by the Feynman diagrams in Fig. 2.1 and the corresponding cross-sections for proton-proton centre of mass energies of $\sqrt{s} = 7$ TeV and $\sqrt{s} = 8$ TeV, adopted by the LHC, are shown in Fig. 2.2. The switch from collisions at 7 to 8 TeV was mostly motivated by searches for physics beyond the SM at the TeV scale. It nevertheless brings a sizeable increase of the production cross-section for the Higgs boson, e.g. by about 27% for the inclusive production at $m_H = 125$ GeV.

"[...] cross-sections for proton-proton centre of mass energies of [...] are shown in Fig. 2.2. The switch from collisions at 7 to 8 TeV was mostly motivated by searches for physics beyond the SM at the TeV scale. It nevertheless brings a sizeable increase of the production cross-section for the Higgs boson, e.g. by about 27% for the inclusive production at $m_H = 125$ GeV.

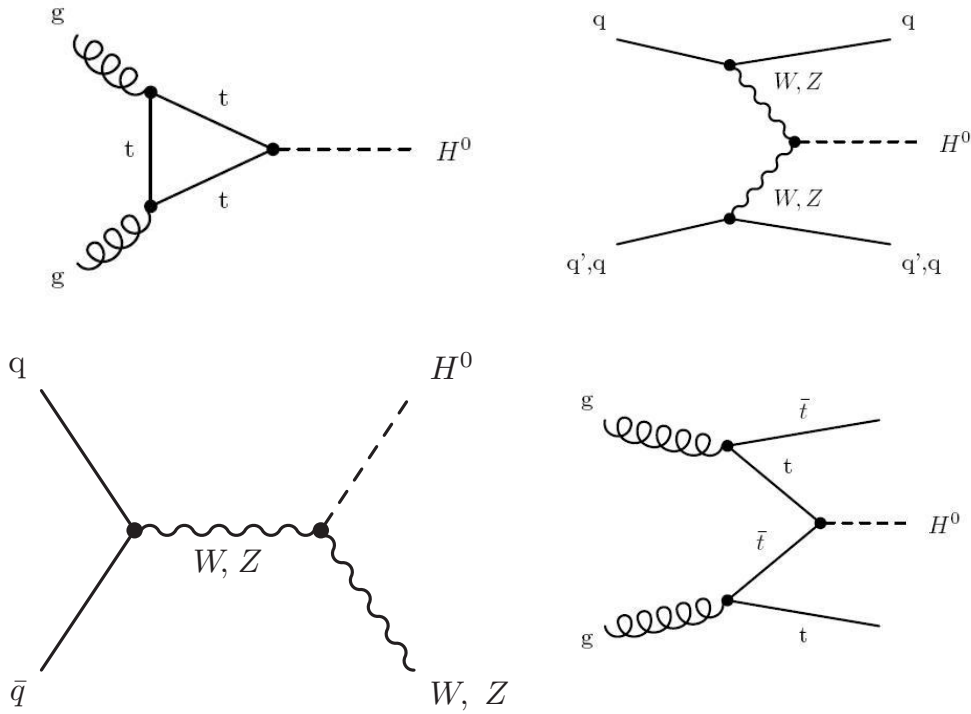


Figure 2.1: Higgs production mechanisms at tree level in proton-proton collisions: (a) gluon-gluon fusion; (b) VV fusion; (c) W and Z associated production (or *Higgsstrahlung*); (d) $t\bar{t}$ associated production.

2.1.1 Gluon-gluon Fusion

The gg fusion is the dominating mechanism for the Higgs production at the LHC over the whole Higgs mass spectrum, because of the high luminosity of gluons at the nominal centre of mass energy. The parton (in particular *gluon*) luminosity, is a convenient measure of the reach of a collider of given energy taking into account relevant Parton Distribution Function (PDF). The high gluon luminosity in pp collisions at LHC energies compared to Tevatron, is the basis for the simplifying slogan—“The Tevatron is a quark collider and the LHC is a gluon collider”. The gg fusion process is shown in Fig. 2.1(a), with a t -quark loop as the main contribution. Next-to-leading order QCD corrections have been found to increase the cross-section for this process by a factor of ~ 2 . Next-to-next-to leading order calculations are also available and show a further increase of about 10% to 30%. Other sources of uncertainty are the higher order corrections (10 \div 20% estimated) and the choice of parton density function ($\sim 10\%$).

2.1.2 Vector Boson Fusion

The Vector boson fusion (VBF) (or VV fusion) shown in Fig. 2.1(b) is the second contribution to Higgs production cross section. It is about one order of magnitude lower than gg fusion for

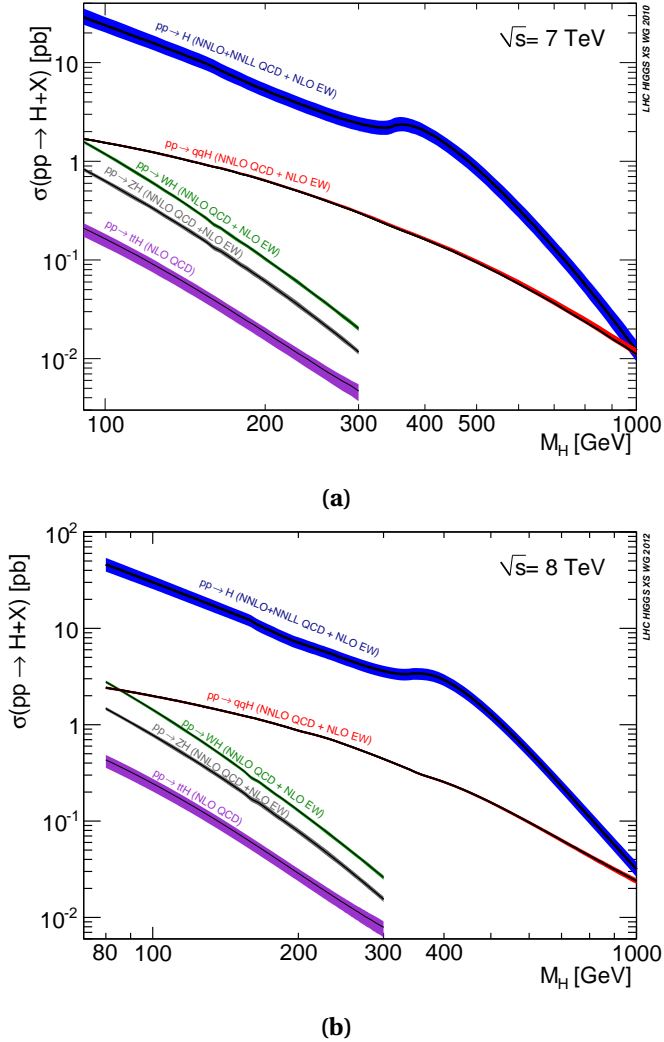


Figure 2.2: Higgs production cross-sections at 7 and 8 TeV as a function of the Higgs mass.

a large range of m_H values and the two processes become comparable only for very high Higgs masses, of $\mathcal{O}(1 \text{ TeV})$. However, this channel is very interesting because of its clear experimental signature: the presence of two spectator jets with high invariant mass in the forward region provides a powerful tool to tag the signal events and discriminate the backgrounds, thus improving the signal to background ratio, despite the low cross-section. Moreover, both leading order and next-to-leading order cross-sections for this process are known with small uncertainties and the higher order QCD corrections are quite small.

2.1.3 Higgsstrahlung and Associated Production

In the *Higgsstrahlung* process shown in Fig. 2.1(c), the Higgs boson is produced in association with a W^\pm or Z boson, which can be used to tag the event. The cross-section for this process is

Chapter 2: Higgs Boson Search at the LHC

several orders of magnitude lower than the gg fusion process, and approaches the production rates from VBF only for masses around $m_H = 100$ GeV. The QCD corrections are quite large for the Higgsstrahlung production modes. The next-to-leading order cross-section is found to be about 1.2–1.4 times larger than the leading-order one.

"The cross-section for this process [...] the gg fusion process, and approaches the production rates from VBF only for masses around [...]

The last process, illustrated in Fig. 2.1(d), is the associated production of a Higgs boson with a $t\bar{t}$ pair. Again the cross-section for this process is almost two orders of magnitude lower than the gg and only several times lower than VBF around $m_H = 100$ GeV. The presence of the $t\bar{t}$ pair in the final state can provide a good experimental signature. The higher order corrections increase the cross-section by a factor of about 1.2.

2.2 Higgs Decay

The branching ratios of the different Higgs decay channels are shown in Fig. 2.3 as a function of the Higgs mass. Fermion decay modes dominate the branching ratio in the low mass region (up to ~ 150 GeV). In particular, the $H \rightarrow b\bar{b}$ channel is the most important contribution, since the b quark is the heaviest available fermion. When the decay channels into vector boson pairs open up, they quickly dominate. A peak in the $H \rightarrow W^+W^-$ decay is visible around 160 GeV, when the production of two on-shell W 's becomes possible and the production of a real ZZ pair is still not allowed. At high masses (~ 350 GeV), also $t\bar{t}$ pairs can be produced.

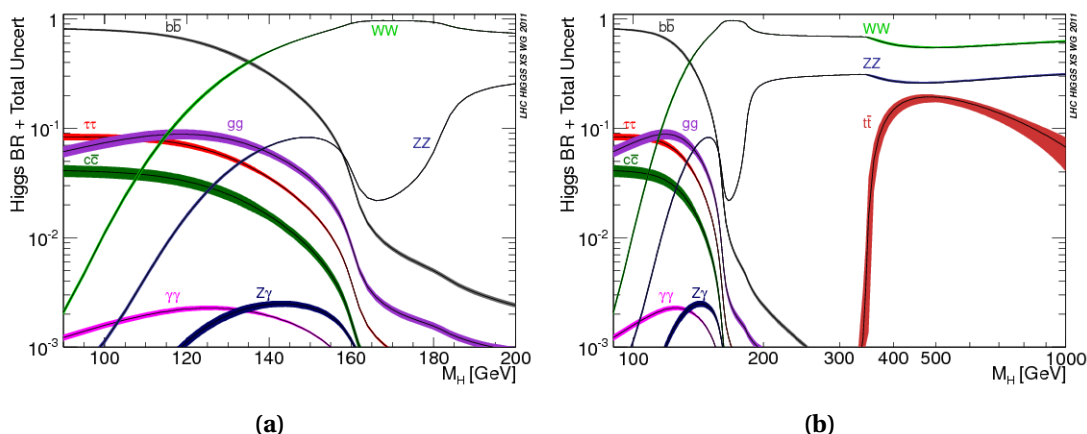


Figure 2.3: Branching ratios for different Higgs decay channels as a function of the Higgs mass in low mass range (a) and full search range (b).

The most promising decay channels for the Higgs discovery do not only depend on the corresponding branching ratios, but also on the capability of experimentally detecting the signal while rejecting the backgrounds. Such channels are illustrated in the following, depending on

the Higgs mass range.

2.2.1 Low Mass Region

Though the branching ratio in this region is dominated by the Higgs decay into $b\bar{b}$, the di-jet background makes it quite difficult to use this channel for a Higgs discovery. However, the $b\bar{b}$ channel has been exploited in the *boosted* regime, in association with a vector boson decaying leptonically, by CMS [18], by ATLAS [19] and by CDF and D0 [20]. The final-state leptons allow to discriminate signal events from QCD backgrounds with only two jets.

For Higgs boson with $m_H < 120$ GeV, the channel $H \rightarrow \gamma\gamma$ seems to be the most promising. Despite of its low branching ratio, the two high energy photons constitute a very clear signature, which only suffers from the $q\bar{q} \rightarrow \gamma\gamma$ and $Z \rightarrow e^+e^-$ backgrounds.

2.2.2 Intermediate Mass Region

For a Higgs mass value between 120 and 135 GeV, the Higgs decays into $WW^{(*)}$, $ZZ^{(*)}$ and $Z\gamma$ open up and their branching ratios increase. Still, there is a significant contribution from the $\gamma\gamma$ decays, so most of the channels are accessible in this range.

The branching ratio of $H \rightarrow WW^{(*)}$ which is higher than the one from $H \rightarrow ZZ^{(*)}/\gamma$ as was explained in section 1.3.1, is here relatively higher given that at least one Z boson in the $ZZ^{(*)}$ channel is pushed further away off mass shell. The $H \rightarrow WW^{(*)}$ is disfavoured from the point of view of observability because of the presence of the two neutrinos in the final state, which makes it impossible to reconstruct the Higgs mass. Such measurement can be performed instead when one W decays leptonically and the other one decays in two quarks. But, in this case, the final state suffers from the high hadronic background.

The decay $H \rightarrow ZZ^{(*)} \rightarrow 4\ell$, despite its lower branching ratio, offers a very clear experimental signature and high signal to background ratio. Furthermore, it allows to reconstruct the Higgs mass with high precision. Therefore, this channel has a major role for a Higgs search in this mass range.

2.2.3 High Mass Region

This region corresponds to Higgs mass values above 135 GeV, where the WW or ZZ decay channel opens up. Although the $H \rightarrow ZZ$ decay width is about 2.4 times lower than $H \rightarrow WW$ one, a decay into four charged leptons (muons or electrons) with extremely clean signature gives rise to the channel nickname—*golden channel* for a high mass Higgs boson search.

2.2.4 Higgs total Decay Width

The total width of the Higgs boson resonance, which is given by the sum over all the possible decay channels, is shown in Fig. 2.4 as a function of m_H . Below the $2 \times m_W$ threshold, the Higgs width is of $\mathcal{O}(\text{MeV})$. It then increases rapidly but remains below 1 GeV for masses up to ~ 190 GeV. A measurement of the intrinsic width is thus impossible at low mass where the measured width is completely dominated by the experimental resolution.

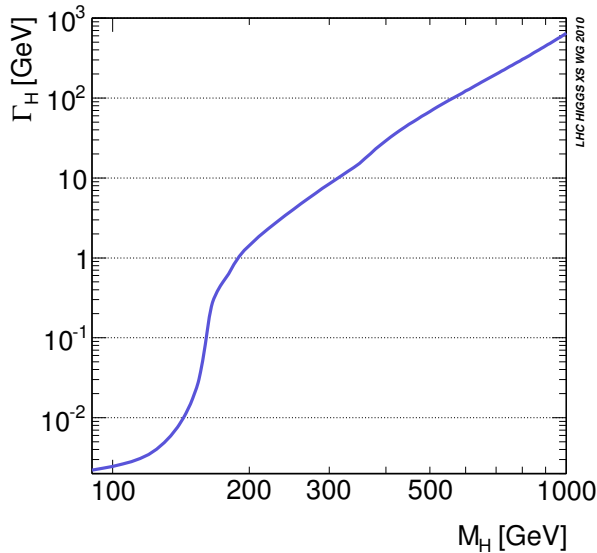


Figure 2.4: Higgs total decay width as a function of the Higgs mass.

In the high mass region ($m_H > 2 m_Z$), the total Higgs width is dominated by the $W^+ W^-$ and ZZ partial widths, which can be written as follows:

$$\Gamma(H \rightarrow W^+ W^-) = \frac{g^2}{64\pi} \frac{m_H^3}{m_W^2} \sqrt{1-x_W} \left(1 - x_W + \frac{3}{4} x_W^2\right) \quad (2.1)$$

$$\Gamma(H \rightarrow ZZ) = \frac{g^2}{128\pi} \frac{m_H^3}{m_W^2} \sqrt{1-x_Z} \left(1 - x_Z + \frac{3}{4} x_Z^2\right), \quad (2.2)$$

where

$$x_W = \frac{4m_W^2}{m_H^2}, \quad x_Z = \frac{4m_Z^2}{m_H^2}.$$

As the Higgs mass grows, $x_W, x_Z \rightarrow 0$ and the leading term in Eqs. 2.1 and 2.2 grows proportional to m_H^3 . Summing over the $W^+ W^-$ and ZZ channels, the Higgs width in the high mass region can be written as

$$\Gamma(H \rightarrow VV) = \frac{3}{32\pi} \frac{m_H^3}{v^2}. \quad (2.3)$$

From Eq. 2.3, it results that $\Gamma_H \approx m_H$ for $m_H \approx 1.4$ TeV. When m_H becomes larger than a TeV

it becomes experimentally very problematic to separate the Higgs resonance from the VV continuum. Actually, being the resonance width larger than its own mass, the Higgs cannot be properly considered as a particle any more. In addition, if the Higgs mass is above 1 TeV, the SM predictions violate unitarity (see Fig. 1.2). All these considerations suggest the TeV as a limit for the Higgs boson mass: at the TeV scale at least, the Higgs boson must be observed, or new physics must emerge.

Accelerate and Collide Part II

3 Large Hadron Collider

Since its creation in 1954, the European Organization for Nuclear Research (CERN) has housed numerous particle accelerators and its experiments played a major role in the construction of the Standard Model of Particle Physics. The Large Electron-Positron Collider (LEP), built inside a 26.7 km circular tunnel located approximately 100 m in the underground, made also a giant step in the hunt for the Higgs boson, that is still ongoing today.

The Large Hadron Collider (LHC) [21, 22] was installed in the tunnel that had been constructed for the LEP machine, and took over in this search. It inherited the Proton Synchrotron (PS) and the Super Proton Synchrotron (SPS) accelerator systems shown schematically in Fig. 3.1. Four interaction regions were equipped, and host four main detectors: ATLAS, CMS, ALICE and LHCb.

The two general purpose experiments, CMS and ATLAS, study SM physics processes (e.g. electroweak processes, physics of the top and bottom quarks). Their main goal is the search for the Higgs boson, and physics beyond the SM.

The LHC is designed for two kinds of collisions: collisions of protons, and collisions of Heavy ions. This section focuses on the case of proton-proton collisions.

3.1 Performance Goals

The LHC was designed to probe the scalar sector, and new physics in case of the absence of a Higgs boson. The unitarity constraint, mentioned in chapter 1.3, sets a limit on the Higgs boson mass: $m_H < 780 \text{ GeV}$. Besides, when applied to the tree-level amplitude for $W_L^+ W_L^- \rightarrow Z_L Z_L$ and in the absence of fundamental Higgs, it imposes that new physics appears at a scale $\Lambda \lesssim 1.2 \text{ TeV}$. Hence the LHC collisions should be able to produce Higgs bosons of masses lower than the TeV; besides they should provide interactions of W_L bosons at a centre of mass energy of the order of the TeV, in order to probe the unitarity constraint. The second requirement is tighter and requires a proton-proton centre of mass energy of the order of 14 TeV.

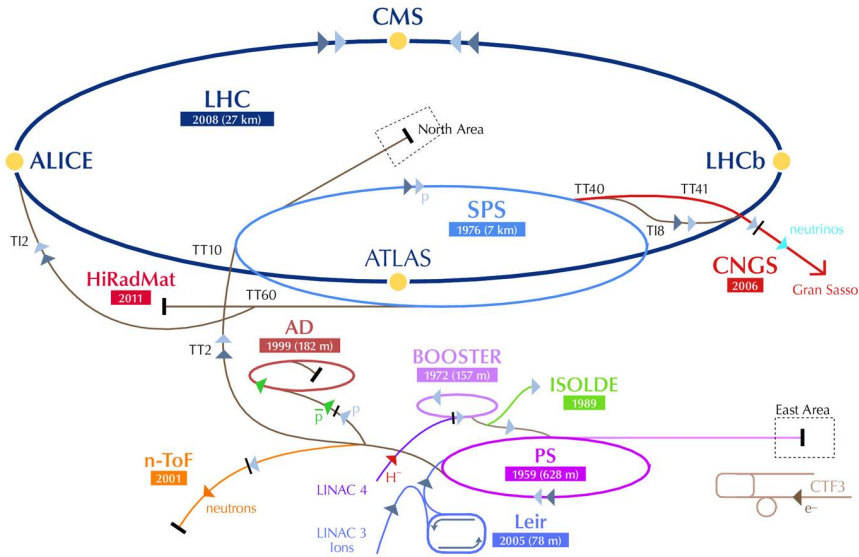


Figure 3.1: The LHC accelerator complex. Proton acceleration starts from a linear accelerator (LINAC) that injects the protons to the Proton Synchrotron (PS), which accelerates them to 25 GeV. In the following stage, the Super Proton Synchrotron (SPS) accelerates the beams to 450 GeV and subsequently injects them into the LHC ring.

The number of events of a given physics process that occur during one second, is directly related to the cross-section of the corresponding process, $\sigma_{process}$, via the luminosity \mathcal{L} of the machine:

$$N = \mathcal{L} \sigma_{process} \quad (3.1)$$

The production cross-sections for the Higgs boson in proton-proton collisions are several orders of magnitude below the background. This is illustrated in Fig. 3.2. While the Higgs boson is expected to be copiously produced at the LHC, it is a rare phenomena with respect to the background, sitting about 10 orders of magnitude below the QCD inelastic collisions cross-section, and 4-5 orders of magnitude below single Z/W production cross-section. In order to detect the Higgs boson, the analysis has to rely on specific final states offering sufficient discrimination against the background. For the production of massive particles such as a Higgs boson, the signal to background ratio improves with increasing \sqrt{s} of the pp collisions. Hence, in order to be able to detect the Higgs boson in rare decay modes, both the luminosity and the centre of mass energy must be as high as possible. For the LHC, the choice focused on a very high collision luminosity, higher than for any collider before.

The nominal centre of mass energy for LHC collisions is $\sqrt{s} = 14$ TeV (7 TeV per beam), and the nominal peak luminosity is $\mathcal{L} = 10^{34} \text{ cm}^{-2}\text{s}^{-1}$ for the CMS and ATLAS experiments. The right axis on Fig. 3.2 shows that for these values¹, a Higgs boson with a mass of 500 GeV would

¹At such a high luminosity, approximately one billion inelastic collisions are created every second. More

3.2. Nominal Centre of Mass Energy and Magnet Systems

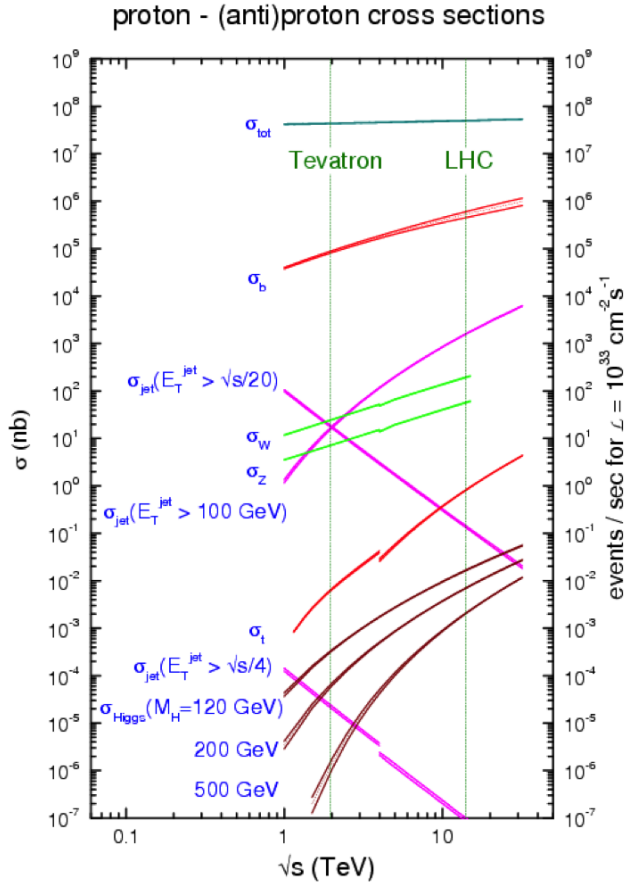


Figure 3.2: Expected cross-section as a function of energy in the centre of mass system for proton-proton collisions. The cross-sections are indicated in the left vertical axis. The right vertical axis shows the number of events expected per second for a luminosity of $\mathcal{L} = 10^{33} \text{ cm}^{-2} \text{s}^{-1}$.

be produced approximately every 100 s. To estimate the number of measured events, one must then take into account the Higgs branching ratios and the experiment reconstruction and (online and offline) selection efficiencies.

3.2 Nominal Centre of Mass Energy and Magnet Systems

The LHC being a proton accelerator with a constrained circumference, the maximal energy per beam is related to the strength of the dipole field that maintains the beams in orbit.

The nominal LHC beam energy of 7 TeV is possible thanks to a global magnet system at the

generally, the low proportion of physics events in comparison to the overall number of inelastic interactions suggests the necessity, for experiments, of an efficient triggering system, to select the events to be recorded.

edge of the technology. The system uses a total of about 9600 magnets.

The 1232 dipole magnets use niobium-titanium (NbTi) cables. They are brought to a temperature of 1.9 K, by pumping superfluid helium into the magnets. A total of 120 t of superfluid helium is used.

At that temperature², the dipoles are in a superconducting state, and when carrying a current of 11850 A they provide a field of 8.33 T. Such a magnetic field is necessary to bend the 7 TeV beams around the 27-km ring of the LHC.

Among the other magnets, quadrupoles play a major role at collision points: they are used to focus the beam, and maximize the probability of collision.

3.3 Nominal Luminosity and Beam Parameters

The very high LHC design luminosity implies many constraints on the proton beam parameters. In the general case of two colliding beams, the luminosity \mathcal{L} writes:

$$\mathcal{L} = f_{rev} n_b \frac{N_1 N_2}{A} \quad (3.2)$$

Where f_{rev} is the revolution frequency, n_b is the number of bunches per beam, N_1 and N_2 are the number of particles in the bunches of each colliding beam, and A is the cross-section of the beams.

At LHC, the bunches are filled with an identical number of protons and $N_1 = N_2 = N_b$. The cross-section of the beam writes:

$$A = 4\pi\epsilon_n \frac{\beta^*}{\gamma_r} \quad (3.3)$$

Where ϵ_n is the normalized transverse beam emittance³ (with a design value of 3.75 μm), and β^* is the beta function at collision point⁴, which is then corrected by the relativistic gamma factor γ_r .

Finally, the expression in (3.2) has to be corrected by a geometric luminosity reduction factor, F , due to the crossing angle at interaction point.

Hence, the final expression of the luminosity writes:

$$\mathcal{L} = \frac{f_{rev} n_b N_b^2 \gamma_r}{4\pi\epsilon_n \beta^*} F \quad (3.4)$$

²NbTi becomes superconducting below a temperature of 10 K. At a temperature of 4.2 K (which is the temperature in the Tevatron collider magnets), the dipoles would produce a magnetic field smaller than 7 T.

³The beam emittance of a particle accelerator is the extent occupied by the particles of the beam in position and momentum phase space.

⁴It measures the beam focalization.

Given the beam velocity ($v \sim c \sim 3 \cdot 10^8 \text{ m s}^{-1}$) and the LHC circumference (26.7 km), the revolution frequency is $f_{rev} = 11 \text{ kHz}$. Besides, the nominal value of the beta function at impact point is $\beta^* = 0.55 \text{ m}$. So the nominal luminosity is reached with $n_b = 2,808$ bunches per beam, and $N_b = 1.15 \cdot 10^{11}$ protons per bunch.

3.4 Lattice Layout

Such a high beam intensity could not be obtained with antiproton beams⁵. This is why a ‘simple’ particle-antiparticle accelerator collider configuration⁶ could not be used at LHC.

The LHC is therefore designed with two rings: two separate magnet fields and vacuum chambers, in a twin-bore magnet design. The only common sections are located at the insertion regions, equipped with the experimental detectors. The configuration is shown in Fig. 3.3.

A summary of the machine parameters [23] is given in Table 3.1. The numbers indicated correspond to the nominal values. In addition to the previously mentioned parameters, the luminosity lifetime is an important parameter at LHC and colliders in general. The luminosity tends to decay during a physics run, because of the degradation of intensities and emittances of the circulating and colliding beams.

Circumference	26.659 km
Center-of-mass energy (\sqrt{s})	14 TeV
Nominal Luminosity (\mathcal{L})	$10^{34} \text{ cm}^{-2}\text{s}^{-1}$
Luminosity lifetime	15 hr
Time between two bunch crossings	24.95 ns
Distance between two bunches	7.48 m
Longitudinal max. size of a bunch	7.55 cm
Number of bunches (n_b)	2808
Number of protons per bunch (N_b)	1.15×10^{11}
beta function at impact point (β^*)	0.55 m
Transverse RMS beam size at impact point (σ^*)	$16.7 \mu\text{m}$
Dipole field at 7 TeV (B)	8.33 T
Dipole temperature (T)	1.9 K

Table 3.1: The LHC nominal parameter values, for proton-proton collisions, relevant for the detectors.

⁵In comparison, the highest luminosity achieved at the Tevatron proton-antiproton collider after the latest upgrades, is $3 \cdot 10^{32} \text{ cm}^{-2}\text{s}^{-1}$: this corresponds to the highest antiproton density ever produced, with the most performant technology. The LHC design luminosity must be two orders of magnitude higher.

⁶In such a configuration, both beams can share the same phase space, so a single ring can be used.

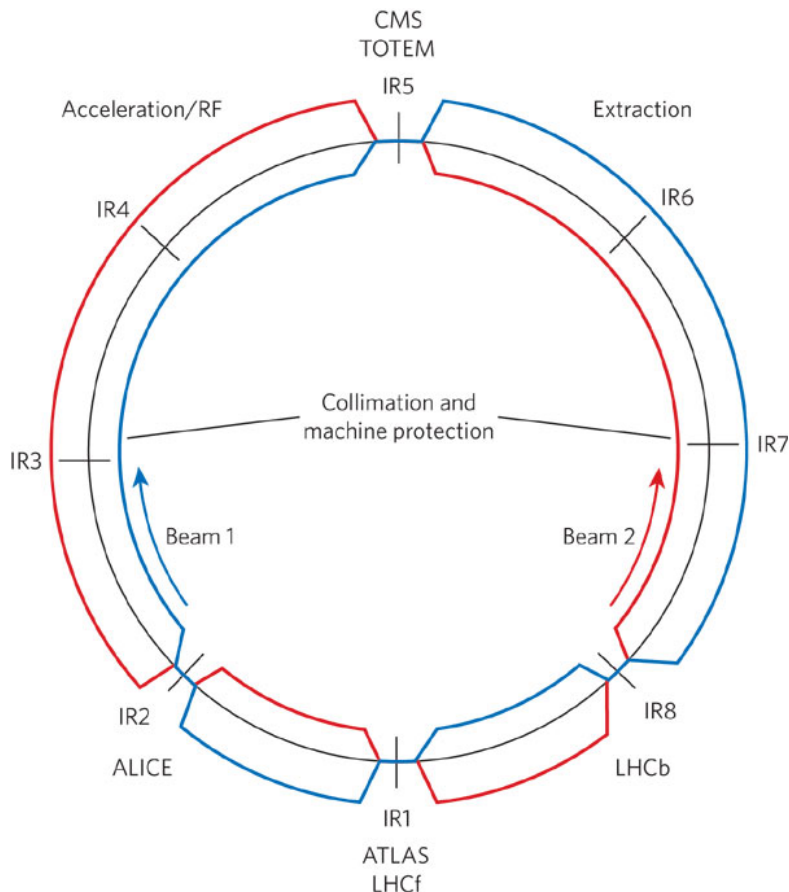


Figure 3.3: Schematic layout of the LHC where Beam 1 is accelerated clockwise and Beam 2 anticlockwise.

3.5 LHC Collision Detectors

The design parameters necessary to reach the high luminosity makes the LHC a unique machine and imposes important constraints for the detectors.

Under nominal conditions, the LHC will produce 10^9 inelastic collision events per second: a bunch crossing rate of 40 MHz (i.e. a bunch crossing spacing of 25 ns), with ~ 20 collision events expected per bunch crossing.

3.5.1 Pile-up Events

Because of the large number of protons per bunch, a significant number of inelastic collisions are expected to occur at each crossing, corresponding to an average of 1000 particles per bunch crossing. To distinguish such events from one another, a high granularity is mandatory, which implies a large number of detector channels.

Besides, the detectors must provide a fast response (mainly concentrated in one bunch spacing, i.e. 25 ns), with a good time resolution (few ns), in order to distinguish the events from two consecutive bunch crossings. This requires a precise synchronization of all detector channels. The limit where two consecutive signals start to overlap is called out-of-time pile-up, and affects the shape of the signal, which is typically a few bunch crossings. This case must also be taken into account.

3.5.2 Collision Rate

Under nominal conditions, the LHC will produce 10^9 inelastic collision events per second. Though the very important computing and storage facilities, events can only be recorded at a rate of ~ 300 Hz. Hence the necessity of an online selection system that determines in a very small amount of time⁷ whether an event is worth being recorded. Not only must this system be fast: it should be very selective to reduce the event rate by seven orders of magnitude. Finally, this selection system must keep a very high efficiency on interesting collision events.

3.5.3 High Radiation

The large flux of particles emitted by LHC collisions implies high radiation levels⁸. So the detectors shall not only be precise and selective, they must be highly resistant to radiations. The same condition applies to their front-end electronics. Detectors were designed to operate during 5 to 7 years at full luminosity and up to 10 years including low luminosity phase.

3.6 Operation from 2010 to 2012

The first injections of beams actually took place in September 10 2008, but due to an accident caused by a faulty resistance of an interconnection between two magnets happened the 19th of the same month, the LHC stopped for more than one year for repairs and for commissioning of further safety measurements. The injections restarted in November 2009 with the first 450 GeV beams circulating through the LHC. The energy of the beams then was raised by steps until in March 2010 it reached 3.5 TeV and the first physics run at the LHC finally started. The data taking proceeded smoothly through the whole 2010, with a slowly yet steadily increase of luminosity which allowed the LHC to deliver a total of 47pb^{-1} up to November 2010, when the proton-proton collisions stopped to start one month of Heavy Ions runs.

The proton-proton collisions started again at centre of mass energy of 7 TeV in March 2011. The better knowledge of the machine allowed to increase the instantaneous luminosity, surpassing

⁷Bunch crossings occur every 25 ns in the case of LHC nominal collisions; during the latency of the first step of the event selection, all information of the event must be stored in the electronics; hence this latency should be at most few orders of magnitude higher than the bunch spacing (25 ns): typically 128 BX.

⁸For example, at nominal luminosity, the CMS electromagnetic calorimeter (located $\sim 2 - 3$ m from the collision point) is submitted to a radiation of ~ 0.2 to 6.5 Gy/h.

in few weeks the collected statistics of the whole 2010 and quickly approaching the design luminosity. During the 2011 run a remarkable integrated luminosity of about 6fb^{-1} was delivered and collected by the experiments. During Chamonix workshop in February 2012 it was decided to run the LHC with an increased energy of 4 TeV per beam during 2012. In addition to this, the instantaneous luminosity has been constantly growing and reached about $10^{33}\text{ cm}^{-2}\text{s}^{-1}$. Fig. 3.4 shows the curve of delivered luminosity and the luminosity recorded by CMS in 2011 (a) and 2012 (b) summing up to a total of incredible 29.6fb^{-1} . On 17th December 2012, LHC has finished its first remarkable first three-year run crowning it by a new performance milestone. The space between proton bunches in the beams was halved from 50 ns to 25 ns to further increase beam intensity. This new achievement augurs well for the next LHC run starting in 2015.

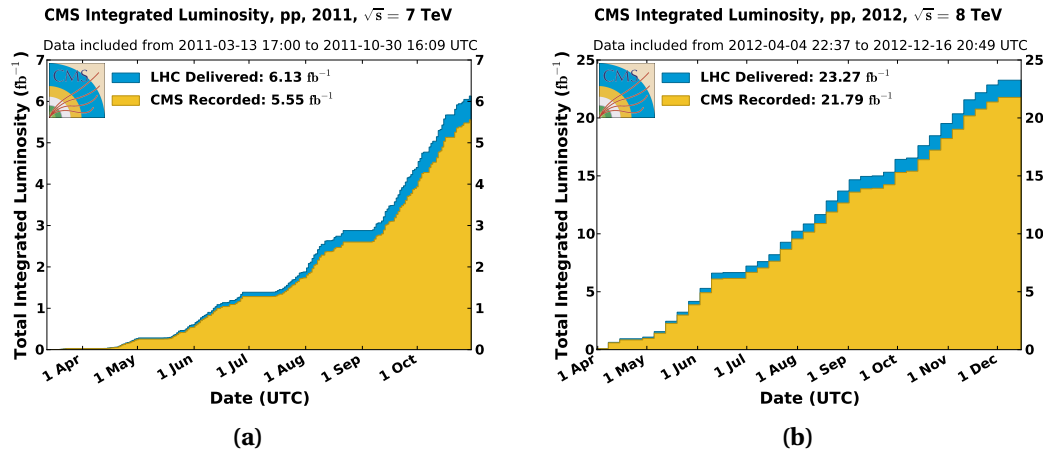


Figure 3.4: Integrated luminosity delivered by LHC (blue) and collected by CMS (yellow) for (a) 2011 and (b) 2012.

4 Compact Muon Solenoid

4.1 CMS Detector and its Magnet

CMS is a multipurpose experiment designed to cover a wide range of measurements in particle physics. The design of the CMS detector [24] was optimized in particular for the search of the Higgs boson, the search for new physics such as the production of supersymmetric matter, and the search for resonances at the TeV scale. The geometry of the CMS detector [25] is illustrated in Fig. 4.1. A particular attention was given to the measurement of muons, electrons and photons.

Muons must be measured over a wide range of momenta to allow for the observation low mass hadronic resonances, of multi-lepton signatures of the Higgs bosons such as $H \rightarrow ZZ^{(*)} 4\mu$, and of TeV resonances such as $Z' \rightarrow \mu^+ \mu^-$. For the search of the Higgs boson in the 4μ decay channel, a precise measurement of the muon momentum, at least for p_T values up to ~ 100 GeV. CMS has chosen to use a superconducting solenoid magnet with a very high field of 3.8 Tesla. This provides enough bending power for the precision measurement of the muon track curvatures in a central tracking detector composed of a pixel and a silicon strip detector. The tracking devices measures the trajectories of all charged particles. The degree of curvature of the trajectory of a particle decreases when its transverse momentum increases, making the charge measurement more difficult and the p_T measurements more imprecise.

Surrounding the tracker and still inside the bore of the solenoid are the fine grained electromagnetic and hadronic calorimeter. Photons or electrons develop electromagnetic showers contained in the electromagnetic calorimeter. Their energy is measured with a relative precision increasing with energy. The more penetrating hadrons such as charged pions initiate hadronic showers which are partly contained in the hadronic calorimeter.

The solenoid field flux is returned through a 10,000-t iron yoke comprising 5 wheels and 2 endcaps, composed of three disks each. The return field extends to a distance of 1.5 m from the solenoid, allowing the integration of 4 muon stations. The instrumented iron plays a main role in muon identification and for triggering purposes.

Chapter 4: Compact Muon Solenoid

The subdetectors and the online selection ('trigger') system are presented in detail in the next sections. The emphasis is put on the electromagnetic calorimeter, which plays a major role in the following chapters.

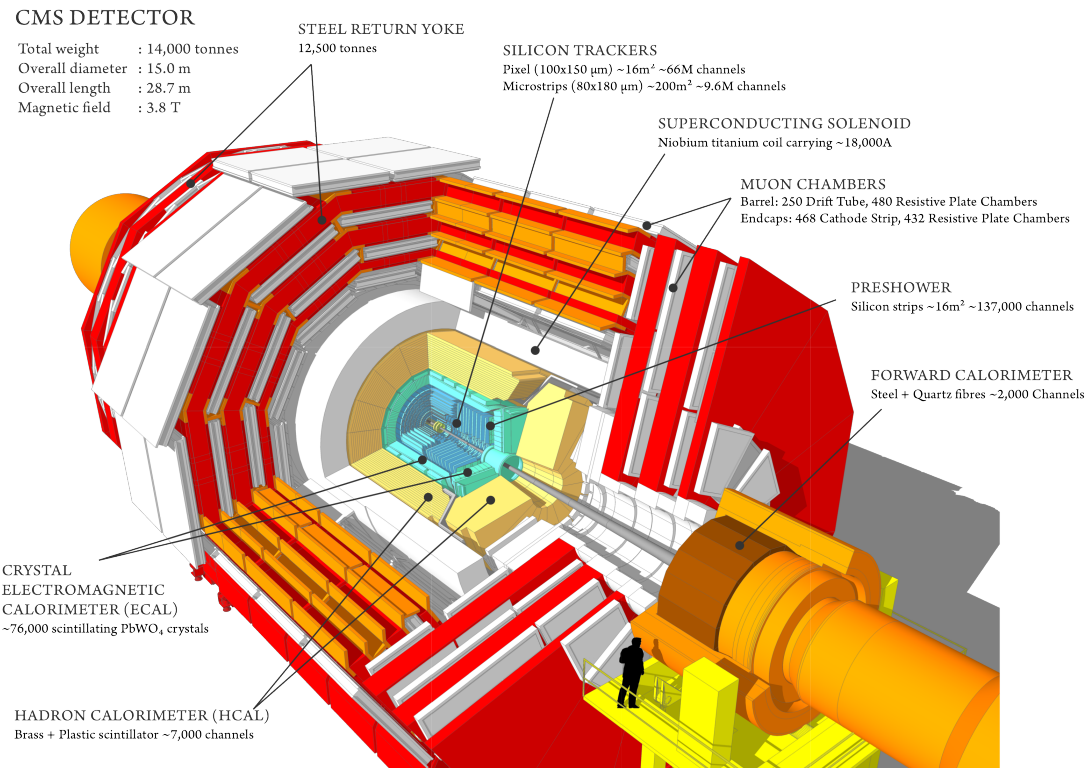


Figure 4.1: A perspective view of the CMS detector with major subsystems indicated.

4.2 Coordinate System

In this section and the following ones, the same system of coordinates will be used when considering the detector: it is illustrated in Fig. 4.2. The detector has a cylindrical shape around the beam axis (z axis).

The origin is centred at the nominal collision point inside the experiment; the x axis points horizontally towards the centre of the LHC, and the y axis points vertically upwards, so the z (longitudinal) axis, horizontal and colinear to the beam trajectory, points towards the Jura mountain.

In the transverse (x - y) plane, the azimuthal angle ϕ is measured from the x axis and the radial coordinate is denoted r . The polar angle θ is measured from the z axis. In particular the

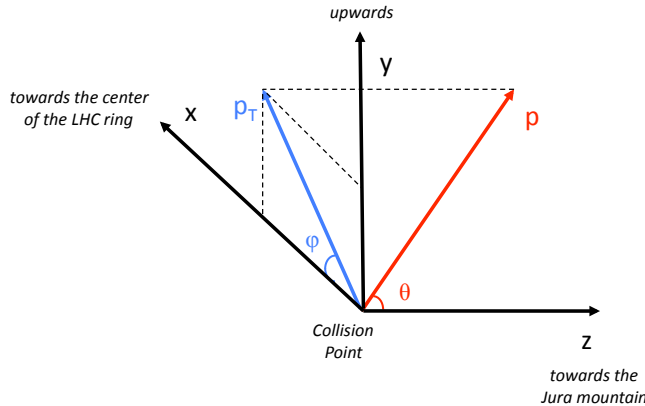


Figure 4.2: The CMS coordinate system.

pseudorapidity¹ η will be used, defined as $\eta = -\ln \tan(\theta/2)$.

The direction of a particle trajectory at production point is described by the coordinates (η, ϕ) .

Keeping in mind the cylindrical shape of the detector, the η coordinate makes the difference between two parts of the subdetectors: the ‘barrel’ corresponds to the central, cylindrical region, and the ‘endcaps’ are the two discs at the extremities that close the detector along the beam axis.

An inelastic collision event is the collision of two partons: one from a proton of the first beam, and one from a proton of the second beam. The energy of each parton is an unknown fraction of the proton energy, so the collision energy is not fixed. However the parton momentum, before the collision, is expected to be longitudinal (along the beam axis): the transverse momentum of each parton being negligible, and the total transverse momentum being conserved during an interaction, the transverse momentum of the collision is expected to be negligible too.

The net transverse momentum of collision being close to zero makes it practical to use the projection of the momentum to the transverse plain. In particular the particle trajectory transverse energy writes: $E_T = E \sin \theta = \frac{E}{\cosh \eta}$. For a massless particle, the transverse energy is equal to the transverse momentum: $E_T = p_T$. For electrons and muons, and for the energies considered², the masses are negligible and one will assume that $E_T = p_T$.

¹The pseudorapidity η is an approximation of the rapidity $\rho = \ln(\frac{E+p_z}{E-p_z})$ in the relativistic limit ($\frac{mc^2}{E} \rightarrow 0$). These units are interesting in particle physics, because a Lorentz boost along the z axis ($\rho = \rho - \frac{1}{2} \ln(\frac{1+\beta}{1-\beta})$), leaves the variable $\frac{dN}{d\rho}$ unchanged ($\frac{dN}{d\rho}$ is the number of emitted particles by rapidity unit).

²Generally, the studied leptons are reconstructed for $E_T \gtrsim 5$ GeV, and their transverse energy distribution is centred at $E_T \sim 40$ GeV, with a main contribution of leptons from the decays of W and Z bosons.

A particle escaping the detection creates an unbalance in the total transverse energy measurement, also called missing transverse energy. If the detector is hermetic, this missing transverse energy can be interpreted as the transverse energy of the particles that the detector is not intended to measure, such as neutrinos or new physics particles that interact as little as neutrinos with matter (e.g. neutralinos).

4.3 Inner Tracking System

The CMS tracker is a fundamental tool for the charge and momentum measurements on charged particles. Surrounding the interaction point, it has a length of 5.8 m and a diameter of 2.5 m. It covers a pseudorapidity range of $|\eta| < 2.5$. Being positioned directly around the collision point, the tracker material must be very resistant to radiation.

Besides, a very fine granularity in the innermost part is essential to identify the different vertices in a bunch crossing: besides the primary vertex, which corresponds to the interaction point of the spotted collision, secondary vertices can indicate another interaction that occurred during the same bunch crossing (pile-up), or the late decay of a particle³.

To meet these conditions, the choice was made of a tracker design entirely based on silicon detector technology. This very powerful system has however some disadvantages: it implies a high power density of on-detector electronics, which requires an efficient cooling system. In addition, particles from collisions may interact with the corresponding high amount of dense material, when they cross the tracker giving rise to multiple scattering, bremsstrahlung, photon conversion and nuclear interactions, thus implying complications in their reconstruction and a loss of efficiency and precision. This effect will be detailed when dealing with electron objects, in particular in Sec. 6.1.

The high number of particles crossing the tracker results in a high hit density, which decreases when the distance to the centre increases. Under nominal LHC conditions (1000 particles every 25 ns), the hit density reaches values reported in Tab.4.1.

Table 4.1: Silicon tracker hit densities.

Hit density	radius (cm)
1 MHz/mm ²	4
60 kHz/mm ²	22
3 kHz/mm ²	115

For a good performance, the occupancy of a detector cell must be kept at or below $\sim 1\%$. Thus,

³Leptons issued from late decays indicate a background event in the $H \rightarrow ZZ^{(*)} \rightarrow 4\ell$ ($\ell = e, \mu$) analysis for example (e.g. b quark decays from $Z b\bar{b}$ events).

the expected hit density of a given region dictates the granularity.

The CMS tracker is made of two kinds of silicon sensors. Silicon pixels constitute the very fine pixel detector in the most inner part, while the rest of the tracker is made of silicon strips; thicker silicon sensors are used for the outer tracker region in order to maintain a signal to noise ratio well above 10. The tracker structure contains several parts of central barrel layers, completed by endcap disks on both sides, as illustrated in Fig. 4.3. For a primary particle, the pixels should provide the three first hits of the track. They allow a very precise measurement of a particle impact parameter and the identification of secondary vertices.

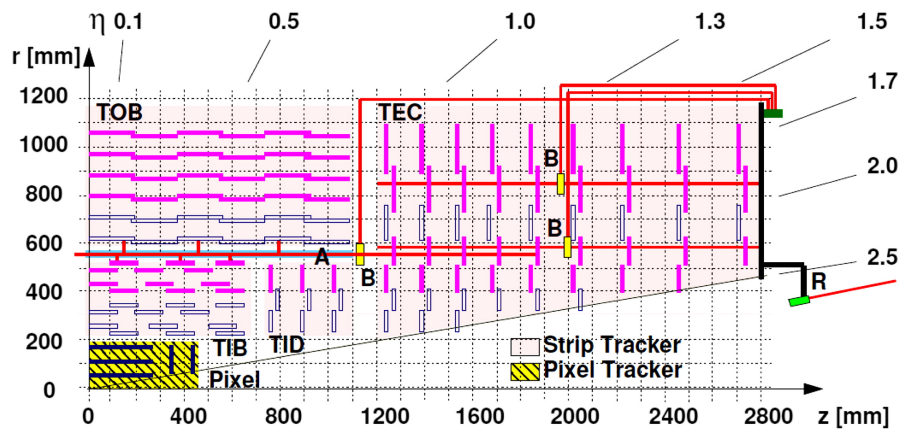


Figure 4.3: Schematic cross-section through the CMS tracker. Each line represents a detector module. Empty dark blue rectangles indicate back-to-back modules which deliver stereo hits. The pixel detector contains barrel and endcap modules; the silicon strip tracker has two collections of barrel modules: the Tracker Inner Barrel (TIB) and the Tracker Outer Barrel (TOB), and two collections of endcap modules: the Tracker Inner Discs (TID) and the Tracker EndCaps (TEC).

Some details about the detector cells can be found in Table 4.2. Overall, the pixel detector covers an area of about 1 m^2 with 66 million pixels. The silicon strip tracker has a total of 9.3 million strips and 198 m^2 of active silicon area.

Table 4.2: Structure of the Silicon Tracker Detector.

region (as in Fig.4.3)		modules	size in $r - \phi$ and z	occupancy
pixel detector	$r < 10 \text{ cm}$ (PIXEL)	pixel detectors	$100 \times 150 \mu\text{m}^2$	10^{-4} per pixel
silicon strip tracker (1)	$20 \text{ cm} < r < 55 \text{ cm}$ (TIB + TID)	silicon microstrip detectors	$10 \text{ cm} \times 80 \mu\text{m}^2$	$2 - 3\%$ per strip
silicon strip tracker (2)	$55 \text{ cm} < r < 110 \text{ cm}$ (TOB + TEC)	thicker silicon sensors	up to $25 \text{ cm} \times 180 \mu\text{m}^2$	$\sim 1\%$ per cell

Chapter 4: Compact Muon Solenoid

To prevent risks of thermal runaway⁴, the silicon tracker is coupled to a cooling system made of liquid Perfluorohexane (C_6F_{14}), and operates only at a temperature below -10°C .

The expected resolution of the tracker on some track parameters is shown in Fig. 4.4, for muons of different transverse momenta and as a function of the pseudorapidity. The transverse momentum resolution varies according to the tracker modules crossed: a resolution of $\sim 1\%$ in the most central region, and raising to $\sim 3\%$ for high pseudorapidities, is expected in the p_T range of W and Z boson decays ($p_T \sim 40\text{ GeV}$).

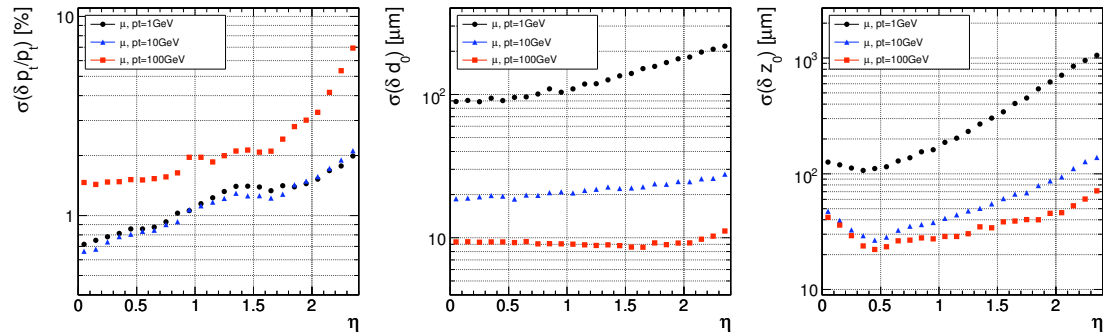


Figure 4.4: Resolution of several track parameters for single muons with transverse momenta of 1, 10 and 100 GeV, using only the tracker information: transverse momentum (left panel), transverse impact parameter (middle panel), and longitudinal impact parameter (right panel).

4.4 Electromagnetic Calorimeter

The Electromagnetic Calorimeter (ECAL) was designed according to the requirements of the $H \rightarrow \gamma\gamma$ search. It is the only subdetector to provide information about photons. For a precise diphoton mass reconstruction (a resolution of $\sim 0.8\text{ GeV}$ for a 100 GeV Higgs boson) a very precise position and energy measurement (a resolution of a few per mille) must be provided by the ECAL.

The ECAL is also of primary importance for the electron reconstruction in a Higgs boson analysis in a multi-lepton final state. The combination of its information with the one from the tracker must ensure a very precise measurement of electrons (position, momentum) and a significant background removal. A good segmentation is essential to distinguish the energy deposit shape of an electromagnetic particle, from the one of a hadronic particle.

The CMS ECAL is a hermetic and homogeneous calorimeter, that covers the rapidity range of $|\eta| < 3$. It is made of 75848 lead tungstate (PbWO_4) crystals, mounted in a barrel ($|\eta| < 1.479$)

⁴The increased detector leakage current can lead to a dangerous positive feedback of the self-heating of the silicon sensor and the exponential dependence of the leakage current on temperature.

and two endcaps ($1.479 < |\eta| < 3.0$).

The crystals are followed by photodetectors that read and amplify their scintillation. Avalanche photodiodes (APD) are used in the barrel. A higher resistivity to radiation dictated the choice of vacuum tubes in the endcaps. Then vacuum phototriodes (VPTs) are used instead of Photomultipliers (PMT) because they are less sensitive to the field effect.

The pion population is particularly important in the forward region, and the decay $\pi^0 \rightarrow \gamma\gamma$, presenting two photons very close to each others, is quite difficult to distinguish from a single photon. For a better photon identification, a preshower detector is installed in front of the ECAL endcaps.

A longitudinal view of the electromagnetic calorimeter is shown in Fig. 4.5.

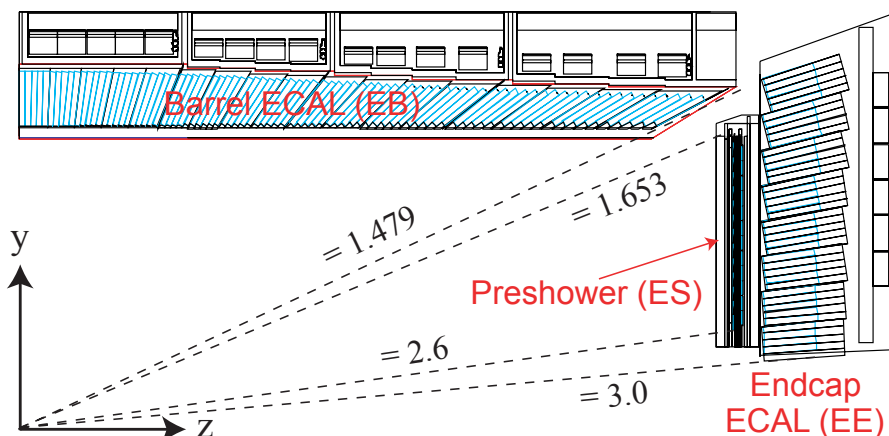


Figure 4.5: Longitudinal view of part of the CMS electromagnetic calorimeter showing the ECAL barrel and an ECAL endcap, with the preshower in front.

4.4.1 ECAL Crystals and Geometry

The choice of lead tungstate crystals is driven by the constraints assigned by the CMS detector design. First, to include both calorimeters inside the magnet, the ECAL must be compact. This condition is fulfilled with lead tungstate: its high density (8.28 g/cm^{-3}) and short radiation length⁵ (0.89 cm) ensure the possibility to absorb electron and photon showers with reasonably short crystals. Crystals of a length of $25.8 X_0$ are used in the barrel and $24.7 X_0$ in the endcaps.

A second requirement is the good separability of electromagnetic showers. This is possible thanks to the small Molière radius⁶ (2.2 cm) of lead tungstate: in short crystals of a material with a small Molière radius, an electromagnetic shower keeps a reasonable size. Hence the use

⁵A material's radiation length is the mean distance over which a high-energy electron loses all but $1/e$ of its energy by bremsstrahlung; this is equal to $7/9$ of the mean free path for pair production by a high-energy photon.

⁶The Molière radius R_μ is a characteristic constant of a material giving the scale of the transverse dimension of the fully contained electromagnetic showers initiated by an incident high energy electron or photon. It is defined

Chapter 4: Compact Muon Solenoid

of crystals with small transverse size and typical cross-section $2.2\text{ cm} \times 2.2\text{ cm}$, which ensures a good shower separation.

Finally, the scintillation decay time of the crystals is as fast as necessary for the context of LHC collisions (80% of the light is emitted in 25 ns).

Nevertheless the light output (i.e. the amount of light transferred to the photodetectors) is relatively low and varies with temperature. To ensure a stable response, a cooling system has been installed, maintaining the crystals and photodetectors at a temperature of $18^\circ\text{C} \pm 0.05^\circ\text{C}$, decoupled from the cold silicon tracker, and the readout electronics. The temperature is also monitored during data taking.

The barrel part of the ECAL covers the pseudorapidity range $|\eta| < 1.479$, with a granularity 360-fold in ϕ and (2×85) -fold in η . The centres of the front faces of the crystals are at a radius 1.29 m.

In comparison, the endcaps cover the rapidity range $1.479 < |\eta| < 3.0$ and are made of crystals with a slightly larger surface. The longitudinal distance between the interaction point and the endcap envelope is 315.4 cm.

A comparison of the number and dimensions of crystals in the barrel and the endcaps is given in Table 4.3.

Table 4.3: Ecal crystals.

	Barrel	Endcaps
number of crystals	61200	14648
crystal cross-section in (η, ϕ)	0.0174×0.0174	not fixed
crystal cross-section at the front face	$22 \times 22\text{ mm}^2$	$28.62 \times 28.62\text{ mm}^2$
crystal cross-section at the rear face	$26 \times 26\text{ mm}^2$	$30 \times 30\text{ mm}^2$
crystal length	230 mm $25.8X_0$	220 mm $24.7X_0$

The crystals are mounted in a quasi-projective geometry to avoid cracks aligned with particle trajectories, so that their axes make a small angle (3° in the barrel, 2° to 8° in the endcaps) with respect to the vector from the nominal interaction vertex, in both the ϕ and η projections.

Structurally speaking, the ECAL barrel is made of 36 identical *Supermodules*, each covering half the barrel length ($-1.479 < \eta < 0$ or $0 < \eta < 1.479$), with a width of 20° in ϕ . Each *Supermodule* is separated into four *Modules* in the η direction (cf Fig. 4.6). The presence of acceptance gaps, called cracks, between *Modules*, complicates the energy reconstruction. A larger crack

as the mean deflection of an electron of critical energy after crossing a width $1X_0$. A cylinder of radius R_μ contains on average 90% of the shower's energy deposition.

is present in the border $\eta = 0$ between *Supermodules*, and an even larger one marks the barrel-endcap transition.

Each ECAL endcap is made of two semi-circular plates called *Dees* (cf Fig. 4.6). Small cracks are also present between the endcap Dees, but their effect negligible.

The energy loss in the barrel cracks has been quantified. It is measured by comparing the energy measured in the ECAL with the momentum measured in the tracker on electrons with little bremsstrahlung, considering that the difference is due to energy loss in cracks. The measured loss is of $\sim 3\%$ for the gaps in ϕ , affecting regions of $\sim 2^\circ$, and $\sim 10\%$ for the gaps in η ($\sim 15\%$ in the barrel-endcap transition), affecting regions of ~ 0.01 unit in η . A recovery method cancels these losses for all gaps, except the border $\eta = 0$ and the barrel-endcap transition, where energy losses of respectively $\sim 5\%$ and $\sim 10\%$ remain.

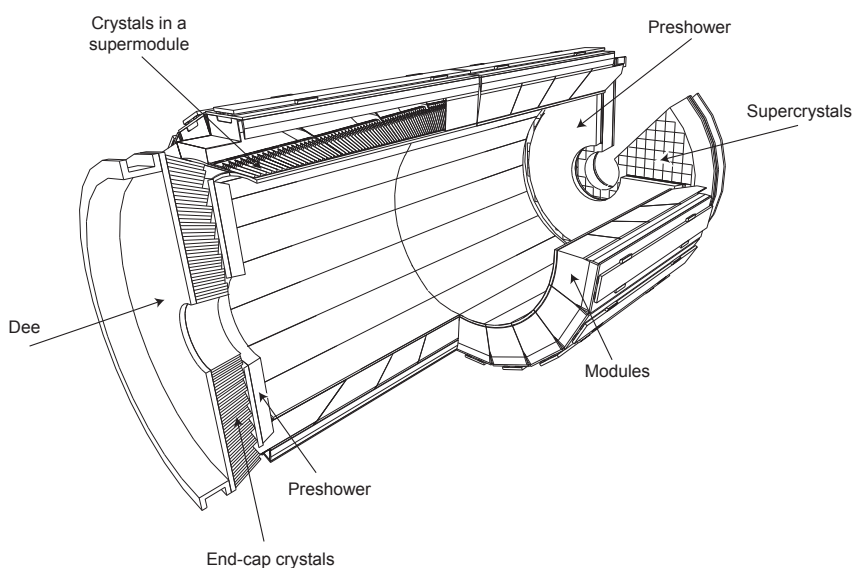


Figure 4.6: Layout of the CMS electromagnetic calorimeter showing the arrangement of crystal modules, supermodules and endcaps, with the preshower in front.

4.4.2 Photodetectors

Photodetectors need to be fast, radiation tolerant, and able to operate in the longitudinal 3.8 T magnetic field. According to the different expected levels of radiation, two different kinds of photodetectors were used for the barrel and for the endcaps; these two devices were developed specially for CMS.

Avalanche photodiodes (APDs) are used in the barrel. Each APD has an active area of $5 \times 5 \text{ mm}^2$; a pair is mounted on each crystal. They are operated at gain 50 and read out in parallel.

Vacuum phototriodes (VPTs) are used in the endcaps. Each VPT is 25 mm in diameter, with an active area of $\approx 280 \text{ mm}^2$; one VPT is glued to the back of each crystal. They have a single gain stage, with a value of ~ 10.2 at zero magnetic field; a 3.8 T magnetic field lowers this value by less than 10%. In comparison with the APDs, the lower quantum efficiency and internal gain of the VPTs is offset by their larger surface coverage on the back face of the crystals.

4.4.3 Preshower

The preshower is a 20-cm thick sampling device, made of two parts located at each end of the tracker, in front of the ECAL endcaps, in the pseudorapidity range $1.653 < |\eta| < 2.6$ (cf Fig. 4.6). Its absorber, made of lead radiators, initiates electromagnetic showers from incoming electrons and photons. Behind each radiator are two layers of silicon strip sensors positioned with orthogonal orientation. These sensors measure the deposited energy and the transverse shower profiles for a better identification of electromagnetic particles.

At a pseudorapidity value of $\eta = 1.653$, the material crossed by a particle in the preshower before it reaches the first sensor plane is $2X_0$, with an additional $1X_0$ before reaching the second sensor plane. A particular attention has been given to a full coverage of lead by silicon sensors, including the effects of shower spread, primary vertex spread, etc.

Each silicon sensor measures $63 \times 63 \text{ mm}^2$, with an active area of $61 \times 61 \text{ mm}^2$, divided into 32 strips. The nominal thickness of the silicon is $320 \mu\text{m}$.

4.4.4 Laser Monitoring

ECAL lead tungstate crystals are resistant, but not insensitive to radiations: their optical transmission is reduced by few percent during a run. This limited but rapid effect is due to the production of colour centres which absorb a fraction of the transmitted light.

The effect is neither constant, nor uniform: it is more visible for higher radiations, e.g. higher luminosity, or higher pseudorapidity for a given luminosity. Besides, at the ECAL temperature of 18°C , this effect tends to be reversed by an annealing effect which by thermal agitation bring atoms back into their ordered structure.

Under LHC conditions of runs (≈ 10 hours) alternating with machine refills (≈ 1 hour), the crystal transparency has a cyclic behavior, with a progressive degradation during runs when the radiation effect dominates, and a fast recovery during breaks due to the annealing.

The magnitude of the changes is dose-rate dependent, and is expected to range from 1 – 2% at low luminosity in the barrel, to tens of per cent in the high η regions of the endcaps at high luminosity.

Such evolutions must be taken into account for a proper calibration of the energy. This is possible thanks to a regular measurement of the crystal transparency, using laser pulses

injected into the crystals via optical fibres. The response is normalized by the laser pulse magnitude measured using silicon PN photodiodes. The ratio of the crystal response to the photodiode measurement gives the crystal transparency.

4.4.5 Detector Calibration

The main source of channel-to-channel disparities is the difference between the crystal scintillation light yields. The total variation among all barrel crystals is $\approx 15\%$; the value is higher in the endcaps ($\approx 25\%$), because of non-negligible variations in the VPTs, like the gain.

Corrections from laboratory measurements and calibration of crystal light yield and photodetector/electronics response reduced the channel-to-channel variation to less than 5% in the barrel, less than 10% in the endcaps.

A good precision on intercalibration constants was further achieved for the whole barrel ($< 2\%$) with the use of cosmic rays, with a further improvement for nine supermodules of the barrel ($\sim 0.5\%$) and 500 crystals in the endcaps ($< 1\%$), with electron test beams.

The ultimate intercalibration precision is to be achieved *in situ*, with physics events. The results on 2010 data allowed to uniformize the precision of the intercalibration constants, which is in 2010 $\sim 0.5 - 1\%$ in the barrel and $\sim 2 - 3\%$ in the endcaps.

Several measurements were combined to obtain this precision: the information from stopped circulated beams (also called splash events) in the barrel was used. Besides, for barrel and endcaps, two data-driven methods were applied. The ϕ -symmetry method [26, 27] is based on the assumption that the total transverse energy deposited from minimum bias events should be the same for all crystals in a ring at a fixed pseudorapidity. The π^0 calibration method [28] consists in uniformizing the peak positions for individual crystals.

To the intercalibration corrections is added a global correction factor, corresponding to the detector energy scale. The ECAL barrel and ECAL endcap energy scales have been measured using $Z \rightarrow e^+ e^-$ events and systematic errors have been evaluated to be 0.5% for the barrel factor and 1.4% for the endcap factor.

4.4.6 Energy Resolution

The energy resolution has been measured using incident electrons, during a beam test in 2004 [29]. The result is shown in Fig. 4.7 and summarized in Tab. 4.4. The resolution is composed of a stochastic, a noise and a constant contribution terms as follows:

$$\left(\frac{\sigma(E)}{E}\right)^2 = \left(\frac{2.8\%}{\sqrt{E}}\right)^2 + \left(\frac{0.12}{E}\right)^2 + (0.30\%)^2, \quad (4.1)$$

Chapter 4: Compact Muon Solenoid

For electrons of energy higher than 15 GeV a resolution better than 1% is achieved while for typical electrons from Z, i.e. 40 GeV electrons it is of 0.6%. Nevertheless, the resolution in situ is affected by the degradation due to material, and the actual resolution for electrons is never better than 1% as will be shown in Fig. 6.10.

Contribution	Barrel ($\eta = 0$)	Endcap ($\eta = 2$)
Stochastic term	2.7%	5.7%
Constant term	0.55%	0.55%
Noise (low luminosity)	0.155 GeV	0.155 GeV
Noise (high luminosity)	0.210 GeV	0.245 GeV

Table 4.4: Contributions to the energy resolution of ECAL.

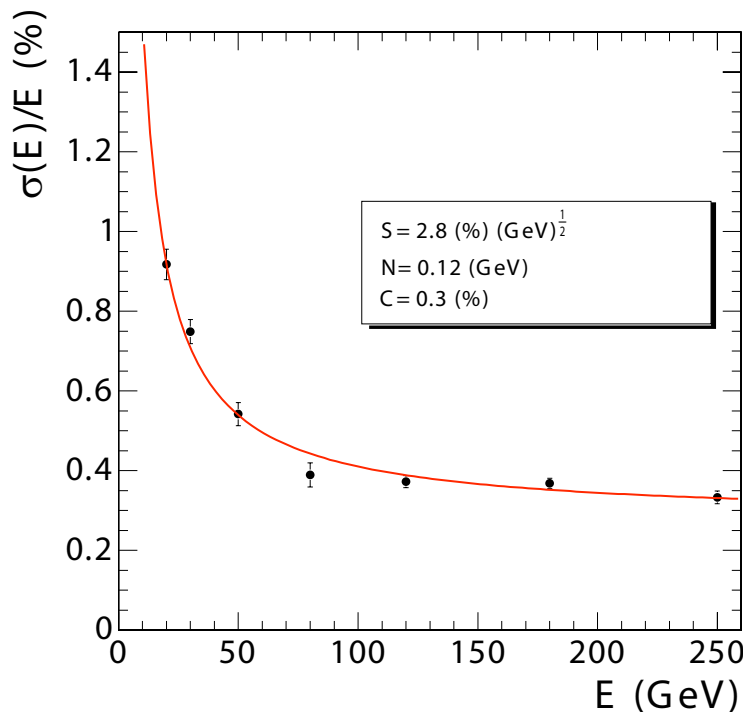


Figure 4.7: ECAL barrel energy resolution, $\sigma(E)/E$, as a function of electron energy as measured from a beam test. The energy was measured in an array of 3×3 crystals with an electron impacting the central crystal. The stochastic, noise, and constant contributions are shown.

These tests correspond to optimal conditions: the electrons hit radially the centre of a crystal, so the energy loss corresponding to crystal junctions, and the effect of the angle of incidence variation due to the magnetic field, are minimized. The same tests applied on electrons hitting uniformly the crystal, showed that after a general energy correction the resolution is $\sim 0.15\%$ worse than the previous results (for 120 GeV electrons).

4.4.7 Position Resolution and Alignment

The ECAL position resolution reflects the fluctuations of the energy measurements, and follows the same dependence in energy as (4.1). Studies based on simulations [30] demonstrate that a resolution of about 10^{-3} units in η and 1.6 mrad in ϕ can be reached on 35 GeV electrons; in terms of distance, this corresponds to ~ 2 mm for each coordinate (x, y).

These expectations were confirmed by test beam experiments [31]. *In situ* measurements taken to align the ECAL and the tracker provide similar results.

4.5 Hadron Calorimeter

Located behind the Tracker and the Electromagnetic Calorimeter as seen from the interaction point, the hadron calorimeter (HCAL) plays a major role in the measurement of hadron jets. Hence, it should provide a sufficient containment to largely stop hadronic showers. Besides, a wide extension in pseudorapidity is necessary to have a precise description of the total collision event, allowing a reliable measurement of the missing transverse energy, and thereby a measurement of neutrinos and some exotic particles. In most of the physics analysis, the limited performance of the HCAL due to the lack of containment is compensated by using a particle flow technique which combines calorimetric and tracking measurements.

From the point of view of a Higgs boson analysis in a multi-lepton final state, the HCAL measurement is very useful to distinguish electrons from hadron jets.

HCAL is installed between ECAL (at a radius $r = 1.77$ m) and the magnet coil (whose inner side is at $r = 2.95$ m), as shown in Fig.4.8. The barrel and endcap parts (HB, HE) extend up to $|\eta| < 3.0$, but a total coverage of $|\eta| < 5.3$ is reached with a forward calorimeter (HF), which provides the required hermeticity. Since the full containment of a hadronic shower is not possible in the detector volume, an outer hadron calorimeter (HO), or *tail-catcher*, is placed outside of the solenoid in the barrel region.

HCAL is a sampling calorimeter composed of plastic scintillators as active elements, interspersed with brass and stainless steel absorbers and read out by wavelength-shifting fibres. The absorber material has been chosen because of its large hadronic interaction length and of its property of being non-magnetic. The HB is split into two half barrels, each containing 18 identical wedges. The HE is organized in 10 sectors, with eighteen 80 mm thick absorber layers. Both HB and HE scintillators have a granularity of $\Delta\eta \times \Delta\phi = 0.087 \times 0.087$, except in the very high η -regions, where it matches the ECAL one. The HF calorimeters (situated about 11 m far from the interaction point) are useful to identify and reconstruct very forward jets. The forward region is characterized by a high radiation field, which is best sustained by quartz fibres as active material. They emit Cherenkov light, detected by PMTs, and they are placed between 5 mm thick steel absorber plates. The total absorber thickness of the hadronic calorimeter is summarized in the table ???. The HCAL depth, expressed in interaction lengths,

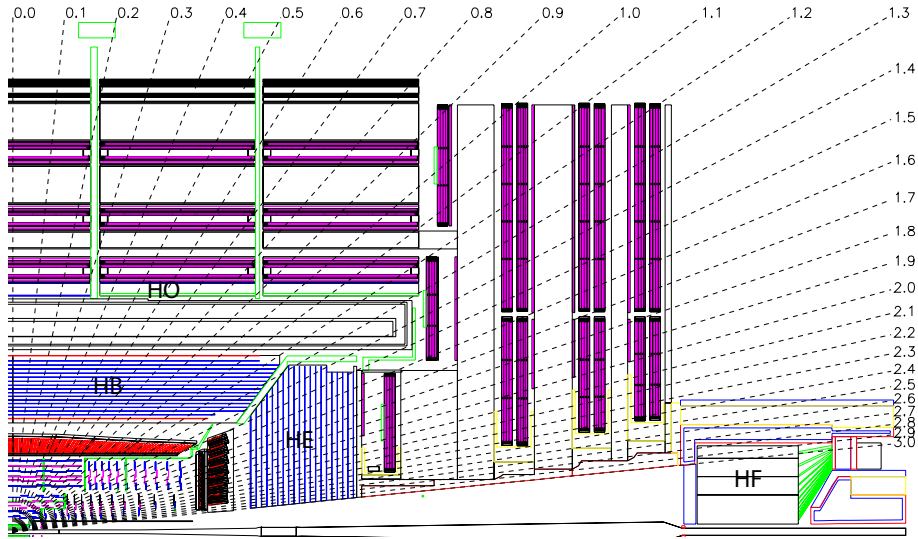


Figure 4.8: Longitudinal view of the CMS detector indicating the locations of the hadron barrel (HB), endcap (HE), outer (HO) and forward (HF) calorimeters.

ranges from $5.1\lambda_I$ at $\eta = 0$ to $9.1\lambda_I$ at $\eta = 1.3$, whereas it is $10.5\lambda_I$ in the endcaps. The design energy resolution is

$$\begin{aligned} \frac{\sigma_E}{E} &= 65\% \sqrt{E} \oplus 5\% && (\text{HB}), \\ \frac{\sigma_E}{E} &= 85\% \sqrt{E} \oplus 5\% && (\text{HE}), \\ \frac{\sigma_E}{E} &= 100\% \sqrt{E} \oplus 5\% && (\text{HF}), \end{aligned} \quad (4.2)$$

with E expressed in GeV.

HCAL total absorber thickness	
Eta	Interaction length λ
$\eta = 0$	5.15
$\eta = 1.3$	9.1
Endcap	10.5

Table 4.5: HCAL total absorber thickness.

4.6 Muon System

In multi-purpose detectors, like CMS, muons are particularly easy to identify and distinguish from backgrounds, thanks to the absorbers constituted by the calorimeters.

Muons play a major role in many physics analyses, particularly for the search of a Higgs boson in a multi-lepton final state. The topology of the final state of $H \rightarrow ZZ \rightarrow 4\mu$ analysis motivates the construction of a muon system with a wide angular coverage, with no acceptance gap.

The muon spectrometer has been designed to provide an efficient muon trigger and a precise measurement of muon momentum and charge, even without relying on information from the tracking system. Given the shape of the CMS solenoid magnet, the muon systems were divided into a cylindrical barrel section, and two planar endcap regions. 25 000 m² of detection planes are used in robust muon chambers.

Muon detectors are embedded in the iron return yoke of the magnet, as shown in Fig.4.9. Other particles than muons, as well as muons with transverse momentum lower than ≈ 5 GeV, do not reach the muon chambers. Three subsystems compose the spectrometer.

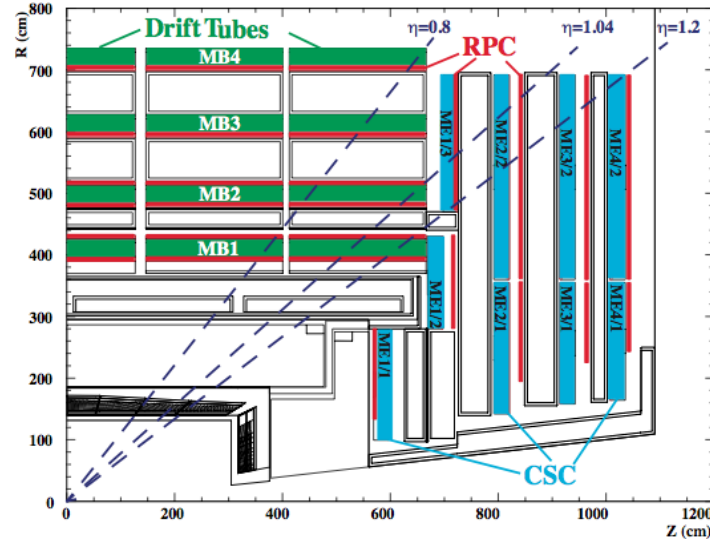


Figure 4.9: The longitudinal view of the muon spectrometer, where DT, RPC and CSC are indicated.

4.6.1 Drift Tube Chambers

Drift tube (DT) chambers are located in the barrel region ($|\eta| < 1.2$), where the residual magnetic field and the track occupancy are low. The DTs are divided in five wheels along the z coordinate, each including 12 azimuthal sectors. Along the radial coordinate, four stations (MB1, MB2, MB3, MB4) are made of 12 chambers each, one per ϕ sector, except for MB4,

which contains 14 chambers.

The basic constituent of a DT chamber is a *cell*, whose size is $42 \times 13 \text{ mm}^2$. A cell is bounded by two parallel aluminium planes and by '*I-shaped*' aluminium beams serving as cathodes. The anodes are $50 \mu\text{m}$ stainless steel wires located in the centre of the cells. Muons passing through a cell ionise the gas mixture that fills the cell volume. The drift time of the resulting electrons is used to measure the distance between the muon track and the wire. The linearity of relation between time and distance is enhanced by means of an additional field shaping, given by two positively biased insulated strips glued on the planes in correspondence to the wire. The gas mixture within a cell is composed of Ar (85%) and CO_2 (15%). It guarantees good quenching properties and the saturation of the drift velocity, which is $\sim 5.4 \text{ cm}/\mu\text{s}$. This corresponds to a maximum drift time of $\sim 390 \text{ ns}$, or 15 bunch crossings. The efficiency of a single cell is $\sim 99.8\%$, its spatial resolution is $\sim 180 \mu\text{m}$. Each chamber has a resolution of $\sim 100 \mu\text{m}$ in the $r - \phi$ plane and of $\sim 1 \text{ mrad}$ along the ϕ coordinate.

4.6.2 Cathode Strip Chambers

Cathode Strip Chambers (CSC) have been installed in the endcaps ($0.8 < |\eta| < 2.4$), where the residual magnetic field between the plates of the return yoke is intense and the particle rate is high. They are multi-wire proportional chambers made of two cathode planes, one of which is segmented into strips, and of an array of anode wires laying between these two planes. A charged track passing through a chamber generates an avalanche that induces a charge on several cathode strips. By interpolating among these strips one reaches a very fine spatial resolution of $50 \mu\text{m}$. The resolution along the ϕ coordinate is 10 mrad. The CSCs consist of four stations (ME1 to ME4), the innermost one including three concentric rings, the other ones only two. The inner rings of stations ME2 to ME4 contain 18 chambers, all the other ones include 36 chambers. The exception is the ME4 outer ring which is planned to be installed during the LHC shutdown stage starting in 2013.

4.6.3 Resistive Plate Chambers

Resistive Plate Chambers (RPC) are located both in the barrel and in the endcaps ($|\eta| < 2.1$), for redundancy purposes. Their spatial resolution is limited, but their time resolution is very good, about 1 ns, a shorter time than the 25 ns LHC bunch spacing. Therefore RPC detectors are used to identify unambiguously a bunch crossing and to provide prompt trigger decisions. RPCs are made of two parallel plates of bakelite, a high-resistivity plastic material, with a few mm thick gas gap in between them and a graphite coat outside of them. Aluminium strips, separated from the graphite layers by an insulating PET (polyethylene terephthalate) film, read out the signals. The gas mixture filling the gap consists of $\text{C}_2\text{H}_2\text{F}_4$ (95%) and of $i - \text{C}_4\text{H}_{10}$ (5%). The geometrical layout of the RPC chambers depends on their position. In the barrel region, six layers of RPCs are there: four of them are attached to each side of the MB1 and MB2 DT chambers, the other two to the inner side of MB3 and MB4. In the endcaps, four disks of

trapezoidal RPC are attached to the CSCs.

4.6.4 Muon Momentum Resolution

The expected resolution of the transverse momentum of muons is of $\sim 10\%$ in the barrel and $\sim 20\%$ in the endcaps, for muons from W or Z boson decays ($p_T \sim 40$ GeV). For global muon objects, the momentum is measured by the combination of the tracker and the muon system informations. Figure 4.10 shows the effect of this combination: in the p_T range below ~ 100 GeV, the tracker contributes mainly to the transverse momentum measurement. However for higher p_T values, the muon system information provides a significant improvement.

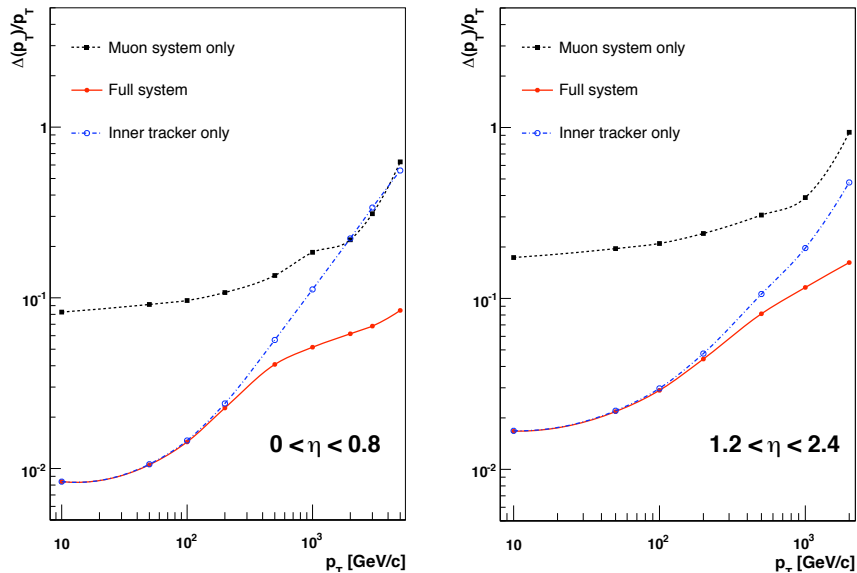


Figure 4.10: The muon transverse momentum resolution as a function of the transverse momentum (p_T) using the muon system only, the inner tracker only, and both. Left panel: $|\eta| < 0.8$, right panel: $1.2 < |\eta| < 2.4$.

4.7 Trigger and Data Acquisition

The trigger system can be seen as the first step of the physics event selection process. Unlike the following steps, this one is not reversible, and needs therefore a very precise upstream study. It performs a fast selection of events likely to be interesting for physics analyses, among the huge amount of events produced by LHC collisions.

This selection must drastically reduce the event rate, from the LHC bunch crossing rate (40 MHz under nominal conditions) to a reasonable rate for data recording, that was fixed at ~ 300 Hz. Besides, all collision data must be kept until the trigger decision, which requires a fast decision.

These constraints lead to a highly flexible two-level trigger system. The Level-1 (L1) Trigger is a hardware system made of largely programmable electronics, that provides a first rate reduction, to 33 kHz at high luminosity, with a fast event scan in a fixed amount of time: $3.2\ \mu s$. To satisfy this timing constraint, it considers coarse granularity objects from the calorimeters and the muon system. During these $3.2\ \mu s$, the complete high-resolution event information is held in pipelined memories.

If the L1 decision is positive, the complete event information is transferred to the next selection step: the High Level Trigger (HLT). This software system is implemented in a filter farm of about one thousand commercial processors. It is based on algorithms of increasing complexity, that use the fine granularity of the event. Hence the HLT decision time varies according to the event, with a mean value of $\langle T \rangle \approx 50$ ms. The HLT can access the complete event data: this flexibility requires a high bandwidth of the order of 1 Tb/s.

In the case of a Higgs boson analysis in a multi-lepton final state, the trigger will naturally search events containing electron or muon signals. For the Level-1 Trigger, an electron signature is a narrow and highly energetic energy deposit in the ECAL, and a muon signature is a track segment or a hit pattern in muon chambers.

The High-Level Trigger considers higher granularity objects (it reconstructs the total energy deposits in the calorimeters, and muon tracks) and combines them with the tracker and preshower information.

4.7.1 Level-1 Trigger Architecture

Figure 4.11 describes the Level-1 Trigger architecture: it is divided in two parallel trigger systems (one corresponding to the calorimeters, the other to the muon chambers). Each system is based on a local, a regional, and a global part, after which they are merged into a Global Trigger for the final L1 decision.

Several categories of Level-1 Trigger candidates are created:

- Muon (built in the Muon Trigger);
- Electron/Photon (isolated and non-isolated: e/γ), Jet (central and forward), Tau (built in the Regional Calorimeter Trigger);
- Total Transverse Energy (ΣE_T), Missing Transverse Energy (E_T^{miss}), Scalar Transverse Energy Sum of all Jets (above a given threshold: H_T) (built in the Global Calorimeter Trigger).

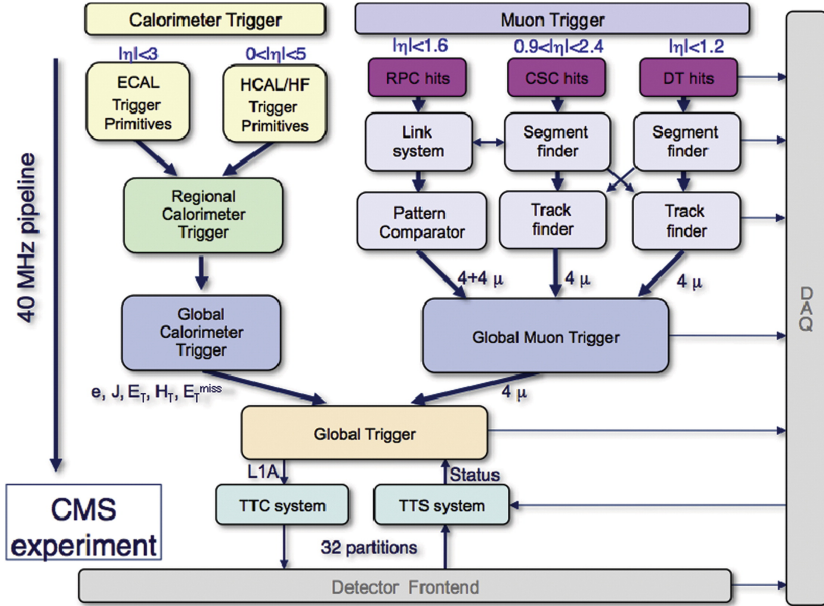


Figure 4.11: Architecture of the Level-1 Trigger.

Local Triggers

On each subdetector the local trigger creates coarse-granularity information. In the calorimeters, this information is a collection of Trigger Primitives.

Regional Triggers

The Regional Calorimeter Trigger collects the local information to build Level-1 Trigger Candidates; it combines the information of both calorimeters, for example for isolation considerations.

For the muon trigger, a DT track finder and a CSC track finder collect the local DT and CSC information to build Level-1 Trigger Candidates as tracks. The RPC trigger is directly regional.

The four most relevant candidates of each category are sent to the Global Calorimeter Trigger, or the Global Muon Trigger respectively. The Regional Calorimeter Trigger also sends the Global Calorimeter Trigger the regional summed transverse energy.

Global Calorimeter Trigger and Global Muon Trigger

Finally, the Global Calorimeter Trigger sorts the Level-1 Trigger Candidates to send the four most relevant ones of each category to the Global Trigger. It also calculates the summed transverse energy (ΣE_T) and the missing transverse energy (E_T^{miss}) of the event, as well as the scalar transverse energy sum of all jets above a given threshold (H_T). This information is also sent to the Global Trigger.

The Global Muon Trigger collects and compares the candidates from the DT, CSC and RPC Triggers. It combines them into four Muon Candidates. It also uses some information from the Regional Calorimeter Trigger for isolation considerations. The four Muon Candidates are sent to the Global Trigger.

Global Trigger

The Global Trigger collects the candidates produced by the Global Calorimeter Trigger and the Global Muon Trigger, and compares them to the Level-1 Trigger Menu. This menu is a list of Level-1 enabled triggers. At most 128 algorithms can be used, possibly prescaled⁷, including at most 64 technical triggers⁸.

If the candidate collection satisfies at least one of the listed triggers, the Level-1 Trigger decision is positive and the fine granularity event information is sent to the High-Level Trigger. Some trigger rules are also applied at that step, to prevent any memory overload. For example, the Level-1 Trigger can not accept two events separated by only one bunch crossing.

A trigger algorithm can consist in a threshold applied to the highest energetic candidate of one category. For example, ‘L1_SingleEG8Iso’ requires at least one isolated (i.e. with little activity in the surrounding calorimeter regions) electron/photon candidate with a transverse energy higher than 8 GeV.

A combined condition is sometimes a better way to reduce backgrounds while keeping a good efficiency on physics: for the same rate reduction, the use of a lower threshold is possible; double triggers also exist, like ‘L1_DoubleEG5Iso’, which requires at least two isolated electron/photon candidates with a transverse energy higher than 5 GeV.

⁷When a trigger is expected to have too high a rate at the considered luminosity, two possibilities appear to reduce the rate. Either the trigger conditions are tightened, or this exact selection is kept, but the rate is reduced by a prescaling factor n : only every n^{th} event satisfying the trigger conditions, is accepted.

⁸Technical triggers are based on technical information, like the LHC beam counters, or the CMS beam scintillators. They provide a way to select events independently from the calorimeter information. They can be a very interesting tool to test the trigger efficiency; however they trigger systematically on collision events, and must be highly prescaled, unless the collision rate is very low ($\lesssim 10^{30} \text{ cm}^{-2}\text{s}^{-1}$).

4.7.2 High-Level Trigger Architecture

The High-Level Trigger builds candidates corresponding to all kinds of reconstructed objects considered in the offline analyses, using very similar algorithms: photons, electrons and muons, τ -jets and hadronic jets, missing transverse energy... Its inner sub-structure is in several steps of increasing complexity, starting at Level 2.

The Level 2 starts generally with the Level-1 Trigger information, and builds fine granularity objects around the Level-1 candidates, using only the information from the calorimeters and the muon system. The tracker information is used, when necessary, starting at the next level: Level 2.5.

The example of electron candidates

Let us explain the role of each of the three steps described above, for the reconstruction of electron objects. In that case three HLT levels are considered: Level 2, Level 2.5 and Level 3.

At Level 2, energy *clusters*, built from the ECAL and preshower information, are matched to Level-1 e/γ candidates. The remaining energy of the initial particle, that was spread by bremsstrahlung, is then collected, forming what is called a *supercluster*. Some conditions are applied to the *supercluster* transverse energy, its shape, and isolation in comparison with the surrounding ECAL and HCAL regions, for it to be consistent with an electromagnetic signal. At this level, no difference is made between electrons and photons.

Level 2.5 extrapolates the position of the *supercluster* towards the innermost part of the tracker (the pixels), taking the curvature from its measured transverse energy, assuming that this *supercluster* corresponds to an electron. Two hits are searched in the corresponding region in the tracker pixel layers, and in the TEC layers in the forward region, to form a *seed*.

If a track seed is found, Level 3 applies a complete track reconstruction.

The selections on the electron transverse energy, its isolation, its *supercluster* shape, and the width of the matching *supercluster-seed* window, are dictated by the HLT menu.

High-Level Trigger menu

The High-Level Trigger uses around 150 trigger algorithms, and sorts the selected events into several datasets with as little overlap as possible. An event passing at least one of these trigger selections, will be accepted by HLT, flagged according to the passed selections, and recorded in the corresponding datasets.

Selecting exceptional events

The signatures of interesting physics events are likely to provide high energy leptons (electrons or muons), missing transverse energy (corresponding to neutrinos or particles described by theories beyond the Standard Model), or jets (τ -jets, or quark jets). Triggers are developed for all these signatures, in particular very high energy triggers, and coupled triggers (electron-muon, electron-jet...), can select exceptional events.

Besides, the trigger presents a high flexibility and if unexpected events of a different topology are noticed, it can be adapted to select also these topologies. The data recorded in 2010 provided interesting events with a high multiplicity of low-energy charged particle. These events are quite interesting to study long-range, near-side angular correlations [32]. Given the flexibility of the HLT, a dedicated high multiplicity trigger was designed and used to select such events.

4.7.3 The Data Acquisition System

The CMS Data Acquisition (DAQ) [33] is responsible for conveying the data from about 650 read-out modules to the filter units that will process the events. Each module provides event fragments with a size of ~ 2 kB. The CMS DAQ structure is outlined in Fig. 4.12. The detector

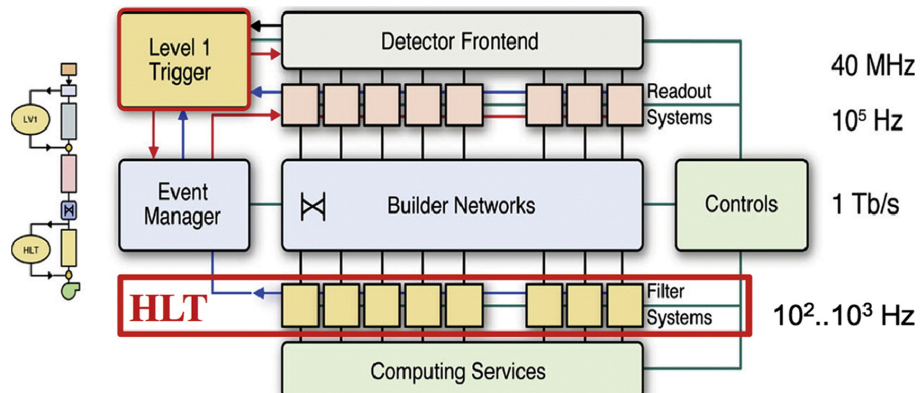


Figure 4.12: The structure of the CMS DAQ system.

sensors are read out by the so-called *Front-End Drivers* (FEDs) through a builder network having a bisectional bandwidth of 100 GB/s. The FEDs are situated in the underground counting room, ~ 70 m far from the detector. Events are passed to the event filter systems at a maximum rate of 100 kHz. This large rate, corresponding to the L1 one, is due to the design choice of building the full event already after the L1 trigger stage, unlike in the standard multi-level trigger systems.

4.8 Leptons Signature in CMS

4.8.1 Electrons

Being charged particles, electrons and positrons deposit energy in the silicon tracker and create hits in the sensors on their trajectory. They are then absorbed in the ECAL, where their energy deposit is measured.

Hence, an electron (or positron) object is the association of a high and local energy deposit in the ECAL with a track in the silicon tracker. Because of the magnetic field, the electron trajectory is curved. The degree of curvature depends on the electron transverse momentum, while the orientation of the curvature determines the charge. A simple electron topology is shown in Fig. 4.13.

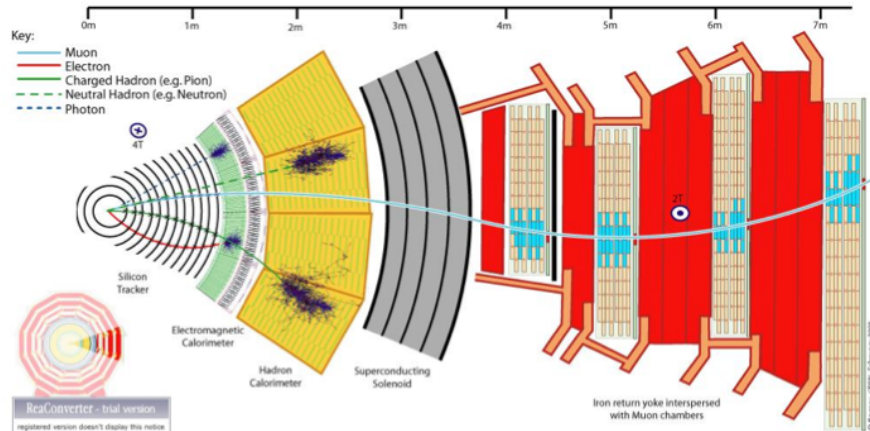


Figure 4.13: The CMS detector transverse section with simple particle topologies indicated.

However, the context of CMS complicates the electron (and positron) topology [34]. The high amount of material crossed by an electron while in the silicon tracker (up to $\sim 2X_0$: see Fig. 4.14) enhances the probability to create an electromagnetic shower (the electron emits bremsstrahlung photons, which can convert into electron-positron pairs, and so on). Finally, the high magnetic field bends the trajectories of the charged particles, spreading the shower in the ϕ direction.

The variation of the track curvature at bremsstrahlung points is taken into account in the track reconstruction algorithms. In the ECAL, an energy ‘cluster’ is reconstructed for each particle that reaches the calorimeter. The clusters that correspond to the same shower are assembled into a *supercluster* corresponding to the initial particle.

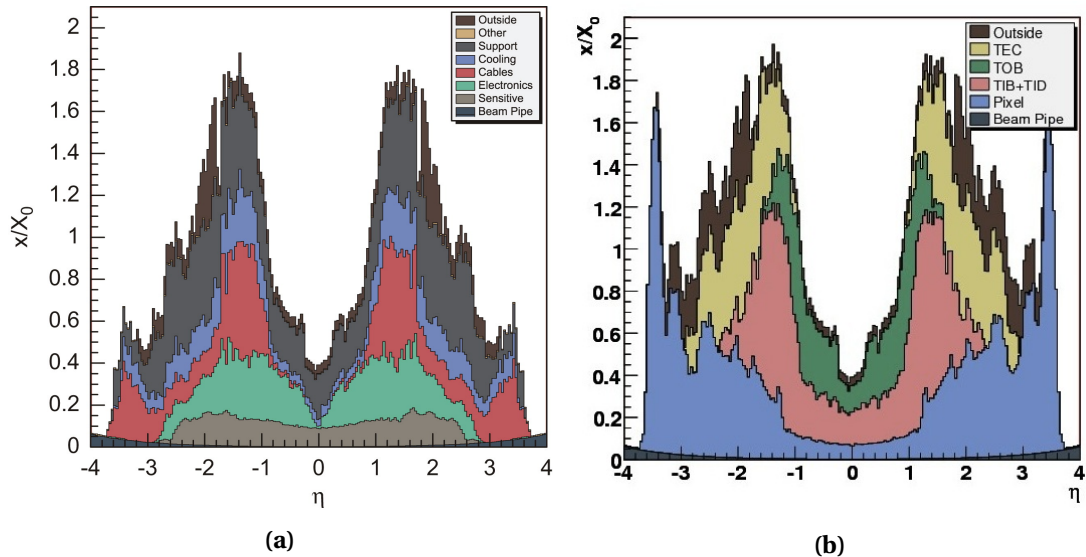


Figure 4.14: Distribution of the tracker material budget with respect to the pseudorapidity as obtained from simulation, in radiation length units. Material budget coming from tracker infrastructure (a) and tracker subparts (b) is indicated.

4.8.2 Muons

Muons and antimuons, being also charged particles, leave a track in the silicon tracker. They deposit little in the calorimeters (ECAL, then HCAL) and keep going through the muon systems as shown in Fig. 4.13. Hence, muon or antimuon objects are the association of two tracks: one in the silicon tracker (or *tracker track*), and a second one in the muon systems (or *standalone track*).

An ideal muon object, called *global muon*, is made of these two tracks: starting from a standalone track in the muon system, a matching tracker track is found and a global-muon track is fitted combining hits from the tracker track and standalone-muon track.

If no complete standalone track is reconstructed, the muon object is built from the inner track: this track is extrapolated to the muon system and matched to a muon segment (i.e. a short track stub made of DT or CSC hits): this is a *tracker muon*.

Finally, if only a standalone track is found, given the very low background rate in the muon systems, the object is also qualified as a muon: a *standalone muon*.

The CMS solenoid subjects the tracker to a 3.8 T longitudinal magnetic field, and the muon chambers to a return field in the opposite direction, of value ~ 2 T. Hence the trajectory of a muon is curved in opposite orientations in the tracker and in the muon chambers.

The degree of curvature gives the muon transverse momentum (p_T), while the orientation of

the curvature determines its charge. For a global muon, these parameters are mainly based on the tracker information, because of the very precise inner tracking system. However at high p_T the length of the muon systems is very useful as a lever arm.

Choose Building Blocks Part III

5 Datasets and Triggers

In this chapter we describe the experimental and Monte Carlo data samples used for the analysis in this thesis.

The first low luminosity proton-proton collision data at 7 TeV collected in 2010 has been mainly used for the commissioning of the detector and reconstruction objects as will be discussed in chapter 6 and 7.

By the summer 2011 (EPS HEP conference in Grenoble and Lepton-Photon conference in Mumbai), the CMS experiment had collected around 1fb^{-1} of data. This data allowed the LHC experiments to reach a comparable or better sensitivity than that of Tevatron experiments for the search of the Higgs boson. The results obtained with 5.05 fb^{-1} of data collected in 2011 which exclude at 95% C.L. a large portion of the Higgs boson mass range are presented in Ref.[35].

In spring 2012, the LHC proton-proton run was restarted, and by summer conferences another 6.5fb^{-1} were collected and 5.3fb^{-1} analysed. This data, together with 2011 integrated luminosity, was sufficient to claim an observation of a new boson at the opening session of the ICHEP conference in Melbourne [1].

After the discovery, LHC continued successful operation together with the experiments. The technical stop in September 2012 defined the HCP (Kyoto) conference dataset with integrated luminosity of 12.21 fb^{-1} . This data, together with the 5.05 fb^{-1} of data in 2011 is used for the analysis presented in this thesis.

5.1 Collision Data

The data sample used in this analysis was recorded by the CMS experiment during 2011 and during 2012. For the sake of sanity of the physics results, a rigorous selection of runs and luminosity sections is imposed requiring high quality data with a good functioning of the different sub-detectors. The selection is provided centrally and it is analysis-independent.

Chapter 5: Datasets and Triggers

The total integrated luminosity collected after good quality data selection in 2011 at 7 TeV is $\mathcal{L} = 5.05 \text{ fb}^{-1}$ whereas in 2012 we have $\mathcal{L} = 12.21 \text{ fb}^{-1}$ at 8 TeV. The absolute pp integrated luminosity is known with a precision of 2.2% [36] in 2011 and 4.4% in 2012.

The analysis relies on primary dataset (PD) produced centrally and organized on basis of High Level Trigger (HLT) content. In detail, the content of the PDs have evolved in phase with the evolution of the trigger menu in order to cope with ever increasing instantaneous luminosity. For the 2011 data, the analysis relies on the so-called "DoubleElectron" and "DoubleMuon" PDs [37]. These PDs are obtained by forming a "OR" between various triggers with symmetric or asymmetric trigger thresholds for the two leptons, with or without additional identification and isolation requirements. They also include triggers requiring three leptons above a low p_T threshold. In 2012 triggers combining different objects were added to recover a few percent inefficiency in the $2e2\mu$ channel at low Higgs boson masses. These are the so-called "MuEG" PD.

The combination of trigger paths (i.e. "OR") is basically requiring the presence of at least a pair of leptons ($\ell = e$ or μ) with $p_T^{\ell 1} > 17 \text{ GeV}$ and $p_T^{\ell 2} > 8 \text{ GeV}$. For the analysis (see chapter 8), minimal thresholds of $p_T^{\ell 1} > 20 \text{ GeV}$ and $p_T^{\ell 2} > 10 \text{ GeV}$ will be imposed in order to be on the plateau of the trigger efficiency.

The PDs and trigger paths used for this analysis are summarized in Table 5.1.

2011 ($\mathcal{L} = 5.05 \text{ fb}^{-1}$)	2012 ($\mathcal{L} = 12.21 \text{ fb}^{-1}$)
Datasets	
/DoubleElectron/Run2011A-16Jan2012-v1	/DoubleElectron/Run2012A-PromptReco-v1
/DoubleMu/Run2011A-16Jan2012-v1	/DoubleMu/Run2012A-PromptReco-v1
/DoubleElectron/Run2011B-16Jan2012-v1	/MuEG/Run2012A-PromptReco-v1
/DoubleMu/Run2011B-16Jan2012-v1	/DoubleElectron/Run2012B-PromptReco-v1
	/DoubleMu/Run2012B-PromptReco-v1
	/MuEG/Run2012B-PromptReco-v1
	/DoubleMu/Run2012A-23May2012-v2/AOD
	/DoubleElectron/Run2012A-23May2012-v2/AOD
	/MuEG/Run2012A-23May2012-v1/AOD
	/MuEG/Run2012A-08Jun2012-v3/AOD
	/DoubleElectron/Run2012A-08Jun2012-v2/AOD
	/DoubleMu/Run2012A-08Jun2012-v2/AOD
Muon triggers	
HLT_DoubleMu7	HLT_Mu17_Mu8
OR HLT_Mu13_Mu8	
OR HLT_Mu17_Mu8	
Electron triggers	
HLT_Ele17_CaloTrk_Ele8_CaloTrk	HLT_Ele17_CaloTrk_Ele8_CaloTrk
Cross triggers	
HLT_Mu17_TkMu8	
OR HLT_Mu8_Ele17_CaloTrk	
OR HLT_Mu17_Ele8_CaloTrk	

Table 5.1: Datasets and triggers used in the analysis for 2011 and 2012. Abbreviated form: CaloTrk = CaloIdT_CaloIsoVL_TrkIdVL_TrkIsoVL

For the 2011 analysis, when applying double muon triggers other then `HLT_Mu17_Mu8` we were requiring 2 offline recoMuons to be matched with L3Muons $p_T > 8 \text{ GeV}$ and $p_T > 17 \text{ GeV}$. Datasets coming from double muon triggers were used to search for 4μ and double electron for the $4e$ candidates. A search for $2e2\mu$ candidates is carried out in both, double electron and double muon datasets. So as to avoid double counting of events, a special care is required, vetoing double electron triggers when searching in double muon dataset and vice versa. In 2012, to recover an observed loss of efficiency in $2e2\mu$ channel coming from triggers, we used in addition MuEG dataset with double electron and double muon triggers vetoed.

For the reference, a full list of triggers used in 2012 is listed in Table 5.2.

Channel	Purpose	HLT path	L1 seed
4e	main	<code>HLT_Ele17_CaloTrk_Ele8_CaloTrk</code>	<code>L1_DoubleEG_13_7</code>
4μ	main	<code>HLT_Mu17_Mu8</code> OR <code>HLT_Mu17_TkMu8</code>	<code>L1_Mu10_MuOpen</code> <code>L1_Mu10_MuOpen</code>
$2e2\mu$	main	<code>HLT_Ele17_CaloTrk_Ele8_CaloTrk</code> OR <code>HLT_Mu17_Mu8</code> OR <code>HLT_Mu17_TkMu8</code> OR <code>HLT_Mu8_Ele17_CaloTrk</code> OR <code>HLT_Mu17_Ele8_CaloTrk</code>	<code>L1_DoubleEG_13_7</code> <code>L1_Mu10_MuOpen</code> <code>L1_Mu10_MuOpen</code> <code>L1_MuOpen_EG12</code> <code>L1_Mu12_EG6</code>
4e	backup	<code>HLT_Ele15_Ele8_Ele5_CaloIdL_TrkIdVL</code>	<code>L1_TripleEG_12_7_5</code>
4μ	backup	<code>HLT_TripleMu5</code>	<code>L1_TripleMu0</code>
$4e$ and $2e2\mu$	Z T&P	<code>HLT_Ele17_CaloTrkVT_Ele8_Mass50</code>	<code>L1_DoubleEG_13_7</code>
$4e$ and $2e2\mu$	Z T&P low pT	<code>HLT_Ele20_CaloTrkVT_SC4_Mass50_v1</code>	<code>L1_SingleIsoEG18er</code>
4μ and $2e2\mu$	Z T&P	<code>HLT_IsoMu24_eta2p1</code>	<code>L1_SingleMu16er</code>
4μ and $2e2\mu$	J/psi T&P	<code>HLT_Mu7_Track7_Jpsi</code> <code>HLT_Mu5_Track3p5_Jpsi</code> <code>HLT_Mu5_Track2_Jpsi</code>	

Table 5.2: HLT and Level-1 triggers used in 2012 data analysis. Abbreviated form: CaloTrk = CaloIdT_CaloIsoVL_TrkIdVL_TrkIsoVL CaloTrkVT = CaloIdVT_CaloIsoVT_TrkIdT_TrkIsoVT

5.2 Simulated Samples

A detailed Monte Carlo (MC) simulations were performed in order to obtain SM Higgs boson signal samples, as well as samples for a variety of electroweak and QCD-induced SM background processes. These datasets were then subject to full reconstruction. Prior to the analysis of the experimental data, the optimization of the event selection strategy was carried out using the signal and background simulated samples. They are further used in the analysis described in this thesis for the comparisons with the measurements, the evaluation of systematics and acceptance corrections. They are also used for the background estimation procedure where measurements in a “background control” region are extrapolated to the region containing “signal” .

The backgrounds include reducible, irreducible and instrumental contributions.

The reducible background are the processes giving rise to four real leptons in the final state that can be suppressed. An example is $(Z/\gamma^*)b\bar{b}$ background with $Z \rightarrow \ell^+ \ell^-$ where additional

two leptons come from decays of heavy mesons produced in the hadronization of b-jets. Typically, this background is reduced using isolation, vertex requirements or flavour matching. In addition to $(Z/\gamma^*)b\bar{b}$, reducible backgrounds also includes production of top quark pairs in the decay mode $t\bar{t} \rightarrow WbW\bar{b} \rightarrow \ell^+\ell^-v\bar{v}b\bar{b}$.

The irreducible background sources are all processes that have four isolated real leptons that can be matched to primary vertex like $Z \rightarrow 4\ell$, $ZZ^{(*)} \rightarrow 4\ell$ and $Z\gamma^{(*)} \rightarrow 4\ell$. A handle to distinguish the contribution of this background is provided by multivariate kinematic discriminant using full kinematic information from the four lepton system which will be introduced in chapter 12.

The instrumental background is a consequence of finite granularity of the measurement which bring fake lepton candidates, e.g. jets that are identified as an electron. In this analysis, for simplicity, we measure background rate and shape from data combining the reducible and instrumental contribution.

Here and henceforward, $ZZ^{(*)}$ stands for $ZZ^{(*)}$, $Z^{(*)}Z^{(*)}$ and $Z\gamma^{(*)}$, i.e. states with one or both Z bosons off-mass-shell or one Z boson replaced by an off-mass-shell photon in the case of the irreducible background. . For the event generation, ℓ is to be understood as being any charged lepton, e, μ, τ .

We make use of the multi-purpose Monte Carlo event generator PYTHIA [38] for several processes including QCD multijet production. This generator serves in two different ways. It is used to generate a given hard process at leading order (LO). Alternatively, in cases where the hard processes are generated at higher orders, it is used only for the showering, hadronization, decays, and for adding the underlying event. This is the case for:

- MadGraph (MadEvent) MC [39] event generators which are used to generate multi-parton amplitudes and events for some important background processes.
- POWHEG NLO generator [40] which is used for the Higgs boson signal and for the ZZ and $t\bar{t}$ background. For the latter the $t\bar{t}$ decays are handled, exceptionally, within POWHEG.
- GG2ZZ [41], a dedicated tool used to generate the $gg \rightarrow ZZ$ contribution to the ZZ cross-section.

For the underlying event, the “PYTHIA tune Z2” in 2011 and “PYTHIA tune Z2 star” in 2012 is used, which rely on p_T -ordered showers. The PDFs of colliding protons are parametrized by the CTEQ6M set except for the POWHEG samples from the “Fall11 and Summer12” which makes use of CT10. The summary of simulated datasets used in this analysis is given in Table 5.3.

The NLO cross-section for background processes is accounted for by proper re-weighting. The Higgs boson signal processes are also taken at NLO except in the case of the Higgs production via the gluon fusion for which the most recent NNLO+NNLL cross-section calculations are taken in account [42]. In the following sections, the event generators and simulated samples

Process	MC generator	$\sigma_{(N)NLO}$	
		7 TeV	8 TeV
Higgs boson $H \rightarrow ZZ \rightarrow 4\ell$			
$gg \rightarrow H$ m _H = 110-1000 GeV	POWHEG	[1-20] fb	[1.2-25] fb
$VV \rightarrow H$	POWHEG	[0.2-2] fb	[0.3-25] fb
ZZ continuum			
$q\bar{q} \rightarrow ZZ \rightarrow 4e(4\mu, 4\tau)$	POWHEG	15.34 fb	76.91 fb
$q\bar{q} \rightarrow ZZ \rightarrow 2e2\mu$	POWHEG	30.68 fb	176.7 fb
$q\bar{q} \rightarrow ZZ \rightarrow 2e(2\mu)2\tau$	POWHEG	30.68 fb	176.7 fb
$gg \rightarrow ZZ \rightarrow 2\ell 2\ell'$	gg2ZZ	3.48 fb	4.47 fb
$gg \rightarrow ZZ \rightarrow 4\ell$	gg2ZZ	1.74 fb	2.24 fb
Other di-bosons			
$WW \rightarrow 2\ell 2\nu$	MadGraph	4.88 pb	5.995 pb
$WZ \rightarrow 3\ell\nu$	MadGraph	0.868 pb	1.057 pb
$t\bar{t}$ and single t			
$t\bar{t} \rightarrow \ell^+ \ell^- v\bar{v} b\bar{b}$	POWHEG	17.32 pb	23.64 pb
t (<i>s</i> -channel)	POWHEG	3.19 pb	3.89 pb
\bar{t} (<i>s</i> -channel)	POWHEG	1.44 pb	1.76 pb
t (<i>t</i> -channel)	POWHEG	41.92 pb	55.53 pb
\bar{t} (<i>t</i> -channel)	POWHEG	22.65 pb	30.00 pb
t (<i>tW</i> -channel)	POWHEG	7.87 pb	11.77 pb
\bar{t} (<i>tW</i> -channel)	POWHEG	7.87 pb	11.77 pb
Z/W + jets ($q = d, u, s, c, b$)			
$W + \text{jets}$	MadGraph	31314 pb	36257.2 pb
$Z + \text{jets}, m_{\ell\ell} > 50$	MadGraph	3048 pb	3503.7 pb
$Z + \text{jets}, 10 < m_{\ell\ell} < 50$	MadGraph	12782.63 pb	915 pb

Table 5.3: MC simulation datasets used for the signal and background processes; Z stands for Z, Z^*, γ^* ; $\ell(\ell')$ means e, μ or τ ; V stands for W and Z ; \hat{p}_T is the transverse momentum for $2 \rightarrow 2$ hard processes in the rest frame of the hard interaction. Comment: $qq \rightarrow ZZ$ samples at 8 TeV have lower cut in m_{ll} , 4 GeV instead of 12 GeV at 7 TeV. TuneZ2 is used for 7 TeV, while TuneZ2star is used for 8 TeV analysis. The low mass Drell-Yann was produced with a filter for the 8 TeV analysis.

are described in more details for the signal and background processes. The procedures used for the re-weighting of the MC samples are also described where relevant.

5.2.1 Signal: $H \rightarrow ZZ^{(*)} \rightarrow 4\ell$

The Higgs boson samples used in the current analysis are generated with POWHEG [40] which incorporates NLO gluon fusion ($gg \rightarrow H$). The CTEQ6M PDF set is used for generation with the Higgs boson widths taken from Ref. [42]. Additional samples with WH , ZH and $t\bar{t}H$ associated production are produced with PYTHIA. The Higgs boson is forced to decay to two Z -bosons, which are allowed to be off-mass-shell, and both Z -bosons are forced to decay via $Z \rightarrow 2\ell$.

Chapter 5: Datasets and Triggers

Generator level events are re-weighted according to the total cross-section $\sigma(pp \rightarrow H)$ which embrace the gluon fusion contribution up to NNLO and NNLL taken from Ref. [43, 44, 42, 45, 46, 47, 48, 49, 50, 51] and the weak-boson fusion contribution at NNLO computed in Ref. [42, 52, 53, 54, 55, 56]. The total cross-section is scaled by the $BR(H \rightarrow 4\ell)$ [42, 57, 58, 59, 60]. Figure 5.1 (a) shows the $H \rightarrow 4\ell$ cross-section as a function of the Higgs mass m_H for $\sqrt{s} = 7$ TeV.

For the Fall11 production, a total of 28 Monte Carlo samples were produced in the range [115, 600] GeV, with a step of 10 GeV up to 230 GeV, and then steps of 25 GeV up to 600 GeV. In Summer12 production additional samples were produced ranging from 650 GeV to 1000 GeV, with a step size of 50 GeV, as well as additional low mass samples with finer granularity. The choice of mass points is driven by the nature of this analyses, i.e. search for a narrow peak over the continuum background. It has been shown that the test masses in the SM Higgs search should not be much farther apart than the observable width of the Higgs peak [61]. A simple model with a Gaussian-shaped signal and flat background shows that if we choose to step in 1σ increments, the loss of sensitivity for a Higgs boson with a mass right in the middle between the chosen test masses is less than 5%. With 2σ increments, the loss of sensitivity can be as high as 20% [61]. The increments in the mass steps are therefore chosen to be close to 1σ . Due to technical limitations, we are using steps greater or equal to 1 GeV.

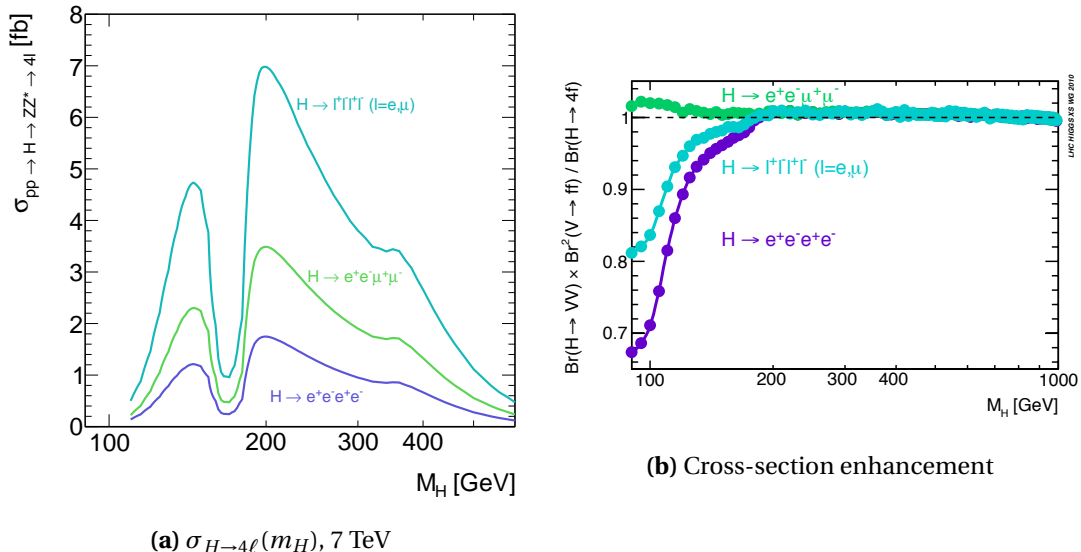


Figure 5.1: Cross-section for SM Higgs in $H \rightarrow 4\ell$, $H \rightarrow 2e2\mu$ and $H \rightarrow 4e$ (or 4μ) as a function of m_H in pp collisions at $\sqrt{s} = 7$ TeV (a). Cross-section enhancement due to the interference of amplitudes with permutations of identical leptons originating from different Z -bosons, as a function of m_H . (b)

In comparison to $\sigma(pp \rightarrow H) \cdot BR(H \rightarrow ZZ^{(*)} \rightarrow 2e2\mu)$, the 4μ and $4e$ channel cross-sections are enhanced in the case of off-mass-shell Z boson due to an interference of amplitudes with permutations of identical leptons originating from different Z -bosons, as shown in Fig. 5.1 (b).

This is correctly taken into account by Prophecy4f [42, 57, 58].

The POWHEG MC program used to simulate the $gg \rightarrow H$ process results in a Higgs Boson p_T spectrum that differs significantly from the best theoretical calculation which is available at NNLL+NLO. A theoretical estimate of this p_T spectrum is computed using the HqT [62] program, which implements such NNLL+NLO calculation. A re-weighting procedure has been studied to be applied to the simulated events. But the effect is very small for this analysis in which no direct constraints are imposed on the transverse momentum of the 4ℓ system, or on the hadronic recoil against this system (e.g. no jet veto or missing transverse momentum cut).

In the current analysis we use only samples for gluon fusion production mechanism and rescale them to the total cross-section including all other production processes (weak-boson fusion, WH, ZH and $t\bar{t}H$ associated production).

5.2.2 Background: $q\bar{q} \rightarrow ZZ^{(*)} \rightarrow 4\ell$

For the current analysis we use the samples $q\bar{q} \rightarrow ZZ^{(*)} \rightarrow 4l$ produced with POWHEG, that include the complete NLO simulation, interfaced to PYTHIA for showering, hadronization, decays and the underlying event.

5.2.3 Background: $gg \rightarrow ZZ^{(*)} \rightarrow 4\ell$

The gluon-induced ZZ background, although technically of NNLO compared to the first order Z -pair production, amounts to a non-negligible fraction of the total irreducible background at masses above the $2M_Z$ threshold. A full NNLO calculation for the ZZ production which would also take these gluon-induced diagrams into account is not available. Therefore the contributions are estimated by using the dedicated tool gg2ZZ [41], which computes the $gg \rightarrow ZZ$ at LO, which is of order α_s^2 , compared to α_s^0 for the LO $q\bar{q} \rightarrow ZZ$. The hard scattering $gg \rightarrow ZZ^{(*)} \rightarrow 4\ell$ events are then showered and hadronized using PYTHIA.

The gg2ZZ tools provide the functionality to compute the cross-section after applying a cut on the mimimally generated invariant mass of the same-flavour lepton pairs (which can be interpreted as the Z/γ invariant mass) $m_{\ell\ell}^{\min} = 10$ GeV. This number is computed by using the LO PDF set CTEQ6L1, and the central renormalization and factorization scales $\mu_R = \mu_F = m_Z$, where $m_Z = 91.188 \text{ GeV}/c^2$ is the nominal Z-boson mass. To estimate the accuracy of this number the renormalization and factorization scales were varied in the range $\mu \in [\mu_0/2, 2\mu_0]$; therefore an error of $^{+28\%}_{-20\%}$ is computed. The large uncertainty is expected, since the calculation is only LO, and only at NLO the scale dependencies start to cancel. It is thus very hard to estimate the accuracy of the convergence of the perturbative series (which contains only the first coefficient here), thus an uncertainty of $\pm 50\%$ on this number is proposed.

The gg2ZZ generator gives the contribution for final states with unlike flavours of the lepton pairs, but it was also used to estimate the like-flavour background. This is an approximation

which is only strictly valid when $m_{4\ell} \geq 2m_Z$. Below this threshold the relative amount of like-flavour events increases compared to unlike-flavour events.

The differential cross-section for $gg \rightarrow ZZ^{(*)}$ as a function of the four lepton invariant mass for different flavour lepton pairs was provided in Ref [63].

5.2.4 Background: Z+jets $\rightarrow 2\ell + \text{jets}$

Z+jets $\rightarrow 2\ell + \text{jets}$ samples was generated with MadGraph, with a statistics of $\approx 40\text{M}$ events representing an equivalent integrated luminosity well above $\mathcal{O}(10)\text{fb}^{-1}$. Both light ($q = d, u, s$) and heavy-flavour ($q = c, b$) jets are included in the sample. A generation cut on two-lepton invariant mass of $m_{2\ell} > 50\text{ GeV}$ is imposed in the simulation. A total NNLO cross-section of 3048 (3503.7) pb is used at 7 (8) TeV.

To separate the contribution from heavy-flavour jets (from now on referred to as the $Zb\bar{b}$ sample) the MadGraph Z+jets sample was partitioned in Z +light jets and Z +heavy flavour jets using a filter selecting events with two b-jets or two c-jets in the final state.

5.2.5 Background: $t\bar{t} \rightarrow 2\ell 2\nu 2b$

A $t\bar{t} \rightarrow 2\ell 2\nu 2b$ sample is generated with POWHEG event generator using CTEQ6M. The theoretical NLO cross-section for the process is $\sigma_{NLO}(pp \rightarrow t\bar{t} \rightarrow 2\ell 2\nu 2b) = 17.32$ (23.64) pb at 7 (8) TeV [64].

A sample of about 10 million events corresponding to an integrated luminosity of more than 600 fb^{-1} is simulated.

6 Leptons and Photons

The reconstruction of the SM Higgs boson in the decay chain $H \rightarrow ZZ^{(*)} \rightarrow 4\ell$ imposes high-performance lepton reconstruction, identification and isolation as well as excellent lepton energy-momentum measurements. The identification of isolated leptons emerging from the event primary vertex allows for a drastic reduction of QCD-induced sources of misidentified, i.e. "fake" leptons. The precision energy-momentum measurements is of major importance to obtain a precise measurement of the Higgs boson mass $m_{4\ell}$, the most discriminating observable in the Higgs boson search.

With four leptons in the final state, and in view of the tiny fraction of the total production cross-section in the 4ℓ channels, a very high lepton reconstruction efficiency is mandatory. For Higgs bosons with masses $m_H < 2m_Z$, one lepton pair at least couples to a virtual Z^* boson. The softest lepton in that pair typically has $p_T^\ell < 10$ GeV for masses $m_H < 140$ GeV (see Fig. 6.1). Maintaining the highest possible reconstruction efficiency whilst ensuring sufficient discrimination against hadronic jets is especially challenging for the reconstruction of leptons at very low p_T^ℓ . In this region a full combination of information provided by the tracker and electromagnetic calorimetry for electrons or by the tracker and muon spectrometer for muons becomes essential.

These very low p_T^ℓ leptons lie at the extreme edge of the domain controlled in CMS using tag-and-probe methods in inclusive single Z production. Otherwise, the single Z production is an ideal candle for this analysis, covering leptons in the p_T range from $\mathcal{O}(10)$ to $\mathcal{O}(100)$ GeV. In the case of muons, the low p_T lepton measurements can be complemented by tag-and-probe using $J/\Psi \rightarrow \mu^+ \mu^-$ production. In the electron case, the background is much harsher to deal with. Currently, there are ongoing studies on $J/\Psi \rightarrow e^+ e^-$ and $Z \rightarrow e^+ e^- \gamma$ as sources of low- p_T electrons.

In this chapter, the basics of lepton reconstruction, identification and isolation are presented. The tag-and-probe measurements, which aim to validate lepton objects and to deduce data-MC scale factors are covered in Chapter 7.

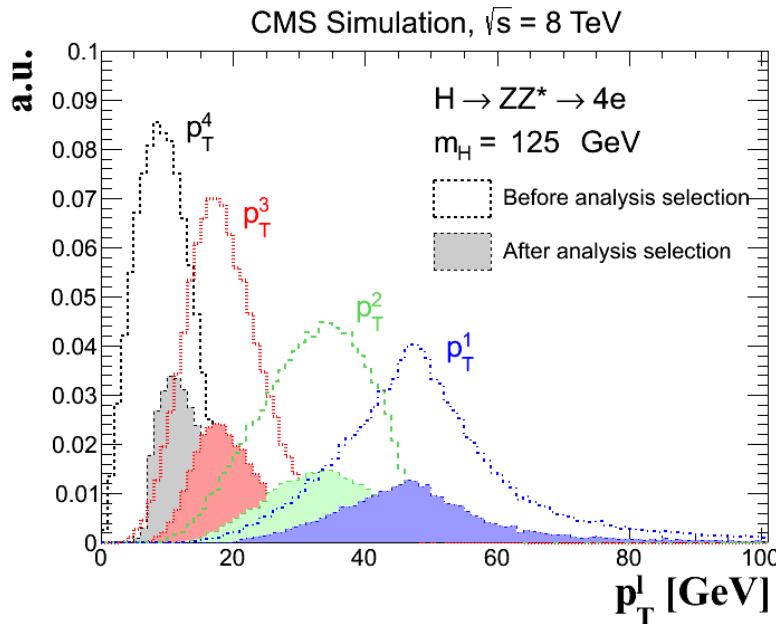


Figure 6.1: Distribution of the transverse momentum (p_T) for each of the four leptons (sorted in p_T) from $H \rightarrow ZZ^{(*)} \rightarrow 4\ell$ signal events and for a mass hypothesis of $m_H = 125$ GeV. The distributions are obtained using MC signal samples and shown at generator level within eta acceptance (empty histograms), and for selected events (shaded histograms) in the $4e$ channel

6.1 Electrons

6.1.1 Reconstruction

Reconstruction algorithm

The electron reconstruction [65] combines Electromagnetic Calorimeter (ECAL) and tracker information. For this analysis, the standard CMS electron reconstruction algorithm is used [66, 67, 68].

The reconstruction starts by reconstructing clusters seeded by hot cells in the ECAL, which are used to form superclusters to further collect the energy coming from bremsstrahlung photons in the tracker volume. These superclusters are then used to select trajectory seeds built from combination of hits from the innermost tracker layers. The seeding algorithm combines pixel and Tracker Endcaps (TEC) in order to gain efficiency in forward region where pixel detector coverage is limited. The selection is made by matching superclusters with trajectory seeds built from triplets or pairs of hits. The procedure takes advantage of the fact that supercluster position is located on the helix of initial electron trajectory. It is then possible to predict the position of the hits by propagating back the parameters of the helix through magnetic field towards the innermost part of the trajectory, before which radiation is unlikely to happen. This strategy, allows for efficient rejection of jets faking electrons.

This ECAL driven electron seeding strategy is very efficient for isolated electrons with $p_T^e > 10 \text{ GeV}$. At lower p_T^e , the ϕ window used for the superclusters starts to be too small and some electrons which radiate lead to electron and photon clusters separated more than 0.3 rad in the magnetic field. Moreover, for the cases of electrons in jets, the energy collected in the superclusters may include some neutral contribution from the jets therefore biasing the energy measurement used to seed electron tracks. For these reasons, the above seeding strategy is complemented by a tracker driven algorithm, developed in the context of the Particle Flow (PF) event reconstruction [69]. The tracker driven seeding starts from the high purity tracks, and makes use of the particle flow clustering which exploits the fine ECAL granularity.

The tracker driven seeding algorithm, described in details in [70], can be illustrated with two extreme cases. When an electron does not radiate energy by bremsstrahlung while traversing the tracker, it gives rise to a single cluster in the ECAL and its track is often well reconstructed by the standard Kalman Filter which is able in these cases to collect hits up to the ECAL entrance. The track can then be matched with a particle flow cluster, and its momentum compared to the cluster energy forming an E/p ratio. If this ratio is close to unity, the seed of the track is promoted to electron seed. Alternatively, when an electron undergoes a significant bremsstrahlung, the standard Kalman Filter is not able to follow the change of curvature, and the track has a small number of hits, and a large χ^2 . Thus, using the tracker as a preshower, and exploiting the differences of characteristics between a pion track and an electron track reconstructed with the standard Kalman Filter algorithm, the electron tracks can be selected. The variety of situations between the two extreme cases illustrated here require a treatment more sophisticated than what was just described. In practice, a refined treatment of the track is applied, and the pure tracking observables are combined with the ECAL-track matching quality variables in a single discriminator with a multivariate analysis.

Seeds from the two algorithms are then merged in a single collection, keeping track of the seed provenance. Figure 6.2 shows the resulting seeding efficiency as a function of generated electron η^e and p_T^e for electrons from a sample of $Z \rightarrow e^+e^-$ decays. The separate contribution of each algorithm is also shown.

Although the tracker driven seeding has been primarily developed and optimized for non-isolated electrons, it brings additional efficiency on isolated electrons, in particular in the ECAL crack regions ($\eta \approx 0$ and $|\eta| \approx 1.5$) and, as expected, at low p_T^e . At 5 GeV, the seeding efficiency is increased by 12.5% by combining with tracker driven seeds. Below this value, the seeding efficiency is entirely dominated by the tracker driven seeds and at high p_T^e , additional efficiency brought by the tracker driven approach is at the 1-2% level.

Electron seeds are then used to initiate a track building and fitting procedure based on a combinatorial Kalman Filter [71] in order to best handle the effect of bremsstrahlung energy loss [72]. Compatible hits on the next silicon layers are first searched for, then an extrapolation is performed, using a Bethe-Heitler modelling of the electron losses. This procedure is iterated until the last tracker layer, unless no hit is found in two subsequent layers or the measured

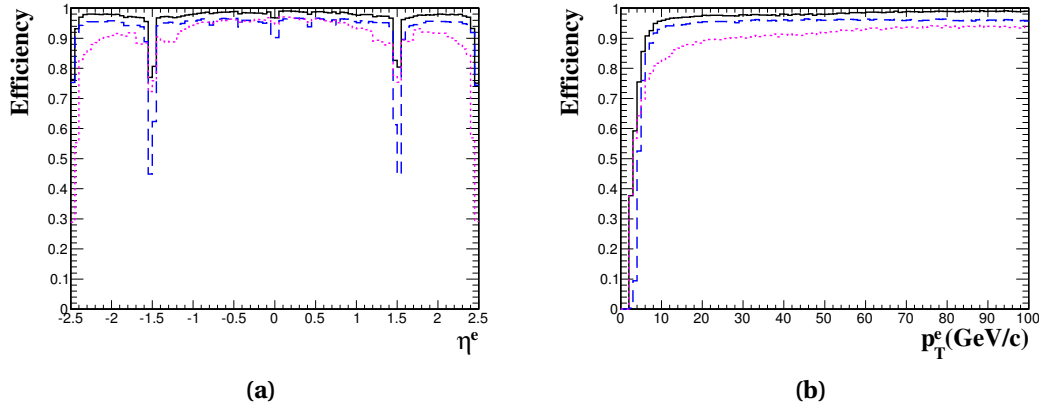


Figure 6.2: Electron seeding efficiency (solid line) as a function of (a) generated electron η^e and (b) generated electron p_T^e for a sample of electrons with uniform distribution in η^e and p_T^e and for $p_T^e > 2$ GeV. The individual contributions from the ECAL driven (dashed, blue) and from the tracker driven (dotted, pink) seeding algorithms are also shown.

curvature falls below a threshold corresponding to $p_T = 2$ GeV. While Kalman Filter track finding works very good for Minimum Ionizing Particles (MIP), in electron case it leads to shorter tracks, stopping the iteration procedure when a significant curvature change occurs due to bremsstrahlung. For this reason a dedicated electron track refitting has been developed allowing to collect hits up to the ECAL, despite the presence of electron energy loss in the tracker material. The procedure is based on Gaussian Sum Filter (GSF) in which the energy loss in each layer is approximated by a weighted sum of Gaussian distributions. The number of collected hits from the electron track reconstruction procedure is compared in Fig 6.3 with the standard Kalman Filter used for pions and muons. The differences arise from the choices of the modelling of the energy loss and of the trajectory building parameters.

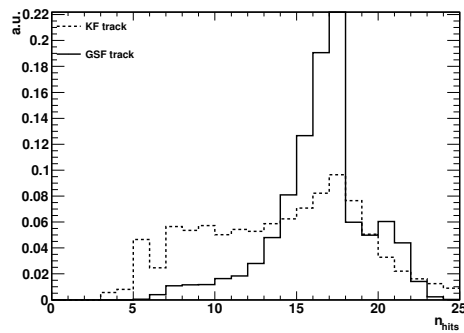


Figure 6.3: Number of reconstructed hits per track for electrons from $Z \rightarrow e^+ e^-$ decays as obtained with the dedicated GSF tracking procedure (solid line) and with the standard Kalman Filter (dashed line).

To illustrate the importance of dedicated GSF track fitting algorithm for collecting bremsstrahlung energy losses, the difference between the momentum magnitude at the outermost track position and at the innermost track position, as an estimate of the true fraction of energy radiated by the electron is computed [65]. The normalized difference called “ f_{brem} ” is shown on Fig. 6.4 for electron from $Z \rightarrow e^+ e^-$ decays and for a background constituted by QCD dijet events with p_T^{hat} within 80 – 120 GeV. The distribution is nearly flat for the signal while for the background it peaks at low f_{brem} values as expected from a background composed of charged hadrons that radiate minimally. This variable is used in the electron classification that enters the final electron momentum estimation and is an important ingredient of electron identification algorithms.

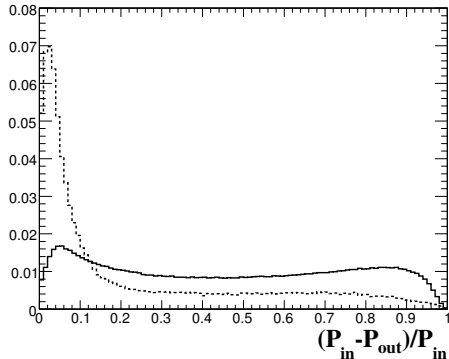


Figure 6.4: Electron bremsstrahlung fraction f_{brem} for electrons (solid line) from $Z \rightarrow e^+ e^-$ decays and background (dashed line) from a sample of QCD dijet events with p_T^{hat} within 80 – 120 GeV.

Preselection

Electron candidates are preselected using loose cuts on track-cluster matching observables to preserve the highest possible efficiency while removing part of the QCD background. The four-momenta of an electron is obtained by taking angles from the associated GSF track, and the energy from a combination of tracker and ECAL information [66]. The information from the track is measured at the distance-of-closest approach to the beam spot position in the transverse plane. Electron tracks are not re-fitted to the common primary vertex. For the analysis, the electron candidates are required to have transverse momentum p_T^e larger than 7 GeV and reconstructed $|\eta^e| < 2.5$. The reconstruction efficiency for isolated electrons is shown on Fig. 6.5. It is expected to be above $\approx 90\%$ over the full ECAL acceptance, apart from narrow "crack" regions. Integrated over the acceptance, the reconstruction efficiency for basic electron objects steeply rises to reach $\approx 90\%$ at $p_T = 10$ GeV, and then more slowly to reach a plateau of $\approx 95\%$ for $p_T^e = 30$ GeV.

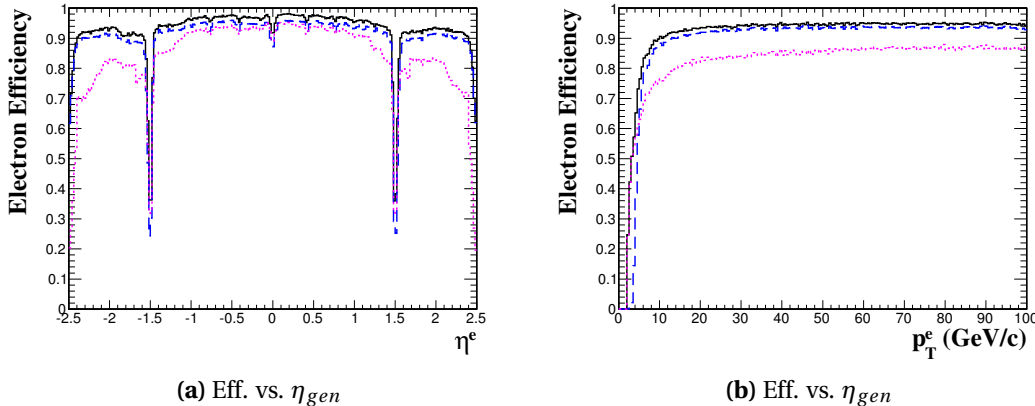


Figure 6.5: Electron efficiency after preselection (solid line) as a function of generated electron η^e (a) and generated electron p_T^e (b) for a sample of di-electron events with uniform distribution in η^e and p_T^e and with $p_T^e > 2$ GeV. The individual contributions from ECAL seeded electrons (dashed line) and from tracker seeded electrons (dotted line) are also shown.

Charge Identification

The electron charge identification is obtained from curvature of an electron track. It suffers from the conversion of radiated photons and more generally from the showering of primary electrons particularly if it happens early in the detector giving rise to charge miss-identification (miss-ID). To reduce the miss-ID, a combination of charge estimate from GSF track, Kalman Filter track and supercluster is used. The final charged attached to an electron is the one on which two out of the three estimates agree.

Electron charge mis-identification has been measured on 2010 data using Z events and a charge mis-ID of 0.004 ± 0.001 (0.028 ± 0.003) was measured in the ECAL barrel (ECAL endcaps) in a very good agreement with the simulation [73]. No significant p_T dependency has been observed in the range of on-shell Z boson decays, also in agreement with the expectation.

ECAL Energy Measurement using a Multivariate Regression

The energy resolution for electrons can be significantly improved using a multivariate regression approach. This has been demonstrated in Ref. [34]. We employ such a technique for the analysis to improve the mass resolution for final states involving electrons. Details of the method and performance can be found¹.

The energy resolution for electrons can be significantly improved using a multivariate regression approach. This has been demonstrated in Ref. [74]. We employ such a technique for the analysis to improve the mass resolution for final states involving electrons. Details of the

¹The text of this section on the electron calibration from a regression [117] of which the writer of this thesis

technique is taken from Ref. is a co-editor.

method and performance². can be found in Ref. [75].

Following the procedure used for the $H \rightarrow \gamma\gamma$ analysis [74], we train the boosted decision tree on the Drell-Yan Monte Carlo sample. Depending on the region of detection of electron in electromagnetic calorimeter, a different set of input variables was used. The variables that are used in the training are listed under Appendix A.

The regression was trained for barrel and endcap electrons separately. Dividing samples into two allowed for testing against the over-training. The first half was used for training, while the remaining half was used to test the performance of the regression. Only non-radiative electrons were used in the training, with radiated energy fraction < 0.01 , to avoid overlapping with final state radiation recovery, for which there is a separate algorithm described in Sec. 6.5.1. The ratio of the generated energy to the raw energy of the supercluster for barrel electrons, and the ratio of the generated energy to the sum of the supercluster raw energy and the preshower energy for endcap electrons was chosen as a target value of the regression.

The combined electron momentum measurement, described in the next subsection is formed by the energy measurement from regression and the momentum measurement from the GSF track. The performance is evaluated using the $Z \rightarrow e^+ e^-$ resonance, where the resolution for the electron pair mass computed using the regression energy measurement and the mass computed using the supercluster corrected energy is compared. This is shown in Fig. 6.6, where we observe an increase in performances. In Fig. 6.7, we also show the comparison of the reconstructed Higgs boson mass for the four electrons and two electrons two muons final state. An improvement in the resolution of more than 10% is seen, in agreement with what is observed using events from Z.

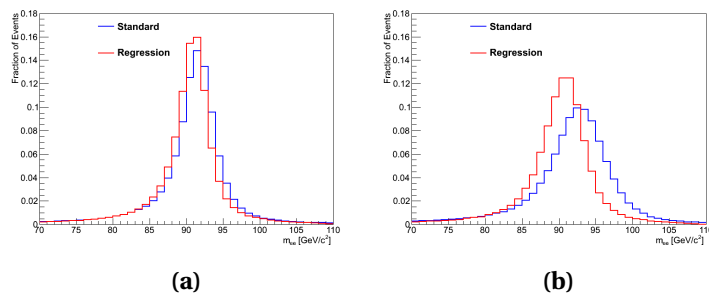


Figure 6.6: A comparison of the reconstructed $Z \rightarrow ee$ mass using the standard electron momentum assignment and the regression assignment are shown for the Monte Carlo simulation separately in events where (a) both electrons are in the central barrel ($|\eta| < 0.8$), (b) both are in the endcap ($|\eta| > 1.479$).

²The text of this section on the electron calibration from a regression technique is taken from Ref. [75] of which the writer of this thesis is a co-editor.

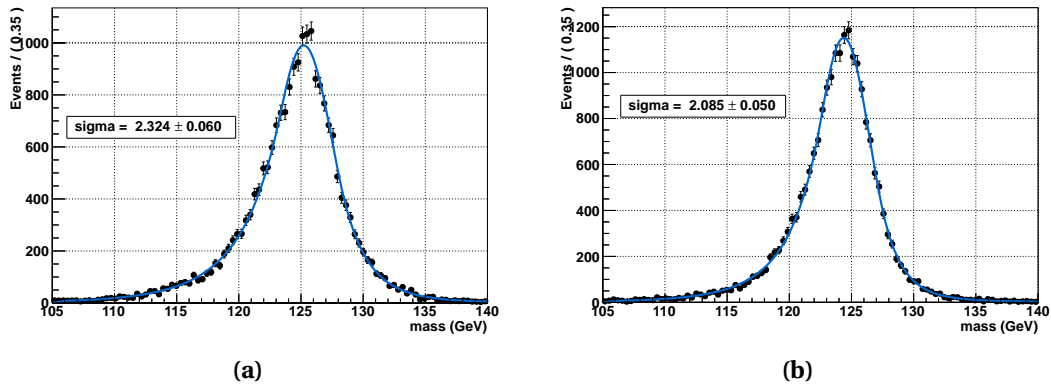


Figure 6.7: A comparison of the reconstructed Higgs boson mass distributions after applying Monte Carlo to data corrections for the standard electron momentum assignment (left) and the regression assignment (right), for the 4e channel.

Momentum Determination and Calibration

The combination of the ECAL and the tracker measurements is used to obtain the electron momentum magnitude. In this way we take the advantage of the track momentum estimate in particular in the low energy region and in the ECAL crack regions. Starting from the energy as obtained from the supercluster after ECAL level corrections (from hereafter labeled E), the momentum magnitude can be further refined by splitting electrons into different classes and performing class Dependant corrections. The electron classification is based on the observed number of clusters inside the supercluster in the ECAL and on the measured bremsstrahlung fraction by the tracker [34]. The classification has been further refined and the electron classes are defined as follows:

1. “golden”, or low bremming electrons with a reconstructed track well matching the supercluster:
 - a supercluster formed by a single cluster (i.e. without observed bremsstrahlung sub-cluster),
 - a ratio $E/p > 0.9$,
 - a measured brem fraction $f_{brem} < 0.5$;
2. “big brem”, or electrons with high bremsstrahlung fraction but no evidence of energy loss effects:
 - a supercluster formed by a single cluster,
 - a ratio $E/p > 0.9$,
 - a measured bremsstrahlung fraction $f_{brem} > 0.5$;
3. “showering”, or electrons with energy pattern highly affected by bremsstrahlung losses:

- a supercluster formed by a single cluster not falling in the “golden” or “big brem” classes, or a supercluster formed by several sub-clusters.

“Crack” electrons are defined as electrons whose supercluster’s starting crystal is close to an η boundary between ECAL modules, or between the ECAL barrel and ECAL endcap, or close to the innermost ring of an ECAL endcap. The population of electrons in the different classes is shown in Fig. 6.8 as a function of the generated η for electrons with a uniform p_T^e distribution between 2 and 150 GeV. The shape of the distribution for the showering class clearly reflects the η distribution of the material thickness. The integrated fractions of reconstructed electrons in the different classes are as follows: 29.8% (golden), 12.2% (big brem), 53.3% (showering) and 4.7% (cracks).

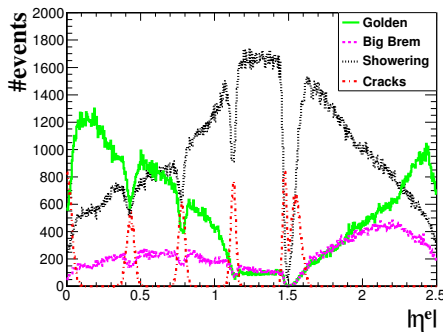


Figure 6.8: The electron population in the different classes as a function of the generated pseudorapidity for di-electrons with an initial transverse momentum uniformly distributed between 2 and 150 GeV.

Figure 6.9 presents the peak value of the distribution of ratio between the supercluster and the generated energy as a function of the supercluster pseudorapidity (as seen from (0,0,0)) and of the supercluster energy for electrons from the golden, big brem and showering classes. The peak value is obtained by fitting the Gaussian part of the distribution in slices of pseudorapidity and energy.

As can be expected, the tracker measurement is more used at low energies as well as in the regions where the precision of the ECAL measurement is poor. The normalized effective RMS of the combined momentum estimate as well as of the ECAL and tracker measurements alone are presented in Fig. 6.10 for electrons in the ECAL barrel and electrons in the ECAL endcaps. Electrons are from a sample of di-electron events with uniformly distributed transverse momentum between 2 and 150 GeV. The precision is clearly improved by using the combined estimate with respect to the ECAL only measurement for energies below $\approx 25 - 30$ GeV.

The normalized effective RMS of the ECAL estimate and of the combined estimate are presented for the different classes in Fig. 6.11 as a function of the generated electron energy for electrons in the ECAL barrel. Golden electrons show a significantly better resolution than the

Chapter 6: Leptons and Photons

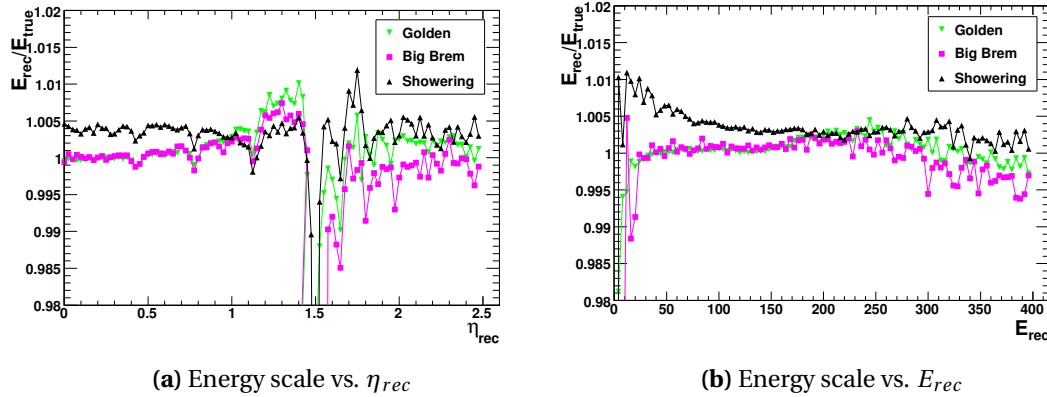


Figure 6.9: Fitted peak value of the reconstructed supercluster energy over the generated energy E/E^e for electrons from the golden (downward triangles, green), big brem (squares, magenta) and showering (upward triangles, black) classes as a function of the reconstructed supercluster pseudorapidity η and the reconstructed supercluster energy E .

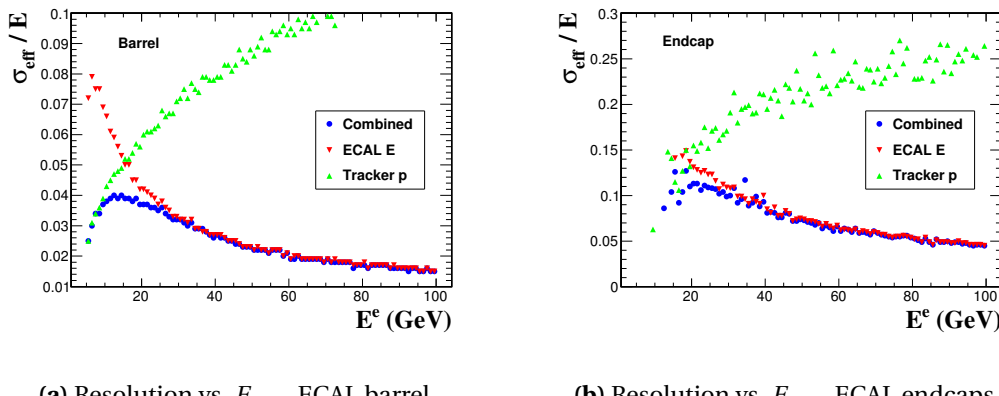


Figure 6.10: Effective resolution for the ECAL, the tracker and the combined momentum estimates as a function of the electron generated energy for (a) electrons in the ECAL barrel and (b) electrons in the ECAL endcaps. Electrons are from a sample of di-electron events with uniformly distributed transverse momentum in range 2 – 150 GeV.

average electron, with an asymptotic effective RMS of $\sim 1\%$. A significant degradation of the resolution is visible for showering electrons as well as for electrons from the crack class.

Finally, when the electron has been found by the tracker driven method and not by the ECAL driven method, the energy built from the tracker driven reconstruction of superclusters is used to construct the 4-momentum. In these cases, the electron momentum is simply constructed from the track direction and the supercluster energy.

The electron momentum scale and resolution can be controlled using Z boson decays to electrons. Fits to the Z line-shape selecting electrons with $E_T > 25$ GeV show differences in

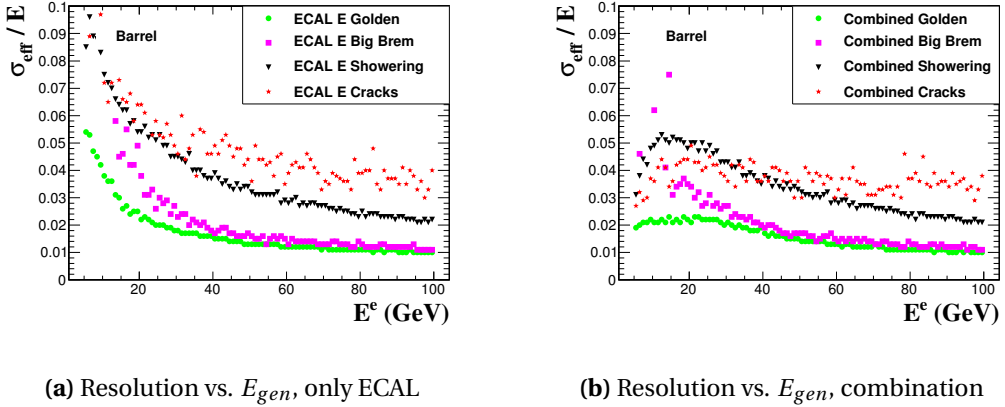


Figure 6.11: Effective resolution for the different electron classes as a function of the electron generated energy for electrons in the ECAL barrel (a) from the ECAL measurement only and (b) after the combination with the tracker measurement. Electrons are from a sample of dielectron events with uniformly distributed transverse momentum between 2 – 150 GeV.

scale between data and MC of 0.3% (0.4%) in the ECAL barrel (ECAL endcap). The electron classification also allows for the identification of electrons accompanied by low bremsstrahlung with smallest measurement error [65, 68] on which the intrinsic energy resolution is checked. Scale factors on the data and additional smearing on the MC as obtained by fits to the Z line-shape [76] are applied on reconstructed electrons to correct for the measured differences between the data and MC. Detailed comparisons between data and MC, after e-scale corrections on DATA and smearing on MC, will be shown in Section 9.3.3.

Chapter 6: Leptons and Photons

6.1.2 Identification

The electron reconstruction in CMS being highly efficient suits for most analysis. At the same time there is a significant amount of jets reconstructed as electrons remaining. To increase the purity of the sample of electron candidates for the analysis we apply identification requirements on top of the basic collection of reconstructed electron objects. In 2011 analysis, a simple cut-based electron identification was used with cuts defined for different electron categories [77]. For the purposes of 2012 analysis, in order to get the best possible signal discrimination of real electrons from jets faking electrons, a new identification tool has been developed using multivariate techniques [78].

The input for the multivariate “blender” are coming from the three main categories of variables: observables matching calorimeters and the tracker (including the preshower) information, pure calorimetric and pure tracking observables. The three classes with its complete list of observables are listed below:

1. Track-calorimeters matching observables:

- E_{tot}/p_{in} , where E_{tot} is the ECAL supercluster energy and p_{in} the track momentum at the innermost track position;
- E_e/p_{out} , where E_e is the energy of the ECAL cluster closest to the electron track extrapolation to ECAL and p_{out} the track momentum at the outermost track position;
- $|\Delta\eta_{in}| = |\eta_{sc} - \eta_{in}^{extrap.}|$, where η_{sc} is the energy weighted position in η of the supercluster and $\eta_{in}^{extrap.}$ is the η coordinate of the position of the closest approach to the supercluster position, extrapolating from the innermost track position and direction;
- $|\Delta\phi_{in}| = |\phi_{sc} - \phi_{in}^{extrap.}|$, where $|\Delta\phi_{in}|$ is a quantity similar to the previous one but in azimuthal coordinates.
- $|\Delta\eta_{out}| = |\eta_e - \eta_{out}^{extrap.}|$, where η_e is the η position of the cluster closest to the electron track extrapolation to ECAL ($\eta_{out}^{extrap.}$).
- $1./E_{tot} - 1./p_{4-mom}$ which measures the deviation of the supercluster energy and electron momentum obtained by combining the tracker and ECAL information p_{4-mom} .
- E_{HCAL}/E_{tot} and E_{ES}/E_{tot} are the ratios of the energy measured in the HCAL and in the preshower (ES) with the supercluster energy. This observables are used to improve the electron-pion discrimination.

2. Pure calorimetric shower shape observables:

- $\sigma_{i\eta i\eta}$ the width of the ECAL cluster along the η direction computed in the 5×5 block of crystals centred on the highest energy crystal of the seed cluster;

- $\sigma_{i\phi i\phi}$ as the former but in azimuthal coordinates,
 - $\eta - width$ supercluster η width,
 - $\phi - width$ supercluster ϕ width,
 - $(E_{5\times 5} - E_{5\times 1})/E_{5\times 5}$: where $E_{5\times 5}$ is the energy computed in block of crystals and $E_{5\times 1}$ is the energy computed in the strip of crystals containing the cluster seed,
 - $R9 = E_{3\times 3}/E_{tot}$ energy sum of 3×3 crystal centred on the most energetic, divided by the supercluster energy.
3. Pure tracking observables aiming to further improve the separation between electrons and charged hadrons:
- $f_{brem} = (p_{in} - p_{out})/p_{in}$ with the GSF track, which measures very well the Bremsstrahlung emission which helps in discriminating against charged hadrons,
 - χ^2_{GSF} indicating the goodness-of-fit of GSF tracking procedure,
 - number of hits of Kalman Filter (KF) track associated to electron,
 - χ^2_{KF} indicating the goodness-of-fit of KF track.

To be confident with the multivariate technique output it is of extreme importance to have all the input variables well described in simulation. For this reason a set of electron validation plots is shown in Fig. 6.12 for track-calorimetry matching observables, in Fig. 6.13 for pure calorimetric observables and in Fig. 6.14 for pure tracking observables. It is very comforting to see that observables agree very well between data and MC.

The profit carried out by the information in these observables is maximized by using a Boosted Decision Trees (BDT) multivariate technique [79, 80, 81] where the signal and background samples for the training have been carefully chosen.

The training of the BDTs for background was performed on a $W + 1$ -fake electron sample taken from data, while for signal, a mixture of MC $H \rightarrow ZZ \rightarrow 4e$ samples with masses 115, 120, 130 and 140 GeV was used. Three different bins of η : $|\eta| < 0.8$, $0.8 \leq |\eta| < 1.479$ and $1.479 \leq |\eta| < 2.5$ were used for training in order to take into account the different material budget in the tracker. Moreover due to the dependencies of the electron observables on p_T it was found that the final signal to background separation was improved when dividing the sample in two bins of p_T : $5 \leq p_T \leq 10$ GeV and $p_T > 10$ GeV.

The output of the BDT is presented in Fig. 6.15 for each of the six bins used for the training. Very good separation between signal and background and very good agreement between fakes in data and MC are observed.

In addition, all electrons are required to have 0 or 1 expected missing inner hits in order to reject photon conversions.

A detailed study and control from 2011 and 2012 data of the efficiency for electron identification with respect to the electron reconstruction is reported in Ch. 7.

Chapter 6: Leptons and Photons

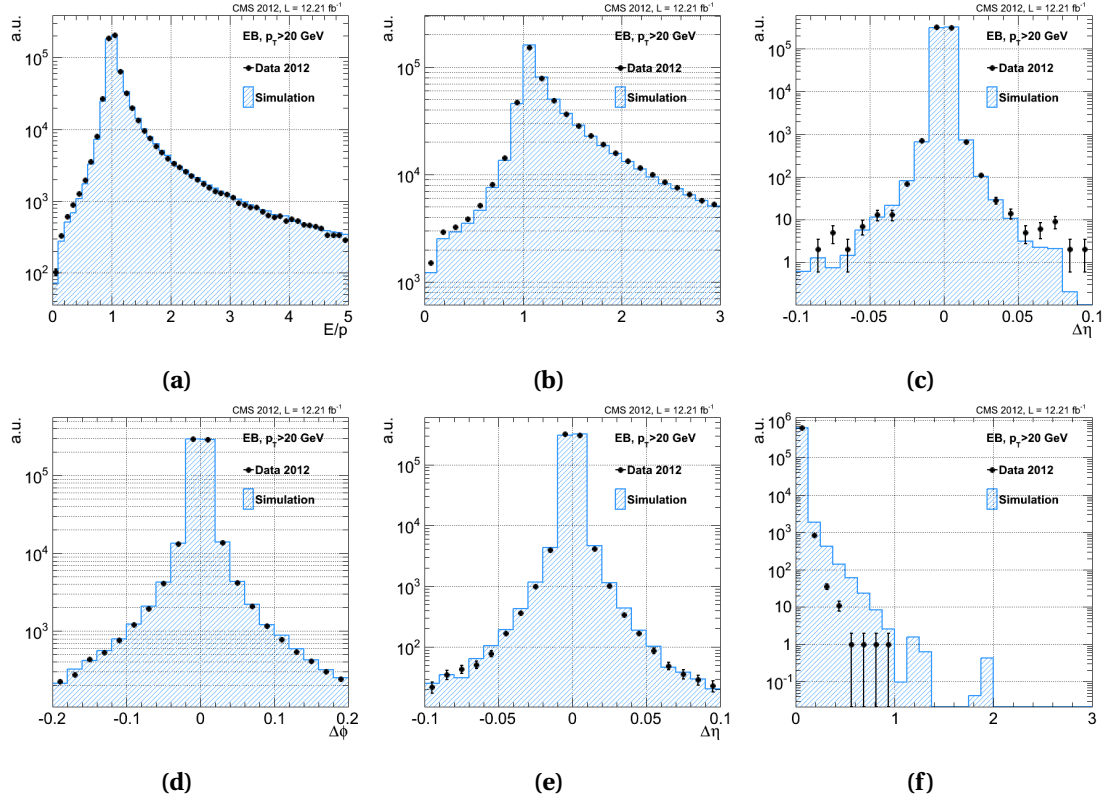


Figure 6.12: Validation of track-calorimetry matching observables used as input for multivariate electron identification with data corresponding to 12.21 fb^{-1} for the 8 TeV data.

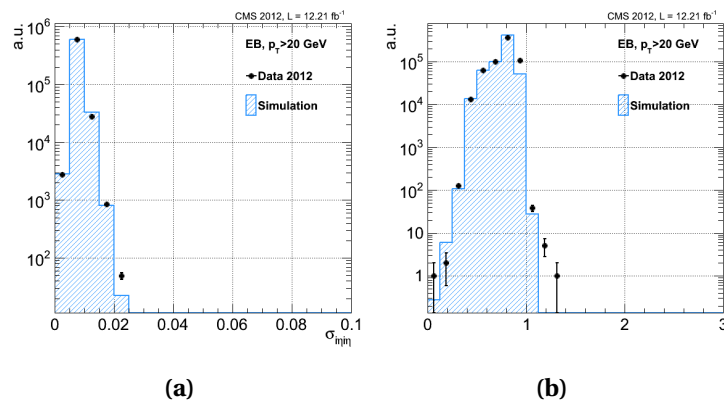


Figure 6.13: Validation of pure calorimetric observables used as input for multivariate electron identification with data corresponding to 12.21 fb^{-1} for the 8 TeV data.

6.1. Electrons

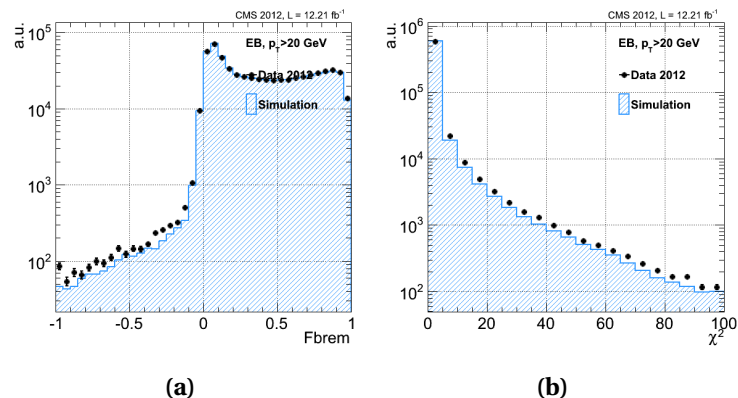


Figure 6.14: Validation of pure tracking observables used as input for multivariate electron identification with data corresponding to 12.21 fb^{-1} for the 8 TeV data.

Chapter 6: Leptons and Photons

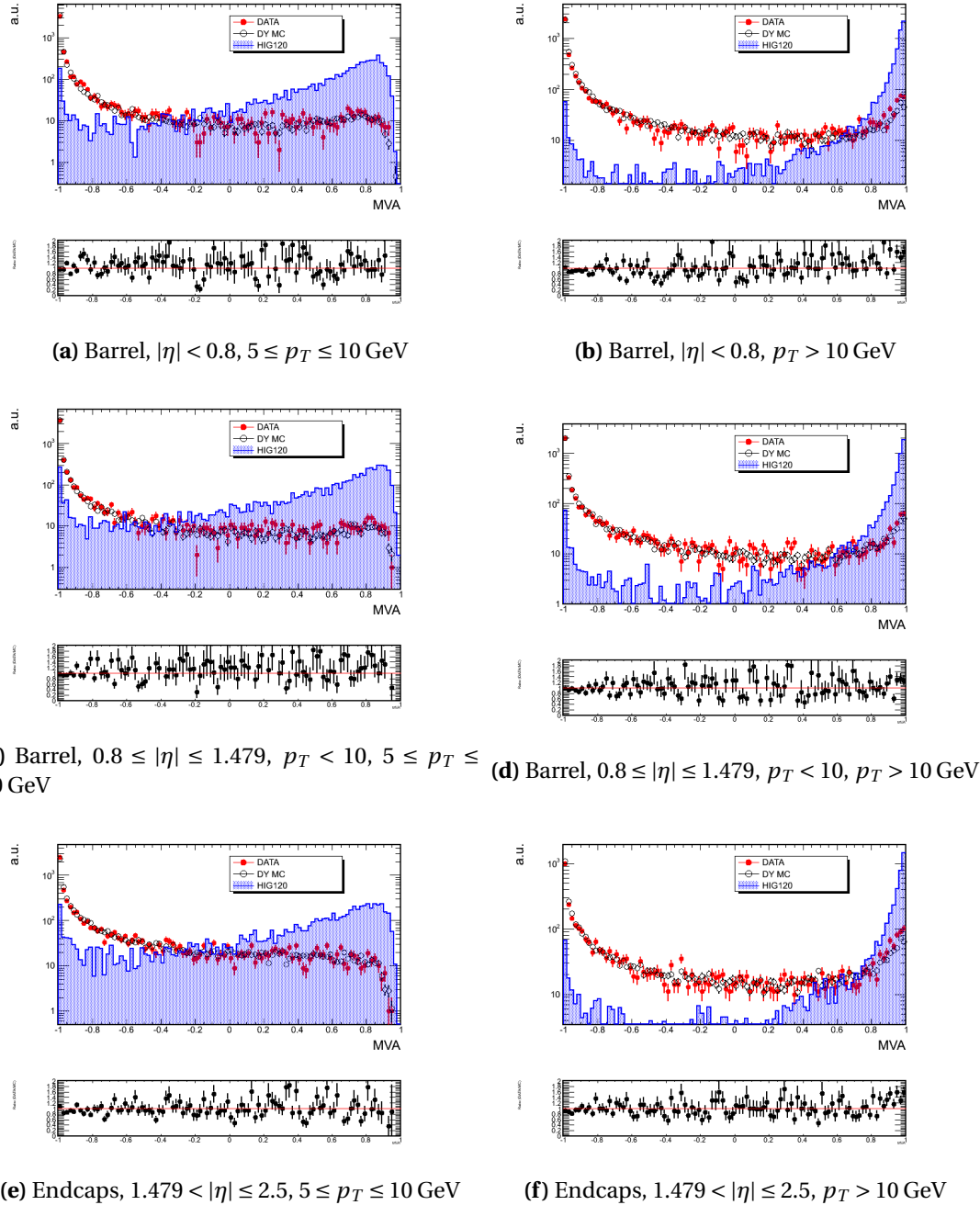


Figure 6.15: BDT output for each of the six categories used in the training. Training sample for background (red plain circles) are overlayed with fake electrons from Drell-Yan + jets sample (black empty circles) and with electrons from Higgs signal (filled area).

Working Point Optimization

An optimization procedure was performed in order to find the BDT working point to be used in this analysis. A Monte Carlo $H \rightarrow ZZ \rightarrow 4e$ sample (with $m_H = 120$ GeV) was used as signal, while background was modelled by a $Z + 1$ -fake electron sample, directly taken from data. The Z selection closely follows the selection used in the 2011 published analysis [35], denoted as “PRL analysis” throughout this document. The additional electron is a *loose electron* as defined in section 8.2.2. In addition, the missing transverse energy reconstructed by the particle flow algorithm was required to be less than 25 GeV in order to suppress contamination from WZ events containing three real leptons.

In each of the six p_T and η bins described above, the cut value on the BDT output was chosen so as to obtain the same background efficiency as the cut-based electron identification algorithm used in the PRL analysis (“Cuts-In-Categories”). As it can be appreciated on the figure 6.16, in each tested bins, the BDT is bringing a sizable improvement with respect to the cut-based electron identification used in 2011. In particular, for $p_T < 10$ GeV, the electron identification efficiency is increased by 30% for the same per-lepton background efficiency as in PRL analysis. The working point, i.e. cut values obtained after “same fake-rate” optimization are displayed in Table 6.1.

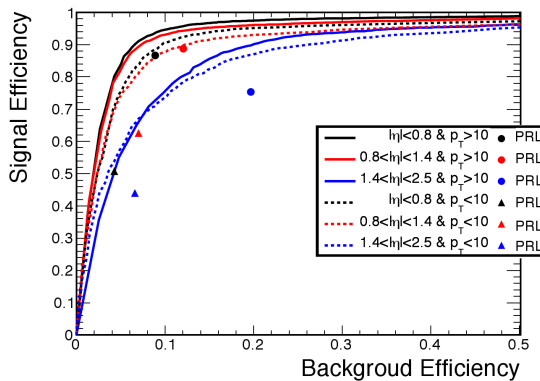


Figure 6.16: Higgs signal efficiency (MC) vs background efficiency from $Z + 1$ -fake electron sample (data). Solid lines represent results for the BDT, while single points show the corresponding ones for the “Cut-In-Categories” electron identification used in the 2011 analysis (PRL). Results are shown for various bins in p_T and η .

Table 6.1: The cut values for the BDT obtained by optimization.

p_T range [GeV]	η range	Cut value (BDT >)
$5 \leq p_T \leq 10$	$ \eta < 0.8$	0.470
	$0.8 \leq \eta \leq 1.479$	0.004
	$1.479 < \eta \leq 2.5$	0.295
$p_T > 10$	$ \eta < 0.8$	0.500
	$0.8 \leq \eta \leq 1.479$	0.120
	$1.479 < \eta \leq 2.5$	0.600

6.2 Muons

6.2.1 Reconstruction

For the standard CMS reconstruction for pp collisions, the muon tracks are first reconstructed independently in the inner tracker and in the outer muon system³. The track reconstructed in the inner tracker are called “tracker track”. The ones reconstructed in the muon system are called “standalone-muon tracks”. Based on these basic reconstruction objects, two muon reconstruction approaches are then used [83]:

1. *Reconstruction of Global Muons(outside-in).*

Each standalone-muon track is matched to tracker track by comparing parameters of the two tracks propagated onto a common surface. A *global-muon track* is fitted combining hits from the tracker and standalone-muon track, using the Kalman Filter technique [84]. At large transverse momenta, $p_T > 200 \text{ GeV}$, the global-muon fit improves the momentum resolution compared to the tracker-only fit [85, 86].

2. *Reconstruction of Tracker Muons(inside-out).*

Tracker tracks with $p_T > 0.5 \text{ GeV}$ and the total momentum $p > 2.5 \text{ GeV}$ are considered in this approach as possible muon candidates and are extrapolated to the muon system taking into account the magnetic field, the average expected energy losses, and multiple scattering in the detector material. If at least one muon track segment made of DT and CSC hits matches the extrapolated track, the corresponding tracker track is promoted to a Tracker Muon.

The requirement of a single muon segment in muon system makes Tracker Muon reconstruction more efficient than the Global Muon reconstruction at low momenta, $p \lesssim 5 \text{ GeV}$. The Global Muon reconstruction is designed to have high efficiency for muons passing through more than one muon station and requires muon track segments in at least two muon stations.

About 99% of muons produced in pp collisions with sufficiently high momentum are reconstructed either as a Global Muon or a Tracker Muon, and very often as both. This is thanks to the high tracker-track efficiency [87] and a very high efficiency of reconstructing segments in the muon system. Muon candidates found both by the Global Muon and the Tracker Muon algorithms sharing the same tracker track are merged into a single candidate. It is also worth to mention that muons reconstructed only as standalone-muons have worse momentum resolution. They also have lower collision muon to cosmic-ray muon ratio than the Global and Tracker Muons and are not used in this analyses.

³The text of this section on the on muon reconstruction as well as of the section on muon identification is taken from Ref. [82] of which the writer of this thesis is a co-editor.

6.2.2 Identification

To achieve an efficient muon reconstruction, several reconstruction algorithms are used. A desired balance between identification efficiency and purity is obtained by applying a selection based on various muon identification variables. For this analysis we choose the *Particle Flow Muon selection*. The CMS particle-flow event reconstruction [88] uses the information from all subdetectors to identify and reconstruct individually particles produced in the collision. The resulting list of particles is then used to construct higher-level particle-based objects and quantities, such as jets and missing transverse energy.

Particle-Flow Muons are identified by carefully selecting the muon candidates reconstructed with the standard Tracker and Global Muon algorithms. This selection has been optimized to identify muons in jets with high efficiency, keeping the misidentification rate from charged hadrons low. This is needed to avoid biases in jet and E_T^{miss} measurements coming from non-identified or misidentified muons. As a result, the Particle-Flow Muon selection retains non-isolated muons, including the muons from hadron decays in flight, which are usually considered as a background in analysis using muons. This virtue is achieved by applying selection criteria depending on muon isolation, and its momentum compatibility with the energy deposit in the calorimeters assigned to the candidate by the particle-flow event reconstruction. In this way the identification criteria on prompt isolated muons can be relaxed, without increasing fake rate defined as probability of a particle other than muon to be identified as muon. The details of the Particle-Flow Muon selection are described in Ref. [89].

For the analysis published in 2011 the muon identification was based only on the Global Muon reconstruction. Comparing with the 2011 choice in Fig. 6.17, we see that the PF muon selection is more efficient on prompt isolated muons. On the other hand, the fake rate has been measured to be compatible with that one expected with the 2011 identification selection.

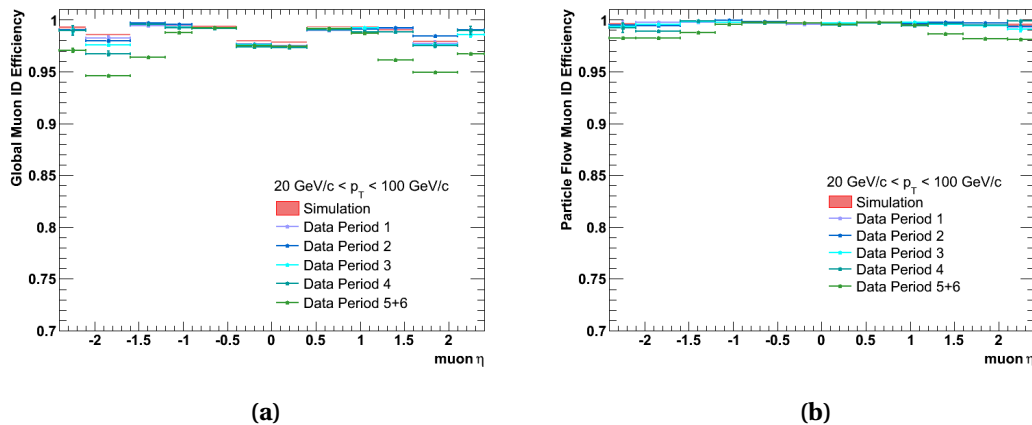


Figure 6.17: Muon reconstruction and identification efficiency for Global muons (left) and Particle Flow muons (right), measured with the tag-ang-probe method (Ch. 7) on different 2011 data periods as function of muon η .

The efficiency of identification criteria was also tested against pile-up. In Fig. 6.18 we can appreciate the stability of the efficiency as a function of vertex multiplicity in the scenario of 2012 data taking.

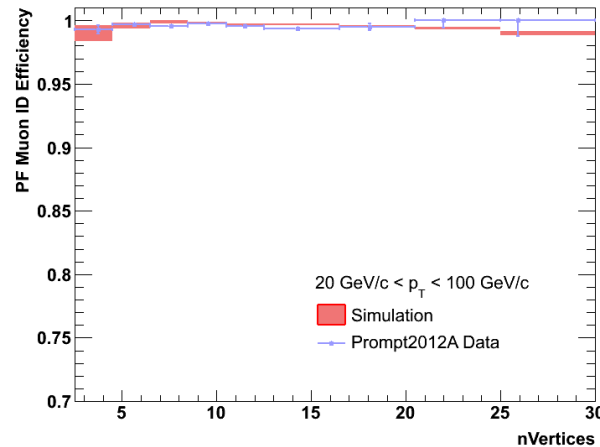


Figure 6.18: Muon reconstruction and identification efficiency for Particle Flow muons, measured with the tag-ang-probe method (Ch. 7) on 2012 data as function of the number of reconstructed primary vertices.

6.3 Lepton Isolation

Leptons from $H \rightarrow ZZ^{(*)} \rightarrow 4\ell$ events have a very clean signature in the CMS detector — four isolated leptons coming from the same event vertex. Hence, the isolation property of leptons is one of the most discriminating Higgs event characteristics in regard to backgrounds having two real and two fake leptons, i.e. Drell-Yan+jets, $Zb\bar{b}$ and $t\bar{t}$ processes.

The exact implementation of the isolation observable depends on the event reconstruction paradigm, but the principal idea of isolation is to compute the energy flow around lepton direction. In 2011 analysis, the detector based isolation was used, defined as scalar sum of transverse momentum of tracks and transverse energy from calorimeters in a cone around lepton direction of $\Delta R = 0.3$ as:

$$R_{\text{iso}}^{\text{det}} = \frac{\sum^{\text{track}} p_T + \sum^{\text{ECAL}} E_T + \sum^{\text{HCAL}} E_T}{p_T^{\text{lepton}}} \quad (6.1)$$

A different approach to isolation based on particle flow event reconstruction has been studied for the purposes of 2012 analysis. Unlike the first method, there is no problem of double counting of the energy of hadrons in ECAL and Hadronic Calorimeter (HCAL). The particle flow isolation is obtained by performing the scalar sum of the transverse momentum of the particle flow candidates reconstructed in a ΔR cone of 0.4, defined as:

$$R_{\text{iso}}^{\text{PF}} = \frac{\sum^{\text{chargedhadron}} p_T + \sum^{\text{neutralhadron}} p_T + \sum^{\text{photon}} p_T}{p_T^{\text{lepton}}} \quad (6.2)$$

In both definitions of isolation, (6.1) and (6.2), a normalization to lepton transverse momentum is used.

Because of the multiple interactions per bunch-crossing in ideal LHC conditions, the isolation can get worsened from the extra energy from pileup entering the isolation cone. The charged particle flow candidates are filtered through the algorithm *pfNoPileup* that does primary vertex association, while the neutral part is corrected according the method described in Sec. 6.3.1.

In case of electrons, the optimal efficiency in the barrel of the association of the brem clusters particle flow photons to the reconstructed particle flow electrons make possible to exploit the full cone area, while in the endcap some inefficiency in the particle flow electron id (to be corrected) makes necessary the usage of some internal vetoes to remove the electron footprint. Then, the particle-based isolation of a GSF electron requires the following vetoes on the candidates in the cone:

- barrel and endcap:
 1. veto all the reconstructed particle flow electrons (in the most of the cases, this requirement removes the pf-electron correspondent to the GSF electron, with all

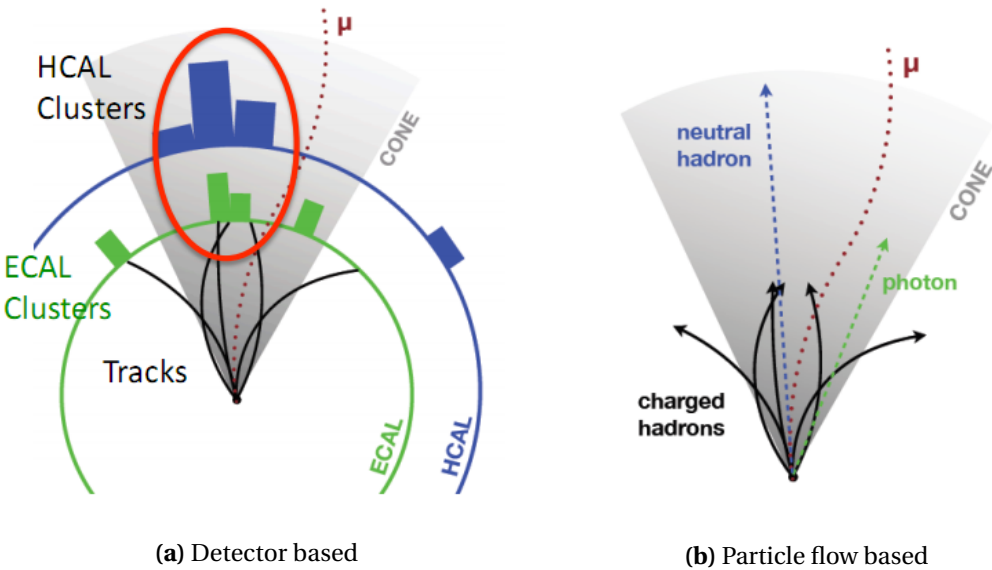


Figure 6.19: An illustration of isolation schemes: The detector based approach used in 2011 and particle flow based used in 2012 analysis. Main advantage of the particle flow approach is the avoiding of energy double counting.

its brem clusters)

2. veto all the charged hadrons that share the same GSF track or the closest CTF track with the electron
- endcap:
 1. veto all the charged hadrons in a cone $\Delta R=0.015$ around the electron
 2. veto all the photons in a cone $\Delta R=0.08$ around the electron

with these vetoes the footprint of the electron in both barrel and endcap is reduced to less than 1% (see [78]). To isolate leptons, the PRL analysis was exploiting the information that come from the energy deposits in the calorimeters (*ECAL and HCAL detector-based isolation*) by performing the scalar sum of the transverse energy of rechits inside a cone $\Delta R = \sqrt{\Delta\eta^2 + \Delta\phi^2}$ (0.3) and the scalar sum of the transverse momentum of the tracks in the same cone (*tracker isolation*). The Figures 6.20 to 6.22 are showing background efficiency as a function of signal efficiency (ie, ROC curves) for various cuts on the isolation algorithms and in several η and p_T bins.

In the high p_T region all the algorithms give approximatively the same performances, while the gain using particle-based isolation is increasing as the electron p_T lowers, justifying the choice to use it in this analysis.

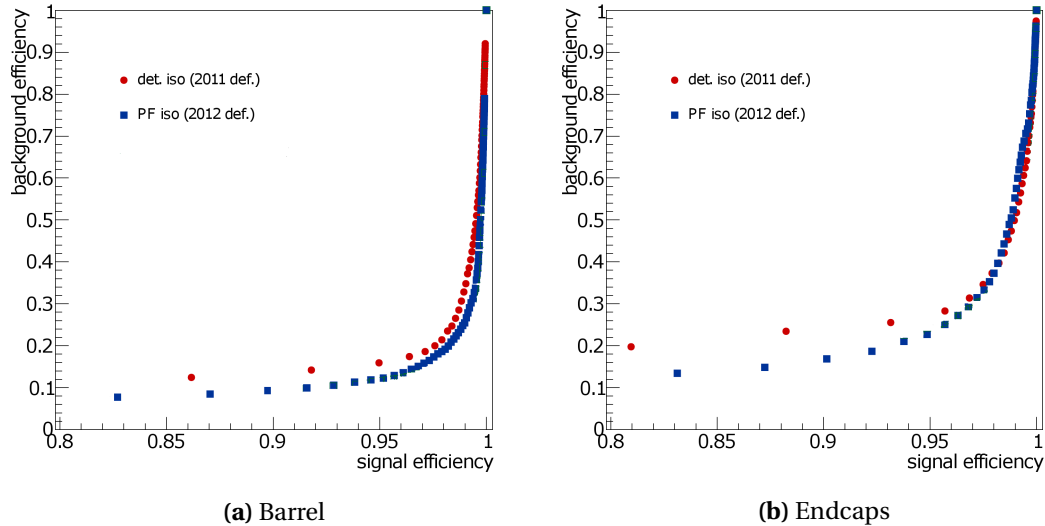


Figure 6.20: Background (electron fakes in $Z + 1$ fake data control sample) versus signal efficiency (electrons MC-truth matched in $H \rightarrow ZZ^{(*)} \rightarrow 4\ell$ signal MC) for electrons with $p_T > 20$ GeV in the barrel (left) and in the endcap (right). Background samples is selected 2011 data sample

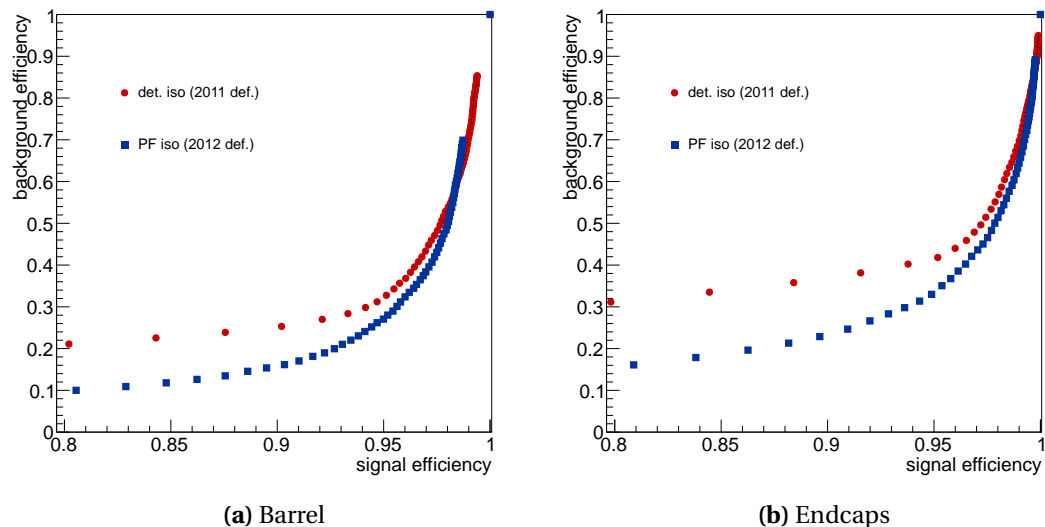


Figure 6.21: Background (electron fakes in $Z+1$ fake data control sample) versus signal efficiency (electrons MC-truth matched in $H \rightarrow ZZ \rightarrow 4l$ signal MC) for electrons with $10 < p_T < 20$ GeV in the barrel (left) and in the endcap (right). Background samples is selected 2011 data sample

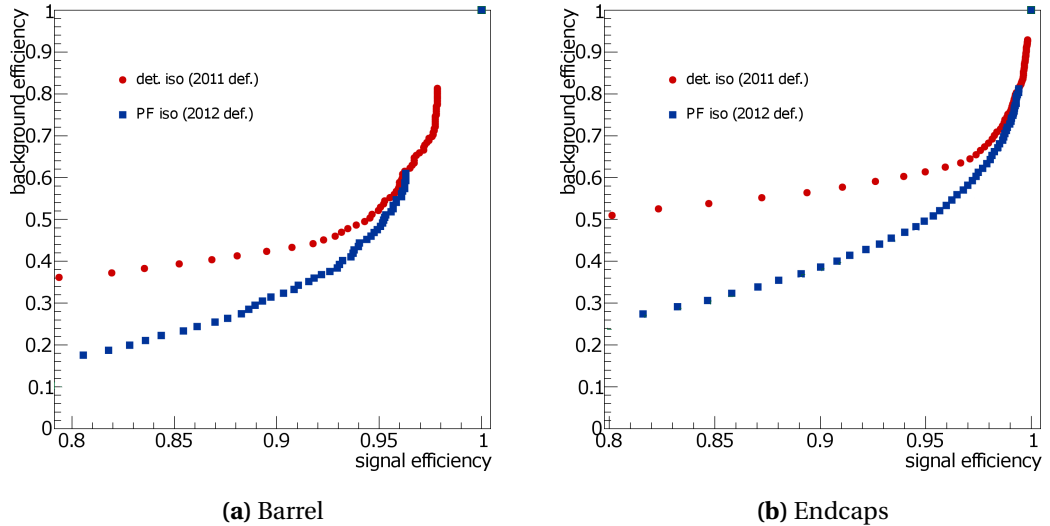


Figure 6.22: Background (electron fakes in $Z+1$ fake data control sample) versus signal efficiency (electrons MC-truth matched in $H \rightarrow ZZ \rightarrow 4l$ signal MC) for electrons with $5 < p_T < 10$ GeV in the barrel (left) and in the endcap (right). Background samples is selected 2011 data sample

6.3.1 Pile-up Subtraction

Isolation variables are among the most pile-up sensitive variables in this analysis. Pile-up causes the mean energy deposited in the detector to increase, leading to the rise of the mean isolation values. Thus, the efficiency of a cut on isolation variables strongly depends on pile-up conditions. In order to have a pile-up robust analysis, the isolation variable has to be corrected.

The degradation of isolation performances due to pile-up can be partly mitigated associating the charged particle flow candidates to the primary vertices. We do this through this association with pfNoPileup association, which consists in filtering the sample of charged particle flow candidates associated with the other primary vertices excluding the one with the highest $\sum p_T^2$ of the associated tracks.

However, the neutral component (neutral hadron and photons), for which this association cannot be trivially done, need a special treatment. Among several correction methods, the one using Fast Jet [90, 91] energy density (ρ) in the event has been chosen to estimate the mean pile-up contribution within the isolation cone of a lepton. A ρ variable is defined for each jet in a given event and the median of the ρ distribution for each event is taken. The correction to the neutral component of the isolation variable is then applied according to the formula :

$$\sum_{neutral}^{corr} p_T = \max(\sum_{neutral}^{uncorr} p_T - \rho \cdot A_{eff}, 0 \text{ GeV}) \quad (6.3)$$

where the *effective area* (A_{eff}) of a given component is defined as the ratio between the slope of the average isolation *iso* and ρ as a function of number of vertices. Main

We are currently using the ICHEP recommendation from the e/g and muon POGs regarding ρ computation and A_{eff} . However, while work is in progress to align the slightly different approaches followed for electrons and muons, we take as a reference for ICHEP what has been proposed by POGs and describe them in what follows.

ρ computation

For 2011, the energy density ρ is calculated using jets reconstructed with k_T algorithm (with $D = 0.6$), taking as input all particles built with the particle-flow algorithm. For 2012, the same ρ definition was taken from muons, except that the charged particles were removed when building jets. For electrons, all particles were considered, up to $|\eta| < 3$.

Effective Areas

It was noticed that the A_{eff} are increasing with the η of the lepton, and this is mainly due to increasing pileup and with the fact that the geometrical isolation cone gets truncated at the end of the tracker acceptance.

6.3. Lepton Isolation

As a consequence, A_{eff} for the neutral isolation component was calculated in fine bins in η , especially in the endcap. In Table 6.2 we report the effective areas measured in 1.6 fb^{-1} of the first 2012 data and in the full 2011 dataset (5.05 fb^{-1}), on the $Z \rightarrow ee$ sample.

η range	2012 data (12.21 fb^{-1})	2011 data (5.05 fb^{-1})
$ \eta < 1.0$	0.19 ± 0.006	0.18 ± 0.002
$1.0 < \eta < 1.479$	0.25 ± 0.006	0.20 ± 0.003
$1.479 < \eta < 2.0$	0.12 ± 0.004	0.15 ± 0.002
$2.0 < \eta < 2.2$	0.21 ± 0.007	0.19 ± 0.003
$2.2 < \eta < 2.3$	0.27 ± 0.02	0.21 ± 0.006
$2.3 < \eta < 2.4$	0.44 ± 0.03	0.22 ± 0.007
$ \eta > 2.4$	0.52 ± 0.05	0.29 ± 0.008

Table 6.2: Effective areas calculated on 2012 data (12.21 fb^{-1}) and 2011 data (5.05 fb^{-1}) for electrons in different η bins, for isolation cone of $\Delta R = 0.4$.

For the muons, the Table 6.3 summarizes the numbers derived for both 2011 and 2012 data periods.

η range	2012 data (12.21 fb^{-1})	2011 data (5.05 fb^{-1})
$ \eta < 1.0$	0.674	0.132
$1.0 < \eta < 1.479$	0.565	0.120
$1.479 < \eta < 2.0$	0.442	0.114
$2.0 < \eta < 2.2$	0.515	0.139
$2.2 < \eta < 2.3$	0.821	0.168
$ \eta > 2.3$	0.660	0.189

Table 6.3: Effective areas calculated on 2012 data (12.21 fb^{-1}) and 2011 data (5.05 fb^{-1}) for muons in different η bins, for isolation cone of $\Delta R = 0.4$.

Summary

Since the charged hadron isolation is already not dependent on the number of vertices, the total corrected isolation sum is the following:

$$\sum^{corr} p_T = \sum^{charged} p_T + \left(\sum^{uncorr}_{neutral} p_T - \rho \cdot A_{eff} \right) \quad (6.4)$$

We validate that the corrections are flattening the average isolation Σ_{corr} in the same dataset where we calibrated the effective areas. The figure 6.23 is showing the average energy flow before and after the corrections for electrons and for two selected η bins. While the average energy flow was growing as the number of vertices increases before the pile-up corrections, a

flat distribution is obtained after applying the recipe described in this section.

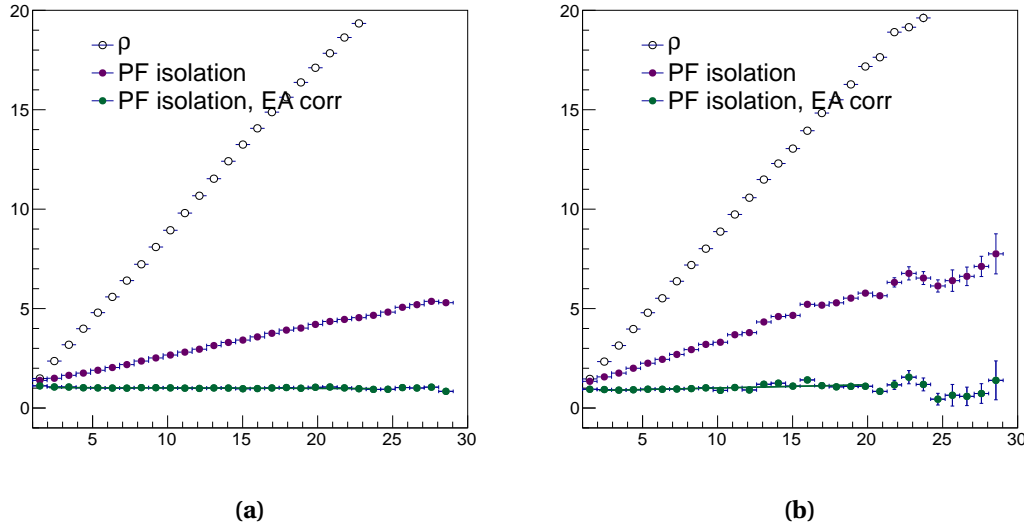


Figure 6.23: Average energy flow in electron isolation cone of $\Delta R=0.4$, before and after the pileup corrections, for identified electrons with a $Z \rightarrow \ell\ell$ selection in 2011 data in two η bins. (a) $|\eta| < 1.0$ (b) $2.2 < |\eta| < 2.3$.

Moreover, the isolation efficiencies for single electrons in the bin $7 < p_T < 100$ GeV as a function of the number of vertices is shown in Figure 6.24, together with MC efficiencies. They were calculated with the tag and probe method. After the pile-up correction treatment, the efficiency shows moderate decrease with increasing number of vertices.

6.3. Lepton Isolation

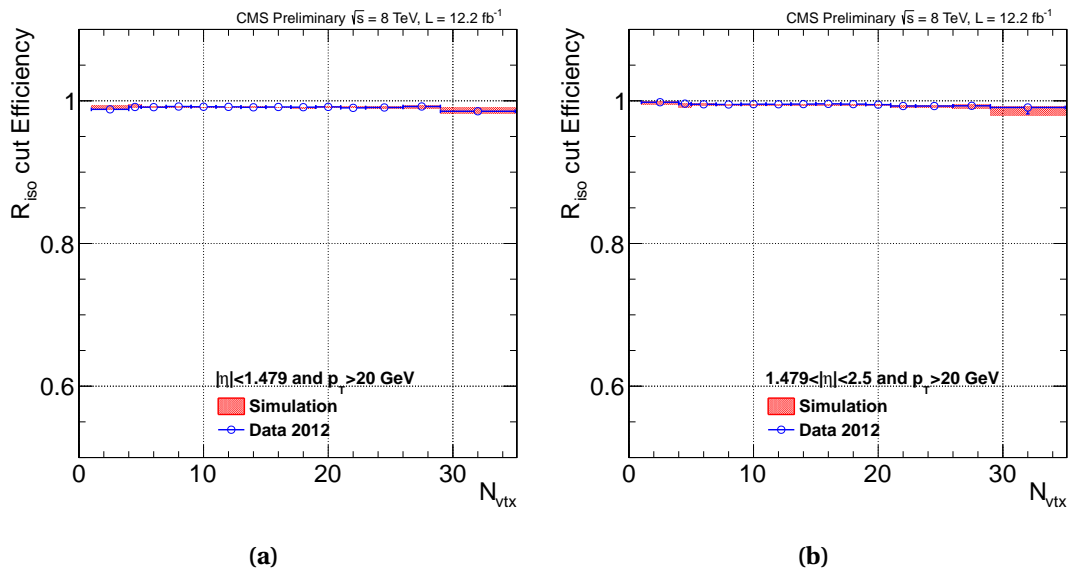


Figure 6.24: Electron isolation efficiencies computed with the tag-and-probe method in the bin $20 < p_T < 100 \text{ GeV}$ as a function of the number of vertices for electrons in ECAL barrel (a) and ECAL endcap (b)

6.3.2 Working Point Optimization

In order to find the best working point for isolation, we followed an optimization of the working point for isolation was done in the phase space defined by applying the most of the analysis requirements. Several options of isolation cuts were studied: simple cut on each lepton leg (1D cut), cut on the sum of isolation of lepton pairs (2D cut). Both, irreducible and reducible background samples were used. The irreducible ZZ background was taken from simulation while reducible background was estimated from collision data. The full procedure of estimation of reducible background from data will be described in Ch. 10. Basically, it can be summarized in two steps:

- select a sample with $Z + \text{two same-sign, same-flavour } loose \text{ leptons}$ with $|\text{SIP}_{3D}| < 4$.
- for each cut value, compute the corresponding fake rate. Apply it on the two legs with *loose leptons* to obtain the number of reducible background events.

The maximal significance of a signal, calculated from a Poisson statistics was used to obtain the optimal cut value. The Fig. 6.25 (left) shows the ratio between the significance and the maximal significance as a function of the cut value on $R_{\text{iso}}^{\text{PF}}$, for both 1D and 2D cut. The 4μ channel from $m_H=120$ GeV signal sample was used. Since two-dimensional cut configuration compared to one-dimensional one gives only 1% improvement, for simplicity reasons, we have chosen a 1D cut option.

In addition to this, it was shown that the optimum cut value had almost no dependence with the mass of the Higgs signal sample tested. Finally, having a different cut for barrel and endcap has been considered. The Fig. 6.25 (right) shows the significance obtained scanning different cuts for muons in the barrel or in the endcap. The maximum significance only differs by 0.5% from the configuration where a single cut ($R_{\text{iso}}^{\text{PF}} < 0.4$) is used irrespective of the muon η .

In case of electrons, similar results were found. In order to use the simplest option, we therefore decided to set $R_{\text{iso}}^{\text{PF}} < 0.4$ for both electrons and muons over the whole η range.

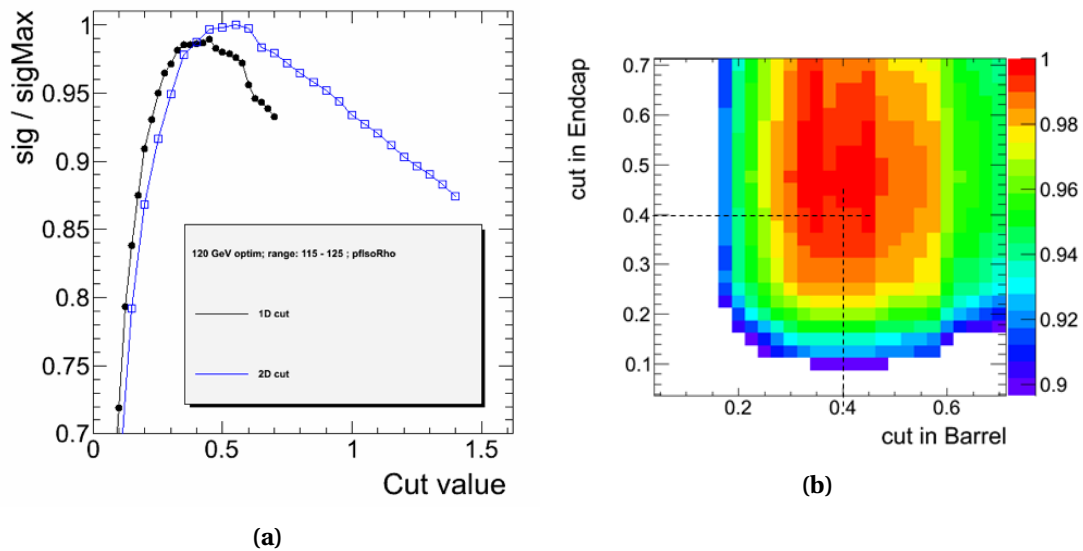


Figure 6.25: Ratio between the significance and the maximal significance as a function of the cut value on $R_{\text{iso}}^{\text{PF}}$, for both 1D and 2D cut (left) and significance obtained scanning different cuts for muons in the barrel or in the endcap (right).

6.4 Leptons common Vertex

The notion of leptons originating from a "common primary vertex" is taken throughout the analysis a meaning that each individual lepton has an associated track with a small impact parameter with respect to the event primary vertex. In practice for the event selection (see Ch. 8), the significance of the impact parameter to the event vertex, $|SIP_{3D}| = \frac{|IP|}{\sigma_{IP}}$ is used where IP is the lepton impact parameter in three dimensions at the point of closest approach with respect to the primary interaction vertex, and σ_{IP} the associated uncertainty. Hereafter, a "primary lepton" is a lepton satisfying $|SIP_{3D}| < 4$.

6.5 Photons

In order to improve on the precision for the invariant mass reconstruction of the Z bosons in the Higgs decay chain, and thus on the mass of the scalar boson itself, the photons from final state radiation (FSR) must be identified and taken into account. The procedure is described in the following sub-sections⁴.

6.5.1 Photon Observables and FSR Recovery

About 8% (15%) of the decays into muons (electrons) are affected by FSR with photon transverse momentum, p_T^γ , exceeding 2 GeV. As the photon emission is most often collinear with one of the leptons, electron measured energies automatically include the energy of a large fraction of the emitted photons in the associated electromagnetic super-cluster. Since muons are reconstructed from tracks only, their measured momenta does not include the emitted photons. Final state radiation is therefore expected to degrade the Z mass resolution when measured with the sole muon pairs, and in turn degrade the Higgs boson mass resolution when measured with the four leptons momenta, especially in the 4μ and in the $2e2\mu$ final states and, to a lesser extent, in the $4e$ final state. It is also expected to reduce the efficiency of the lepton isolation cut when the emitted photon is in the lepton isolation cone

Maximal selection efficiency and an excellent Higgs boson mass resolution are key ingredients in view of the small production cross-section in the 4ℓ channels, in particular to discriminate the Higgs boson signal with the background continuum. The purpose of this algorithm is to recover the FSR photons with large efficiency and purity, to remove the energy of the recovered photons from the lepton isolation cones, and to measure the mass of the Higgs boson candidate from the momenta of the leptons and the recovered photons.

Final state radiation tends to favour low energy photon emission collinear to the lepton. An efficient recovery thus requires photon identification and reconstruction in the vicinity of other particles, down to photon transverse momenta of the order of the Higgs mass core

⁴The text of this section on final state radiation recovery is taken from Ref. [82] of which the writer of this thesis is a co-editor.

resolution, i.e. down to a few GeV. Photons with lower energies are not expected to degrade the mass resolution significantly. On the other hand, these low energy photons are difficult to reconstruct and separate from the background.

6.5.2 Photon Reconstruction, Identification and Isolation

The particle-flow concept developed in CMS [92] includes identification of low energy photons that overlap with other particles.

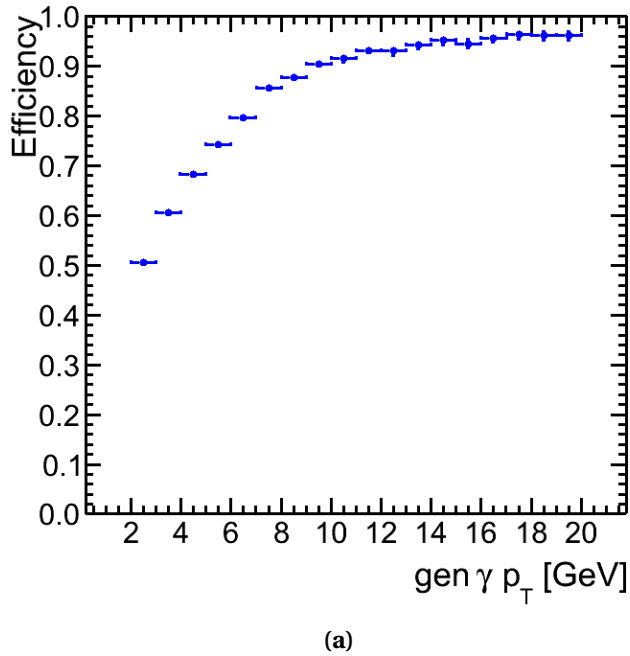
A specific clustering algorithm identifies and reconstructs photons (type 1). This algorithm is efficient down to an energy of 230 MeV in the ECAL barrel and 600 MeV in the ECAL end-caps. The determination of the photon energies and directions is monitored in the data with $\pi^0 \rightarrow \gamma\gamma$ decays, and is shown to be accurate, reliable, and in agreement with the predictions from simulation [93, 94].

Showering muons are also identified by the particle-flow reconstruction. The algorithm is tuned for energetic muons. In the rare cases in which such a showering muon is identified, the energies of the particle-flow clusters linked to the muon do not give rise to separate particles. The showering muon probability is vanishingly small for the kinematic region typical to the low-mass Higgs boson search. This entails the loss of a not entirely negligible fraction of collinear FSR photons. Particle-flow ECAL clusters linked to identified showering muons are therefore identified as photons (type 2) in this analysis. Specifically, the energy of these photons is set to ECAL energy deposit from muons and its direction is chosen to be that of the muon. In the four-muon final state, about 20% of the FSR photons are of type 2.

There are rare cases in which the particle-flow reconstruction identifies a photon although it is already included in the electron super-cluster, due to imperfect cross cleaning. It is therefore required that photons be further away from the direction of any electron by 0.05 in pseudo-rapidity, and by 2.0 rad in azimuth.

Figure 6.26 shows the total efficiency of the photon reconstruction for $p_T^\gamma > 2$ GeV and $|\eta_\gamma| < 2.4$, determined by matching reconstructed photons to generated photons from FSR with a matching cut $\Delta R < 0.10$ as a function of p_T^γ in the four-muon final state.

The absolute photon isolation is computed as a sum of transverse momenta of the charged hadrons, photons and neutral hadrons. The isolation cone size is set to $\Delta R = 0.30$ around the photon direction. In this cone, all charged hadrons originating from the signal primary vertex and with a p_T larger than 200 MeV, all photons and neutral hadrons with a p_T larger than 500 MeV are included in the computation. In order to achieve separation from photons that are produced in pileup interactions, an additional isolation term is defined ($\sum^{PU} p_T$) that corresponds to the charged particle sum from the vertices other than the primary vertex. The final, pileup-corrected relative isolation is obtained by dividing the absolute isolation by the



(a)

Figure 6.26: Reconstruction efficiency for photons produced by final state radiation in $H \rightarrow ZZ \rightarrow 4\mu$ events.

photon transverse momentum, p_T^γ . and is given by:

$$R_{iso, \gamma}^{PF} = \frac{\sum^{\text{chargedhadron}} p_T + \sum^{\text{neutralhadron}} p_T + \sum^{\text{photon}} p_T + \sum^{\text{PU}} p_T}{p_T^\gamma} \quad (6.5)$$

6.5.3 Building Z bosons with FSR Photon Recovery

Leptons passing all selection criteria, including isolation, are used to form a Z candidate. When a FSR photon candidate is selected in the event, the isolation sum may have to be modified. This section describes how the building of Z candidates is made in presence of an FSR photon. Only photons with $p_T^\gamma > 2$ GeV and within the tracker acceptance ($|\eta| < 2.4$) are considered, and assigned to a lepton in the following way:

- Photons are considered only if the minimum ΔR distance wrt any of the Z leptons is smaller than $\Delta R < 0.5$.
- If the distance of the photon to the closest lepton is between 0.07 and .50, the probability that this photon arise from pile-up or, to a lesser extent, from the underlying event, becomes appreciable, because of the large annulus area. To enrich the photon sample in genuine FSR photons, the p_T^γ cut is tightened to 4 GeV and the photon is required to

be somewhat isolated from other particles: the relative PF isolation including pileup contribution is required to be smaller than 1.0.

- For both Z candidates, only the photons that make a mass with a lepton pair closer to the nominal Z mass (taken here to be 91.2 GeV) but with a maximum $m_{\ell\ell\gamma} < 100$ GeV are kept.
- After the photons have been selected with the above criteria the best photon is selected as following:
 - If there is at least one photon with $p_T > 4$ GeV the one with the highest transverse momentum is associated to the Z boson
 - If there is no photon with $p_T > 4$ GeV the closest photon to any of the leptons is associated to the Z

There can be zero to two selected FSR photon candidates per event. The selected photons are removed from the corresponding lepton isolation cones (if in the isolation cones), and the standard event selection defined in Ch 8 proceeds with the modified lepton isolations, and with the Z candidate masses determined with the corresponding lepton pair and the associated photon. As a result of the procedure, the Higgs boson candidate mass is determined from the momenta of the four leptons and those of all FSR photon candidates.

6.5.4 Performance of FSR Photon Recovery

To quantify the performance of the FSR identification algorithm, samples from simulation and data were used. The gain of the FSR algorithm is two fold

- improved mass resolution — events with associated photons move to the nominal reconstructed mass,
- increased selection efficiency — new events migrate into the signal phase space by the higher isolation efficiency and the improved definition of the mass of the Z.

To quantify the performance of FSR reconstruction we used the following figures of merit:

- *Efficiency*: Number of Identified FSR photons matched to generated FSR photons with $p_T > 2$ GeV and $|\eta| < 2.4$ divided by the number of generated FSR photons with $p_T > 2$ GeV and $|\eta| < 2.4$
- *Rate*: Number of Events with Identified FSR photons divided by the total number of events after all selection requirements
- *Purity*: Number of Events with Identified FSR photons where the mass of the system consisting of the leptons and the photons is nearer to the nominal mass of the studied resonance wrt the mass of the leptons alone.

Chapter 6: Leptons and Photons

- *Yield Gain*: Number of events after all selection requirements after applying the FSR recovery algorithm divided by the number of events after all selection requirements without applying the FSR recover algorithm.

To quantify the performance of the algorithm in the signal and irreducible background we used simulated $H \rightarrow ZZ$ and SM ZZ samples with an average pileup of 20 interactions. The performance studies have also been performed in data exploiting decays of $Z \rightarrow \ell\ell, Z \rightarrow 4\ell$. Studies of the shapes and rates of the reducible backgrounds have also been performed in signal free control regions.

Studies on $H \rightarrow ZZ$ and ZZ Samples

In this study we used simulated Higgs signal sample with a mass of 126 GeV with on average 20 pileup interactions. To obtain the total efficiency comparison we run the full selection with and without the FSR algorithm applied. Figure 6.27 shows the comparison of the invariant mass distribution before and after FSR recovery for events with an identified FSR photon and overall events. The FSR algorithm improves performance by moving the events from the FSR tail back to the Higgs peak bulk distribution.

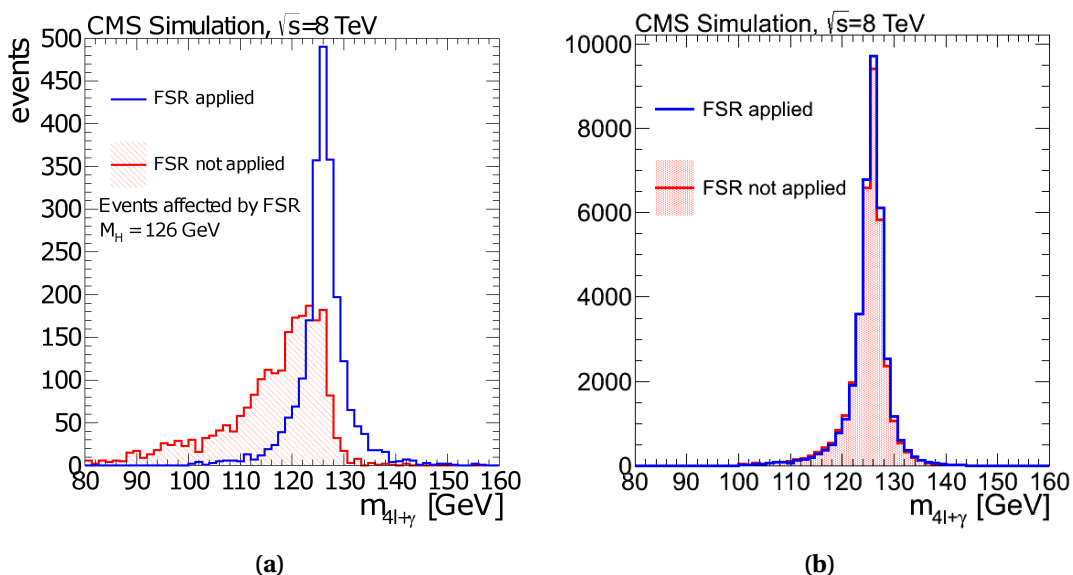


Figure 6.27: Invariant mass reconstruction of the Higgs candidate of the events with an identified FSR photon (left) and all events (right) for Higgs signal with $m_H = 126$ GeV.

Due to the isolation requirements and the redefinition of the masses of the Z bosons, more events enter the signal phase space after FSR recovery. In the case of Higgs signal, the tails are reduced and the arithmetic RMS is improved from 7.1% to 6.9% while the Gaussian RMS is not modified showing that the effect on the bulk distribution due to the impurity is negligible. In

the case of the ZZ continuum the performance is expected to be similar.

The rate, efficiency and purity for Higgs signal and SM ZZ is presented in Table 6.4. As already mentioned, the effect of FSR on electrons is small due to the electron reconstruction which absorbs nearby FSR photons in the electromagnetic supercluster. As a consequence, the four muon final state is affected the most. An increase in the total efficiency of $\tilde{2}\%$ is expected.

final state	rate (%)	purity (%)	gain (%)
$H \rightarrow ZZ(\text{all})$	6.0	80	2.0
$H \rightarrow ZZ \rightarrow 4\mu$	9.1	82	3.0
$H \rightarrow ZZ \rightarrow 2e2\mu$	5.0	78	0.6
$H \rightarrow ZZ \rightarrow 4e$	1.4	72	1.8
SM $ZZ(\text{all})$	6.7	81	2.1
SM $ZZ \rightarrow 4\mu$	10.1	83	3.0
SM $ZZ \rightarrow 2e2\mu$	6.5	77	0.6
SM $ZZ \rightarrow 4e$	1.8	72	1.8

Table 6.4: Rate, purity and efficiency gain for signal and ZZ background

Studies on Data

Z decays in two or four leptons provide a sample suitable for the study of performance of FSR algorithm on data. The performance of the FSR recovery algorithm in Z decays is presented in Fig. 6.28. Excellent performance is observed in Z data as the Z peak becomes steeper. The observed rate on $Z \rightarrow \ell\ell$ events is 1.9% while the efficiency gain is 0.9%. Significant improvement is observed in the reconstruction of the Z peak from $Z \rightarrow 4\ell$ decays.

In order to study The effect of FSR in the reducible background shape, a background enriched region was selected by requiring the Z_2 leptons to have same sign, and to fail identification and isolation criteria. Figure 6.29 shows the FSR effect on this control region. The effect on the background shape is explained by the result of the FSR algorithm in jets. If a lepton is inside a jet, a possible π^0 can be attributed to FSR therefore the rate is much higher than in the case of isolated leptons and corresponds to a total of 60%. The fake photons associated as FSR helps flatten the background shape resulting in reduced background in the region of interest.

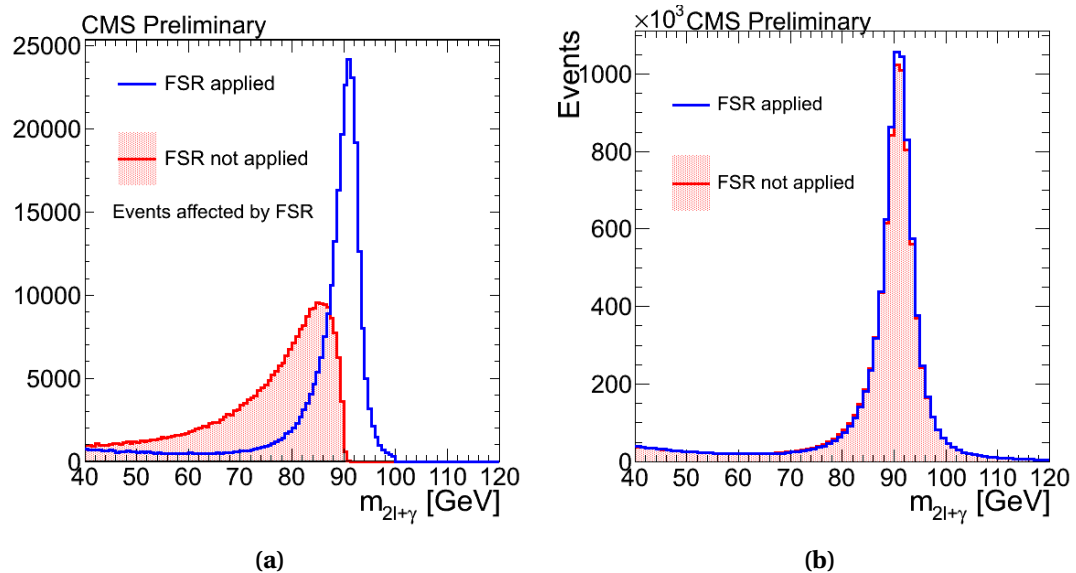


Figure 6.28: Invariant mass of the Z before and after FSR recovery for events with an identified FSR photon(left) and overall number of events for $Z \rightarrow \ell\ell$ decays

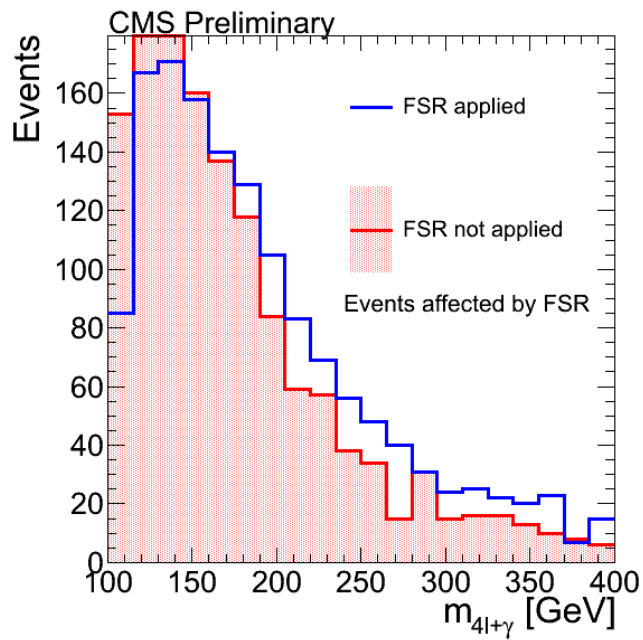


Figure 6.29: Invariant mass of the four lepton system for the background enriched region for events affected by FSR.

7 Lepton Selection Validation from Data

The analysis is all about selection of events and, of course, statistical interpretation in the end. Making the event selection we can efficiently reduce the background contamination while keeping the signal rates almost untouched, but still not completely untouched. Therefore, signal efficiencies are an important ingredient for obtaining the final results of the analysis. These efficiencies can be extracted from simulation of the signal events, but then they can be strongly biased by unpredicted and not well modelled effects arising from insufficient event description and the lack of understanding of the detector. Mitigating the biases from MC is achieved by measuring selection efficiencies directly from data using widely known tag-and-probe technique [83, 95].

In this chapter we will elaborate on the signal efficiencies extraction for various cuts on electrons and muons separately by using tag-and-probe technique. These are then exploited to get the data-to-MC scale factors and corresponding systematic errors, both entering the final yield computation that will be exhaustively presented in the chapters to come.

7.1 Tag-and-probe Method

The efficiencies for reconstruction, identification, isolation, impact parameter cut and trigger for electrons and muons can be measured with data. We rely on a selection of events of inclusive single Z production as a natural source of electrons and muons. J/Ψ is used as a source of low transverse momentum in case of muons. The tag-and-probe technique [83, 95] combines the requirements of the invariant mass constraint (typically 60–120 GeV) on a pair of basic objects (e.g. tracks for muons, or clusters of calorimetry cells for electrons) with a tight lepton selection applied on one leg (the "tag"), ensuring sufficient purity. The other leg (the "probe") is used to measure the efficiency of a given lepton selection criteria. The efficiency is defined as the ratio of the number of passing probes N_P to the total number of probes before the cut:

$$\epsilon_{TP} = \frac{N_P}{N_P + N_F} \quad (7.1)$$

where N_F is the number of probes that fail the selection.

To avoid introducing biases, it is important to perform such a measurement with the exact electron and muon objects as used in this analysis. By using appropriate definitions for probes, the overall efficiency per lepton can be factorized allowing for an independent measurement of each term:

$$\epsilon = \epsilon_{\text{track, clustering}} \times \epsilon_{\text{RECO|track, clustering}} \times \epsilon_{\text{ID|RECO}} \times \epsilon_{\text{ISO|ID}} \times \epsilon_{\text{SIP|ISO}} \quad (7.2)$$

Each term in this illustrative equation represents the efficiency for the probe to pass a given selection or reconstruction step, given that it passes the criteria for all previous steps, more precisely:

- $\epsilon_{\text{track, clustering}}$ is the efficiency of track finding (clustering) for muons (electrons),
- $\epsilon_{\text{RECO|track, clustering}}$ is the efficiency of reconstruction after the track (supercluster) is found for muon (electron),
- $\epsilon_{\text{ID|RECO}}$ is the efficiency of identification of leptons give the reconstructed lepton,
- $\epsilon_{\text{ISO|ID}}$ is the efficiency of lepton isolation cut given an identified lepton,
- $\epsilon_{\text{ISO|SIP}}$ is the efficiency of lepton 3D impact parameter given an isolated lepton.

In practice, the tag-and-probe method is applied in two different ways depending on the purity of the Z selection before applying the cut under study. If the purity is very high, simple cut-and-count gives very good estimate of the efficiency [96]. Cut-and-count cannot be used in presence of significant background contamination, since it seriously biases the measurement. In this case we fit the Z invariant mass resonance and the background underneath in passing and failing probes sample. By the virtue of this procedure, signal and background components are separated and we can take the signal count as integral under the fit function used to model the Z invariant mass spectrum.

By applying the method to both data and simulation we derive data to simulation scale factors. These scale factors are later used to either correct the signal efficiency in the simulation using in this case their uncertainty as systematic error or to provide systematic uncertainties as will be discussed in Sec. 9.3.2. In the computation of the final systematics on the signal efficiency the systematics on the tag-and-probe method are also considered; they are evaluated varying the signal and background modelling.

The tables with all numbers for the efficiencies measured with the tag-and-probe technique on data, MC and the data/MC ratio are collected in Appendix B.

7.2 Electron measurements

For electrons, we define three group of tag requirements — one for reconstruction and identification efficiency measurements, one for isolation and impact parameter and one for trigger measurements. The three definitions are as follows:

1. Reconstruction and identification tags:

- $p_T > 20 \text{ GeV}$, $|\eta| < 2.5$ and $E_T^{miss} < 25 \text{ GeV}$
- pass a set of Vector Boson Task Force (VBTF) cuts, Working Point 60% (WP60) which involves cuts on pure identification variables ($|\Delta\eta_{in}|$, $|\Delta\phi_{in}|$, H/E and $\sigma_{in\eta\eta}$), track and calorimeter isolation as well as conversion removal [97].
- matched geometrically to the leg of the double object trigger used for the study that has requirement on the electron ID at trigger level,

2. Isolation and impact parameter tags:

- $p_T > 20 \text{ GeV}$, $|\eta| < 2.5$ and $E_T^{miss} < 25 \text{ GeV}$
- pass a set of VBTF cuts, WP80 (80% efficient) which is relaxed with respect to previously defined WP60,
- particle based isolation

3. Trigger tags:

- $p_T > 20 \text{ GeV}$, passing "Tight Trigger Working Point 2012" (tighter than trigger requirements), and spatially matched ($\Delta R < 0.1$) with an online HLT electron with $E_T > 20 \text{ GeV}$, tight identification and loose isolation,

In the later case, the purity of the tag-and-probe sample is higher, justifying the looser selection choice, since reconstruction and identification criteria already removes a lot of background from fake electrons.

The bulk results show good consistency between data and simulation giving scale factors for further analysis close to one. The uncertainties to scale factors, which are propagated into final per-electron systematic uncertainties in Sec. 9.3.2 are at 1-2% level.

Following the methodology described in Ref. [96], the reconstruction, identification, isolation and impact parameter efficiencies are measured in several p_T and η bins by performing a simultaneous extended likelihood fit of the passing and failing sample invariant mass distribution in each bin. A Breit-Wigner (BW) convoluted with a Crystall-Ball function (CB) is used to model the signal peak. Breit-Wigner shape is fixed to the Z -pole mass (91.2 GeV) and width (2.5 GeV) [98] to describe the natural shape of the Z . Crystall-Ball function is suited for describing the detector resolution effects as well as the low-mass radiative tail. However, by careful study of the shape from MC Drell-Yan sample requiring the matching between the generated and reconstructed electrons, two additional effects were noted:

- exponential tail of Drell-Yan spectrum for low p_T bins
- threshold effect for the bin around 20 GeV

For this reason an $\exp(m_{TP})$ or an $\text{erf}(m_{TP}) \times \exp(m_{TP})$ is added to the signal model, where m_{TP} is invariant mass of the tag and probe system, $\text{erf}(m_{TP})$ is error function and $\exp(m_{TP})$ exponential. Purely exponential function is added to the signal model when fitting the tail of Drell-Yan spectrum in low p_T bins and exponential times error function is used to model the threshold effect for the bin around 20 GeV. A few example MC fits are shown on Fig. 7.1. This method minimizes dependence on simulation and uses a minimum set of parameter values obtained from fits in simulation to constrain the data fit. The ratio between the integral under the exponential tail and the $BW \otimes CB$ core and the CB tail parameters are fixed for the fit to data while other parameters are left floating with initial values taken from the MC fit. This turned out to give the best fit stability and tail control with minimum number of parameters fixed from the fit to simulation.

The functional forms to describe the remaining background is again an error function times an exponential. In some cases where the charge miss-identification permitted, to avoid the interference with signal tail description, parameters for the background were constrained from the signal-free phase space asking for the same sign leptons.

The fit method was cross-checked with the template method where all the parameters are fixed from the simulation and the fit function normalization is left floating when fitting to data. As in the fit method, the simultaneous fit to dielectron invariant mass distribution in tag+passing and tag+failing samples is done. Efficiency is a fit parameter so that fit uncertainties are automatically propagated through the likelihood contours. The two methods are combined for final results which will be discussed in more details in Sec. 7.2.5 where we bring the final scale factors.

Very good agreement between two methods in the high $p_T > 20$ GeV region is observed. In the low $7 < p_T < 20$ GeV region some discrepancies between two methods were observed mainly due to the background contamination of the invariant mass distribution which makes fitting very challenging.

7.2.1 Reconstruction

The clustering efficiency in Eq. (7.2) for electrons is assumed to be 100% efficient which is checked by MC to be the case within few per mille in the p_T range of interest for this analysis. Electron reconstruction efficiency $\epsilon_{\text{RECO}|clustering}$ for the 2011, i.e. 7 TeV data sample, has been measured following the methodology described in Ref. [96] and the results reported in Ref. [99].

Special tag-and-probe triggers present in “SingleElectron” dataset are used in 2012 8 TeV data, and a matching of a tag with the triggered electron is required to avoid bias. Then, if a probe

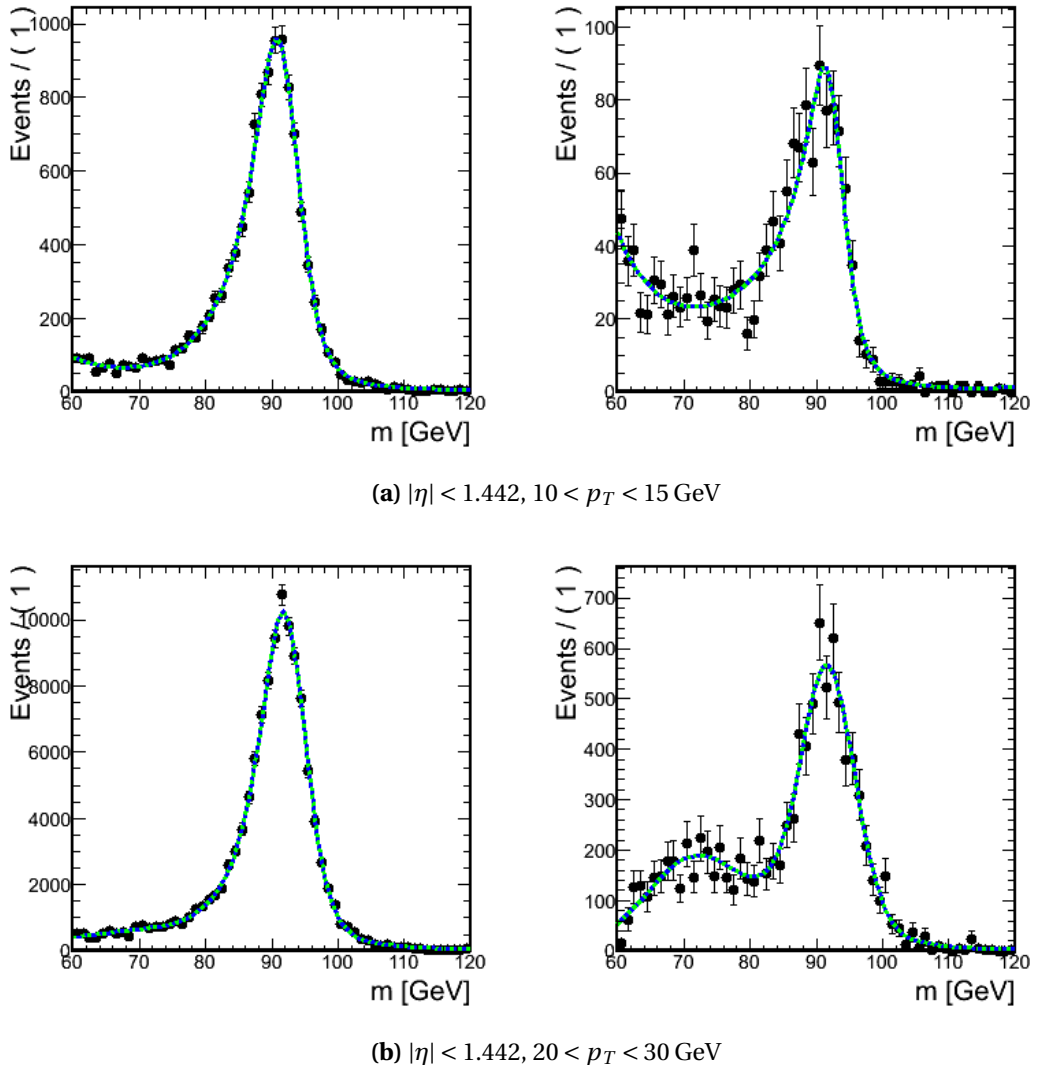


Figure 7.1: Fits for simulated invariant mass of the tag and probe electron pair matched with generated electrons with an error times exponential or pure exponential part added to the signal model. The tag and probe system with probe passing the selection is shown on the left while invariant mass of the system where probe fails given selection is shown on the right. (a) The exponential tail covers the residual Drell-Yan falling spectrum. (b) The error times exponential accounts for the threshold effect.

supercluster is geometrically matched to a GsfElectron in the event, it is considered passing.

The measured reconstruction efficiencies for single electrons as a function of the supercluster probe E_T (with $E_T > 10 \text{ GeV}$) are shown in Fig. 7.2 for 8 TeV data, for electrons in ECAL barrel and in ECAL endcaps.

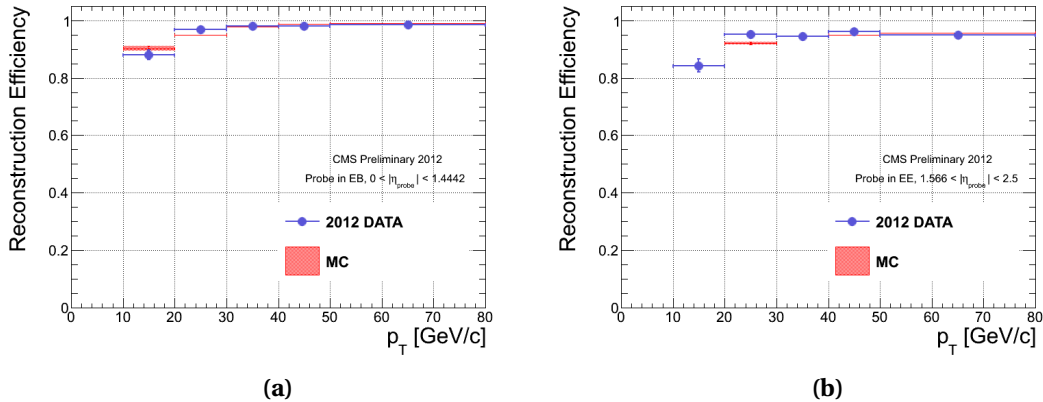


Figure 7.2: Electron reconstruction efficiencies computed with the tag-and-probe method as a function of the supercluster probe E_T in two different η bins: (a) $|\eta| < 1.442$, (b) $1.442 < |\eta| < 2.5$. Results are for 8 TeV data.

7.2.2 Identification

The measured identification efficiencies for single electrons as a function of the electron probe p_T (with $p_T > 7$ GeV) are shown in Fig. 7.3 for 7 TeV data and in Fig. 7.4 for 8 TeV data, together with MC efficiencies. The latter were obtained fitting signal simulation, where the probe electron is matched with a generated electron. In addition, the tail in data is constrained by what is obtained from MC. The efficiencies are computed in bins of η coverage and all data taking periods are considered together. Given the limited statistics available for 8 TeV, only two η bins are currently shown. All numerical values are tabulated in Appendix B.

There is an overall good data/MC agreement in the barrel and the endcaps. Only statistical errors are reported on the plots. The differences observed at low p_T and in the endcaps between data and MC are mostly due to the background estimation (with higher background in the low p_T and high η regions) and the known discrepancies between data and MC of some of the variables used for the electron ID.

As an example, the m_{TP} distributions for passing and failing probes used for the measurement of the electron identification efficiency in the $(10 - 15)$ GeV p_T bin and for $1.566 \leq |\eta| < 2$ in 2011 data is shown in Fig. 7.5.

7.2.3 Isolation and Impact Parameter

For electron isolation and impact parameter, $|SIP3D|$, efficiencies measurement are done simultaneously. The probes are identified electrons satisfying the BDT requirements described above. The tag requirement as already described is relaxed with respect to identification, moving from VBTF WP60 to WP80 and using particle based isolation. The pile up corrected particle based isolation is used instead of the one provided by the VBTF. In this way we avoid

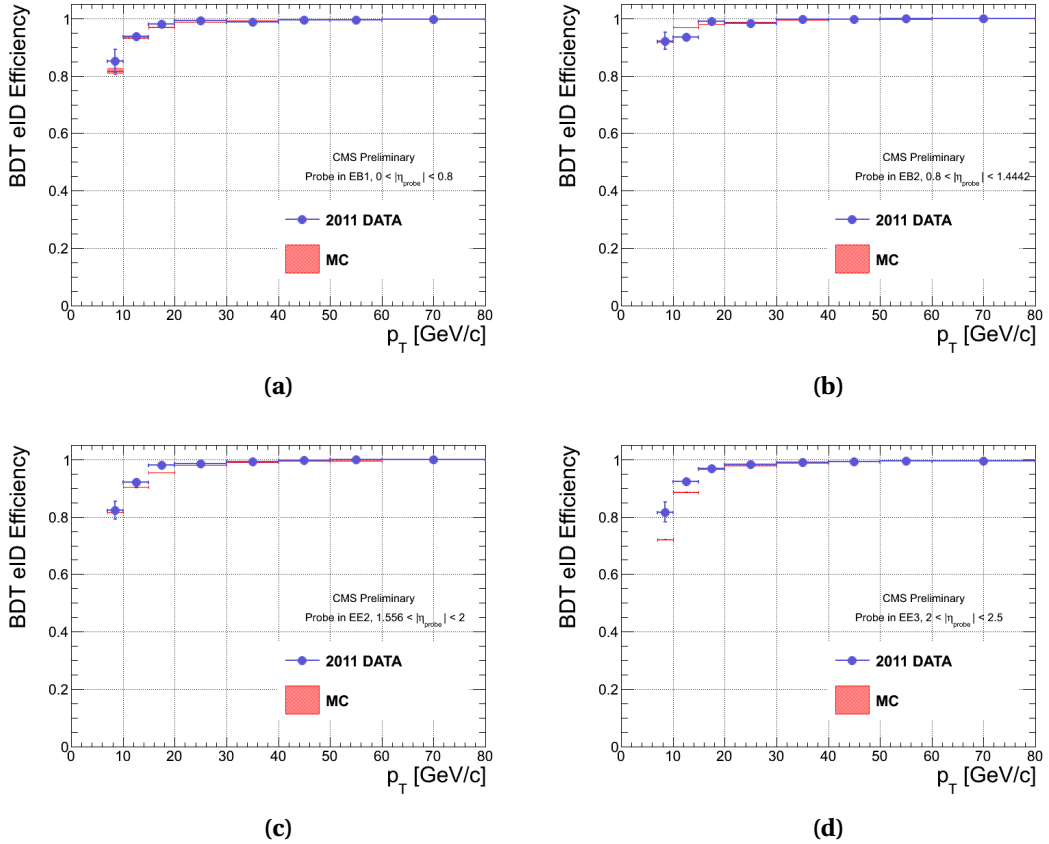


Figure 7.3: Electron identification efficiencies computed with the tag-and-probe method as a function of the probe p_T in four different η bins (a) $|\eta| < 0.8$, (b) $0.8 \leq |\eta| \leq 1.442$, (c) $1.566 \leq |\eta| < 2$ and (d) $2 \leq |\eta| < 2.5$. Results are for 7 TeV data.

biasing sample towards events with lower number of interactions. The passing criteria for probes is simply $R_{iso} < 0.4$ and $|SIP3D| < 4$. The isolation+ $|SIP3D|$ efficiency relative to the identified electrons is measured by requiring the probe electron to fulfill the identification criteria, thus reducing significantly the amount of background events in the sample.

In the low p_T ($p_T < 20$ GeV) and high p_T ($p_T > 50$ GeV) bins for the probe, the Drell-Yan content of the sample is enhanced, creating a tail in the low mass and high mass region respectively. In these cases an $erf(m_{TP}) \times \exp(m_{TP})$ function is added to the signal function describing the tail made of genuine signal electrons. The Drell-Yan over Z ratio is taken from the simulation. Especially in the low p_T bin, this procedure ensures that the Drell-Yan signal and background contributions are disentangled without completely introducing a pdf taken from the simulation. In this case the background model is constrained by the fit in same sign leptons region which is signal-free.

In addition, for the low p_T bins ($p_T < 20$ GeV), the identification criteria has been tightened on

Chapter 7: Lepton Selection Validation from Data

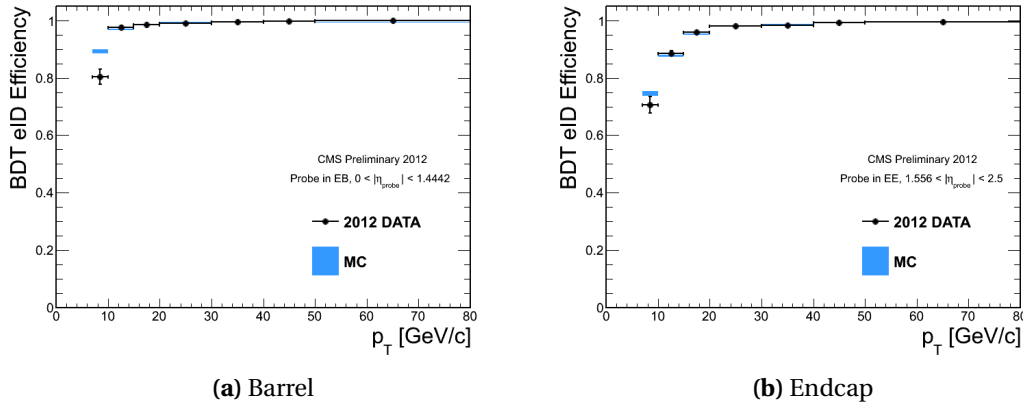


Figure 7.4: Electron identification efficiencies computed with the tag-and-probe method as a function of the probe p_T in two different η bins

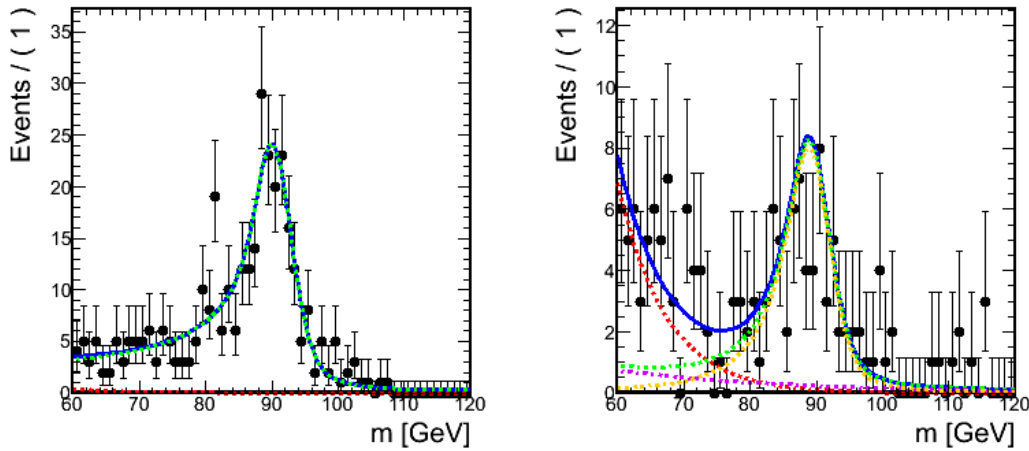


Figure 7.5: The m_{TP} distributions and fits for passing (left) and failing probes (right) used for the electron identification efficiency measurement in the (7 – 10) GeV p_T bin and for $0 \leq |\eta| < 1.479$. Black points are 2012 data, green dashed line is signal model, yellow dashed line is $BW \otimes CB$ part of the signal function, purple dashed line is exponential part of the signal function, red line is background model and blue line is signal+background.

the probe in order to reject more background, under the assumption that the small correlation between the identification and the isolation and impact parameter is either fully negligible or correctly reproduced by the simulation so that the data/MC scale factors remain unchanged. This assumption has been verified from simulation events.

Some examples of m_{TP} distributions for passing and failing probes used for the the measurement of the electron isolation+ $|SIP3D|$ efficiency in the (15 – 20) GeV and (30 – 40) GeV p_T

bin for endcap end barrel in 2012 data is shown in Figure 7.6.

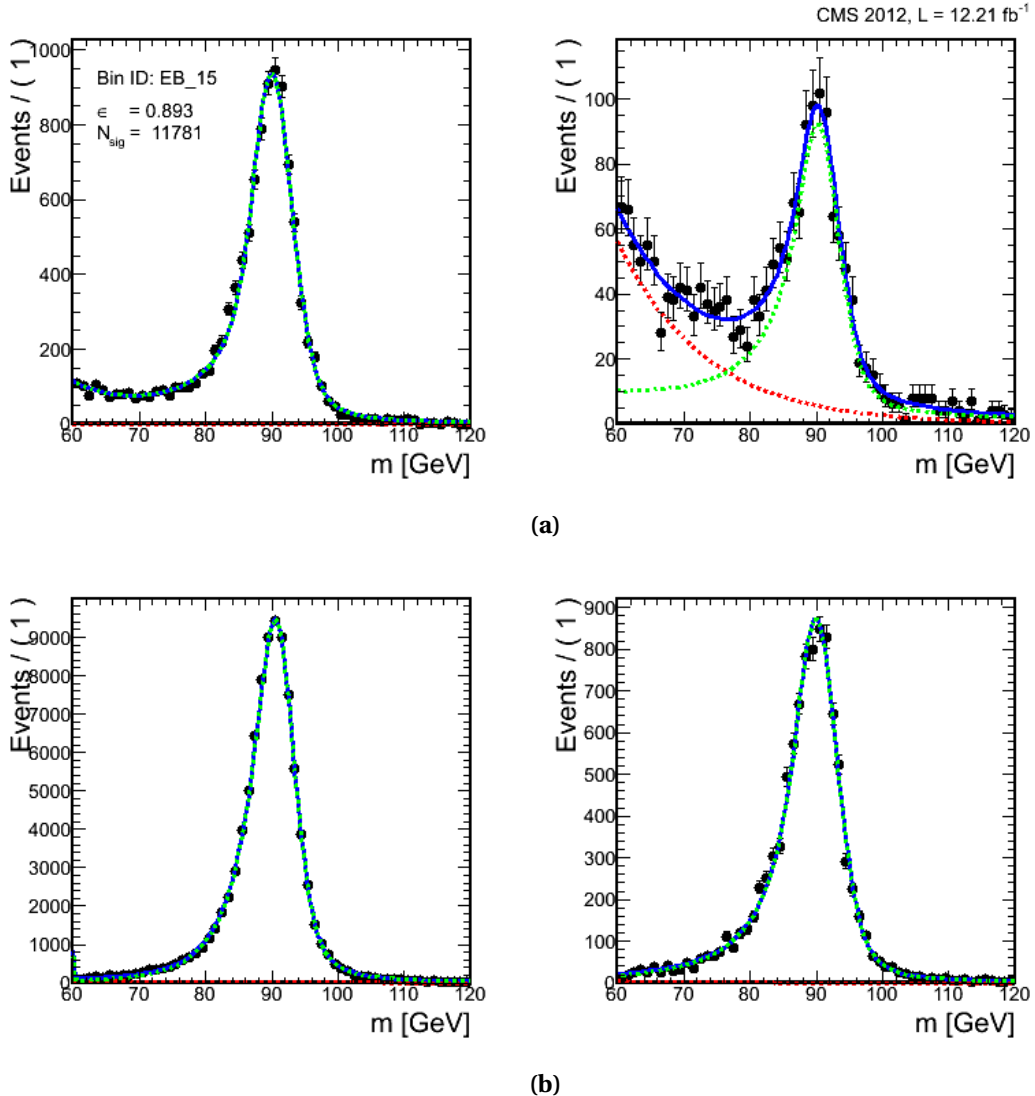


Figure 7.6: The m_{TP} distributions and fits for passing (left) and failing probes (right) used for the electron isolation and $|SIP3D|$ efficiency measurement in (a) the $(15 - 20)$ GeV p_T bin in the barrel and (b) the $(30 - 40)$ GeV p_T bin in the endcap. Black points are 2012 data, green dashed line is signal model, red line is background model and blue line is signal+background.

The measured identification+isolation+ $|SIP3D|$ efficiencies for single electrons as a function of the probe p_T , together with MC efficiencies, are shown in Figure 7.7 for 2011 data and Figure 7.8 for 2012 data. In 2011, the measurement in the ECAL barrel to ECAL endcap transition region ($1.442 < |\eta| < 1.566$) has been performed in a single bin, integrated over the whole p_T range. Both, statistical and systematic errors are reported on the plots. The overall agreement is very good.

Chapter 7: Lepton Selection Validation from Data

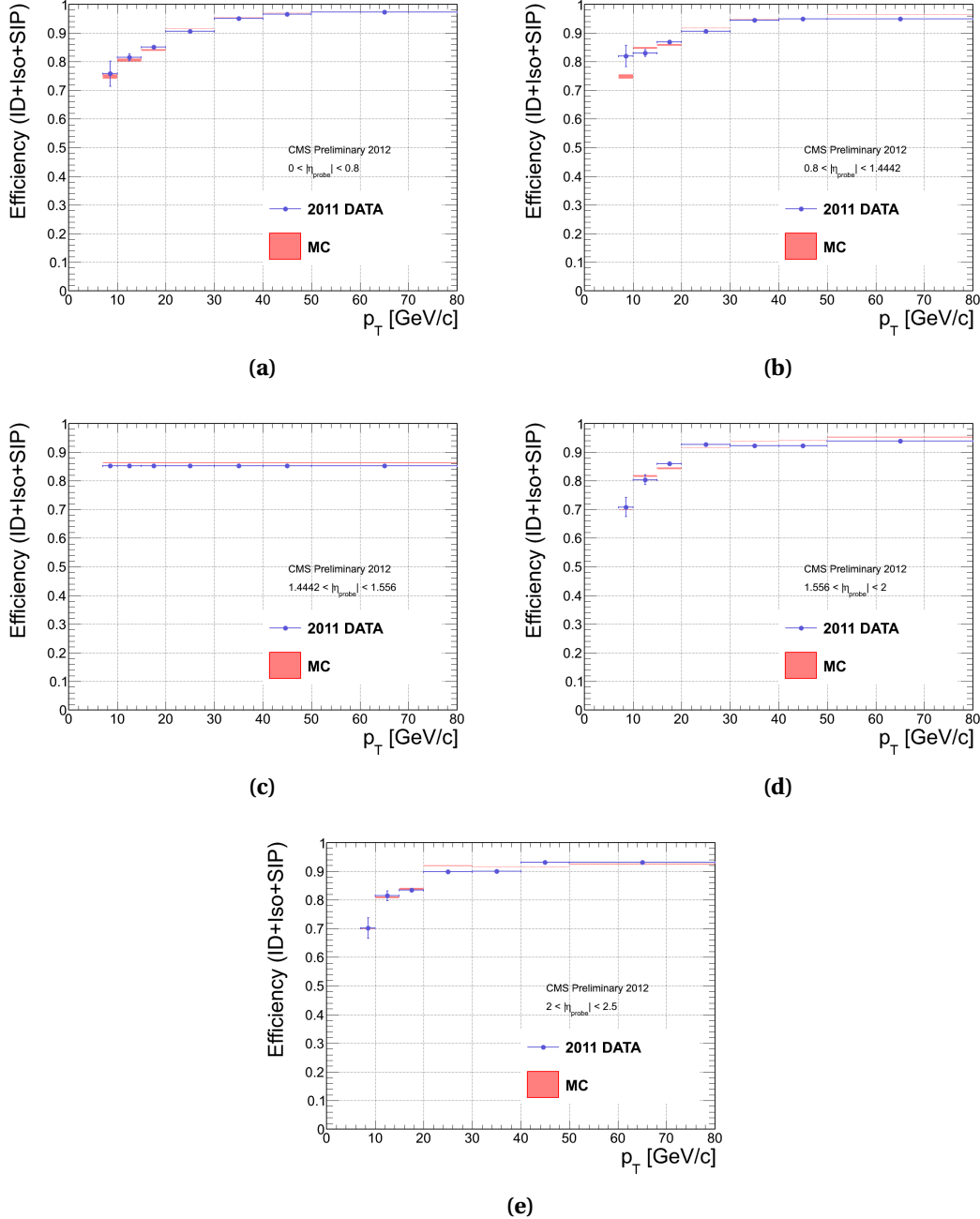


Figure 7.7: Electron identification+isolation+ $|SIP3D|$ efficiencies computed with the tag-and-probe method as a function of the probe p_T in five different η bins: (a) $0 < |\eta| < 0.78$, (b) $0.78 < |\eta| < 1.442$, (c) $1.442 < |\eta| < 1.566$, (d) $1.566 < |\eta| < 2$ and (e) $2 < |\eta| < 2.5$. The measurement in (c) has been performed in a single bin, integrated over the whole p_T range. Results are shown for 7 TeV data.

The tables B.2 and B.1 (in Appendix B) are summarizing the numerical values for the efficiencies measured in both data and MC for the full electron selection requirement (ID+Iso+SIP).

7.2. Electron measurements

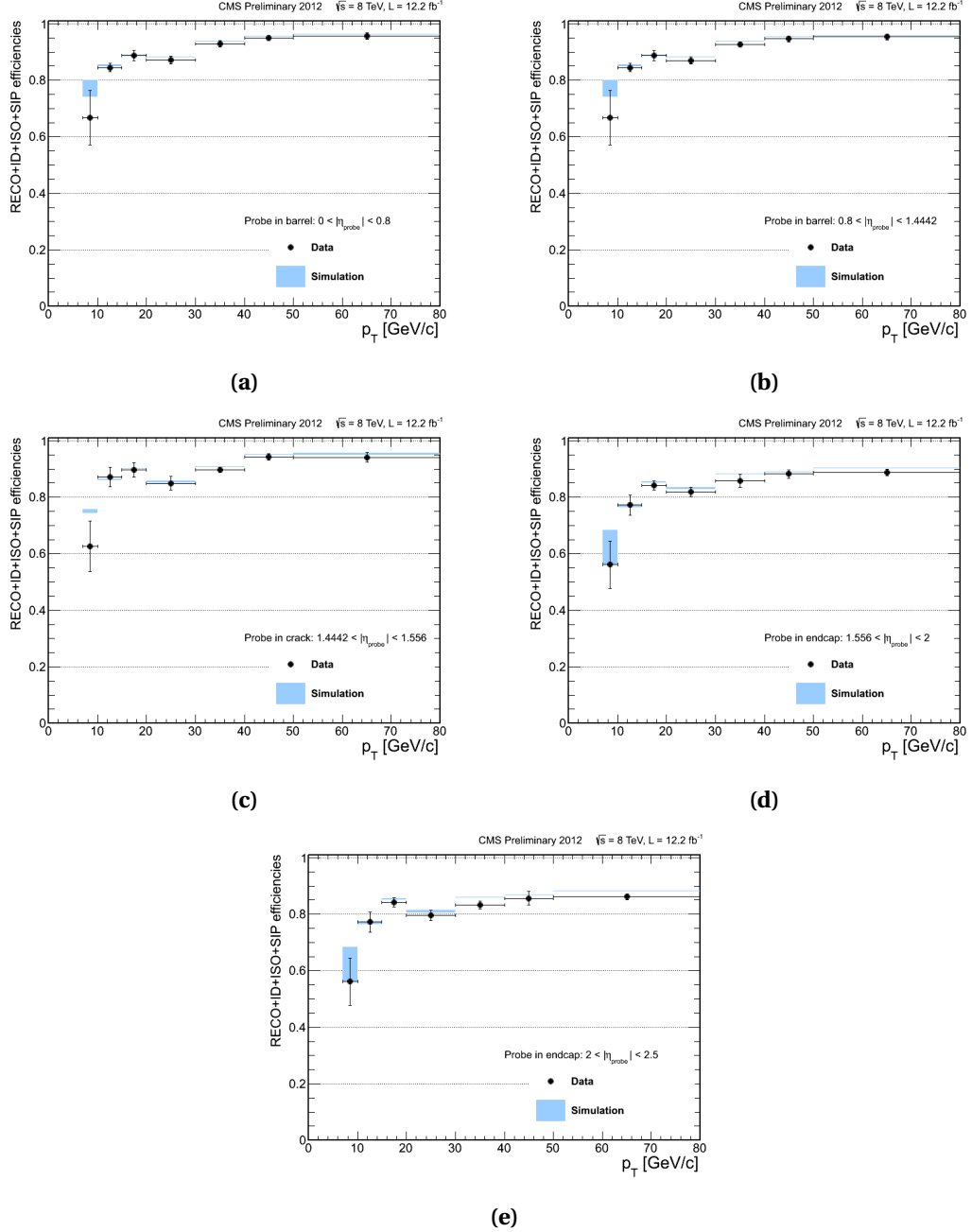


Figure 7.8: Electron identification+isolation+ $|SIP3D|$ efficiencies computed with the tag-and-probe method as a function of the probe p_T in five different η bins: (a) $0 < |\eta| < 0.8$, (b) $0.8 < |\eta| < 1.4442$, (c) $1.4442 < |\eta| < 1.556$, (d) $1.556 < |\eta| < 2$ and (e) $2 < |\eta| < 2.5$. Results are for 8 TeV data.

Systematics errors are also reported. They have two origins.

- signal tail: the number of events under the tail are varied by two times, up and down,

Chapter 7: Lepton Selection Validation from Data

and the efficiency is re-computed. The difference to nominal measurement is taken as systematic error.

- peak modelling: a 1% is assigned, based on past studies [96], changing the signal function to a Voigtian which is essentially a convolution of Gaussian and Lorentzian shapes.

Additionally, for 8 TeV tag-and-probe results, the difference between fit and template method is also taken into account as systematic error.

7.2.4 Trigger

The Tag-and-Probe technique was used on 2012 data to measure the trigger efficiency for the Double Electron trigger used in the analysis. This trigger requires two electrons with $E_T > 17 \text{ GeV}$ and $E_T > 8 \text{ GeV}$ passing certain calorimetric and track identification and isolation criteria.

This HLT path is composed by three so-called HLT filters requiring:

- A One electron with $E_T > 17 \text{ GeV}$ and with tight identification and loose isolation,
- B One electron passing condition A and an additional electron with $E_T > 17 \text{ GeV}$, tightly identified and loosely isolated,
- C Two electrons passing condition B originating from the same vertex.

An event fired the trigger if the three filters are satisfied. To measure the trigger efficiency, events should satisfy the following selection:

- Tag: electron with $p_T > 20 \text{ GeV}$, passing "Tight Trigger Working Point 2012" (tighter than trigger requirements), and spatially matched ($\Delta R < 0.1$) with an online HLT electron passing the HLT filter with $E_T > 20 \text{ GeV}$, tight identification and loose isolation,
- Probe: electron passing the analysis selection, i.e. multivariate electron identification, particle isolation and impact parameter selection from Ch. 6 and spatially matched ($\Delta R < 0.1$) with an online HLT electron passing the HLT filter requiring $E_T > 4 \text{ GeV}$ and invariant mass with the tag greater than 50 GeV,
- Tag and Probe electrons must have opposite sign and their invariant mass must be reconstructed between 60 and 120 GeV.

We want to measure the efficiency of an electron to pass the $E_T > 8 \text{ GeV}$ and $E_T > 17 \text{ GeV}$ requirement together with the identification and isolation criteria. For simplicity, we denote

these requirements as *Ele8* and *Ele17* requirements. It is not possible to measure the *Ele8* efficiency directly. Indeed, the second and third filter (B and C) are requiring two electrons: one with $E_T > 17$ GeV and one with $E_T > 8$ GeV. Now we make a valid assumption that all electrons passing 17 GeV threshold are passing the 8 GeV one. The efficiency to pass the *Ele8* can therefore be computed from electrons passing these filters. The efficiency to pass *Ele8* is calculated as the number of probes passing A and C conditions over the total number of probes as in

$$\epsilon_A = \frac{N_{A\&C}}{N_{total}} \quad (7.3)$$

The efficiency to pass *Ele17* requirements is calculated simply as the number of probes passing A over the total number of probes as in:

$$\epsilon_A = \frac{N_A}{N_{total}} \quad (7.4)$$

The Fig. 7.9 is showing the comparison between data and MC of the trigger efficiency for the *Ele17* and *Ele8* requirements for electrons in ECAL barrel and endcaps.

Data and simulation are in fair agreement for the *Ele17* requirement. The differences are less than 0.3% for the plateau and 0.5% for the turn-on region. Discrepancies are slightly higher for the *Ele8* requirement with a difference of about 1 GeV in the plateau for electrons in the ECAL barrel (0.5 GeV in the endcaps) and a difference of 1-2 GeV in the turn-on.

These turn-ons have been used to compute the efficiency of signal events to pass the trigger requirements. The following prescription was used for each of the four electron candidates on an per-event basis. For each electron, with a given p_T and η , the probability to pass a given filter is computed from the turn-ons. A random number is thrown between 0 and 1. If the number is below the probability, the electron is passing the filter considered. If a minimum of 2 electrons are passing *Ele17Ele8dZ Ele8* and at least one electron is passing *Ele17*, the event fired the trigger. The trigger efficiency has been computed after all other analysis cuts and has been compared to the direct measurement, requiring the trigger bit.

As can be seen from the Fig. 7.10, the efficiency computed with turn-ons (red or blue curves) are higher than the ones obtained directly. This is understood as being an effect due to the different algorithms used at HLT and offline levels for the electron isolation. Particle-based isolation is indeed used at offline level, removing other lepton's deposit in the isolation cone as described in Sec. 6.3, while detector-based isolation is used at HLT level, without any veto on additional leptons. Events with nearby electrons therefore tend to fail the trigger requirements.

The turn-ons computed on single electrons don't allow to compute the "real" trigger efficiency. However, comparing the trigger efficiency obtained this way with turn-ons measured on data and simulation allows to estimate a possible correction to apply to the direct measurement. It can be appreciated on Fig. 7.10 that there are little differences between data (blue) and simulation (red). As a consequence, we don't apply any correction to the simulation related to

Chapter 7: Lepton Selection Validation from Data

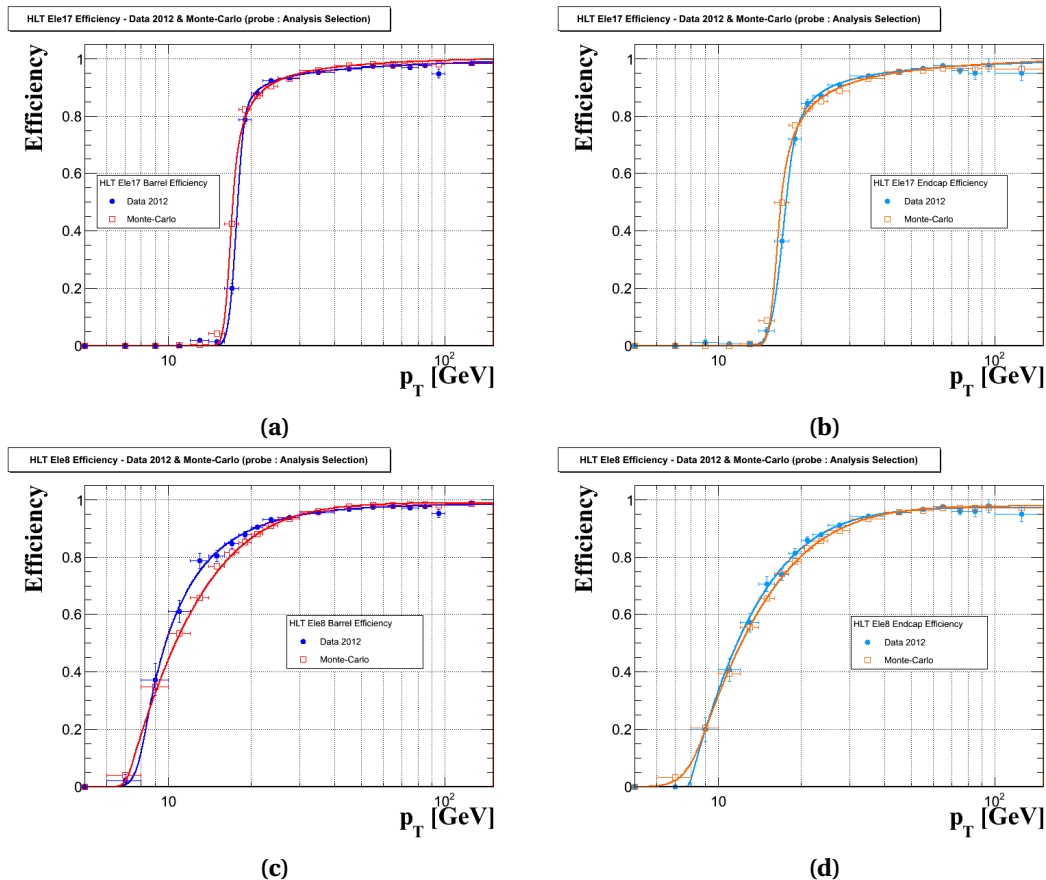


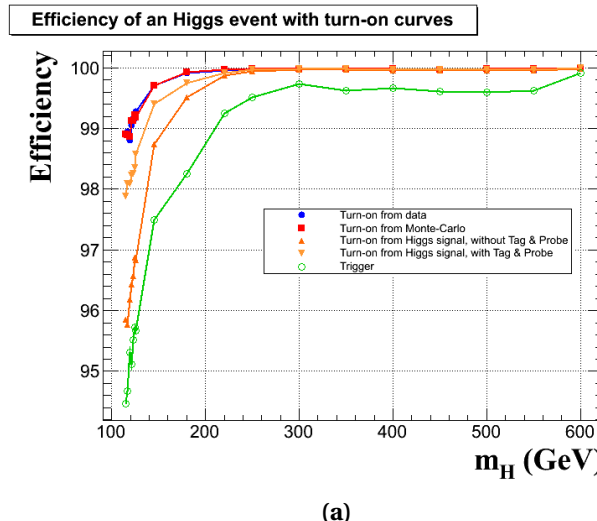
Figure 7.9: Electron HLT Trigger efficiency for the Ele17 (top) and Ele8 requirement (bottom) as a function of the probe p_T for electrons in ECAL barrel (left) and endcaps (right). Results are shown for 8 TeV data (blue) and Summer12 MC (red), with parameterizations superimposed. Probes are required to pass ID, Isolation and SIP requirements of the analysis.

trigger.

The trigger efficiency is not 100%, especially at low mass. It has been shown that the usage of the logical “OR” between the Double Electron and a Tri-Electrons trigger permits to recover 3.3% efficiency for $m_H = 125$ GeV as can be seen on Fig. 7.11(right). This is one of the novelties of this analysis with respect to the analysis performed for discovery paper [1], applied for both 2011 and 2012 datasets.

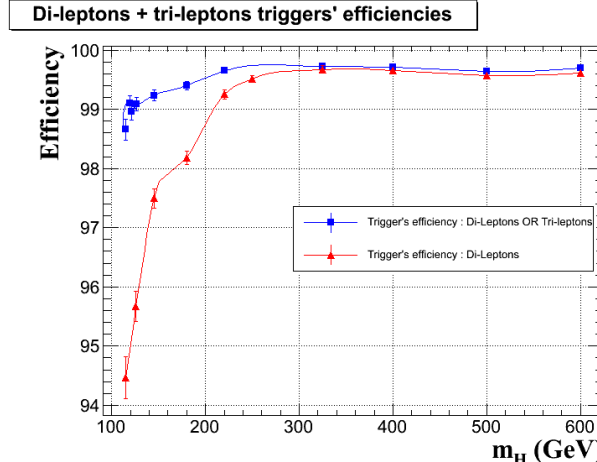
7.2.5 Electron Scale Factors

Efficiencies measured in data and simulation using the tag-and-probe method in a grid of (p_T, η) -bins are presented in preceding sections. They will be used in final statistical analysis either to correct MC yields and as a source of systematic uncertainties. In this section, we briefly discuss and bring data-to-MC scale factors as obtained by tag-and-probe method on



(a)

Figure 7.10: Electron HLT Trigger efficiency of the Double Electron Trigger computed with turn-ons measured on $Z \rightarrow ee$ events in data (red) and simulation (blue), and on $H \rightarrow ZZ^{(*)} \rightarrow 4\ell$ events with (orange), without (dark orange) Tag & Probe technique and with the trigger bit (green) as a function of the Higgs mass.



(a)

Figure 7.11: Electron HLT trigger efficiency of the Double Electron trigger (red) and of a OR between the Double and Tri-Electrons triggers, computed with the trigger bit as a function of the Higgs mass. The trigger efficiencies are computed after all other analysis cuts.

electrons as well as adjacent systematic uncertainties.

The systematic errors on the absolute efficiencies associated with the method are known to be about 0.5-1% [100]. However, they can be avoided altogether if, instead of calculating the correction factor as a ratio of the tag-and-probe efficiency measured in data to the MC-truth

efficiency:

$$c = \frac{\epsilon_{\text{T\&P}}(\text{data})}{\epsilon_{\text{MCtruth}}}, \quad (7.5)$$

one defines the correction as the ratio of tag-and-probe efficiencies, as evaluated from data and MC:

$$c = \frac{\epsilon_{\text{T\&P}}(\text{data})}{\epsilon_{\text{T\&P}}(\text{MC})}. \quad (7.6)$$

In such a ratio, the systematic errors associated with the technique itself (e.g. arising from a choice of fit functions for Z line shape and substrate background) would tend to cancel since the distributions observed in data and MC are not much different.

By dividing the entire MC samples into several segments according to the various data taking periods, the method properly captures the overall efficiency for prompt leptons averaged over the entire dataset used for extracting the signal, regardless how much the running conditions during that period were changing.

Still, not all systematic errors are canceled by using the ratio (7.6). For instance, systematic uncertainties due to background modelling and Drell-Yan tail miss-modelling still have to be accounted for. In order to be conservative, we varied the number of events in the tails by a factor of two up and down recomputing the efficiency and taking the difference to the value assessed from fit as a systematic uncertainty. The uncertainties arising from the background normalization is not accounted for. An additional systematic of 1% from the Z pole modelling as suggested by Ref. [96] is used and combined in quadrature with other sources to obtain a final scale factor.

Additionally, for 8 TeV data two different methods had to be taken into account. As a final result for 8 TeV data the mean value of scale factors obtained with fit and template methods was taken. As a systematic error the envelope between two methods was taken.

The scale factors together for the combination of reconstruction, identification, isolation and impact parameter are shown on the Fig. 7.12 and on Fig. 7.13 and reported in Tab. 7.1 for 8 TeV dataset. The values in the table indicate that the scale factors are consistent with one to 1-2% level. The exception is the lowest p_T region from 7–10 GeV where the scale factor is ~ 0.85 . This region is difficult, as previously mentioned, for few reasons: the low statistics, the low signal to background ratio. The errors quoted are a combination of statistical and systematic uncertainties. They are all propagated as systematic errors in the final analysis.

7.2. Electron measurements

Table 7.1: Reconstruction, Identification, Isolation and IP efficiencies and scale factors for single electrons, measured with the Tag-and-Probe technique on data. All measurements are obtained using Z decays in 2012 data.

p_T range (GeV)	η range	Data Eff.	MC Eff.	Scale factor (\pm sys. \pm stat.)
7 - 10	0 - 1.566	0.669	0.7712	$0.8670^{+0.117}_{-0.117} \pm 0.043$
10-15	0 - 0.8	0.845	0.8514	$0.9926^{+0.002}_{-0.002} \pm 0.013$
15-20	0 - 0.8	0.887	0.8873	$0.9999^{+0.015}_{-0.015} \pm 0.004$
20-30	0 - 0.8	0.871	0.8830	$0.9868^{+0.010}_{-0.010} \pm 0.002$
30-40	0 - 0.8	0.930	0.9389	$0.9900^{+0.006}_{-0.006} \pm 0.001$
40-50	0 - 0.8	0.950	0.9563	$0.9937^{+0.001}_{-0.001} \pm 0.000$
>50	0 - 0.8	0.956	0.9628	$0.9934^{+0.004}_{-0.004} \pm 0.001$
10-15	0.8 - 1.4442	0.845	0.8514	$0.9926^{+0.002}_{-0.002} \pm 0.013$
15-20	0.8 - 1.4442	0.887	0.8873	$0.9999^{+0.015}_{-0.015} \pm 0.004$
20-30	0.8 - 1.4442	0.870	0.8827	$0.9856^{+0.007}_{-0.007} \pm 0.004$
30-40	0.8 - 1.4442	0.927	0.9370	$0.9891^{+0.004}_{-0.004} \pm 0.001$
40-50	0.8 - 1.4442	0.947	0.9542	$0.9921^{+0.002}_{-0.002} \pm 0.001$
>50	0.8 - 1.4442	0.953	0.9591	$0.9941^{+0.003}_{-0.003} \pm 0.001$
7 - 10	1.4442 - 1.566	0.626	0.8998	$0.8347^{+0.053}_{-0.053} \pm 0.108$
10-15	1.4442 - 1.566	0.872	0.8545	$1.0100^{+0.033}_{-0.033} \pm 0.022$
15-20	1.4442 - 1.566	0.897	0.9072	$0.9966^{+0.021}_{-0.021} \pm 0.011$
20-30	1.4442 - 1.566	0.850	0.9511	$0.9944^{+0.025}_{-0.025} \pm 0.003$
30-40	1.4442 - 1.566	0.897	0.9530	$0.9884^{+0.002}_{-0.002} \pm 0.003$
40-50	1.4442 - 1.566	0.943	0.6237	$0.9913^{+0.003}_{-0.003} \pm 0.003$
>50	1.4442 - 1.566	0.941	0.7676	$0.9878^{+0.015}_{-0.015} \pm 0.003$
7 - 10	1.566 - 2.5	0.562	0.6237	$0.9011^{+0.080}_{-0.080} \pm 0.108$
10-15	1.566 - 2	0.773	0.7676	$1.0065^{+0.040}_{-0.040} \pm 0.022$
15-20	1.566 - 2	0.842	0.8532	$0.9874^{+0.003}_{-0.003} \pm 0.011$
20-30	1.566 - 2	0.819	0.8315	$0.9855^{+0.014}_{-0.014} \pm 0.002$
30-40	1.566 - 2	0.859	0.8816	$0.9740^{+0.024}_{-0.024} \pm 0.002$
40-50	1.566 - 2	0.883	0.8886	$0.9933^{+0.013}_{-0.013} \pm 0.001$
>50	1.566 - 2	0.887	0.9037	$0.9818^{+0.006}_{-0.006} \pm 0.002$
10-15	2 - 2.5	0.773	0.7676	$1.0065^{+0.040}_{-0.040} \pm 0.022$
15-20	2 - 2.5	0.842	0.8532	$0.9874^{+0.003}_{-0.003} \pm 0.011$
20-30	2 - 2.5	0.797	0.8102	$0.9832^{+0.019}_{-0.019} \pm 0.002$
30-40	2 - 2.5	0.832	0.8597	$0.9683^{+0.012}_{-0.012} \pm 0.002$
40-50	2 - 2.5	0.857	0.8679	$0.9871^{+0.025}_{-0.025} \pm 0.002$
>50	2 - 2.5	0.862	0.8829	$0.9758^{+0.006}_{-0.006} \pm 0.002$

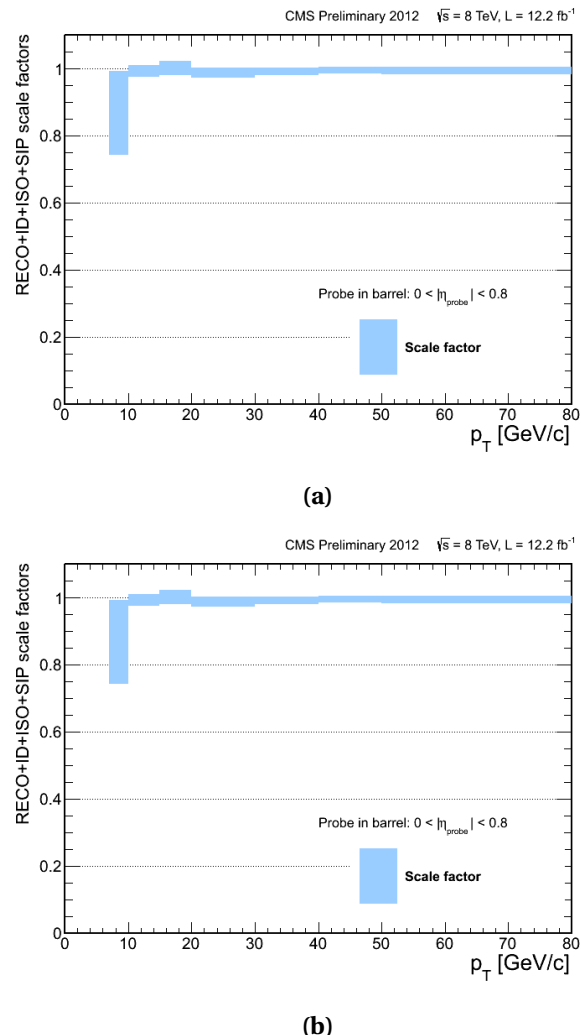


Figure 7.12: Electron total scale factors obtained from tag-and-probe method for 7 TeV data in (a) barrel and (b) endcap.

7.2. Electron measurements

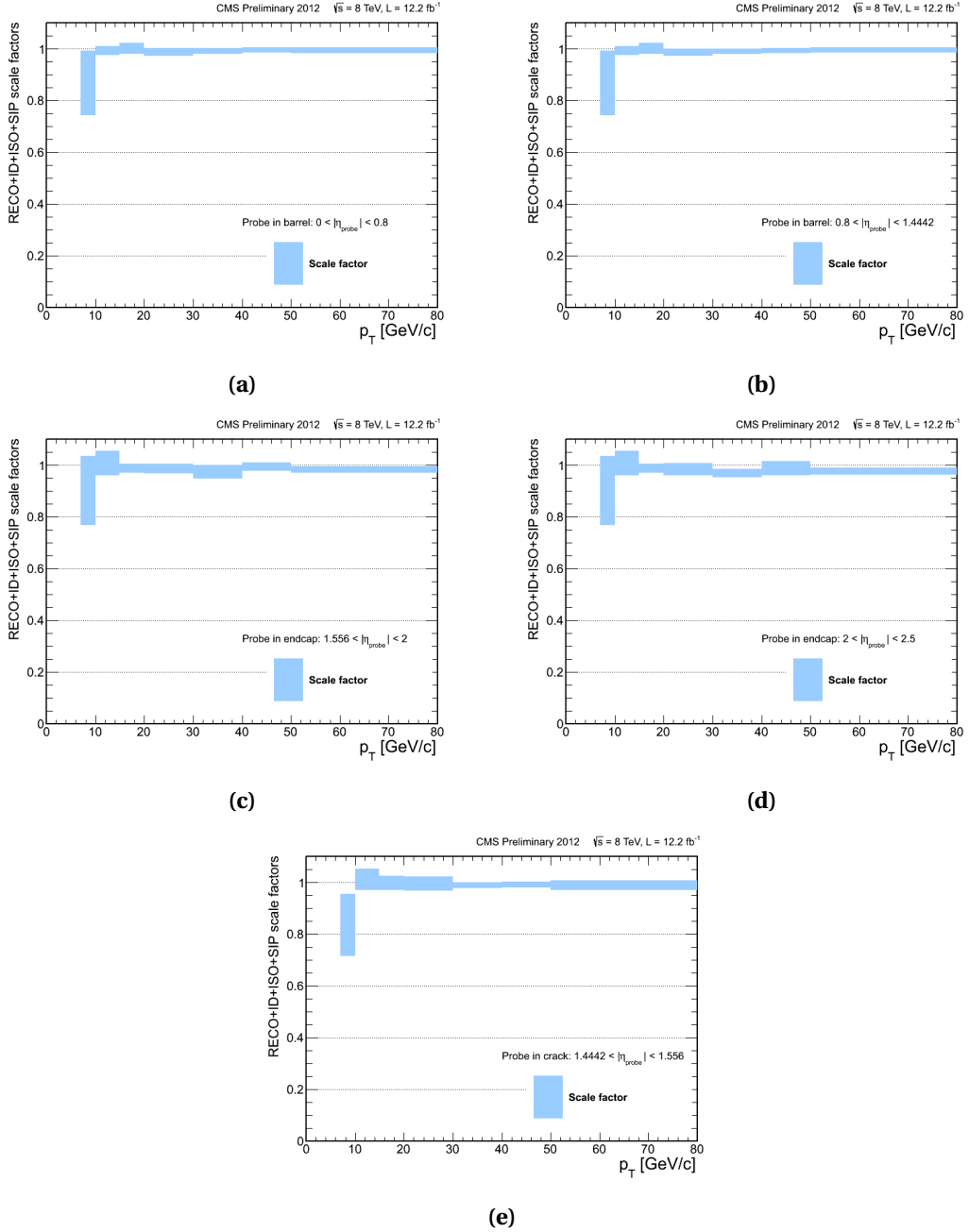


Figure 7.13: Electron total scale factors obtained from tag-and-probe method for 8 TeV data in several η regions: (a) $0 < |\eta| < 0.8$, (b) $0.8 < |\eta| < 1.4442$, (c) $1.556 < |\eta| < 2$, (d) $2 < |\eta| < 2.5$ and (e) $1.4442 < |\eta| < 1.556$.

7.3 Muon Measurements

The overall offline selection efficiency for muons is factorized as in Eq. (7.2) on page 112 and can be rewritten in the following way:

$$\epsilon = \epsilon_{\text{track}} \times \epsilon_{\text{ID|track}} \times \epsilon_{\text{SIP|ID}} \times \epsilon_{\text{ISO|SIP}} \quad (7.7)$$

- ϵ_{track} is the efficiency to reconstruct a muon track in the inner detector,
- $\epsilon_{\text{ID|track}}$ is the efficiency of the Particle Flow muon reconstruction and identification for muons that have been successfully reconstructed in the inner tracker,
- $\epsilon_{\text{SIP|ID}}$ is the efficiency of the impact parameter requirement for identified muons,
- $\epsilon_{\text{ISO|SIP}}$ is the efficiency of the isolation requirement, for muons passing all other selection criteria.

The scale factors arising from the data-to-simulation differences in muon selection that have to be applied in the further analysis are overall consistent with 1.0 at the 1% level. More details are given in the following sub-sections¹.

7.3.1 Reconstruction and Identification

The track reconstruction efficiency from a muon in the inner tracker has been measured on 2010 and 2011 data[101], and found to be close to 100%, and in agreement with the predictions from simulation within less than 0.2%.

The performance of the reconstruction in the muon system and the identification criteria for Particle Flow muons has been measured in 2011 and 2012 data using the tag-and-probe method using dimuons from Z for muons with $p_T > 15$ GeV and J/Ψ decays for muons with $p_T < 15$ GeV. A detailed description of the method can be found in Ref. [83]. The efficiencies measured from data, and the corresponding values of the efficiencies and data-to-simulation correction factors are reported in the appendix B. The simulated events used for comparisons in the two datataking periods have been reconstructed with the same software algorithms as the data and were properly re-weighted to match the pile-up distribution from data.

The results of the measurement on data are in very good agreement with the simulation for the barrel region ($|\eta| < 1.2$) and p_T above 5 GeV. For the 2011 data, the plateau value of the efficiency is reproduced within 0.3% or better. In the endcaps, the plateau value of the efficiency is about 0.8% lower in data than in the simulation, due to some issues in the CSC readout system during the second part of the 2011 data taking. The statistical accuracy at low

¹The text of this section on the control of the muons efficiencies from data is taken from Ref. [82] of which the writer of this thesis is a co-editor.

transverse momenta with 2012 data has been limited at the time of the measurement, but similar agreement is observed.

7.3.2 Impact Parameter

To measure the efficiency of the requirement on the significance of the 3D impact parameter, for muons passing the Particle Flow identification requirements, the standard tag-and-probe method has been used. For this measurement, only muons from Z decays can be used, since J/Ψ are typically produced in B hadron decays resulting in non-prompt muons.

The efficiency of the $|SIP3D| < 4$ requirement is found to be above 99.5% in the barrel, and about 99% in the forward part of the detector. In the forward region, the efficiency measured in data is about 0.4% lower than the one from simulation. Again, all the results are reported and visualized in appendix B.

7.3.3 Isolation

To measure the efficiency of the requirement on the muon isolation $R_{iso} < 0.4$, for muons that pass the Particle Flow identification and the $|SIP3D| < 4$ criteria, the standard tag-and-probe method has been used once more. Similarly to the efficiency measurement of impact parameter requirements, only muons from Z decays can be used, since muons from J/Ψ would tend to bias the measurement being non-isolated, especially for non-prompt J/Ψ mesons. The number of muon probes is statistically limited in the (5-10) GeV p_T bin on 2012 data, but otherwise an excellent agreement is observed between data and expectations from simulation (see Fig. B.3 in App. B).

7.3.4 Trigger

The single muon efficiencies for double muon triggers have been measured, again using the tag-and-probe method. The requirements for either leg of the double muon trigger are always looser than the single muon trigger used to select the tags. This means that the tag+probe pair can satisfy a given double muon trigger requirement whenever the probe satisfies the requirements of a leg of that muon trigger. The requirements of double muon trigger are asymmetric for the two legs, but the information stored in the HLT objects can be used to check if the probe leg passes the requirements only of the loose leg or also of the tight one.

The measurement has been carried out in 2011 for the dimuon trigger with p_T thresholds of 17 and 8 GeV. For the earlier part of the data taking this trigger was not used but to ensure the uniformity of the analysis, it has been emulated by requiring the events to fire a dimuon trigger with lower thresholds and then requiring corresponding HLT objects to have p_T above 17 and 8 GeV. For the 2012 running period, measurements have been performed for the dimuon triggers with only L3 muons as in 2011, for the one exploiting also tracker muon reconstruction

and for the logical “OR” of the two.

The trigger efficiency turn-on curve as function of pt measured on data is in very good agreement with the simulation for all the triggers considered (see Fig. B.4 in App. B). When performing a measurement of the plateau trigger efficiency as function of pseudorapidity η a lower efficiency in data compared to simulation in the endcaps and in the narrow transition between the two wheels of the barrel has been observed. The effect of this inefficiency is however mitigated by the fact that multiple leptons in the event can fire the trigger, resulting in marginal per-event inefficiencies, so no correction factor is finally applied for the analysis.

Come Together Part IV

8 Analysis Strategy and Event Selection

The $H \rightarrow ZZ^{(*)} \rightarrow 4\ell$ analysis, has a very clean signature — 4 isolated leptons — but suffers from a substantially low cross-section defined as

$$\sigma_{final}(H \rightarrow ZZ^{(*)} \rightarrow 4\ell) = \sigma(pp \rightarrow H) \times BR(H \rightarrow ZZ^{(*)}) \times BR(Z \rightarrow 2\ell)^2 . \quad (8.1)$$

To mitigate this obvious disadvantage a careful analysis strategy and event selection with highest lepton reconstruction, identification and isolation efficiencies had to be chosen in order to separate Higgs boson signal from backgrounds.

The background yield receives an irreducible contribution from $ZZ^{(*)}$ production via $q\bar{q}$ and gluon-induced processes. Further on, it receives the main reducible background contributions from $Zb\bar{b}$ and $t\bar{t} \rightarrow W^+ bW^- \bar{b}$, with W undergoing leptonic decay, where the final states contain two isolated leptons and two b jets possibly giving rise to secondary leptons. Reconstructed 4ℓ events can also arise from instrumental background such as $Z+jets$ or $WZ+jet(s)$ where jets are misidentified as leptons.

In addition to very low cross-section there is another challenge of this analysis. For Higgs boson masses below $2 \times m_Z$, i.e. below 180 GeV, one or both Z s have to be off-mass-shell, typically giving rise to at least one lepton with transverse momentum below 10 GeV as shown in Fig. 8.1. Low p_T leptons suffer from lower reconstruction efficiency and identification purity which introduces instrumental background. These leptons have to be given special attention in order to optimally cover the Higgs boson decay phase space. It is worth mentioning that this analysis has always been a driving force for the low p_T lepton studies and improvements in terms of reconstruction and identification always keeping in mind the highest lepton efficiency and the best possible instrumental background rejection.

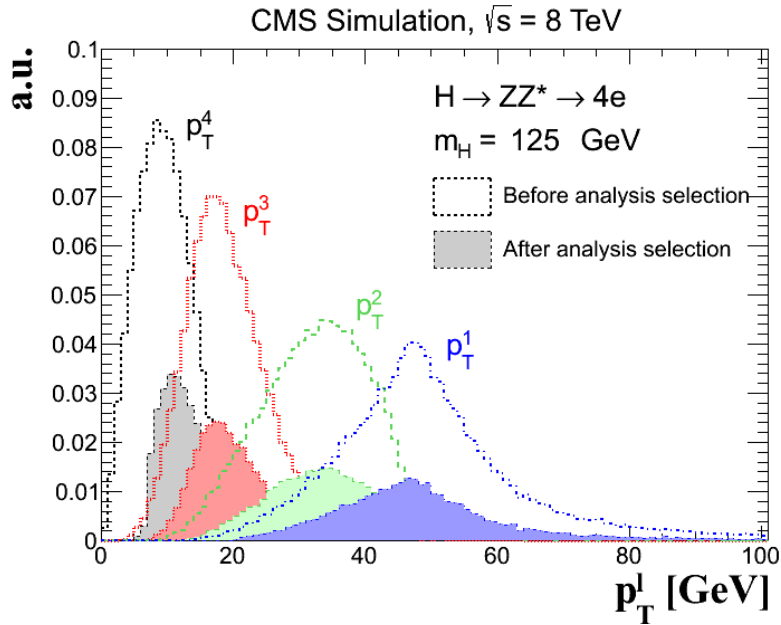


Figure 8.1: Distribution of the transverse momentum (p_T) for each of the four leptons (sorted in p_T) from $H \rightarrow ZZ^{(*)} \rightarrow 4\ell$ signal events and for a mass hypothesis of $m_H = 125$ GeV. The distributions are obtained using MC signal samples and shown at generator level within eta acceptance (empty histograms), and for selected events (shaded histograms) in the $4e$ channel

8.1 General Analysis Strategy

The analysis presented in this thesis is developed on basis of a similar analysis [35] published with 2010 and 2011 dataset at 7 TeV in Physics Review Letters—sometimes denoted as “PRL analysis”. The PRL analysis strategy was designed for the Higgs boson search in mass range from 110 GeV to 600 GeV. It was relying on a simple Higgs-boson-mass-independent selection of leptons using identification, isolation and kinematic criteria.

It has been shown in previous studies [86, 102, 103, 63] that an optimal working point can be found where the contribution from the reducible and instrumental backgrounds are quasi-eliminated. This is achieved by applying cuts on the maximum allowed energy flow in the isolation cones around leptons and on the maximum impact parameter of lepton tracks with respect to the primary interaction vertex. The analysis aims at the highest possible lepton reconstruction, identification and isolation efficiencies, that are compatible with a quasi-negligible reducible and instrumental background, in the acceptance range used for this analysis, i.e. with transverse momentum and pseudorapidity for electrons of $p_T^e > 7$ GeV, $|\eta^e| < 2.5$, and for muons of $p_T^\mu > 5$ GeV, $|\eta^\mu| < 2.4$. It has been shown by recent studies that further relaxing of the transverse momentum thresholds brings modest efficiency improvements at the cost of introducing significant amount of instrumental background. Therefore, $p_T^e > (5)7$ GeV for muons(electrons) has been preserved as optimal choice.

A special effort was undertaken to establish data driven techniques for the evaluation of

8.1. General Analysis Strategy

systematic uncertainties and background contributions. Since the expected significance was insufficient to claim discovery at any Higgs boson mass hypothesis, the emphasis was put on simplicity and robustness of the strategy in order to gain confidence in the measured values.

The PRL analysis gave the needed confidence and allowed for further developments using higher level methods and additional event information with changes always confronted to the PRL reference analysis. The improvements carried out throughout 2012 led to a discovery announcement on 4th of July during the opening session of the ICHEP2012 conference. Special parts of the analysis have been continuously improved also after ICHEP, but the general strategy has been essentially unchanged. Since 2011 analysis has already excluded large portion of Higgs invariant mass range and the phase space where Higgs boson could be has been left quite narrow, a special search improvement policy had to be adopted to help Higgs hunters preserve an objective mind. This policy, known as “blinding policy” states as follows:

“In the channel with low background and high resolution, $H \rightarrow ZZ \rightarrow 4\ell$, do not look (either make no plots with such events or exclude events at ntuple level) at m_{4l} between 110 and 140, and above 300 GeV. The m_{4l} distribution can be checked in the full mass range either in the control regions (with no signal expected) or with significantly relaxed cuts (when signal cannot be seen under about 100 larger background).”

“The blinding procedure applies both to the analysis of 2011 (if any change with respect to published analysis is done) and 2012 data.”

As previously said, the analysis essentially relies on high lepton reconstruction, identification and isolation efficiencies. Reconstruction, identification and isolation observables which are specially challenging for electrons were already described in Ch. 6. As opposed to 2011 simple cut based identification of leptons, new electron identification relies on a multivariate BDT and muons are required to fulfil the Particle Flow Muons criteria. In 2011, the lepton isolation was computed in a spacial cone around lepton direction by summing up the energy flow in calorimeters and transverse momentum flow from tracks originating from primary vertex. The 2012 analysis uses the Particle Flow approach and is corrected from pile-up contributions attaching charged particles to the primary vertex and correcting neutral component with the so-called “effective area” methodology.

The $pp \rightarrow ZZ \rightarrow 4\ell$ background prediction relies fully on the theory. All instrumental uncertainties associated with selecting four prompt leptons (trigger, reconstruction, isolation and impact parameter cuts) are derived directly from data.

The remaining contribution of reducible backgrounds is evaluated using data driven techniques. This includes the overall rates of 4ℓ events, passing all selection cuts, and their mass distributions. With respect to 2011 analysis, in 2012 two different techniques are used and described in Ch. 10. Comparable background counts in the signal region are found within

uncertainties from both methods and an envelope comprising these results is used as the final estimate.

The 2012 analysis profits from the full four lepton system information by introducing a Kinematic Discriminant (KD) presented in Ch. 12. Kinematic Discriminant (KD) is built using variables fully describing the decay kinematics of the $H \rightarrow ZZ \rightarrow 4\ell$ (five angles and two masses). It is constructed based on the probability ratio of the signal and background hypotheses, $KD = P_{sig}/(P_{sig} + P_{bkg})$. The signal and $q\bar{q} \rightarrow ZZ$ background pdf's are coming from fully analytical parametrization.

The statistical analysis of selected events, presented in Ch. 13, is based on their four-lepton mass ($m_{4\ell}$) distribution. The presence of the Higgs boson is expected to manifest itself as a resonance over the continuum $m_{4\ell}$ distribution of the $pp \rightarrow ZZ \rightarrow 4\ell$ origin. The width of the peak for a SM Higgs boson with a low mass ($m_H < 250$ GeV) is expected to be defined by the detector resolution. For higher masses, SM Higgs boson's intrinsic width quickly overtakes the detector resolution. For the analysis in 2012, all final results (exclusion limits, p-values,...) are extracted via simultaneous likelihood fit of:

- six (3 final states for signal and background) one-dimensional ($m_{4\ell}$) distributions,
- six two-dimensional ($m_{4\ell}$, KD) distributions and
- six three-dimensional ($m_{4\ell}$, KD, per-event mass errors) distributions,

for each mass hypothesis, using the standard statistical approaches adopted by CMS [104].

8.2 Event Selection

Since only a handful of events is needed to claim the existence of a 4ℓ resonance it is vital to have a good control of all efficiencies and backgrounds. It is known that Monte Carlo generators cannot perfectly describe all the observables used in the analysis. Essentially, this means that we have to rely on collision data to accurately measure efficiencies as well as background rates and shapes.

The event selection is designed to gradually bring analysis to the signal phase space, while preserving ability to have a good control of efficiencies and background at each step.

We could categorize steps in three major groups, depending on their objective:

1. trigger selection — technical steps to reduce data to manageable level
2. lepton selection — selecting collection of input elements for composing Z candidates and background control

3. final Z and H candidates selection and combinatorics — combining leptons into Z s and Z s into Higgs boson candidate

8.2.1 Trigger Selection

Data events entering the analysis are taken from DoubleElectron, DoubleMuon and MuEG primary datasets which are characterized by their trigger content. Trigger selection can be considered as a technical step towards bringing event rates down to a level at which PD data can be recorded. Details on triggers and datasets can be found in chapter 5.

8.2.2 Lepton Selection

At this stage, we select two sets of leptons, first *loose leptons* to be used for reducible background measurement described in Sec. 10 and than *good leptons* to be used for the main analysis. The selection criteria for the two groups is as follows:

1. **loose leptons:** electrons within the geometrical acceptance of $|\eta^e| < 2.5$, with $p_T^e > 7 \text{ GeV}$ and having 0 or 1 expected missing inner hits, muons (global or tracker) satisfying $|\eta^\mu| < 2.4$, $p_T^\mu > 5 \text{ GeV}$. Both electrons and muons should satisfy loose requirements on the transverse ($d_{xy} < 0.5 \text{ cm}$) and longitudinal ($d_z < 1 \text{ cm}$) impact parameter with respect to the primary vertex. Non-global tracker muons are arbitrated. In addition, it is required that $\Delta R > 0.02$ between the leptons.
2. **good leptons:** these are *loose leptons* on which additional criteria are imposed. Namely:
 - electrons should pass the electron identification criteria as described in section 6.1, muons should meet the Particle Flow Muons requirements (see section 6.2)
 - Relative PFIso < 0.4 (see section 6.3)
 - the significance of the impact parameter to the event vertex, SIP_{3D} (see section 6.4), is required to satisfy $|\text{SIP}_{3\text{D}} = \frac{\text{IP}}{\sigma_{\text{IP}}}| < 4$ for each lepton, where IP is the lepton impact parameter in three dimensions at the point of closest approach with respect to the primary interaction vertex, and σ_{IP} the associated uncertainty.

Before building *good leptons* collection, an e/μ cross cleaning procedure is applied. *Loose electrons* are discarded if they satisfy: $\Delta R(e, \mu) < 0.05$, where the muons considered are *loose muons* passing Particle Flow or Global muon Global muons criteria.

The events are then requested to have fired the relevant electron and muon triggers, consistently in data and MC as described in Ch. 5.

8.2.3 Final Selection and Combinatorics

After choosing sets of leptons described in previous section, we can now start combining them into Z and Higgs boson candidates. We denote this step as candidate selection (CS). As already said, it is crucial to preserve maximum signal efficiency and the phase space for background estimates and evaluation of systematic uncertainties.

We therefore impose the following sequence of selection requirements:

- CS1 **First Z:** a pair of *good lepton* candidates of opposite charge and matching flavour ($e^+ e^-$, $\mu^+ \mu^-$) with reconstructed mass $m_{1,2}$ closest to the nominal Z boson mass is retained and denoted Z_1 . The selected pair should satisfy $40 < m_{Z_1} < 120$ GeV .
- CS2 **Three or more leptons:** at least another *good lepton* candidate of any flavour or charge.
- CS3 **Four or more leptons and a matching pair;** a fourth *good lepton* candidate with the flavour of the third lepton candidate from the previous step, and with opposite charge.
- CS4 **Choice of the “best 4ℓ ” and Z_1, Z_2 assignments:** retain a second lepton pair, denoted Z_2 , among all the remaining $\ell^+ \ell^-$ combinations. If more than one Z_2 combination satisfies all the criteria, the one built from leptons of highest p_T is chosen. The selected pair should satisfy $4 < m_{Z_2} < 120$ GeV. At this stage, it is required that any two leptons from the four selected have $p_{T,i} > 20$ GeV and $p_{T,j} > 10$ GeV.
- CS5 **QCD suppression:** the reconstruction mass of opposite-sign and same-flavour lepton pair must satisfy $m_{\ell\ell} > 4$ GeV.
- CS6 **$m_{4\ell}$, Z and $Z^{(*)}$ kinematics:** with $m_{4\ell} > m_{4\ell}^{\min}$, $m_{Z_1}^{\min} < m_{Z_1} < 120$ GeV and $m_{Z_2}^{\min} < m_{Z_2} < 120$ GeV, where $m_{Z_1}^{\min}$ and $m_{Z_2}^{\min}$ are defined below.

The first four steps are designed to reduce the contribution of the instrumental backgrounds from QCD multi-jets and $Z +$ jets. The very first step ensures that the leptons in the preselected events are on the high efficiency plateau for the trigger. Control samples for the $Z +$ jet, $Z b\bar{b}/c\bar{c}$ and $t\bar{t}$ backgrounds are obtained as subsets of the event sample remaining after the first step. The second step allows for control of the three-lepton event rates such as WZ di-boson production events. This step, together with fourth step, also reduces the number of jets misidentified as leptons, letting fewer combinatorial ambiguities to arise when assigning the leptons to candidate Z bosons. The choice of the best combination of four leptons completes the four first steps. In the fifth step, the low mass resonances as well as multiple hadron decays are removed.

Finally, three sets of kinematic requirements are introduced aiming to allow study of the s -channel Z production contribution, maximal sensitivity in different ranges of Higgs boson mass hypothesis and measurement of the ZZ cross-section. The three sets are labeled as:

- **$Z \rightarrow 4\ell$ phase space** analysis defined with $m_{Z2}^{min} \equiv 4$ GeV and $m_{Z1}^{min} \equiv 40$ GeV, $m_{4\ell}^{min} \equiv 70$ GeV and $m_{4\ell}^{max} \equiv 110$ GeV. This phase space is used to provide a 4ℓ standard candle enabling direct measurement of 4ℓ scale and resolution.
- **Higgs phase space** analysis defined by imposing $m_{Z2}^{min} \equiv 12$ GeV and $m_{Z1}^{min} \equiv 40$ GeV and $m_{4\ell}^{min} \equiv 100$ GeV. This phase space provides a best search sensitivity for masses $100 < m_H > 600$ GeV.
- **$ZZ \rightarrow 4\ell$ phase space** analysis is defined by asking $m_{Z2}^{min} \equiv 60$ GeV and $m_{Z1}^{min} \equiv 60$ GeV. This phase space is used for measuring $ZZ \rightarrow 4\ell$ cross-section.

8.2.4 Event Selection Performances and Control

In this section we show performance of the event selection illustrated in the previous section as well as distributions of used observables from control regions. Generally, a nice data/MC agreement is found.

The signal detection efficiencies from MC for a 4ℓ system within the geometrical acceptance as a function of Higgs boson mass hypothesis are shown in Fig. 8.2 for the baseline selection. The geometrical acceptance is defined by having generated electrons satisfying $|\eta^e| < 2.5$ and generated muons satisfying $|\eta^\mu| < 2.4$, with no p_T cut. The efficiency rises from about 28% / 58% / 38% at $m_H = 125$ GeV to about 60% / 85% / 72% at $m_H = 400$ GeV for the $4e$ / 4μ / $2e2\mu$ channels.

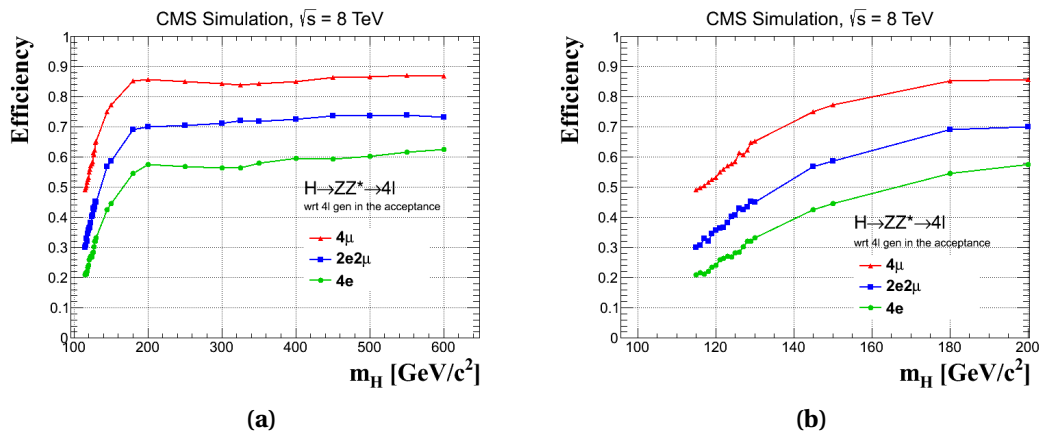


Figure 8.2: Signal detection efficiencies from MC for a 4ℓ system within the geometrical acceptance in the $4e$ (green), 4μ (red) and $2e2\mu$ (blue) channels as a function of Higgs boson mass hypothesis in (a) full mass range and (b) low mass range.

The invariant mass of two good leptons (Z_1) as built in the first step of the selection is shown in Fig. 8.3 for both electron and muon channels and for both 7 and 8 TeV data. A nice agreement can be appreciated between data and Monte Carlo expectations.

Chapter 8: Analysis Strategy and Event Selection

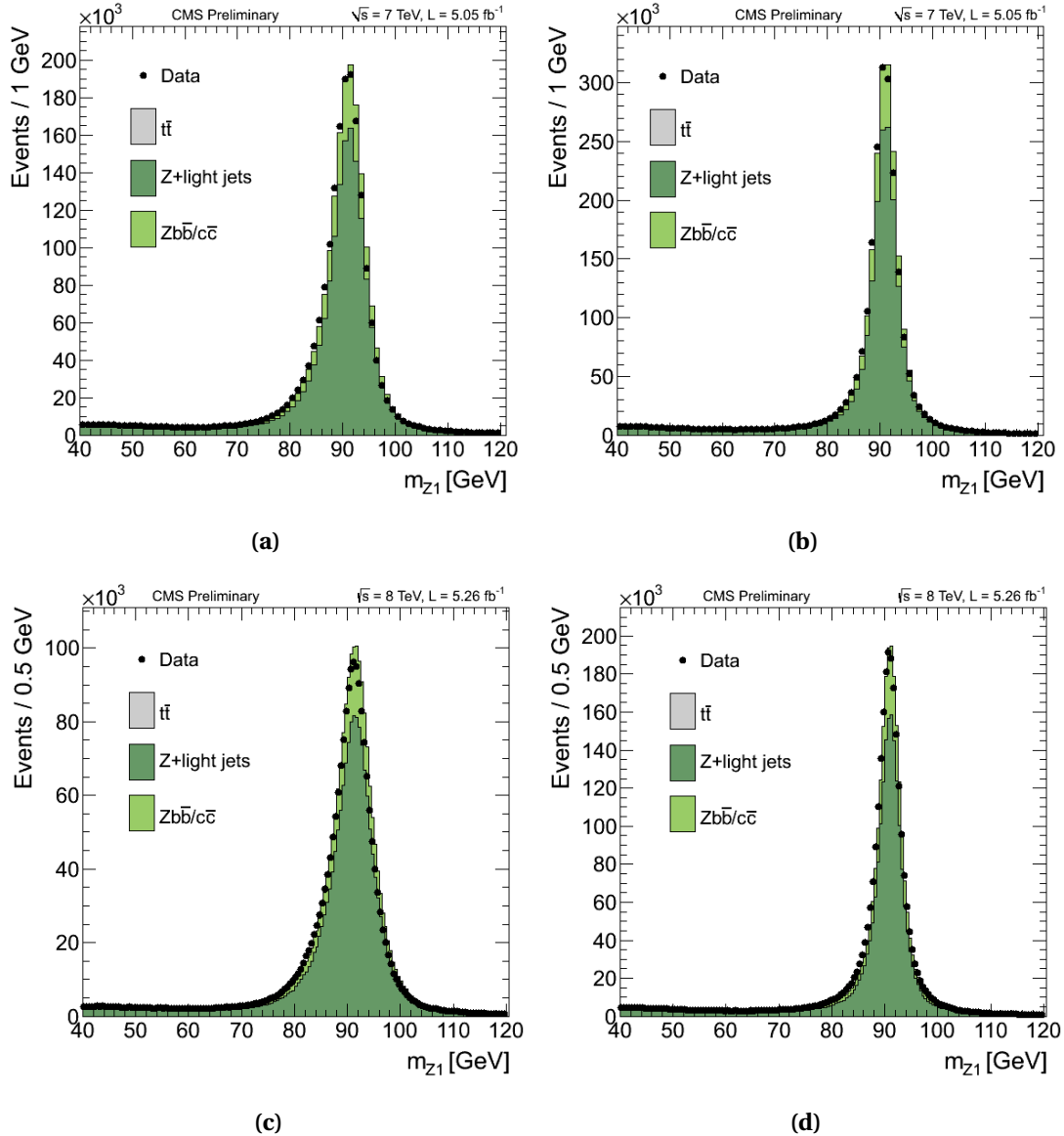


Figure 8.3: Comparison of Z_1 invariant mass in ee (left) and $\mu\mu$ (right) channels at 7 (top) and 8 TeV (bottom) between data and MC expectations. The samples correspond to an integrated luminosity of $\mathcal{L} = 5.05 \text{ fb}^{-1}$ for the 7 TeV data, and 12.21 fb^{-1} for the 8 TeV data.

The events yields as a function of the selection steps are shown in Fig. 8.4 and Fig. 8.5 for the baseline selection in the $4e$, 4μ and $2e2\mu$ channels and for 7 and 8 TeV analysis.

Figure 8.6 and Figure 8.7 show a comparison between data and MC at an early stage of the event selection (see Sec. 8.2.3) where four or more leptons are reconstructed and where a pair of leptons have been assigned to the Z_1 (step CS1) for both 7 and 8 TeV analysis. The comparison is made here relaxing the flavour and sign requirements on the second pair of

8.2. Event Selection

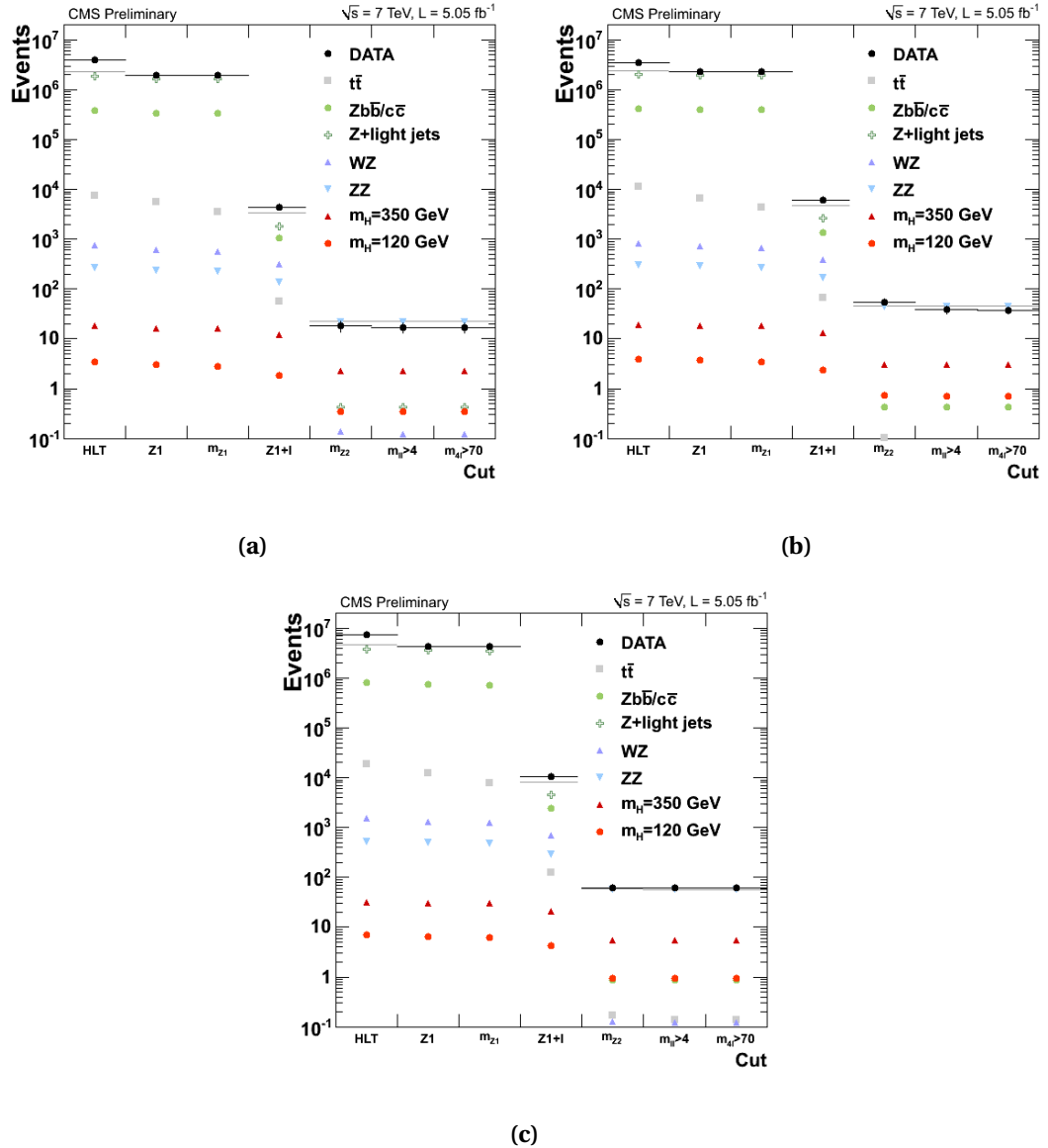


Figure 8.4: Event yields in the (a) $4e$, (b) 4μ and (c) $2e2\mu$ channels for each event selection step. The MC yields are not corrected for background expectation. The samples correspond to an integrated luminosity of $\mathcal{L} = 5.05 \text{ fb}^{-1}$ of 7 TeV data.

leptons such that the sample contains signal-like and background-like events. At this stage we don't necessarily expect a perfect data to MC agreement as this sample is dominated by fake leptons and no additional scale factors are applied. In the analysis, the reducible background is in the end taken from data while Monte Carlo simulation is only used to check the background composition.

Chapter 8: Analysis Strategy and Event Selection

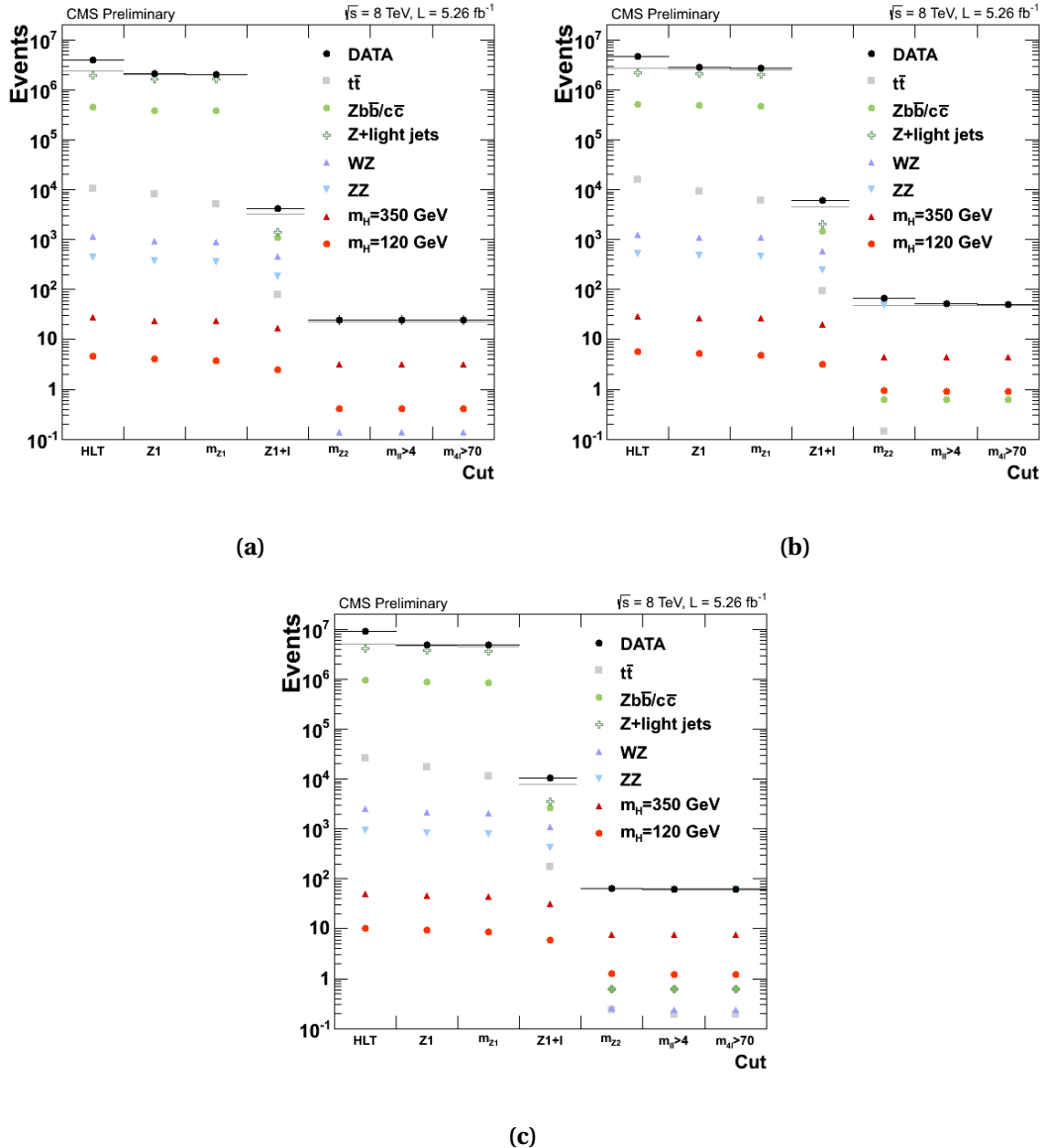


Figure 8.5: Event yields in the (a) $4e$, (b) 4μ and (c) $2e2\mu$ channels for each event selection step. The MC yields are not corrected for background expectation. The samples correspond to an integrated luminosity of $\mathcal{L} = 12.21 \text{ fb}^{-1}$ of 8 TeV data.

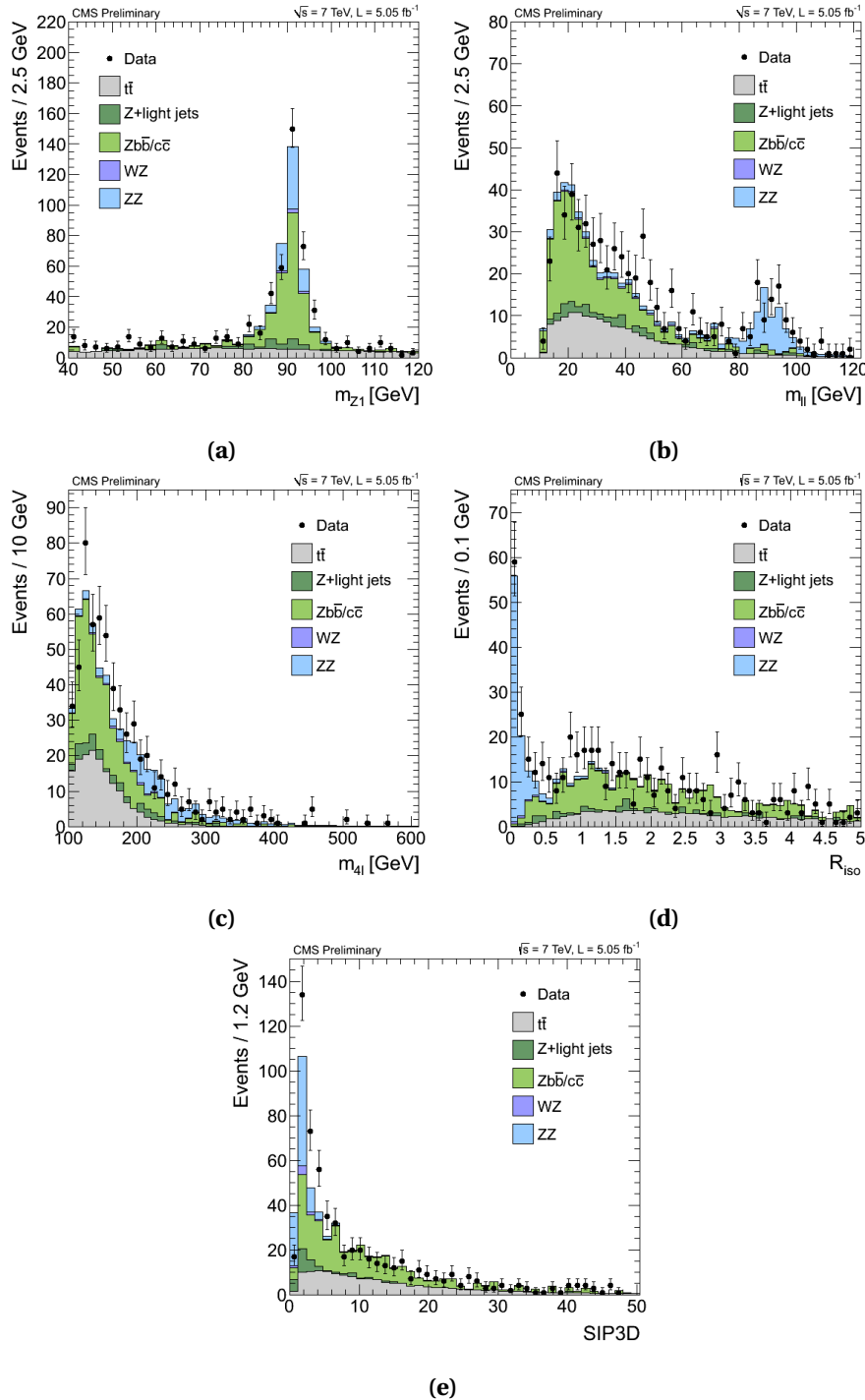


Figure 8.6: Comparison between 7 TeV data and MC at an early stage of the event selection (CS1) where four or more leptons are reconstructed and where a pair of leptons have been assigned to the Z_1 . Points with statistical uncertainties represent data while shaded histogram areas represent MC expectations corrected for background expectation. The samples correspond to an integrated luminosity of $\mathcal{L} = 5.05 \text{ fb}^{-1}$. $R_{iso,\ell}$ and SIP_{3D} values correspond to maximum relative isolation and significance of impact parameter for the lepton in the second pair.

Chapter 8: Analysis Strategy and Event Selection

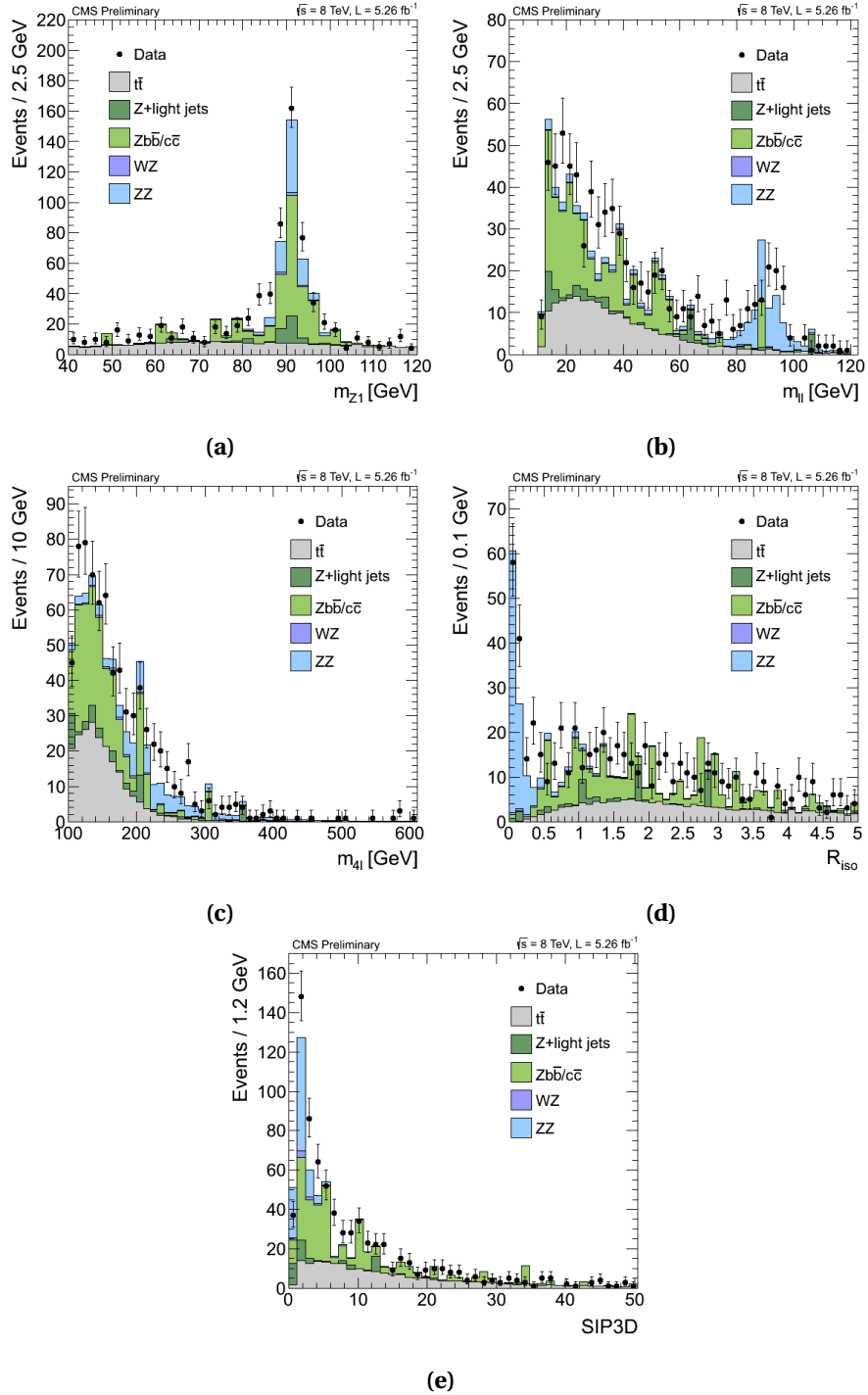


Figure 8.7: Comparison between 8 TeV data and MC at an early stage of the event selection (CS1) where four or more leptons are reconstructed and where a pair of leptons have been assigned to the Z_1 . Points with statistical uncertainties represent data while shaded histogram areas represent MC expectations corrected for background expectation. The samples correspond to an integrated luminosity of $\mathcal{L} = 12.21 \text{ fb}^{-1}$. $R_{iso,\ell}$ and SIP_{3D} values correspond to maximum relative isolation and significance of impact parameter for the lepton in the second pair.

9 Signal Modelling and Uncertainties

In order to achieve a better sensitivity in Higgs searches one needs to make better use of all observed events including those thrown away off the main peak in the $m_{4\ell}$ -distribution. A possible and plausible solution is a $m_{4\ell}$ -distribution parametrization. However, in contrast to ad hoc parameterizations fully relying on MC simulation and built for a fixed set of simulated m_H -points, the parameterization used in this analysis has an explicit functional form

$$\frac{dN_{sig}}{dm_{4\ell}} = F_{sig}(m_{4\ell} | m_H, \text{parameters}) \cdot N_{sig} \quad (9.1)$$

$$\frac{dN_{bkg}}{dm_{4\ell}} = F_{bkg}(m_{4\ell} | m_H, \text{parameters}) \cdot N_{bkg} \quad (9.2)$$

where $m_{4\ell}$ is an observed four-lepton mass, m_H is an arbitrary Higgs boson mass. All experimental and phenomenological parameters are built-in the parametrization as explicit functions of $m_{4\ell}$.

Besides giving a good intuition for relative roles and an interplay of different factors in defining the four-lepton mass shape and event rates, such an explicit parameterization has the following advantages in application to actual data analyses:

- It allows for a smooth scan over Higgs boson masses without having to generate numerous MC samples. It must be noted that in a search with actual data, the scanning step in Higgs boson mass m_H must be much smaller than the mass peak width that is as small as $\mathcal{O}(1 \text{ GeV})$ for a wide range of Higgs boson masses.
- Observing a local excess of events in data, the description of the $m_{4\ell}$ -distribution with an explicit functional dependence on m_H as a sole parameter allows for a straightforward fit for the best Higgs mass m_H .
- The parameterization explicitly factors out all experimental effects, specifically: detector fiducial acceptance, reconstruction efficiency, resolution and efficiency of cuts used in the analysis. All these factors can be measured in data. Hence, in case data shows that

the default MC simulation needs further tuning, one does not have to wait for such a tuning to happen and can immediately fold in the directly measured efficiencies and resolutions into the analysis.

- Once we are confident in predicting the per-event four-lepton mass resolution from the measurements of individual leptons, we can use these together with the expected response probability density function $g(m_{4\ell})$ to perform an un-binned likelihood analysis to further improve the search sensitivity of the Higgs boson.
- Finally, a sensibly factorized parametrization gives one a better understanding of the role of various systematic uncertainties, including their correlations within a single process as well as between different processes.

In this chapter, we build, step by step, the signal model and explain different inputs, specifically, model uncertainties, data-to-MC scale uncertainties and $m_{4\ell}$ scale and resolution. The signal model has to be divided into low and high-mass models because narrow-width approximation brakes down for the Higgs boson masses greater than 400 GeV. In addition to this, in this chapter we introduce an advance analysis technique that takes into account mass resolutions assessed on the per-event basis providing a significant gain in the Higgs boson mass measurement.

9.1 Signal Model at Low Masses

For the low mass range, where the narrow-width approximation is considered, we model the signal $f(m_{4\ell}|m_H)$ PDF as a convolution of the relativistic Breit-Wigner $RBW(m_{H^*}|m_H)$ and Double Crystal Ball function $DCB(m_{4\ell}|m_{H^*})$:

$$f(m_{4\ell}|m_H) = DCB(m_{4\ell}|m_{H^*}) \otimes RBW(m_{H^*}|m_H). \quad (9.3)$$

The Breit-Wigner PDF is described in Ref. [105] and it is fully determined by the Higgs boson mass:

$$RBW(m_{4l}|m_H) = \frac{\Gamma_{gg}(m_{4l}) \cdot \Gamma_{ZZ}(m_{4l}) \cdot m_{4l}}{(m_{4l}^2 - m_H^2)^2 + m_{4l}^2 \cdot \Gamma^2(m_{4l})} \quad (9.4)$$

The Double Crystal Ball function $DCB(m_{4\ell}|m_{H^*})$ has six independent parameters, and is captures the Gaussian core (σ_m) of the four-lepton mass resolution function, mass scale Δm_{H^*} of the peak, and the tails originating from leptons emitting bremsstrahlung photons in the tracker material, and from the non-Gaussian mis-measurements specific to electrons

9.1. Signal Model at Low Masses

interacting with the detector material (two parameters, n and α , for each side of the mean):

$$DCB(\xi) = N \cdot \begin{cases} A \cdot (B + |\xi|)^{-n_L}, & \text{for } \xi < \alpha_L \\ A \cdot (B + |\xi|)^{-n_R}, & \text{for } \xi > \alpha_R \\ \exp(-\xi^2/2), & \text{for } \alpha_L \leq \xi \leq \alpha_R \end{cases} \quad (9.5)$$

where $\xi = (m_{4\ell} - m_{H^*} - \Delta m_{H^*})/\sigma_m$. The emergence of the left and right hand tails is defined the power n_L, n_R , respectively. The parameters α_L, α_R define where the splicing of the tails and the core are made, in units of σ_m . Parameters A and B ensure the continuity of the function itself and its first derivatives, while N is the normalizing constant.

The parameters of the Double Crystal Ball are obtained from the fit of simulated signal events, after the full lepton and event selections are applied. Figure 9.1 shows the fits for 4μ (left), $4e$ (center) and $2\mu 2e$ (right) events simulated with $\sqrt{s} = 8$ TeV for two example mass points in the low mass range.

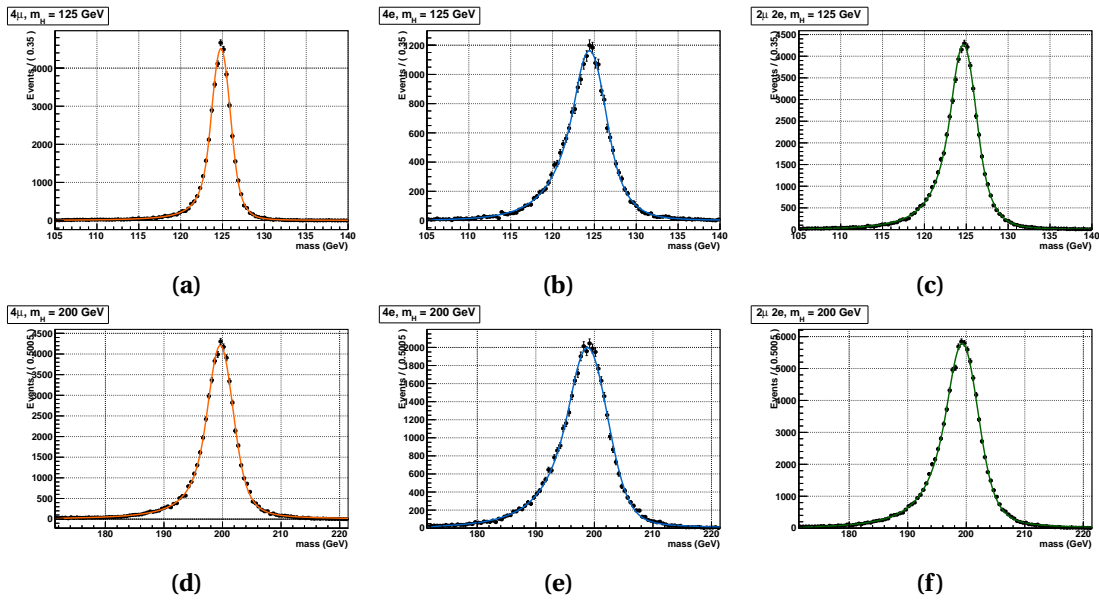


Figure 9.1: Parametrization $f(m_{4l}|m_H)$ for the Higgs boson mass at the reconstruction level after the full lepton and event selections are applied. The distributions obtained from 8 TeV MC samples are fitted with the model described in the text for 4μ (left), $4e$ (center) and $2\mu 2e$ (right) events. The fits are shown for two Higgs boson mass points: 125 GeV (top) and 200 GeV (bottom). The figures are taken from Ref. [106].

After the parameters of the signal model are obtained for all the simulated samples, the parameters are fitted to obtain the signal model parameterization also for the intermediary mass values. Figure 9.2 shows the Double Crystal Ball parameters for all the simulated mass bins at 8 TeV together with the simple polynomial parametrization which simplifies the statistical analysis allowing for a continuous scan over Higgs boson masses.

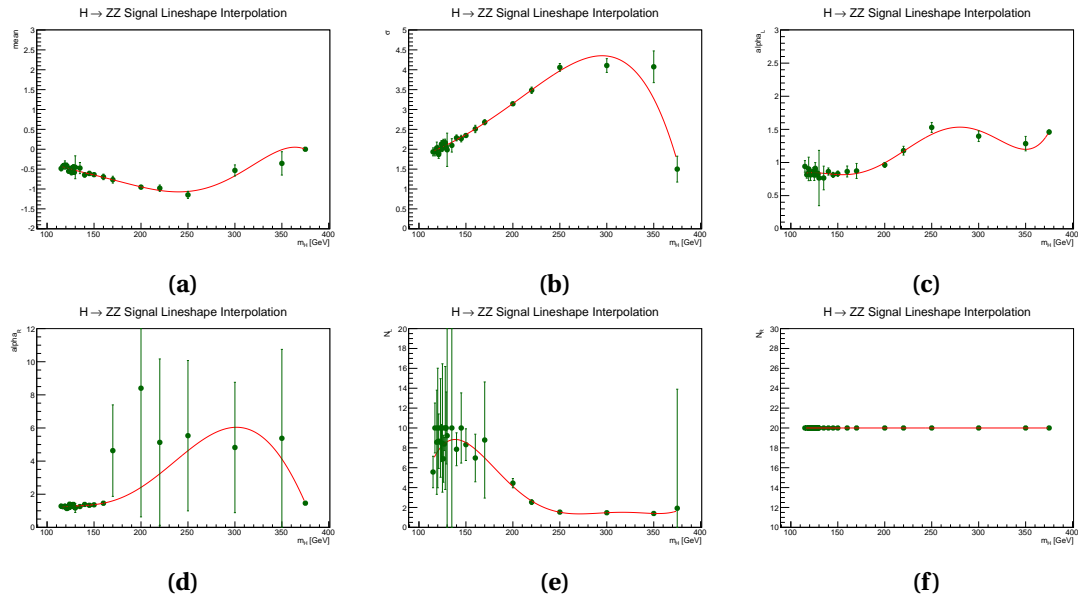


Figure 9.2: Linear and constant fits of the six parameters describing the signal $f(m_{4l}/m_H)$ PDF as a function of m_H . The PDF is modelled as a Double Crystal Ball function convoluted with the relativistic Breit-Wigner function described in the text with parameters: (a) mean, (b) σ , (c) α_1 , (d) α_2 , (e) n_1 and (f) n_2 . Parameters are shown for $4e$ events simulated with $\sqrt{s} = 8$ TeV. The figures are taken from Ref. [106].

9.2 Signal Model at High Masses

The Higgs search at low mass is carried out in the framework of narrow-width approximation, describing the Higgs lineshape with a Breit-Wigner distribution. This approximation breaks down at high Higgs mass (typically > 400 GeV) due to the very large Higgs width (> 70 GeV). Therefore, a new signal parametrization has been found, using the Complex Pole Scheme (CPS). In this section we bring the high-mass parametrization together with its uncertainties.

9.2.1 Lineshape with Complex Pole Scheme

The narrow-width approximation breakdown at high Higgs boson masses has been discussed in details in Ref. [107] and a more correct approach to describe the Higgs invariant mass distribution has been proposed—the Complex Pole Scheme (CPS). The total Higgs production cross-section has been recomputed by the Higgs Cross-Section Working Group to include corrections due to CPS at high Higgs mass [108]. In the present work we rely on those updated values for the total cross-section and we exploit a new functionality developed in POWHEG [40] in order to reweight Higgs-signal samples to match the Higgs lineshape predicted in the CPS approach.

At high Higgs mass the interference between the Higgs signal and the $gg \rightarrow ZZ$ background becomes very large, as recently discussed in Ref. [109]. The effect of interference has been

shown to be constructive below the Higgs mass peak and destructive above. It has therefore a negligible effect on the total cross-section (1-2%) but it strongly biases the ZZ invariant-mass distribution. Moreover the interference has been computed only at LO while the signal is known at NNLO. In this analysis we follow the so-called “intermediate” approach proposed in Ref. [109] to estimate the uncertainty due to missing higher perturbative order on the interference. Given the signal at NNLO ($S_{NNLO} = S_{LO} \times K$) and the interference at LO (I), we can estimate the signal + interference as

$$S_{LO} \times K + I \times K' \quad (9.6)$$

where the ratio (K') is between NNLO Higgs-diagrams with only gg initial state and LO Higgs-diagrams:

$$K = \frac{S_{NNLO}(gg \rightarrow Hg + qg \rightarrow Hq + qq \rightarrow Hg)}{S_{LO}(gg \rightarrow H)} = K' + K^{rest} \quad (9.7)$$

$$K' = \frac{S_{NNLO}(gg \rightarrow Hg)}{S_{LO}(gg \rightarrow H)} \quad (9.8)$$

Figure 9.3 shows the effect of the CPS and interference corrections on the $H \rightarrow ZZ$ invariant-mass distribution.

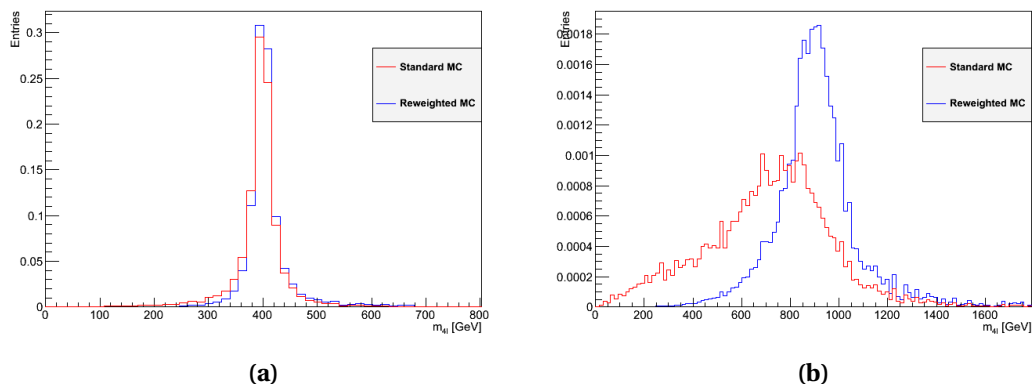


Figure 9.3: The four leptons invariant mass distribution at generator level before and after the CPS + interference corrections for an Higgs mass of 400 GeV (left) and 900 GeV (right).

In addition to the uncertainties caused by missing terms in the perturbative QCD expansion and those from parton distribution functions, there are other electroweak corrections that play important role at high Higgs mass, such as corrections in the Higgs production (affect cross-section), corrections for complex pole (affect lineshape) and uncertainty for the decay (affect lineshape)

For Higgs masses larger than the top mass (m_t), an additional uncertainty should be considered: the computation of the NNLO Higgs cross-section as well as the generation of the NLO Monte Carlo samples used in this analysis are done in the approximation of an effective theory

with $m_t \rightarrow \infty$ (HQ approximation). This approximation breaks down at large Higgs mass but it is expected to have negligible effect on the total cross-section and on the Higgs lineshape. The effect of the HQ approximation and of the EW corrections in the Higgs production, previously mentioned, are studied at NLO with a new version of POWHEG which implements CPS, EW production and HQ corrections.

While the effect of the EW corrections and of the interference on the Higgs lineshape may be different in gluon-gluon production and Vector Boson Fusion (VBF), in the present inclusive analysis we use the $gg \rightarrow H$ lineshape to describe both the cases since the gluon-gluon contribution dominates in most of the Higgs mass spectrum.

9.2.2 Evaluation of the High-mass Corrections Systematic Uncertainties

The illustration of the uncertainties on the shape given by the high mass corrections are shown on Fig. 9.4. In order to propagate this systematic effect on the UL and p-value calculations, we refit the signal shape function with the two alternative hypotheses proposed in Ref. [109]. In this fit only the Γ parameter of the Breit-Wigner function is left floating. In this way we propagate the uncertainty on the high-mass corrected shapes to the parameter representing the width of our theoretical PDF. The systematic uncertainty on Γ is taken as the largest variation between the fits for two different hypothesis. Performing this calculation for all the mass points, we measure the systematic effect on Γ to be between 3% and 5%. Being conservative, we choose a systematic of 5% for all Higgs mass hypothesis.

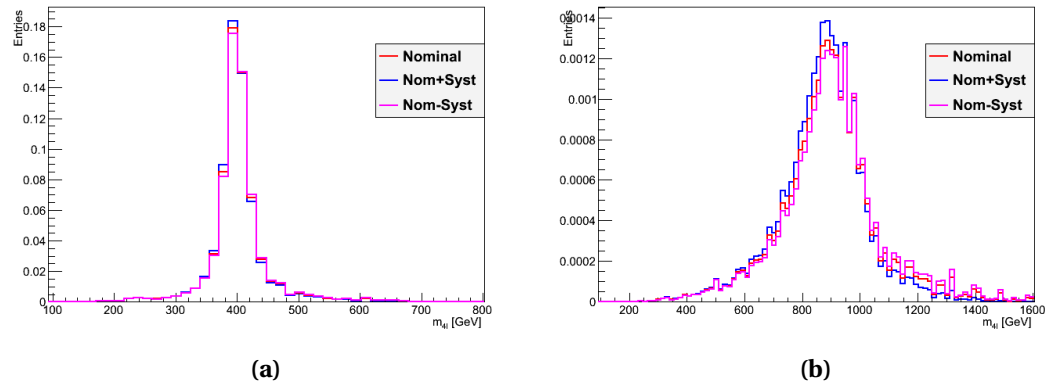


Figure 9.4: The reconstructed four-lepton invariant mass for a 400 (900) GeV invariant mass Higgs boson after the CPS + interference corrections. The alternative shapes to describe the lineshape uncertainty are also shown.

9.2.3 High Higgs Boson Mass Signal Model

For the high mass range, after the re-weighting described above, instead of using the typical form used for low mass in Eq. (9.4) we use a modified version of the Breit-Wigner with the

following form:

$$RBW(m_{4l}|m_H) = \frac{m_{4l}}{(m_{4l}^2 - m_H^2)^2 + m_{4l}^2 \cdot \Gamma^2(m_{4l})} \quad (9.9)$$

where the Γ parameter left floating in the fit. This means that the Γ has lost its full meaning as physical Higgs boson width but has allowed to get a good fit.

We then use a convolution of this high mass Breit-Wigner with the Double Crystal Ball in the same way as in the low mass model. The parametrization is then achieved by performing a constrained likelihood fit to the signal Monte Carlo events assuming that the physical width of the Higgs for $m_H > 400$ GeV is larger than the experimental resolution, regulated by σ_{DCB} . For illustration, we show the example fits for two of the high Higgs mass points in Fig. 9.5 for simulation at 8 TeV. Afterwards, following the same procedure used for the low mass model, we obtain a Higgs boson mass dependent parameterization of the signal interpolated with a polynomial function.

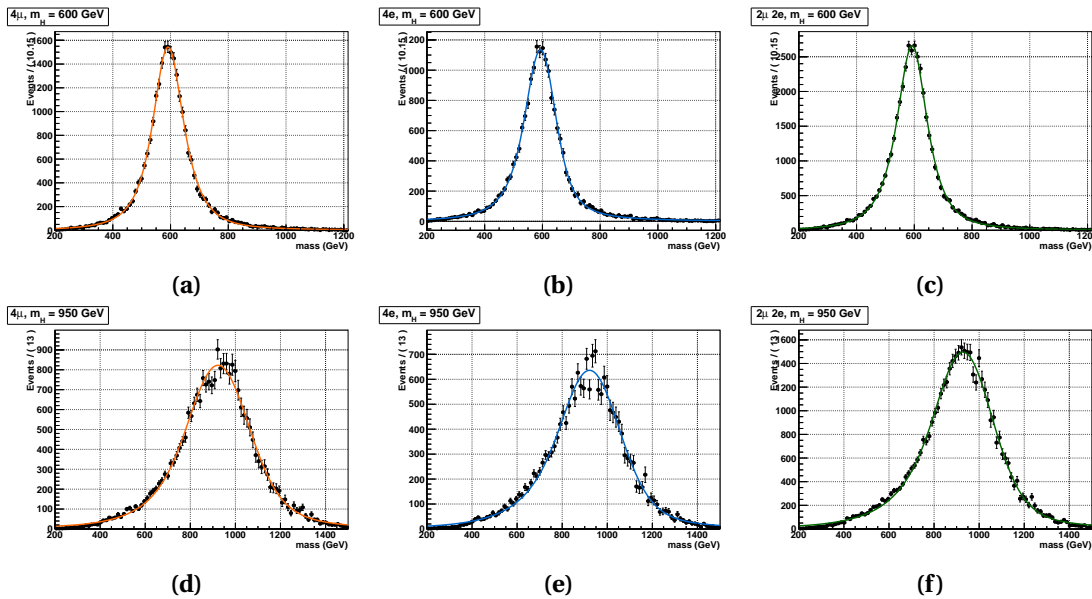


Figure 9.5: Parametrization $f(m_{4l}|m_H)$ for the Higgs boson mass at the reconstruction level after the full lepton and event selections. The distributions obtained from 8 TeV MC samples are fitted with the model described in the text for 4μ (left), $4e$ (center) and $2\mu2e$ (right) events. The fits are shown for 600 GeV (top) and 950 GeV (bottom) Higgs boson mass hypothesis.

9.3 Signal Model Uncertainties

At this stage, it is important to account for all the systematic uncertainties affecting signal model. The uncertainties on the signal model can be factorized into those affecting the overall event yield, i.e. normalization and those affecting the shape of signal distributions.

The uncertainties affecting the overall event yields are:

- Theoretical total cross-section uncertainties;
- Theoretical uncertainties on the $H \rightarrow ZZ$ branching fraction;
- Theoretical uncertainties on signal event acceptance within kinematic cuts on leptons;
- Instrumental uncertainties on data-to-MC corrections $C(m_H)$.

The uncertainties affecting the shape of event distributions:

- Theoretical uncertainties on the distribution $\mathcal{P}(m_{H^*} | m_H)$, Eq. (9.4);
- Instrumental uncertainties on the detector response function $CB(m_{4\ell} | m_{H^*})$, Eq. (9.5);
- Theoretical uncertainties on KD distribution $\mathcal{P}(KD | m_H)$ to be introduced in Sec. 12;
- Instrumental uncertainties on the KD distributions, presently assumed negligible.

In the next sections these systematic effects will be presented, except for uncertainties on KD distributions, which is explained in detail in Sec. 12.

9.3.1 Theoretical Uncertainties

Total Signal Cross-section and Branching Ratio $BR(H \rightarrow 4l)$

Systematic errors on the signal total cross-section for each production mechanism and for all Higgs boson masses are fully defined in the report by *LHC Higgs Cross Section Working Group* in Ref. [110]. They come from PDF+ α_s systematic errors and from theoretical uncertainties evaluated by varying QCD renormalization and factorization scales μ_R and μ_F . The PDF+ α_s and QCD scale uncertainties are to be treated as uncorrelated, while 7 and 8 TeV uncertainties are assumed to be 100% correlated.

The uncertainty on $BR(H \rightarrow 4l)$ is taken to be 2% [111] and assumed to be m_H -independent.

Signal Acceptance

The lepton kinematic cuts restrict the signal acceptance to $\mathcal{A} \sim 0.6 - 0.9$ depending on the Higgs boson mass [105]. The acceptance uncertainties $\delta\mathcal{A}/\mathcal{A}$ are evaluated using MCFM

generator [112]. For calculations, we used the $pp \rightarrow H \rightarrow ZZ \rightarrow ee\mu\mu$ process at 7 TeV with fiducial cuts for leptons similar to those in the analysis:

- $m_{ee} > 12$ GeV, $m_{\mu\mu} > 12$ GeV,
- $p_T > 7$ GeV and $|\eta| < 2.5$ for electrons,
- $p_T > 5$ GeV and $|\eta| < 2.4$ for muons.

The minimal jet-lepton and lepton-lepton ΔR_{min} -distances were set to zero. The cross-sections are calculated in an inclusive way for any number of jets found at Next-to-Leading-Order (NLO). Again, it is assumed that uncertainties on acceptance at 8 TeV are the same as at 7 TeV and are 100% correlated.

The sensitivity of the signal acceptance to the renormalization and factorization scales is evaluated by varying them by a factor of two up and down. The results are shown in Table 9.1. We find that the acceptance errors are very small (0.1-0.2%) and, therefore, can be neglected.

Table 9.1: Signal acceptance \mathcal{A} for different QCD scales.

Higgs boson mass m_H (GeV)	120	200	400	500	600
Default \mathcal{A}_0 ($\mu_R = \mu_F = m_H/2$)	0.5421	0.7318	0.8120	0.8421	0.8637
\mathcal{A}_{up} ($\mu_R = \mu_F = m_H$)	0.5417	0.7317	0.8128	0.8427	0.8644
\mathcal{A}_{down} ($\mu_R = \mu_F = m_H/4$)	0.5430	0.7328	0.8119	0.8418	0.8632
$\delta\mathcal{A}/\mathcal{A} = \max \Delta\mathcal{A} /\mathcal{A}_0$	0.17%	0.14%	0.11%	0.07%	0.08%

For estimation of the PDF+ α_s systematic errors, we use the PDF4LHC prescription [113]. The three PDF sets used are CT10 [114], MSTW08 [115], NNPDF [116]. The results, the envelope containing all variations for the three sets of PDFs, is shown in Fig. 9.6. We assign a 2% mass-independent error to account for these uncertainties.

Following the general recommendation from Ref. [61], we treat the acceptance and total cross-section uncertainties as uncorrelated. The exact same error is assigned to all production mechanisms and 100% correlation is assumed.

The Higgs p_T distribution in the POWHEG $gg \rightarrow H$ MC is harder than what the most recent NLO+NNLO calculations predict (HqT [117]). Therefore, the $H \rightarrow 4\ell$ leptons in the POWHEG sample get an additional boost and the signal acceptance may be somewhat overestimated. To estimate the scale of the effect, re-weighting of Higgs boson events $H \rightarrow 2e2\mu$ in MC has been performed to make their p_T spectrum match the one obtained in HqT . After that, the change in the signal acceptance arising from the lepton kinematic cuts used in the analysis is evaluated. The relative change in the $H \rightarrow 4\ell$ acceptance is <2%. Since the change is so small, we assign an additional systematic error on acceptance depending on the Higgs boson mass rather than correcting for it.

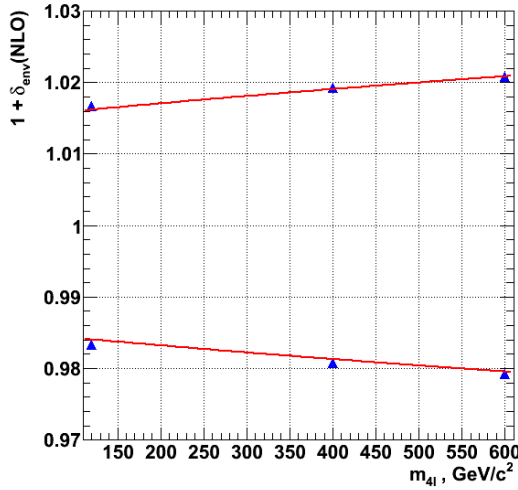


Figure 9.6: PDF+ α_s uncertainties for $pp \rightarrow H \rightarrow ZZ \rightarrow 4\ell$ vs. Higgs boson mass at $\sqrt{s} = 7$ TeV. The points are evaluated uncertainties. The curves are the fit.

Theoretical Uncertainties on the Distribution $\mathcal{P}_1(m_{H^*}|m_H)$

When the Higgs boson total width Γ_H becomes very large, there are additional uncertainties related to the theoretical treatment of running Higgs width and due to non-negligible effects of the signal-background interference between $gg \rightarrow H \rightarrow ZZ$ and $gg \rightarrow ZZ$. Following the prescription given in Ref. [108], we add one more uncertainty on the Higgs boson cross-sections for all sub-channels, $150\% \times (m_H/\text{TeV})^3$, covering all systematic errors specific to high mass Higgs bosons.

9.3.2 Data-to-MC Scale Factors from Efficiencies

The full determination of the differential yield for the signal model in Eq. (9.1) can be achieved by rewriting in the form:

$$\frac{dN}{dm_{4\ell}} = C(m_H) \cdot N^{MC}(m_H) \cdot F_H(m_{4\ell} | m_H). \quad (9.10)$$

where $N^{MC}(m_H)$ is the event yield predicted from the MC used, $C(m_H)$ is the cumulative data-to-MC correction factor for all per-lepton efficiencies from trigger, reconstruction, identification, impact parameter, and isolation selection. In this section the method to determine event scale factors arising from data-to-simulation discrepancies together with adhered uncertainties is presented.

All four leptons in the signal $H \rightarrow ZZ^{(*)} \rightarrow 4\ell$ are prompt. This means that their trigger, reconstruction, identification, impact parameter and isolation selection efficiencies can be in principle evaluated directly from data using the standard tag-and-probe (T&P) method applied generally to $Z \rightarrow \ell\ell$ events. The results of these measurements are reported in Ch. 7. In order to propagate the measured per-lepton efficiencies and their errors, two methods were used, giving comparable results.

Per-lepton Method

The observed data-to-MC discrepancy in the lepton selection chain efficiencies measured with the data-driven techniques described in Ch. 7 are used to correct the simulation on an per-event basis. The uncertainties on this efficiency correction are propagated independently to obtain a systematic uncertainty on the final yields for signals and ZZ background.

In practice, the per-lepton data-to-MC ratios are multiplied to give weight to an individual event. To obtain systematic errors, five hundred toy MC experiments are ran for each event in MC sample. In each experiment, we pick up a value from a Gaussian distribution with mean given by the central value of the data-to-MC ratio and the width given by the associated error. The systematic uncertainty is taken as the RMS of the distribution of the total number of expected events in the five hundred toys. Figures 9.7 and 9.8 show the obtained systematic errors for the 7 and 8 TeV analysis.

In addition, we add in quadrature a 1.5% uncertainty related to trigger. The errors related to the momentum energy scale and resolution will be discussed later in this section.

Per-event Method

This method uses the same efficiencies measured in data and simulation using the T&P method in a grid of (p_T, η) -bins given already in Ch. 7. To obtain per-event correction factors $C(m_H)$, we propagate the measured per-lepton correction factors $c(p_T, \eta)$ using the method

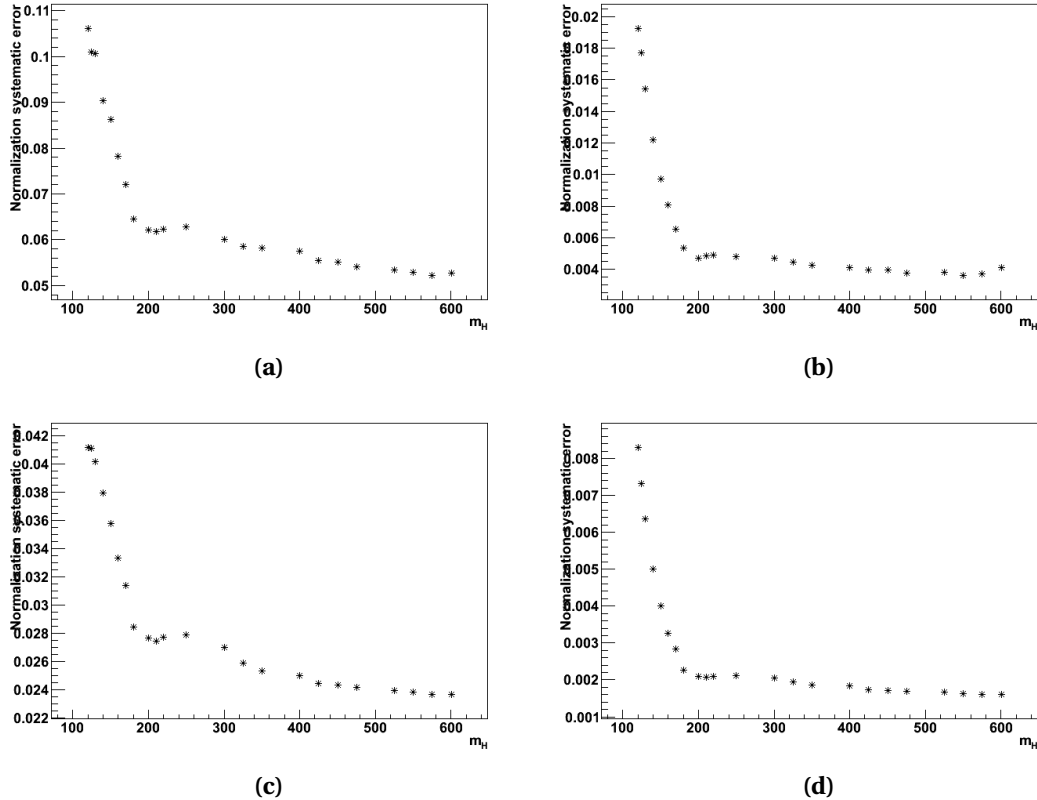


Figure 9.7: Instrumental Uncertainties related to data/MC differences in efficiencies in reconstruction, identification, isolation and $|SIP|$ as a function of m_H , for (a) $4e$ channel, (b) 4μ channel (c) $2e2\mu$ channel (electron only uncertainties), (d) $2e2\mu$ channel (muon only uncertainties). Results are for 7 TeV data.

of Lepton Kinematic Templates (LKT). First, using the $gg \rightarrow H \rightarrow 4\ell$ MC, we prepare a table listing (p_T^i, η^i) of four signal leptons ($i = 1, 2, 3, 4$) in each MC event. Then, we ran over this list multiple times, and give each event a weight

$$C = \prod_i \tilde{c}(p_T^i, \eta^i), \quad (9.11)$$

where \tilde{c} are drawn as random numbers from the Gaussian pdf 's with mean and sigma corresponding to the correction factors and their uncertainties as measured with the T&P method for (p_T^i, η^i) -bins. We properly take into account the uncorrelation nature of bin-by-bin statistical uncertainties while we also preserve the correlation among leptons which belong to the same (p_T^i, η^i) -bin in a event. The average \bar{C} is the data-to-MC correction.

To obtain the statistical uncertainties on the per-event correction factors $\delta C(m_H)$, we ran over again the list multiple times, but now the \tilde{c} are drawn as random numbers from the Gaussian

9.3. Signal Model Uncertainties

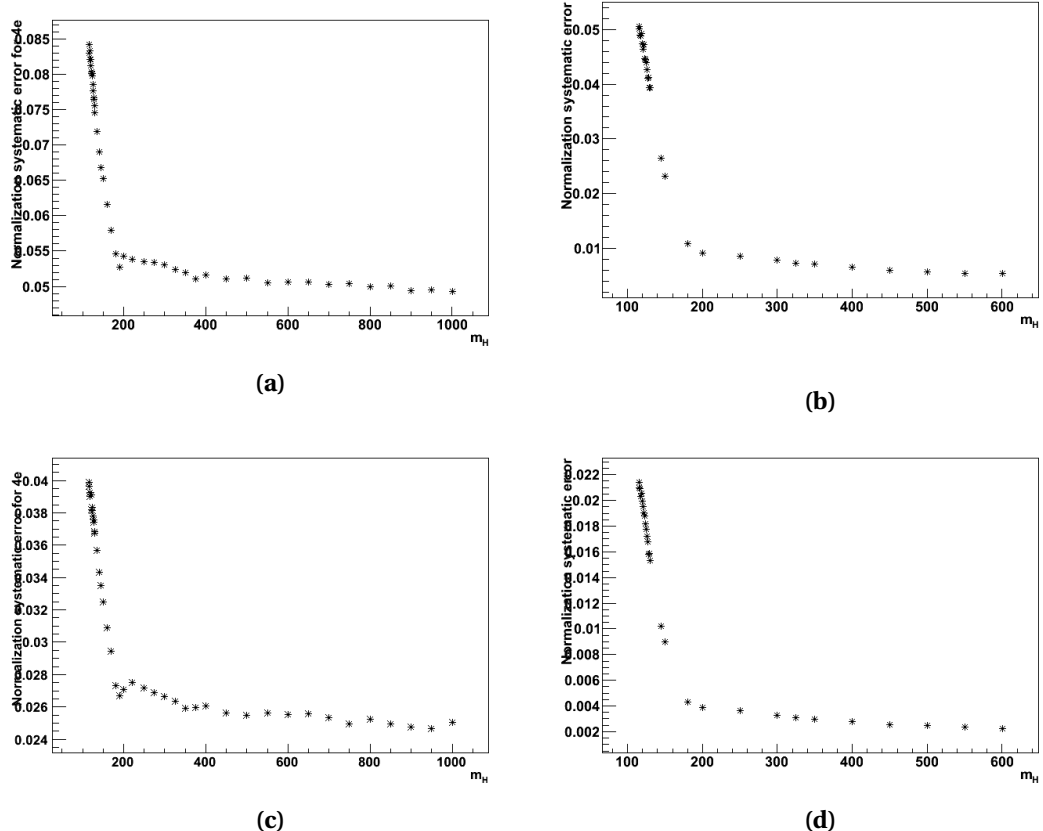


Figure 9.8: Instrumental Uncertainties related to data/MC differences in efficiencies in reconstruction, identification, isolation and $|SIP|$ as a function of m_H , for (a) 4e channel, (b) 4 μ channel (c) 2e2 μ channel (electron only uncertainties), (d) 2e2 μ channel (muon only uncertainties). Results are for 8 TeV data.

pdf's with mean = 1 and sigma corresponding to the relative uncertainties as measured with the T&P method for (p_T^i, η^i) -bins. The $\pm 1\sigma$ spread δC is the correction factor uncertainty defined by the statistical precision of the T&P measurements. The method can be easily adopted to evaluate correction factors and their uncertainties for the di-lepton triggers as well.

The uncertainties on the correction factors in the statistical analysis are taken as mass independent and are taken as the largest error from the entire m_H mass range. Finally, these mass-dependent corrections are used to rescale the MC predictions for the Higgs boson event yields.

9.3.3 Four-lepton mass Scale and Resolution

Higgs boson candidates are built from leptons. The quality of the momentum measurement of both electrons and muons can substantially vary depending on the leptons characteristics. For electrons, the resolution is dominated by the fluctuations of the measured energy due to bremsstrahlung in the tracker material. For muons the resolution is mainly dependant of the muon p_T and η .

Therefore this causes the 4ℓ mass resolution to vary considerably, by as much as a factor of 2-3. Therefore, mixing together events with well and poorly measured 4ℓ masses weaken the Higgs search sensitivity. In this section, an advanced analysis technique that takes into account mass resolutions assessed on the per-event basis is introduced.

The gain in sensitivity is not expected to be as much as in $H \rightarrow \gamma\gamma$ search, where events with better $m_{\gamma\gamma}$ resolution have smaller backgrounds. In the case of the $H \rightarrow ZZ^{(*)} \rightarrow 4\ell$ analysis, the $m_{4\ell}$ observable does not help in improving the signal-to-background ratio. The whole gain comes from the proper accounting for the signal mass resolutions in individual events.

Scale and Resolution via $Z \rightarrow \ell\ell$

To validate the level of accuracy with which we know the absolute mass scale and resolution, we use $Z \rightarrow \ell\ell$ events. In muon case, we also use the J/ Ψ and Y resonances as source of low p_T muons. The events are separated into the relevant categories according and the dilepton mass distributions in each category are fitted to extract the mass scale and resolution. As the signal lineshape for the $H \rightarrow ZZ^{(*)} \rightarrow 4\ell$ search is extracted from simulated events, only the relative difference between data and simulation in the momentum scale and resolution is relevant.

Electrons The $Z \rightarrow ee$ invariant mass distributions are built in different bins of η and different quality categories to separate well and badly measured electrons using the electron classification. This classification, used for the evaluation of the E-p combined momentum, describes the amount of energy radiated by bremsstrahlung and the quality of reconstruction, thus separating different momentum resolutions. Events are looked at in low and high pile-up regimes. The distributions are fitted with a Breit-Wigner (fixed parameters) convoluted with a Crystal Ball (free parameters). Figures 9.9 and 9.10 show the obtained results in 2012 data compared to expectations from simulation.

Systematic uncertainties on electron energy scale is estimated as the maximum deviation between data and MC of fitted $Z \rightarrow ee$ peak position in different categories of pseudorapidity and electron classes. Generally, the agreement of data to simulation is within 0.4%, reaching 0.1% for electrons in the ECAL barrel, and up to 0.4% for electrons in the ECAL endcaps.

The dependency of the electron momentum scale with respect to pile-up obtained by using

9.3. Signal Model Uncertainties

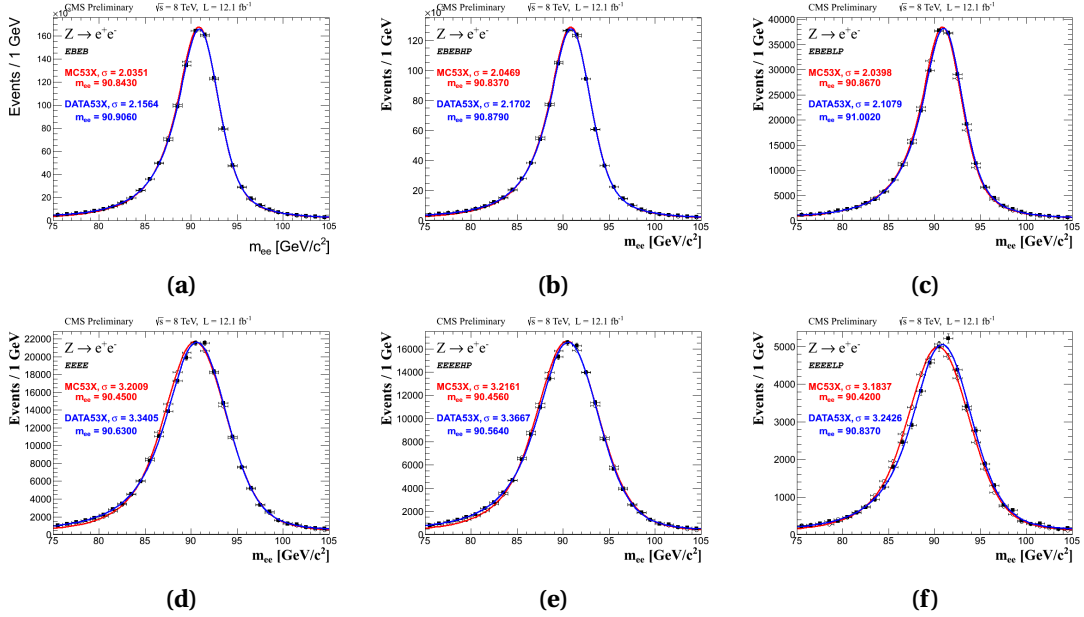


Figure 9.9: $Z \rightarrow ee$ events with: both electrons in ECAL barrel (a) and for high (b) and low (c) pile-up regime, both electrons in ECAL endcaps (d) and for high (e) and low (f) pile-up regime. Black points are 2012 data with a fit superimposed (blue line). Open square is MC with a fit superimposed (red line).

the above procedure in vertex multiplicity bins is shown on Fig. 9.11. No significant pile-up dependent variation of the Z peak and good agreement between data and MC is observed.

For the resolution, a similar strategy has been adopted, comparing the fitted σ_{CB} between data and MC. The largest relative difference amounts to 22% which we take as systematics on the resolution for 2012 data.

Due to kinematic properties of leptons from Z decays, the above consideration mainly checks the scale for electrons with relatively high momenta. An additional systematic in the momentum estimation appears when propagating the electron calibration estimated at the Z scale to the scale typical of the electrons of an Higgs with mass $m_H \approx 125$ GeV. These further data-to-simulation discrepancies may be due to the insufficient description of the material budget in front of the ECAL or due to insufficient detector geometry description. Figure 9.12 shows that there is a residual shift when going to lower p_T values, while the shift is negligible around the point where the calibration was performed. The maximum drift is $\approx 0.4\%$ in the barrel and $\approx 0.9\%$ in the endcap for the 8 TeV data. To remain conservative, we take these values as systematic uncertainty.

The impact of this non linearity in data-to-MC is propagated to the 4-lepton mass scale applying the expected shift to the electrons in a Higgs MC sample with $m_H = 125$ GeV, and recomputing the invariant mass. The difference in the fitted mean between the nominal and the shifted distribution is taken as systematic uncertainty with values 0.2%(0.1%) for $4e(2e2\mu)$

Chapter 9: Signal Modelling and Uncertainties

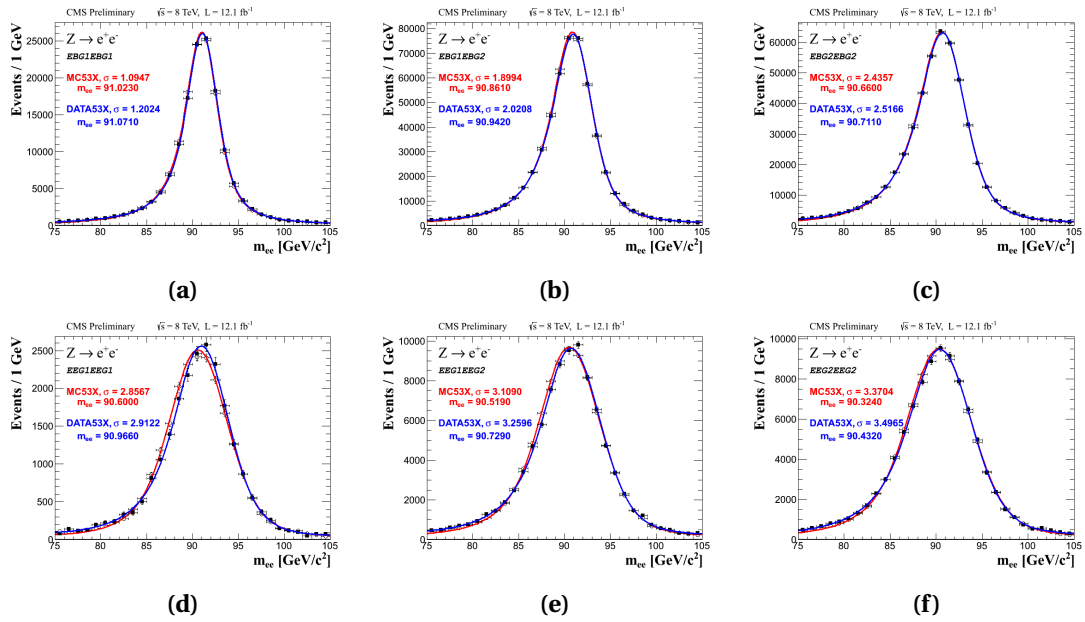


Figure 9.10: $Z \rightarrow ee$ events categorized regarding the electrons classification with both non-showering electrons (golden or big-brem) (a) (d), one non-showering, one showering (showering, bad-track or cracks) (b) (e), both showering electrons (c), (f). Top row shows the case with two electrons in ECAL barrel and bottom the case when both electrons are in ECAL endcaps. Black points are 2012 data with a fit superimposed (blue line). Open square is MC with a fit superimposed (red line).

final states. The effect on the invariant mass is marginal because the core of the distribution is dominated, for kinematic and efficiency reasons, by electrons of moderate p_T in the barrel region where the scale is more precise.

Muons The momentum scale and resolution after the calibration are validated in data using dimuons from J/Ψ , Υ and Z decays, to cover the full momentum range relevant for the $H \rightarrow ZZ^{(*)} \rightarrow 4\ell$ search. PF muons with $p_T > 5 \text{ GeV}$ are considered, and for Z decays the PF isolation and SIP3D criteria used in the ZZ analysis are also applied.

The full fitting procedure used to extract the muon scale and resolution is described in detail in Ref. [106].

The results for the momentum scale and resolution are shown in Fig. 9.13 and 9.13, respectively. In 2011, after the calibration the relative momentum scale is stable to within 0.1%, and the resolution within about 10%. The calibration for 2012 data is still preliminary, and slightly less accurate at low momentum than the 2011 one.

9.3. Signal Model Uncertainties

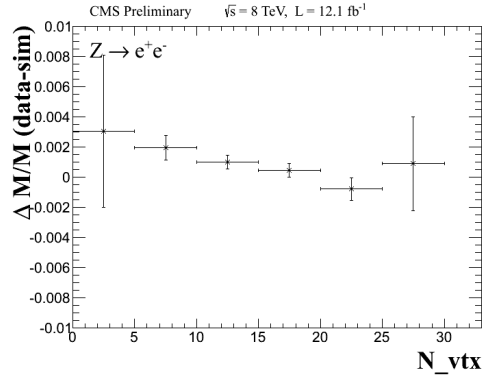


Figure 9.11: Electron momentum scale deviation from MC value as a function of the number of vertices (pile-up) normalized to the peak position from simulation.

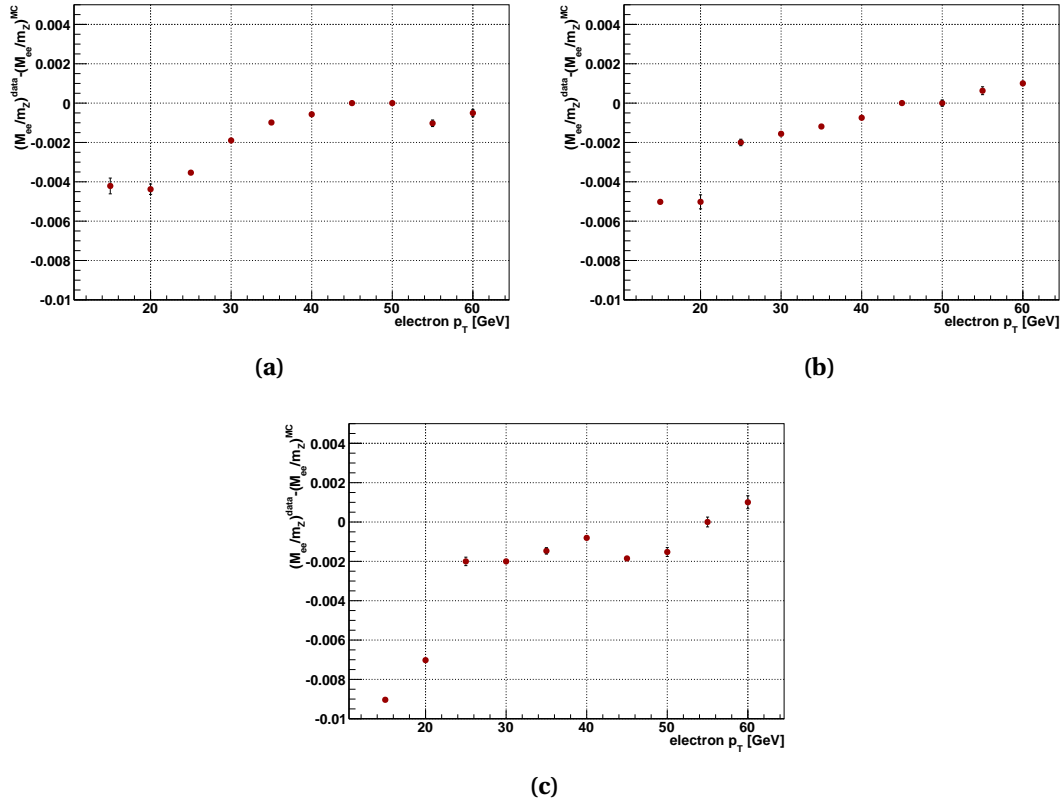


Figure 9.12: The residual data-to-MC shifts as a function of electron p_T for $|\eta| < 1$ (a), $1 < |\eta| < 1.479$ (b) and $|\eta| > 1.479$ (c) for 8 TeV data.

Chapter 9: Signal Modelling and Uncertainties

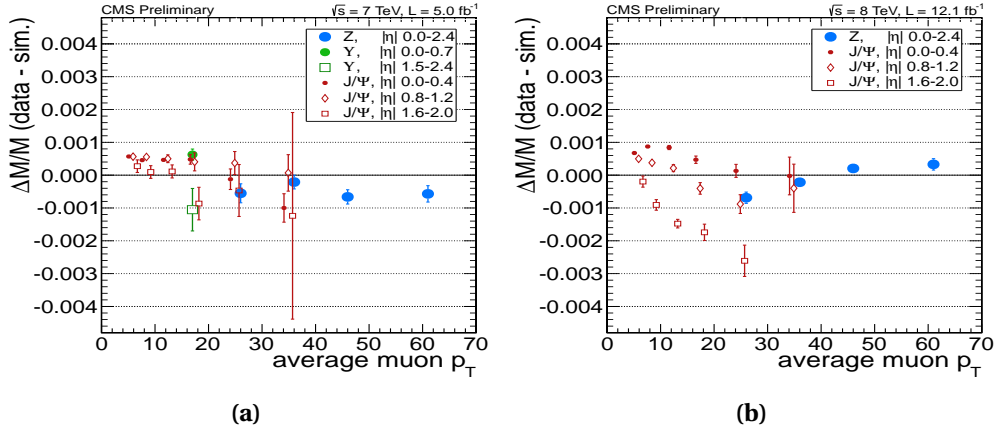


Figure 9.13: Relative difference between the dimuon mass scales in data and simulation extracted from J/Ψ , Y and Z decays, as function of the average muon p_T for the 2011 data (a) and 2012 data (b). Markers for different p_T bins are slightly displaced horizontally for legibility purposes. The uncertainties shown are statistical only.

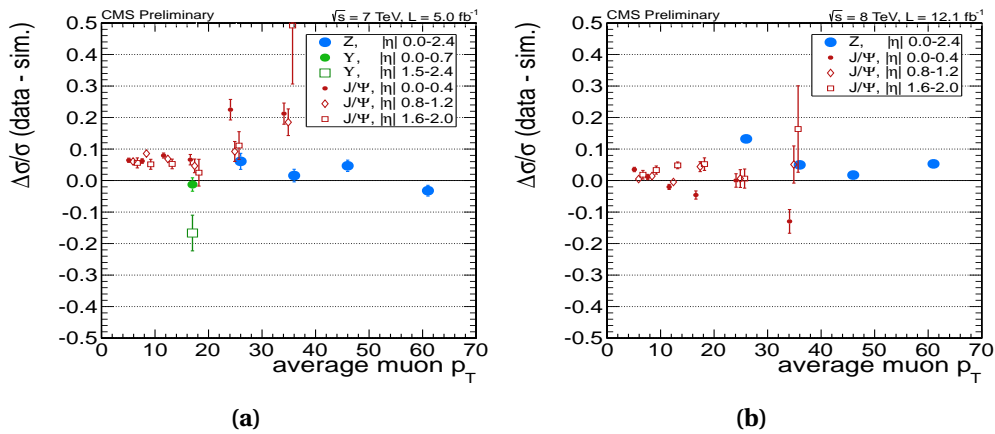


Figure 9.14: Relative difference between the dimuon mass resolutions in data and simulation extracted from J/Ψ , Y and Z decays, as function of the average muon p_T for the 2011 data (a) and 2012 data (b). Markers for different p_T bins are slightly displaced horizontally for legibility purposes. The uncertainties shown are statistical only.

Scale and resolution via $Z \rightarrow 4\ell$

The $Z \rightarrow 4\ell$ decays give a clean resonant peak in the four-lepton invariant mass distribution, which can be used as a standard candle in the context of the Higgs boson search in the $H \rightarrow ZZ \rightarrow 4\ell$ decay mode [118]. The number of events in the $Z \rightarrow 4\ell$ peak at $m_{4\ell} = m_Z$ is at least 5 times larger than the expected number of events for the SM Higgs boson with a mass near 125 GeV. Therefore, the $Z \rightarrow 4\ell$ peak can be used for a direct validation of our understanding of the four-lepton mass scale and the four-lepton mass resolution in the phase space just next to the Higgs boson four-lepton decays. To enhance the peak, the low end of the m_{Z2} -cut is relaxed from 12 to 4 GeV.

In the fit function, the background shape is taken from $pp \rightarrow ZZ \rightarrow 4\ell$ simulation, with the overall normalization floating in the fit. The signal shape is a convolution of the Breit-Wigner and Crystal Ball functions. The central value and width of the Breit-Wigner function are fixed at the Z boson mass m_Z and width Γ_Z [98]. The Crystal Ball parameters are free in the fit. One can split the events in the $Z \rightarrow 4\ell$ peak into those dominated by electron resolution ($Z \rightarrow 2e2\ell$) and those dominated by muon resolution ($Z \rightarrow 2\mu2\ell$), as is done with $Z \rightarrow 2\ell$ events, in order to better validate the scale and resolution for electrons and muons.

Figure 9.15 shows the fit of the four-lepton mass distribution for the observed $Z \rightarrow 4\ell$ events in 7 TeV and 8 TeV data, where we note that the average peak offset is 0.40 ± 0.28 GeV ($0.4 \pm 0.3\%$). Table 9.4 shows a summary of the scale and resolution parameters. These numbers can be used to validate the systematic errors of the four-lepton mass scale. With the current data, we see that the average four-lepton mass scale does not show any significant bias with the 70% statistical uncertainty and we can measure the average four-lepton mass resolution with about 25% statistical uncertainty. The statistical error on the measured scale is now nearly comparable to the systematics used in the statistical analysis.

Table 9.2: Fit results from GEN $Z \rightarrow 4\ell$ events in MC.

Final state	m_Z (GeV)	
	7 TeV	8 TeV
$2e2\ell$	91.252 ± 0.010	91.2461 ± 0.0097
$2\mu2\ell$	91.2536 ± 0.0068	91.2409 ± 0.0068

Table 9.3: Fit results from RECO $Z \rightarrow 4\ell$ events in MC.

Final state	δm (GeV)		σ (GeV)	
	7 TeV	8 TeV	7 TeV	8 TeV
$2e2\ell$	-0.41 ± 1.4	-0.1721 ± 0.026	1.85 ± 0.89	2.179 ± 0.031
$2\mu2\ell$	0.028 ± 0.011	0.062 ± 0.015	1.194 ± 0.016	1.306 ± 0.020

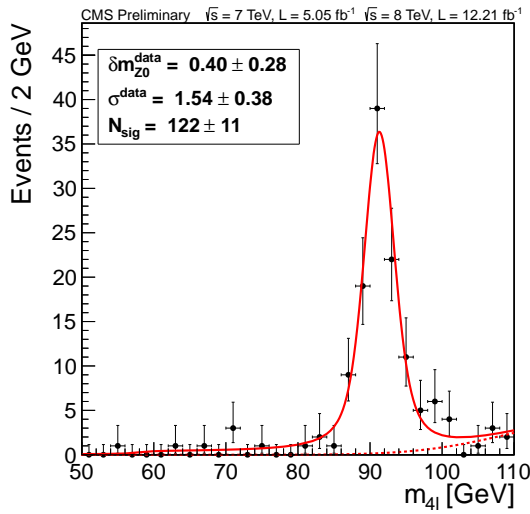


Figure 9.15: Four-lepton mass distribution in the 7 plus 8 TeV data. Data are shown with points. The three final states, $4e$, 4μ , and $2e2\mu$, are added together. The solid line represents a simultaneous fit for the background and Z boson peak (see text for details).

Table 9.4: Fit results from $Z \rightarrow 4\ell$ events in Data.

Final state	δm (GeV)		σ (GeV)	
	7 TeV	8 TeV	7 TeV	8 TeV
4ℓ	0.12 ± 0.42	0.53 ± 0.35	0.97 ± 0.47	1.88 ± 0.43
$2e2\ell$	-0.002 ± 0.071	0.2 ± 1.1	0.1 ± 1.1	2.5 ± 1.3
$2\mu2\ell$	0.08 ± 0.51	0.69 ± 0.38	1.11 ± 0.47	1.52 ± 0.51

9.4 Event-by-event Mass Errors

Per-event mass errors can be evaluated starting from the errors on the individual lepton momenta in different ways.

Individual lepton errors are computed on a per-event basis for muons using the full error matrix as obtained from the muon track fit, and using the estimated momentum error as obtained from the combination of the ECAL and tracker measurement for the electrons , neglecting the uncertainty on the track direction. For FSR photons, the PF parametrization is used.

Presently, there are two approaches for deriving mass errors. In the first approach the individual lepton momentum measurement errors are propagated to the 4ℓ mass error and to the Z_1 and Z_2 mass errors using an analytical error propagation including all correlations. In the alternative approach, the directional errors for muons are additionally neglected, and to propagate uncertainties of individual leptons to the uncertainty on the invariant mass, each δm corresponding to individual lepton momentum variation is calculated separately,

and then the measured resolution on the invariant mass of the four leptons is taken as the quadrature sum of the four individual δm :

$$m_0 = F(p_{T1}, \phi_1, \eta_1; p_{T2}, \phi_2, \eta_2; p_{T3}, \phi_3, \eta_3; p_{T4}, \phi_4, \eta_4) \quad (9.12)$$

$$\delta m_i = F(\dots; p_{Ti} + \delta p_{Ti}, \phi_i, \eta_i; \dots) - m_0 \quad (9.13)$$

$$\delta m = \sqrt{\delta m_1^2 + \delta m_2^2 + \delta m_3^2 + \delta m_4^2} \quad (9.14)$$

The two approaches give similar results with difference within 1%, nicely cross-checking each other [106]. It is also important to note that the statistical uncertainty on the mass resolution is currently 20%.

9.4.1 Calibration of Per-event Mass Errors

The per-event uncertainties on the lepton momenta obtained by the CMS Software (CMSSW) reconstruction need to be calibrated before they can be used to describe the expected four-lepton mass spectrum.

Single-lepton Calibration from Simulation

For electrons, this level of calibration using simulated events is not needed, as the energy regression and calibration procedures result in estimated energy uncertainties that correctly describe the core of the energy resolution.

In the case of muons, a first level of calibration is done at the per-muon level on the basis of simulated events, to take into account the improvement in the resolution in the endcaps from the momentum scale calibration and for the smearing introduced in the simulation to bring the resolution closer to the one observed in data. This correction is derived in fine bins of p_T and η by requiring the RMS of the pull distribution of $1/p$ to be equal to one; the $1/p$ variable is used instead of p_T since its distribution is more Gaussian. The calibration factor range between 0.7 and 1.5. The correction factors are larger for higher p_T muons, since the resolution in the low momentum region is dominated by multiple scattering, fairly well modelled in the simulation, and unaffected by the calibration which is mainly aimed at correcting for weak modes in the tracker alignment [106].

Corrections from Z and J/ Ψ Events

Studies on simulated signal events and on Z and J/ Ψ events in data show that a calibration of the Gaussian core of the per-lepton resolution is not sufficient to achieve a correct modelling of the invariant mass distribution from multiple leptons. Several factors contribute to this

discrepancy: the contribution of the non-Gaussian tails at single-lepton level to the Gaussian core of the multi-lepton resolution, the unrecovered final state radiation, and the presence of non-uniform energy scale biases as function of the lepton kinematic and quality.

A calibration factor for the estimated per-lepton momentum resolutions is therefore determined from fits to the invariant mass distribution of reconstructed Z decays in data and simulation, in several regions of pseudorapidity. In the case of muons, separate correction factors for low p_T are determined from J/ Ψ events. These correction factors are summarized in Tab. 9.5. Their values are in the 5 – 15% range for muons, and about twice as much for electrons, as expected given the larger non-Gaussian tails and the larger non-uniformity of the energy scale in the electron case.

muons, $p_T < 20$	2011 Data	2011 Sim.	2012 Data	2012 Sim.
$ \eta < 0.8$	1.00	1.06	1.03	1.08
$0.8 < \eta < 1.6$	0.98	1.07	1.01	1.08
$1.6 < \eta < 2.4$	0.96	1.07	0.99	1.06
muons, $p_T > 20$	2011 Data	2011 Sim.	2012 Data	2012 Sim.
$ \eta < 0.8$	1.09	1.16	1.03	1.07
$0.8 < \eta < 1.6$	1.16	1.03	1.07	1.05
$1.6 < \eta < 2.4$	0.95	0.99	1.09	1.03
electrons	2011 Data	2011 Sim.	2012 Data	2012 Sim.
$ \eta < 0.8$	1.25	1.27	1.30	1.27
$0.8 < \eta < 1.5$	1.16	1.11	1.24	1.22
$1.5 < \eta < 2.0$	1.30	1.30	1.22	1.17
$2.0 < \eta < 2.5$	1.16	1.24	1.14	1.13

Table 9.5: Correction factors for the per-lepton momentum uncertainties derived from Z and J/ Ψ events in data and simulations. For muons, these corrections are on top of the ones derived from pull distributions at the single lepton level. For electrons in 2012 data a slightly different binning in $|\eta|$ is used, [0.0, 1.0, 1.5, 1.9, 2.5], yielding a more uniform correction factor within each bin.

9.4.2 Expectations from Simulation

The error evaluation is checked on MC performing pull distributions. It has been demonstrated using toy MC experiments that if the errors are defined as the sigma of the Gaussian part of the lepton momentum distribution, the sigma of the Gaussian part of the pull should be 1, and if the errors are defined as the effective RMS it is the effective RMS of the pull distribution which should be one. So, if the errors are correctly evaluated the pull should have a sigma of 1 in the case of Gaussian distribution of momentum errors. In case of asymmetrical lepton momentum distributions, the RMS of the pull should be one with the errors defined as the RMS of the lepton momentum distributions.

The Figure 9.16 shows the MC pull distributions for the 4e channel, for electron momentum

and mass measurement of the Higgs boson at 125 GeV. This shows that the individual pull width is different from the Higgs pull width. This effect is understood to be mostly induced by the asymmetry of the electron momentum distribution. When combining asymmetrical distributions from individual leptons to form the $m_{4\ell}$ distribution, one sees that a pull on individual lepton with an effective RMS at 1 propagates into a pull for the $m_{4\ell}$ distribution with an effective RMS greater than 1. This means the errors on $m_{4\ell}$ are underestimated. This has been studied using toy MC experiments, the Figure 9.17 shows the effective RMS of the $m_{4\ell}$ pull distributions and of the lepton momentum pull distributions vs asymmetry, defined as the mean-mode of the relative lepton momentum distribution from toy MC experiments.

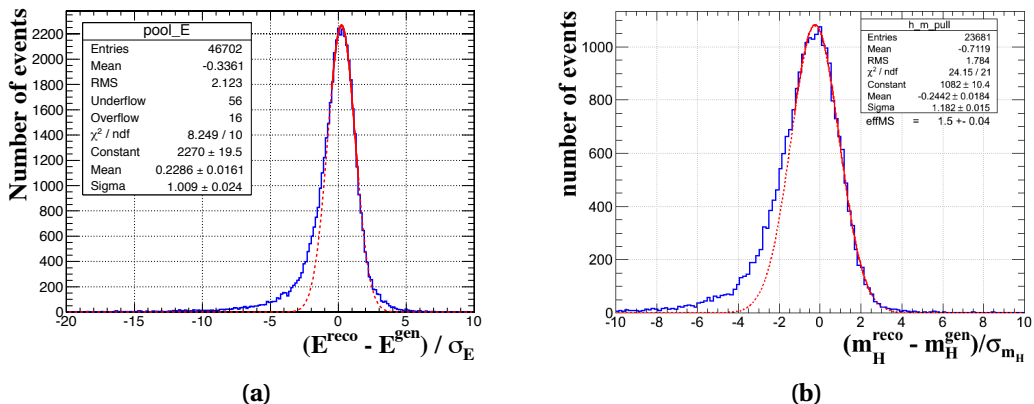


Figure 9.16: MC pull distributions for a Higgs mass of 125 GeV decaying in the $4e$ channel. (a) pull per electron (b) pull per Higgs event.

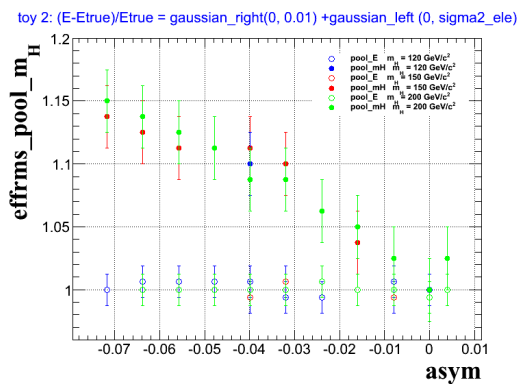


Figure 9.17: Effective RMS of the $m_{4\ell}$ pull distributions (plain dots) and of the lepton momentum (open dots) pull distributions vs asymmetry for different m_H .

The Figure 9.18 is shown only for illustration of the MC pull distributions for the (a) $4e$, (b) 4μ and (c) $2e2\mu$ final states as a function of the $m_{4\ell}$ reconstructed mass. In the case of electrons, where the momentum distributions show large asymmetries, the errors have been chosen as the effective RMS (effRMS). This choice implies that the effRMS of the pull for the case of electrons

Chapter 9: Signal Modelling and Uncertainties

is rather shown, together with the σ for comparison.

As will be shown in the following sections, applying the corrections to the single lepton errors, the pulls of 4-lepton mass distributions will be close to one, demonstrating a good control of the per-event errors.

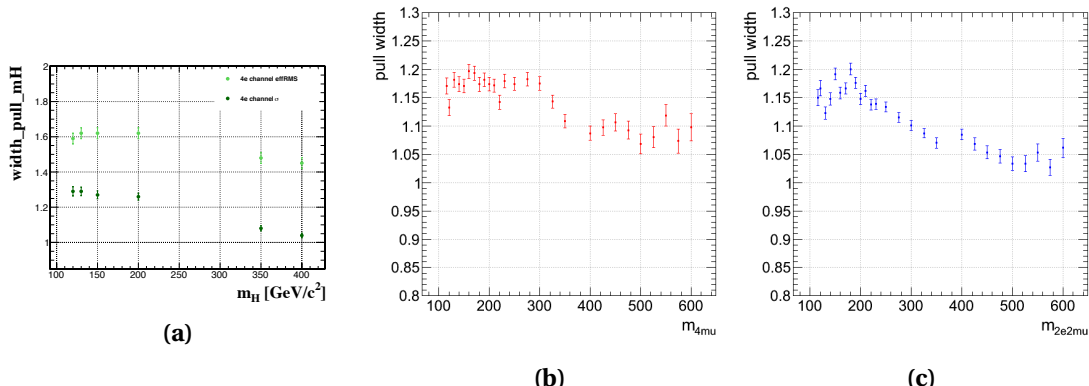


Figure 9.18: Widths of the MC pull distributions in function of the Higgs mass hypotheses for the (a) $4e$, (b) 4μ and (c) $2e2\mu$ final states.

Figure 9.19 shows the simulation based prediction for $m_{4\ell}$ mass resolution versus reconstructed mass for and $H \rightarrow ZZ \rightarrow 4\ell$ Monte Carlo samples. The uncertainties on lepton p_T used in calculations of $m_{4\ell}$ uncertainties are taken from simulation also.

9.4.3 Validation of Per-event Mass Errors from Data

To deduce the systematic error of the absolute mass scale and resolution, we use $Z \rightarrow \ell\ell$ events. The Z events are classified into ten categories based on what mass resolution we would predict. The corrections on per-lepton p_T error are propagated in to the dilepton mass error, and as a results, the predicted mass resolution. The Z mass shape of these events in each category is typically fit with the convoluted Breit-Wigner with fixed parameters from the PDG [98] and Crystal Ball with free parameters.

Figure 9.20 shows the observed relative mass peak shift and relative instrumental width for the di-electron (top) and di-muon (bottom) Z events¹. The dashed lines represent the systematic errors we can assign to our ability to predict absolute momentum scale and momentum resolution. Summarizing, we assign $\pm 0.4\% (\pm 0.3\%)$ uncertainty on absolute electron (muon) momentum scale and $\pm 20\%$ uncertainty on electron and muon momentum resolution.

To better asses the mass scale and resolution, all Z events are categorized according to leptons' pseudorapidity, i.e. barrel-barrel, barrel-endcap and endcap-endcap. In each category, we

¹The results presented in this section on the mass resolution are taken from Ref. [106] of which the author of this thesis is a co-editor.

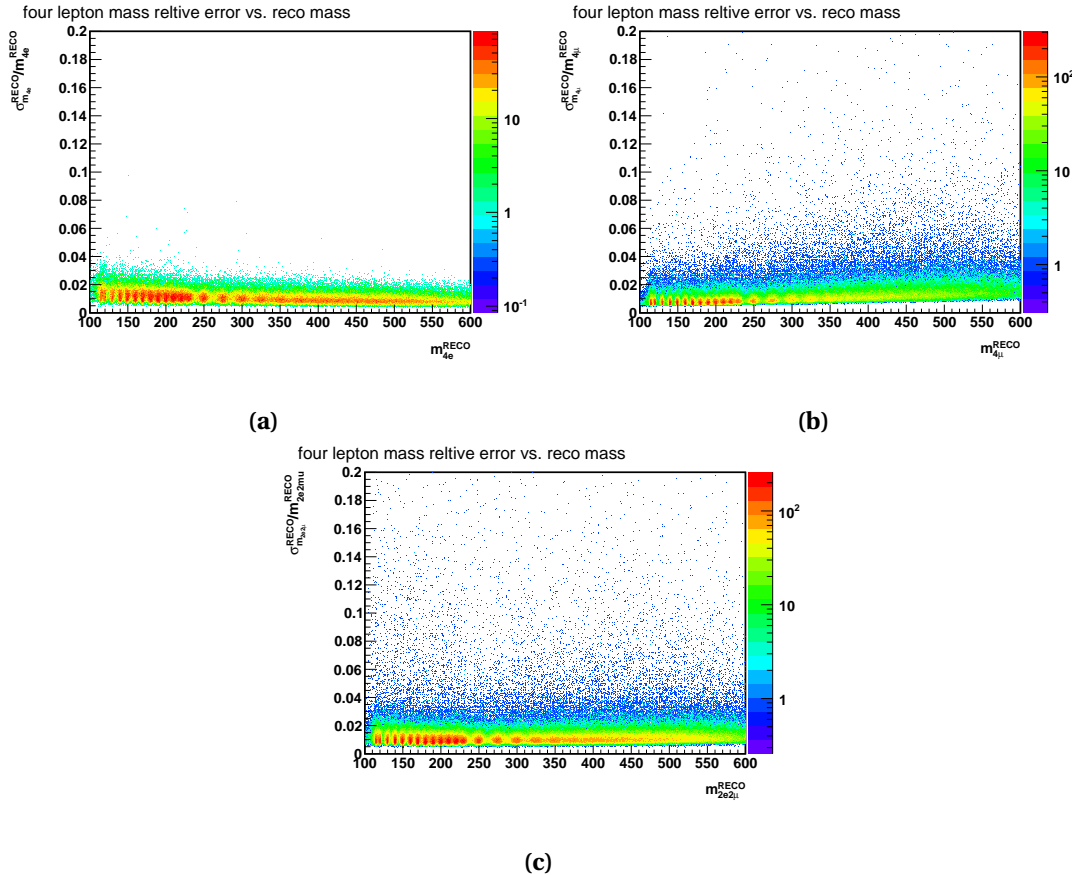


Figure 9.19: Expected Higgs boson mass resolutions versus Higgs candidates reconstructed mass in 4e (a), 4 μ (b) and 2e2 μ (c) final states.

then further divide them into sub categories according to the predicted mass resolution. In case of $Z \rightarrow ee$, we also categorize them according to both electrons' classification. The best category is made of two electrons both are in barrel and non-showering. The worst category is made of two electrons both are in endcap and showering. The rest of the Z events form the medium category. It has been noted in Ref. [106] that the mass resolution is within the systematics quoted above, except the worst category.

The agreement on the mass error distribution after lepton p_T corrections between the data and simulation has also been investigated for the four-lepton system in several control regions. Figure 9.22 demonstrates a good agreement between data and MC in the $Z \rightarrow 4\ell$, the $ZZ \rightarrow 4\ell$ and the $Z + X$ control regions for the 2e2mu final state, which is the best populated one.

Chapter 9: Signal Modelling and Uncertainties

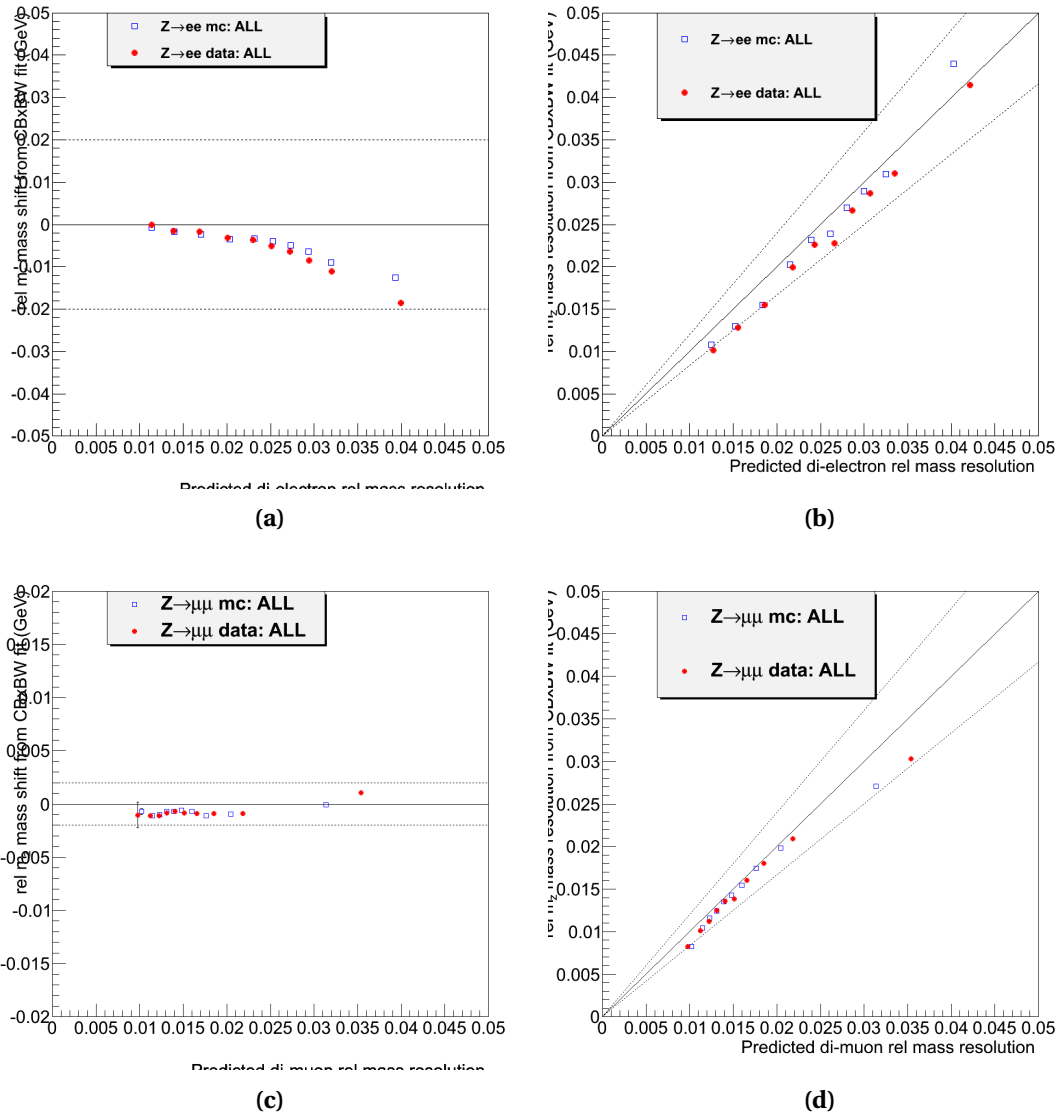


Figure 9.20: Plots validating our knowledge of the electron (top) and muon (bottom) mass scale (left) and resolution (right). The figures are taken from Ref. [106].

9.4. Event-by-event Mass Errors

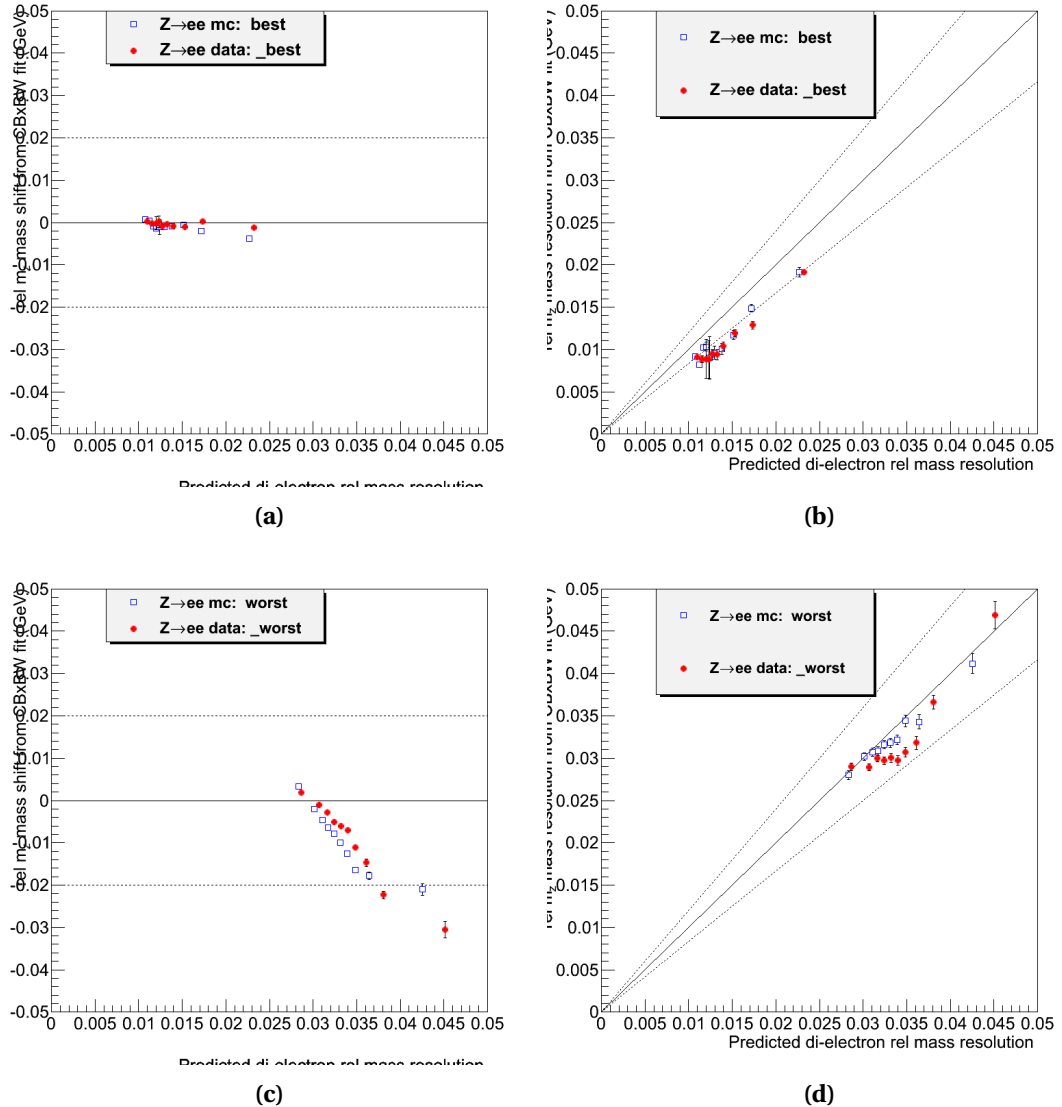


Figure 9.21: Plots validating our knowledge of the electron mass resolution for best (top) and worst (bottom) categories. Left for mass scale shift and right for mass resolution. The figures are taken from Ref. [106].

Chapter 9: Signal Modelling and Uncertainties

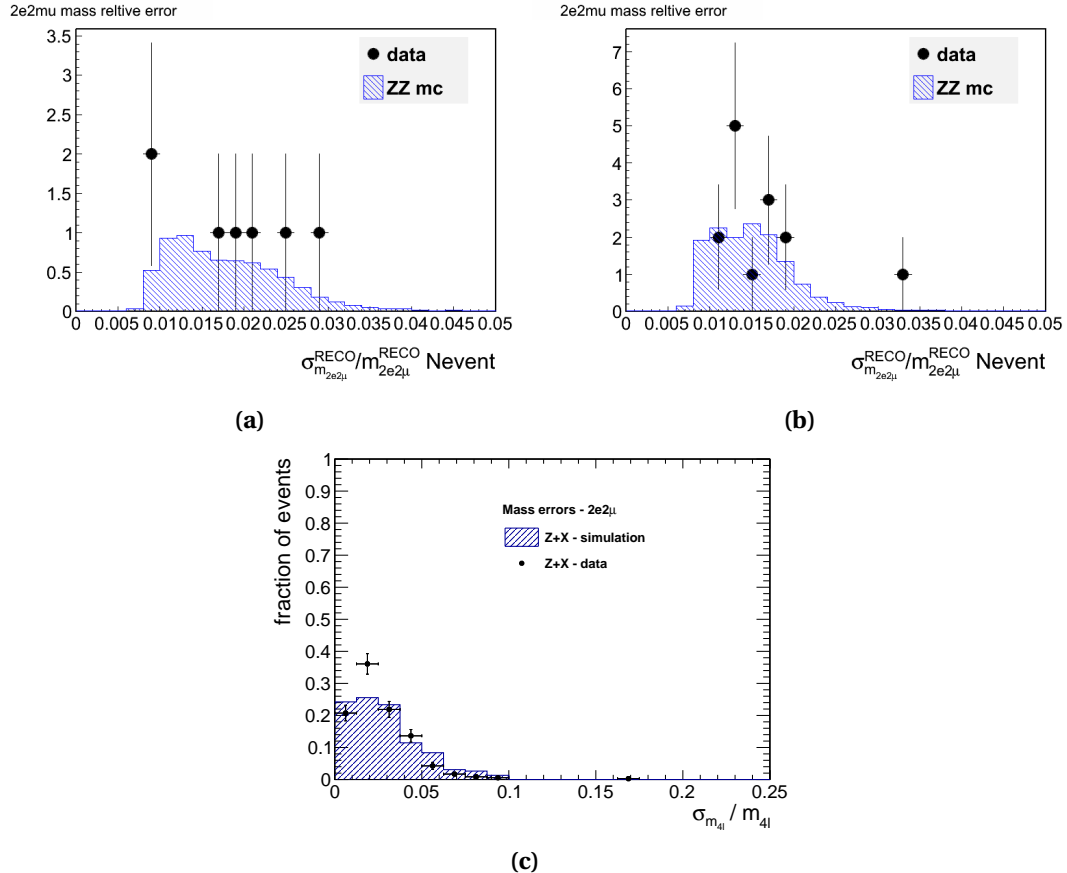


Figure 9.22: Relative mass error distribution for data and simulation in (a) $Z \rightarrow 4\ell$ region with $m_{4\ell}$ in [80–100 GeV], (b) $ZZ \rightarrow 4\ell$ region with $m_{4\ell}$ in [180–200 GeV] and (c) $Z + X$ control region with $m_{4\ell}$ in [110–130 GeV]. The distributions are shown for $2e2\mu$ final state and are taken from Ref. [106].

9.5 Event-by-event Mass Errors Model

Depending on the leptons characteristics, the quality of the momentum measurement of both electrons and muons can substantially vary, making the 4ℓ mass resolution vary broadly, by as much as a factor of 2-3. Thus, taking into account the per-event mass resolution could improve the search sensitivity and, particularly, the Higgs boson mass measurement. In this section, we introduce an advance analysis technique that basically weights events according to their measured mass resolutions. The gain in the expected Higgs boson mass measurement is 7% which will be shown in section 13.2 when discussing the statistical methodology of using the per-event mass error distributions. In addition, using per-event errors will allow for the best estimate of the error on the boson mass with the current data.

The mass error distributions of signal and ZZ are taken from simulation, and Z+jets from data control region. For ZZ and signal 4μ channel, the shapes are fitted with a functional form composed from *Landau* and *log-normal* distributions. In signal 4μ events, the relative mass error distributions remains the same across the whole mass window. For ZZ and signal $4e$ and $2e2\mu$ channels, the shapes are fitted with a functional form composed from *Landau* and *Gaussian*. Figure 9.23 illustrates the fits for 125 GeV Higgs signal (left) sample and ZZ background sample (right) in the mass range from 120 to 130 GeV in case of $2e2\mu$ final state.

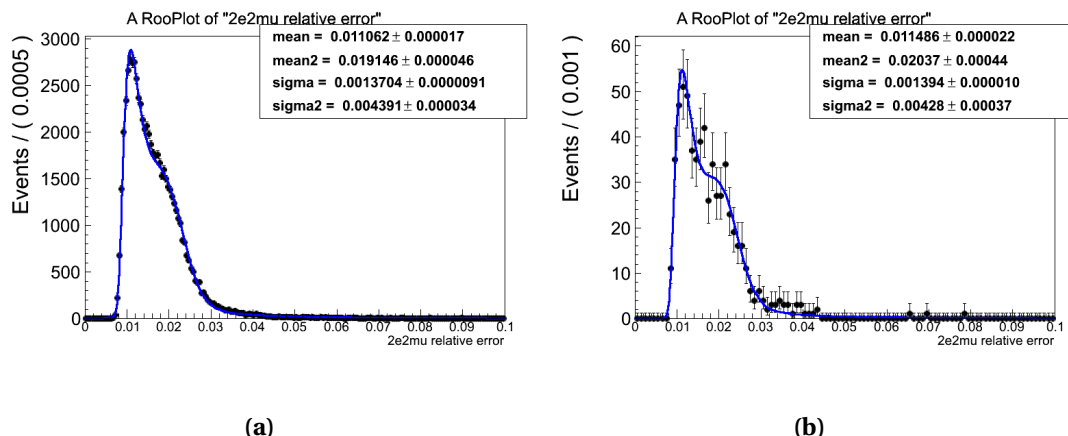


Figure 9.23: Four-lepton mass error distributions (points) and fits for signal (left) and ZZ background (right) in simulated samples for $2e2\mu$ final state. The figures are taken from Ref. [106].

To facilitate the statistical analysis, we parametrize the fit parameters by simple polynomials as function of the Higgs boson mass for signal and ZZ background separately. Figures 9.24 and 9.25 show this parametrization for $4e$ final channel.

For reducible backgrounds, we use control region with relaxed cuts to gain statistics. We compare the mass error distribution of the events in control region with ZZ background and Z+jets from simulated samples. In 4μ case, since Z+jets distribution is similar to ZZ one, we simply take ZZ fits for both. This is a consequence of the fact that real muons dominate the

Chapter 9: Signal Modelling and Uncertainties

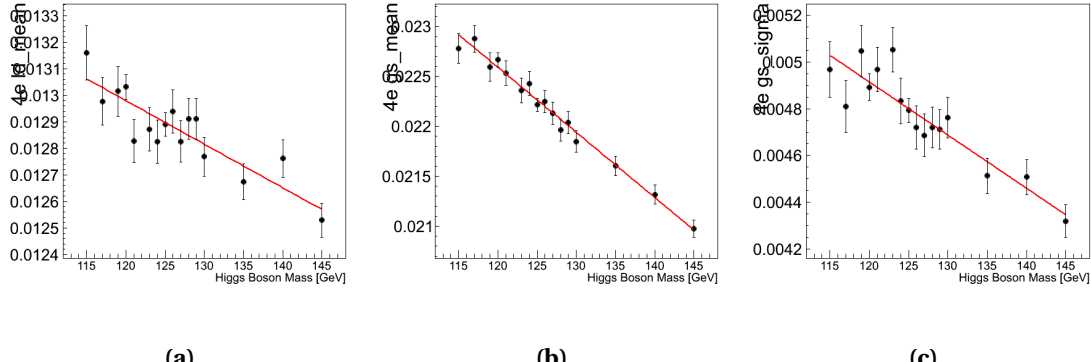


Figure 9.24: Polynomial mass dependent parameterization of the fits on $4e$ relative mass error distributions for signal: (a) Landau mean, (b) Gaussian mean and (c) Gaussian sigma. The figures are taken from Ref. [106].

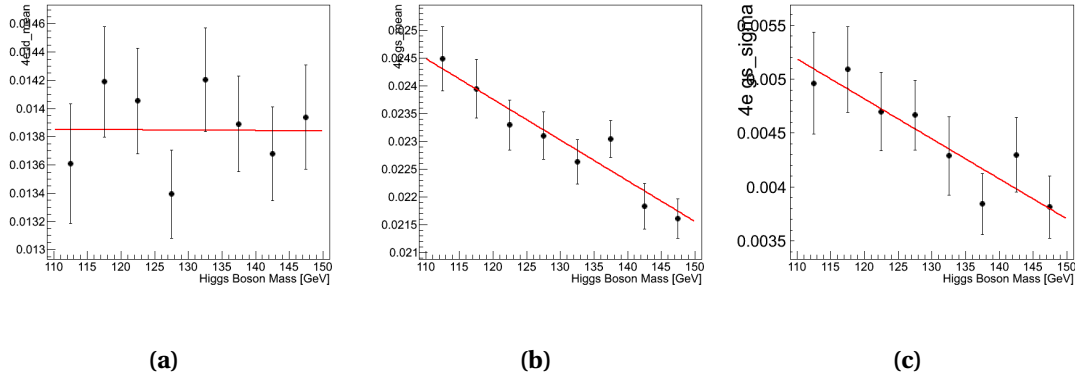


Figure 9.25: Polynomial mass dependent parameterization of the fits on $4e$ relative mass error distributions for ZZ background. (a) Landau mean, (b) Gaussian mean and (c) Gaussian sigma. The figures are taken from Ref. [106].

reducible 4μ background. In the final states involving electrons, the main contribution comes from jets faking electrons which have degraded resolution. The Z+jets $4e$ and $2e2\mu$ distributions are again fitted with a PDF composed by Landau and Gaussian. Since the control region statistics doesn't allow for the Higgs boson mass dependent parametrization, we simply take the one integrated over the mass range from 120 to 130 GeV, assuming that distribution would not change significantly in different mass windows.

10 Reducible Background Modelling and Uncertainties

The reducible backgrounds for the $H \rightarrow ZZ \rightarrow 4\ell$ analysis are processes which contain one or more non-prompt leptons in the four-leptons ad final state. The main sources of non-prompt leptons are non-isolated electrons and muons coming from decays of heavy-flavour mesons, mis-reconstructed jets (usually originating from light-flavour quarks) and electrons from photon conversions. For the sake of further discussion, we consider “fake lepton” any jet mis-reconstructed as a lepton and any lepton originating from a heavy meson decay. In a similar way, any electron originating from a photon conversion will be considered “fake electron”.

10.1 Reducible Background Estimation

We estimate the rate of reducible background processes by measuring fake rates, i.e. the probability for fake electrons — (f_e) and fake muons (f_μ), already passing predefined loose selection criteria to pass the final selection requirements. Then we apply measured fake rates to dedicated control samples in order to extract the background yield expected in the signal region. The loose lepton selection criteria, already defined in Sec. 8.2.2, are summarized in Table 10.1. The selection can be viewed as final selection requirements for leptons with relaxed identification and isolation criteria.

Table 10.1: Definition of loose selection criteria for muon and electron objects used for the measurement of fake ratios.

Parameter	Selection for muons	Selection for electrons
Algorithm	Global OR Tracker (with arbitration)	GSF Electrons
“duplicate” μ cleaning cone ΔR	0.02	-
e/μ cross object cleaning cone ΔR	-	0.05
Missed inner pixel hits	-	≤ 1
$ SIP3D $	< 4	< 4
p_T	$\geq 5 \text{ GeV}$	$\geq 7 \text{ GeV}$
$ \eta $	≤ 2.4	≤ 2.5

10.2 Methodology

This method can be used to make an inclusive and simultaneous measurement of all the main reducible backgrounds.

The control sample is obtained as subset of the events passing the *First Z* step of the selection described in Sec. 8.2.3, by requiring an additional pair of *loose leptons* of same sign and same flavour (SS-SF: $e^\pm e^\pm, \mu^\pm \mu^\pm$). The SS criteria is used to avoid signal entering the control region. These leptons are requested to pass SIP_{3D} cut while no identification or isolation requirements are imposed. The reconstructed invariant mass of the SS-SF leptons has to satisfy the baseline or the high-mass selections exposed in Sec. 8.2.3 as well. In addition, the reconstructed four-lepton invariant mass is required to satisfy $m_{4\ell} > 100$ GeV.

To obtain the final inclusive number of reducible background events in the signal phase space, we profit from the the, just described, control sample taking into account probability for the two additional leptons to meet identification and isolation criteria. Expected number of background events is given by the following expression:

$$N_{\text{expect}}^{\text{Z+X}} = N^{\text{DATA}} \times (\frac{\text{OS}}{\text{SS}})^{\text{MC}} \times \epsilon_1(p_T, \eta) \times \epsilon_2(p_T, \eta) \quad (10.1)$$

where:

- N^{DATA} is the number of events in the control region,
- $(\frac{\text{OS}}{\text{SS}})^{\text{MC}}$ is a correction factor between opposite sign and same sign control samples,
- $\epsilon_i(p_T, \eta)$ is the fake rate for each additional *loose leptons* ($i = 1, 2$) in function of p_T and η .

In the following paragraphs the extraction of fake rates $\epsilon_i(p_T, \eta)$ and ratio $(\frac{\text{OS}}{\text{SS}})$ is presented.

Fake rates. In order to measure the lepton fake ratios f_e, f_μ , we select samples of $Z(\ell\ell) + e$ and $Z(\ell\ell) + \mu$ events that are expected to be completely dominated by final states which include a Z boson and a fake lepton.

These events are required to have two same flavour, opposite charge leptons with $p_T > 20/10$ GeV passing the tight selection criteria, thus forming the Z candidate described as CS1 step in Sec. 8.2.3. In addition, there is exactly one lepton passing the loose selection criteria as defined in table 10.1. This lepton is used as the probe lepton for the fake ratio measurement. Each event is required to have missing transverse energy $E_T^{\text{miss}} < 25$ GeV to suppress contamination from WZ and $t\bar{t}$ processes resulting in prompt leptons.

In this approach the fake ratios are measured by using a relaxed invariant mass requirement of $40 \text{ GeV} < M_{\text{inv}}(\ell_1, \ell_2) < 120 \text{ GeV}$ which is consistent with the dilepton invariant mass requirement in the Higgs selection. This is done to have a background composition in the fake

rate sample which is similar to the expected reducible background composition in the signal region.

The measured differential p_T distributions of the fake ratios using the relaxed Z mass requirement are shown in Figure 10.1. A clear dependency of fake rates on p_T can be seen. Particularly, the fake ratios increase in the region of high p_T . This effect is in part caused by the fact that the criteria used to suppress the WZ and $t\bar{t}$ processes are not efficient in this region of p_T .

The dependance of the fake ratios on the exact composition of background processes in a region of interest is one of the main sources of the systematic uncertainties of the method. The procedures to estimate these systematic effects in data and simulation will be discussed in the section 10.3.

SS to OS ratio. Figures 10.2 and 10.3 show the comparison between data and MC of samples selected with SS-SF and OS-SF samples for all three channels for both 7 and 8 TeV data. A reasonable agreement is achieved between data and MC for the 7 TeV. For 8 TeV, a very limited MC statistics is a drawback preventing us from bringing a meaningful conclusion. The number of events in OS and SS regions in MC samples, with ZZ contribution subtracted, are used to compute the correction factor in Eq. (10.1) for the final data-driven estimation. The ZZ contribution is subtracted from the OS sample to compare only the reducible backgrounds. As the shapes are slightly different, the OS sample will be used later on as a model of the reducible background in the statistical interpretation of the results. They are estimated as 0.97(1.23, 1.01) for the $4e(4\mu, 2e2\mu)$ final states with 7 TeV samples. Due to lack of statistics for the 8 TeV MC samples, the same factors are applied to the 8 TeV analysis.

A good agreement in shapes and rates between data and MC shown in Figure 10.2 allows us to use the simulation for the extraction of reducible background shapes.

At the very begining of this section we said that only main reducible background can be estimated using this method. In fact, the method, by construction, can not be accurate in estimating the reducible background containing three real leptons and one jet faking lepton like e. g. $WZ+jets$. This three real lepton background is currently included in the control region $Z1+2$ SS-SF leptons, but it's underestimated. On the other hand, studies on MC reveal that the overall contribution of $WZ+jets$ to the total reducible background is rather small (5 – 10%). The total reducible background estimated with the $Z+X$ method may therefore be underestimated by a small amount (about 7%). This is taken into account by increasing the systematic uncertainty of the $Z+X$ method by 10%.

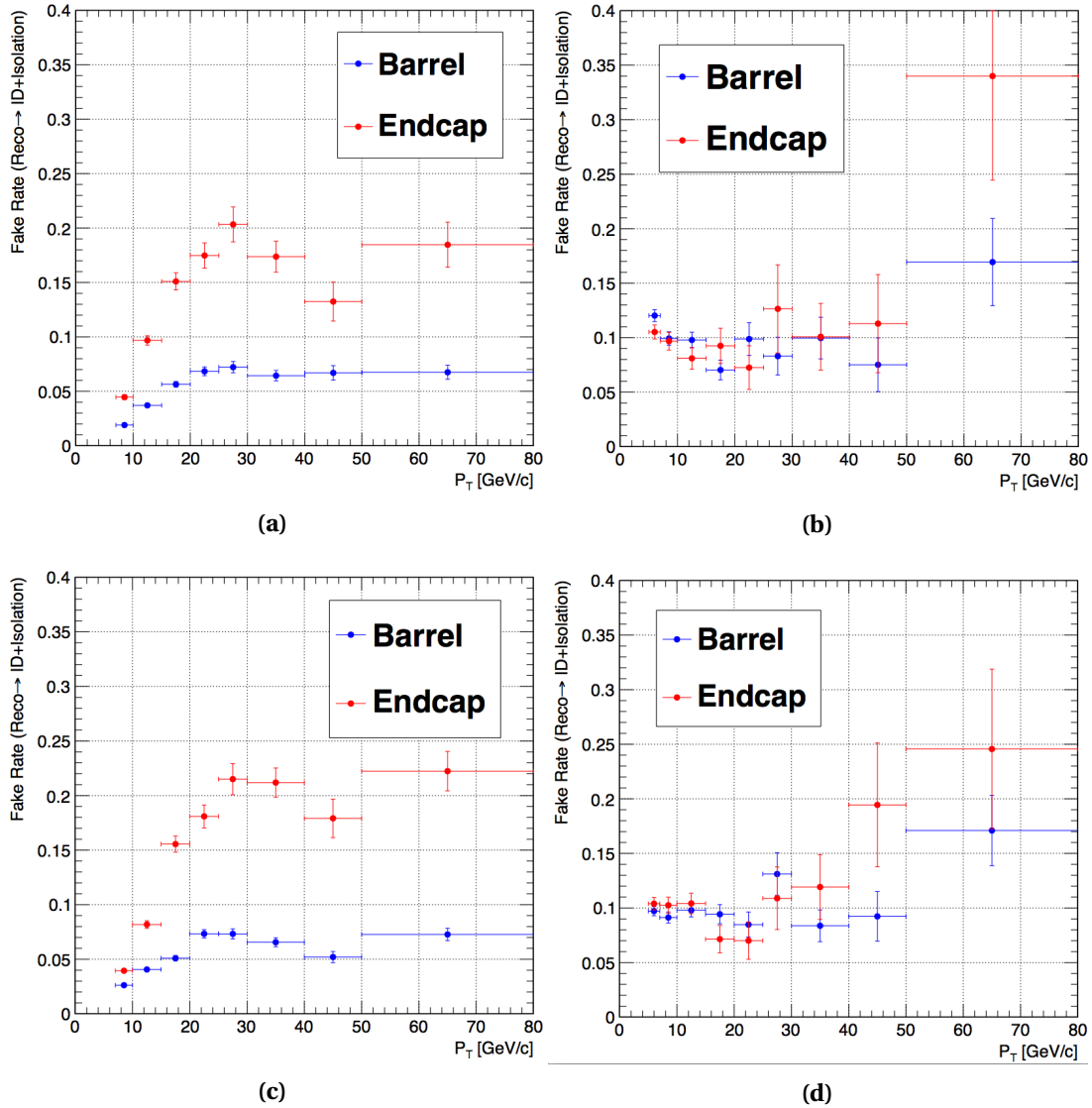


Figure 10.1: Fake rate measured for a probe lepton which satisfy loose selection, in the $Z(\ell\ell) + e$ (left) and $Z(\ell\ell) + \mu$ (right) samples as defined in the text. The sample of Z events is selected using the *First Z* (CS1) selection criteria $40 \text{ GeV} < |M_{inv}(\ell_1, \ell_2)| < 120 \text{ GeV}$ as defined in Sec. 8.2.3. Plots show fake ratios measured in 7 (top) and 8 TeV data (bottom).

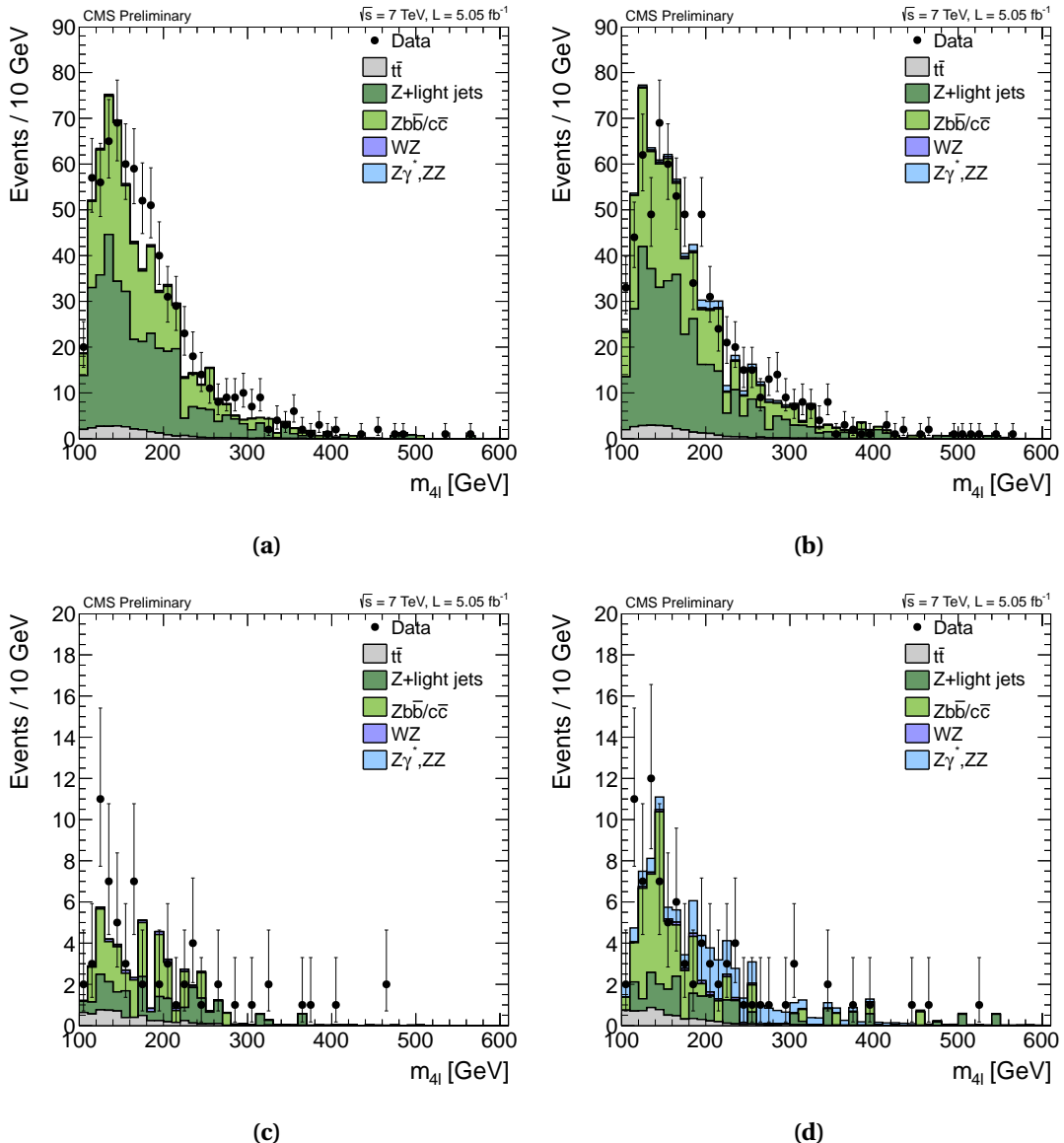


Figure 10.2: Data to MC comparison of the SS-SF (left) and OS-SF (right) samples in the $Z+X$ background control samples for the $4e$ (top) and 4μ (bottom) final states. The distributions correspond to 5.05 fb^{-1} of 7 TeV data.

Chapter 10: Reducible Background Modelling and Uncertainties

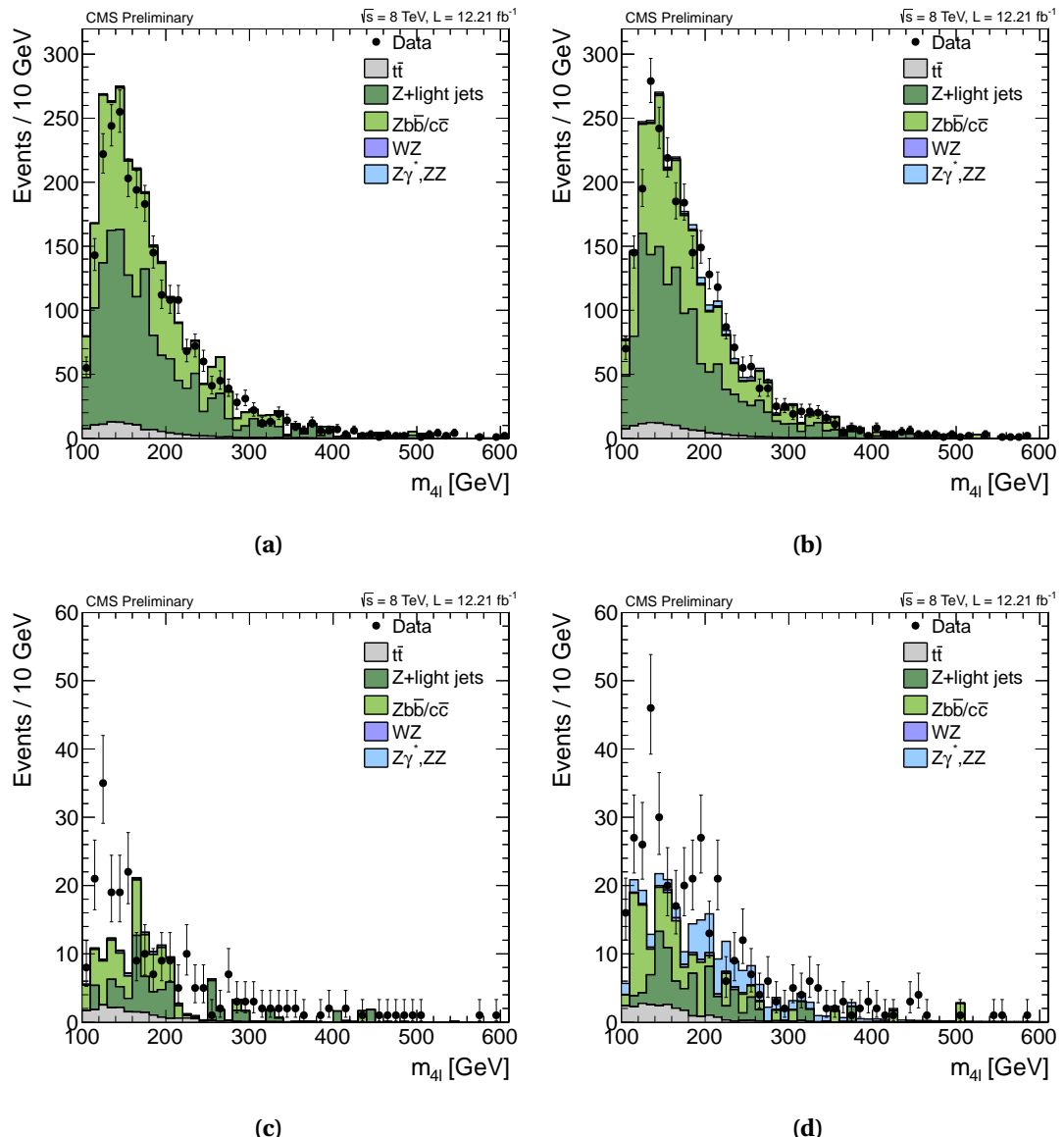


Figure 10.3: Data to MC comparison of the SS-SF (left) and OS-SF (right) samples in the $Z+X$ background control samples for the $4e$ (top) and 4μ (bottom) final states. The distributions correspond to 12.21 fb^{-1} of 8 TeV data.

10.2.1 Results on Data

With the 5.05 fb^{-1} of collected integrated luminosity at 7 TeV and 12.21 fb^{-1} at 8 TeV, the number of events from $Z+X$ expected and the relative systematics and statistical errors in the signal region in a mass range [100, 600 GeV] for the Higgs phase space selections are listed in table 10.2. The statistical errors quoted represent the number of events in the control region, while the systematic uncertainties are extracted varying the fake rates by $\pm 1\sigma$ and increased by 10% according to the $WZ+\text{jets}$ underestimation.

Table 10.2: The number of events from $Z+X$ expected and the relative systematics and statistical errors in the signal region in a mass range [100, 600 GeV], for Higgs phase space selection in 7 and 8 TeV data.

	\sqrt{s}	$4e$	4μ	$2e2\mu$
7 TeV	$2.2 \pm 0.1_{\text{stat.}} \pm 1.1_{\text{syst.}}$	$0.8 \pm 0.1_{\text{stat.}} \pm 0.4_{\text{syst.}}$	$3.0 \pm 0.1_{\text{stat.}} \pm 1.5_{\text{syst.}}$	
8 TeV	$6.1 \pm 0.1_{\text{stat.}} \pm 3.1_{\text{syst.}}$	$2.2 \pm 0.1_{\text{stat.}} \pm 1.1_{\text{syst.}}$	$8.9 \pm 0.2_{\text{stat.}} \pm 4.5_{\text{syst.}}$	

10.2.2 Alternative Method

This method differentiates between two and three prompt lepton backgrounds by using two control samples obtained as subsets of four lepton events which pass the “Higgs candidate” selection step, as described in previous sections. First control sample is obtained by requiring two leptons to fail the final identification and isolation criteria, but to pass the loose lepton requirements as defined in Table 10.1. The other two leptons should pass the final selection criteria. This sample is denoted as “2 Prompt + 2 Fail” (2P+2F) sample. It is expected to be populated with events that intrinsically have only two prompt leptons (e.g. DY , $t\bar{t}$). Second control sample is obtained by requiring one of the four leptons not to pass the final identification and isolation criteria, but to pass the loose lepton requirements. The other three leptons should pass the final selection criteria. This control sample is denoted as “3 Prompt + 1 Fail” (3P+1F) sample. It is expected to be populated with the type of events that populate the 2P+2F region, as well as with the events that intrinsically have three prompt leptons (e.g. WZ , $Z\gamma^{(*)}$).

The control samples obtained in this way are expected to be enriched with the fake leptons and are used to estimate the rate of the reducible background events in the signal region.

The expected number of reducible background events in the 3P+1F region $N_{3\text{P}1\text{F}}^{\text{bkg}}$ can be computed from the number of events observed in the 2P+2F control region $N_{2\text{P}2\text{F}}$ by weighting each of the events in the region with the factor $(\frac{f_i}{1-f_i} + \frac{f_j}{1-f_j})$, where f_i and f_j correspond to the fake ratios of the two loose leptons in the event:

$$N_{3\text{P}1\text{F}}^{\text{bkg}} = \sum \left(\frac{f_i}{1-f_i} + \frac{f_j}{1-f_j} \right) N_{2\text{P}2\text{F}} \quad (10.2)$$

The expected contribution of reducible background processes with two fake leptons in the

signal region can be computed from the number of events observed in the 2P+2F control region $N_{2\text{P}2\text{F}}$ by weighting each of the events in that region with the factor $\frac{f_i}{1-f_i} \frac{f_j}{1-f_j}$, where f_i and f_j correspond to the fake ratios of the two loose leptons. Similarly, the expected contribution of reducible background processes with one fake leptons in the signal region can be computed from the difference between the number of observed events in the 3P+1F control region $N_{3\text{P}1\text{F}}$ and the expected contribution from the 2P+2F region and ZZ processes in the signal region $N_{3\text{P}1\text{F}}^{\text{ZZ}} + N_{3\text{P}1\text{F}}^{\text{bkg}}$. The $N_{3\text{P}1\text{F}}^{\text{bkg}}$ is given by the equation 10.2 and $N_{3\text{P}1\text{F}}^{\text{ZZ}}$ is the contribution from ZZ which is taken from simulation. Therefore, the full expression for the prediction can be symbolically written as:

$$N_{\text{SR}}^{\text{bkg}} = \sum \frac{f_i}{(1-f_i)} (N_{3\text{P}1\text{F}} - N_{3\text{P}1\text{F}}^{\text{bkg}} - N_{3\text{P}1\text{F}}^{\text{ZZ}}) + \sum \frac{f_i}{(1-f_i)} \frac{f_j}{(1-f_j)} N_{2\text{P}2\text{F}} \quad (10.3)$$

The Table 10.3 shows the expected number of events in the signal regions from the reducible background processes, both for the 7 TeV and 8 TeV data. Only statistical uncertainties are quoted in the table. More details on the method can be find in [106].

Table 10.3: The contribution of reducible background processes in the signal region for the Higgs phase space with full mass range predicted from measurements in data using the alternative method. The quoted predictions correspond to the 7 TeV and the 8 TeV data.

	\sqrt{s}	4e	4 μ	2e2 μ
7 TeV	1.6 \pm 0.1 _{stat.}	1.1 \pm 0.1 _{stat.}	2.9 \pm 0.1 _{stat.}	
8 TeV	3.0 \pm 0.1 _{stat.}	2.0 \pm 0.1 _{stat.}	5.2 \pm 0.1 _{stat.}	

10.3 Reducible Background Uncertainties

After introducing methods for measuring reducible backgrounds directly from data, it is crucial to estimate well both, statistical and systematic uncertainties. There are several sources of uncertainties:

- Statistical uncertainty due to the limited size of the samples in the control regions where we measure and where we apply the fake ratio method,
- Different compositions of reducible background processes (DY , $t\bar{t}$, WZ , $Z\gamma^{(*)}$) in the region where we measure and where we apply the fake ratio method,
- Choice of the functional form for the $m_{4\ell}$ shape used to extrapolate from the full range of the invariant $m_{4\ell}$ mass to the range of interest.

To estimate the systematic uncertainty, two different approaches were used:

- Estimate the systematic uncertainty for the prediction method using the MC closure test,
- Estimate directly the systematic uncertainty for the prediction method using the “orthogonal” $4l$ data samples with the “wrong combination of charge and flavour”.

10.3.1 Statistics in 4ℓ control sample

The size of samples in the control regions where we measure and where we apply the fake ratios is quite limited, giving rise to the statistical uncertainties of the method. The dominating statistical uncertainty is driven by the number of events in the control region and is typically in the range of 5-10%. This uncertainty, as opposed to systematic ones, is decreasing as more data events are analysed.

10.3.2 Functional form for $m_{4\ell}$ shape

The functional form for the m_{4l} shape that is used to extrapolate from the full range of the invariant m_{4l} mass to the range of interest is also one source of the systematic uncertainty. In order to estimate this uncertainty we have looked at the differences between the shapes of predicted background distributions for all three channels. The envelope of differences between these shapes of distributions is used as a measure of the uncertainty of the shape. The uncertainty is estimated to be up to 10 - 15%. Since the difference of the shapes slowly varies with m_{4l} , it is taken as a constant term and is practically absorbed in the much larger uncertainty on the predicted yield of backgrounds (see previous chapter). The shapes of predicted background m_{4l} distributions for $4e$ and 4μ channels are shown in Figure 10.4.

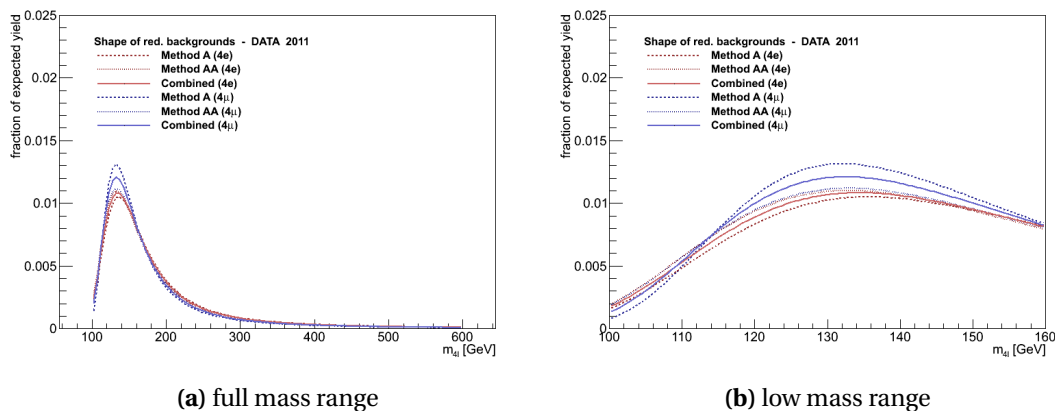


Figure 10.4: The shapes of predicted background $m_{4\ell}$ distributions for $4e$ and 4μ channels. The envelope of differences between the shapes of distributions is used as a measure of the shape uncertainty. The uncertainty is estimated to be in the range 10 - 15% and is absorbed in the much larger uncertainty on the predicted yield of backgrounds.

10.3.3 Closure Test with Z and Opposite Flavor Leptons

A closely related closure test has been performed for the main method, using samples of Z plus two opposite flavour leptons (e, μ).

A “signal” sample is selected using the selection and kinematic cuts of the Higgs phase space defined in section 8.2.3, the only difference being that $e^\pm \mu^\mp$ pairs are used, instead of $l^\pm l^\mp$ pairs, to make the “ Z_2 ” candidate. The “signal” sample is expected to be dominated by events where the “ Z_2 ” candidate is made from two fake leptons. This reducible background component is obtained by applying the main method to a control sample of Z_1 plus two loose leptons of same sign and opposite flavour ($Z_1 + e^\pm \mu^\pm$). For simplicity, the OS to SS correction factor is taken to be the same as for the main analysis.

21 events are observed in the 2012 $Z_1 + e\mu$ “signal” sample (10 events where $Z_1 \rightarrow \mu\mu$ and 11 events where $Z_1 \rightarrow ee$). The corresponding four-lepton invariant mass distribution is shown in Fig. 10.5. The reducible background component obtained is shown as the green histogram. The predicted yield amounts to 13.7 ± 2.1 events, where the error combines the (subleading) uncertainty due to the statistics of the control sample (3063 events) and the uncertainty due to the fake rate fractions. Events with one or two genuine e or μ leptons also contribute to the “signal” sample and this contribution is estimated from Monte-Carlo samples. The contribution of ZZ events (where one Z decays to ee or $\mu\mu$, and the other Z decays into $\tau\tau$ followed by $\tau \rightarrow e\bar{v}v$ and $\tau \rightarrow \mu\bar{v}v$) amounts to 4.7 ± 0.15 events. An additional source of $Z + e\mu$ events comes from the production of a Z boson in association with a $t\bar{t}$ pair, where both top quarks decay semi-leptonically leading to two isolated leptons. This amounts to 1.75 ± 1.15 events. WZ events with an additional fake lepton contribute 0.9 ± 0.1 event. Finally, a small but visible contribution from Higgs bosons is expected, dominated by ZH production with $H \rightarrow \tau\tau$ followed by leptonic decays of both taus. For a Higgs mass of 125 GeV it amounts to ~ 0.3 event. The total expected background of 21.4 events compares well with the number of observed events. Despite the limited statistics, this allows the predictions of the main method to be validated within 35 – 40%.

Comparisons between the observations and the predictions have also been made separately for $Z_1 \rightarrow ee$ and $Z_1 \rightarrow \mu\mu$, and for the distribution of the transverse momentum of the e and μ that make the “ Z_2 ”, showing an acceptable level of agreement within the small statistics.

10.4 Reducible Background Summary

The main method together with a short description of the alternative method for the prediction of the contribution of reducible background in the signal region have been used. The Table 10.4 shows the summary of the results from both methods. We take the mean value of the results of the two methods as the final estimate of this contribution, while as the uncertainty we quote the one that covers the uncertainties of both methods. Fig. 10.6 is a visual representation of the predictions of individual methods and the combined results.

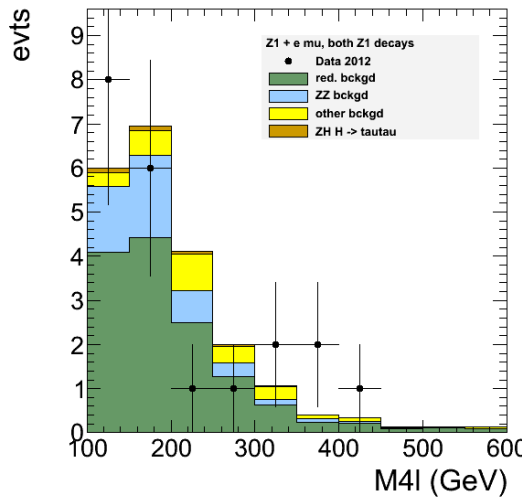


Figure 10.5: Invariant four-lepton mass distribution of $Z + e\mu$ events for 2012 data (dots), compared to the expectation from Z plus two fake leptons as predicted by the main method (green histogram), from ZZ events (blue histogram), from WZ and $t\bar{t}Z$ production (yellow histogram), and from Higgs production (orange histogram).

Table 10.4: The summary of the results of two methods for the prediction of the contribution of reducible background processes in the signal region. The arithmetic mean value of the results of the two methods is taken as the final estimate of this contribution, while the uncertainty of the result is the one that covers the uncertainties of both methods. The table shows symmetric individual uncertainties for two methods. The quoted predictions correspond to the 5.05 fb^{-1} of 7 TeV data and the 12.21 fb^{-1} of 8 TeV data.

	7 TeV	$4e$	4μ	$2e2\mu$
Main method		1.6	1.1	2.9
Alt. method		2.2	0.8	3.0
Combined central value	1.9	1.0	3.0	
Combined κ_{\min}	0.4	0.4	0.5	
Combined κ_{\max}	2.3	2.5	2.0	
	8 TeV	$4e$	4μ	$2e2\mu$
Main method		3	2.0	5.2
Alt. method		6.1	2.2	8.9
Combined central value	4.5	2.1	7.1	
Combined κ_{\min}	0.3	0.5	0.4	
Combined κ_{\max}	2.7	2.1	2.6	

Chapter 10: Reducible Background Modelling and Uncertainties

Table 10.5: The summary of the parameters of the predicted shape of reducible background processes in the signal region for 7 TeV and 8 TeV of data. The estimated uncertainty on the shape is found to be below 10-15% and is included in the uncertainties quoted above (as discussed in the text).

	7 TeV	n_0	m	c
$4e$	–	148.0	20.6	
$2e2\mu$	–	143.1	19.9	
4μ	–	133.8	15.4	
	8 TeV	n_0	m	c
$4e$	–	148.9	20.2	
$2e2\mu$	–	146.4	19.6	
4μ	–	140.3	21.7	

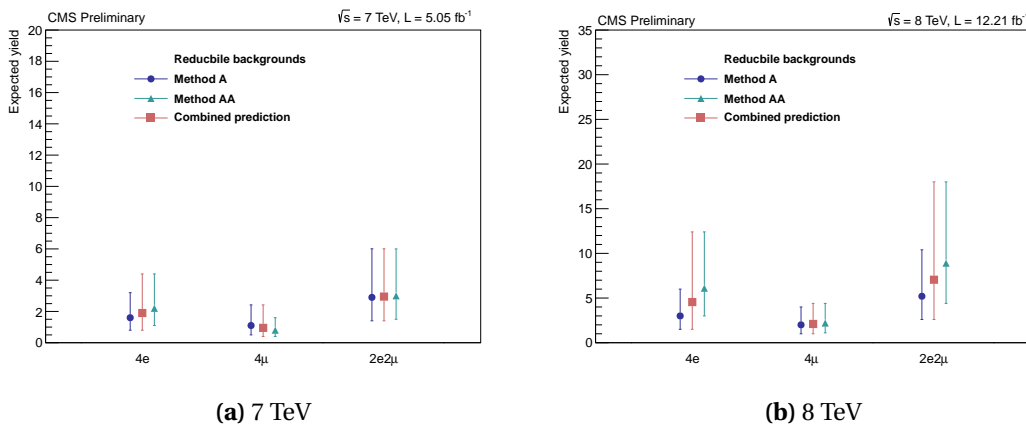


Figure 10.6: The visual representation of the predictions of individual methods and the combined results of the two methods. The combined estimate is taken as the arithmetic mean of the values allowed by the two methods. The uncertainty of the result is the one that covers the uncertainties of both methods (symmetric log-normal distribution).

11 Irreducible Background Modelling and Uncertainties

$H \rightarrow ZZ^{(*)} \rightarrow 4\ell$ analysis has a very clean signature, i.e. four isolated leptons coming from the same event vertex. These two characteristics of the Higgs event have very good discrimination power against all instrumental backgrounds where jets fake leptons, or where true leptons are produced but with displaced vertices. The later is the case for $Zb\bar{b}$ and $t\bar{t}$ backgrounds. However, these attributes can not be used against simple ZZ or $Z + DY$ double parton interaction processes giving four real leptons in the final state. Therefore, these backgrounds are considered irreducible. Example of the dominant Standard Model $ZZ \rightarrow 4\ell$ process is shown in Fig. 11.1.

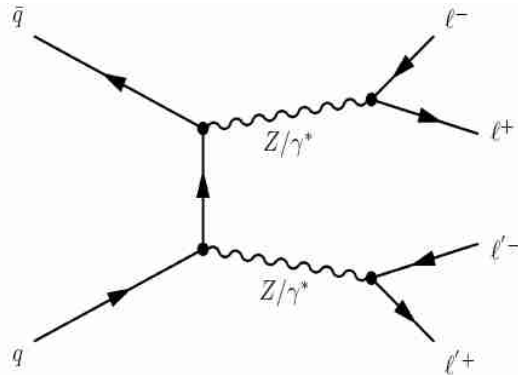


Figure 11.1: The leading order $ZZ \rightarrow 4\ell$ process giving rise to irreducible background for the $H \rightarrow ZZ^{(*)} \rightarrow 4\ell$ Higgs search.

In the following sections we bring ZZ irreducible background modelling with uncertainties.

11.1 ZZ^(*) Background Model

The expected rate for a given mass range $[m_1, m_2]$ is obtained directly from the rate predicted by the simulation:

$$N_{\text{expect}}^{\text{ZZ}} [m_1, m_2] = \int_{m_1}^{m_2} \left(\frac{dN}{dm_{4\ell}} \right)_{\text{MC}} dm_{4\ell} \quad (11.1)$$

We took into account differences between data and MC already in the differential yield $\left(\frac{dN}{dm_{4\ell}} \right)_{\text{MC}}$ in terms of scale factors.

When comparing with data, this background estimate is affected by the systematics uncertainties on the pp integrated luminosity, the theory errors and systematic errors on acceptance within analysis cuts.

The $pp \rightarrow ZZ \rightarrow 4\ell$ background models for $q\bar{q} \rightarrow ZZ$ at NLO and $gg \rightarrow ZZ$ are factorized in the same way as the signal model in Sec. 9.1:

$$\text{ZZ@NLO: } \frac{dN}{dm_{4\ell}} = C(m_{4\ell}) \cdot N^{\text{MC}}(m_{4\ell}) \cdot F_{\text{ZZNLO}}(m_{4\ell}), \quad (11.2)$$

$$\text{gg} \rightarrow \text{ZZ: } \frac{dN}{dm_{4\ell}} = C(m_{4\ell}) \cdot N^{\text{MC}}(m_{4\ell}) \cdot F_{\text{gg2ZZ}}(m_{4\ell}). \quad (11.3)$$

where the overall data-to-MC correction factors $C(m_{4\ell})$ are assumed to be the same as for the Higgs signal events with $m_H = m_{4\ell}$. We address the validity of this assumptions in the section on systematic errors.

The functions $F_{\text{ZZNLO}}(m_{4\ell})$ and $F_{\text{gg2ZZ}}(m_{4\ell})$ are parameterized separately for $4e$, 4μ , and $2e2\mu$ channels using the simulated $m_{4\ell}$ spectrum in the following way:

$$F_{\text{ZZNLO}}(m, \vec{a}, \vec{b}, \vec{c}) = f_1(m, \vec{a}) + f_2(m, \vec{b}) + f_3(m, \vec{c}) \quad (11.4)$$

$$F_{\text{gg2ZZ}}(m, \vec{a}, \vec{b}) = f_1(m, \vec{a}) + f_2(m, \vec{b}) \quad (11.5)$$

where $f_i (i = 1, 2, 3)$ components are:

$$f_1(m, \vec{a}) = \left(\frac{1}{2} + \frac{1}{2} \operatorname{erf} \left(\frac{m - a_1}{a_2} \right) \right) \cdot \frac{a_4}{1 + e^{(m - a_1)/a_3}} \quad (11.6)$$

$$f_2(m, \vec{b}) = \left(\frac{1}{2} + \frac{1}{2} \operatorname{erf} \left(\frac{m - b_1}{b_2} \right) \right) \cdot \left(\frac{b_4}{1 + e^{(m - b_1)/b_3}} + \frac{b_6}{1 + e^{(m - b_1)/b_5}} \right) \quad (11.7)$$

$$f_3(m, \vec{c}) = \left(\frac{1}{2} + \frac{1}{2} \operatorname{erf} \left(\frac{m - c_1}{c_2} \right) \right) \cdot \frac{c_4}{1 + e^{(m - c_1)/c_3}} \quad (11.8)$$

The first part of functional form takes care of modelling the ZZ threshold around $2 \times m_Z$ while the second part parametrizes the high mass tail. The shape of the fits are shown in Fig. 11.2. Having the irreducible background parametrization in hand, it is very important for the final statistical analysis to acquire the knowledge about all possible sources of uncertainties. This

point is discussed in the next section.

Chapter 11: Irreducible Background Modelling and Uncertainties

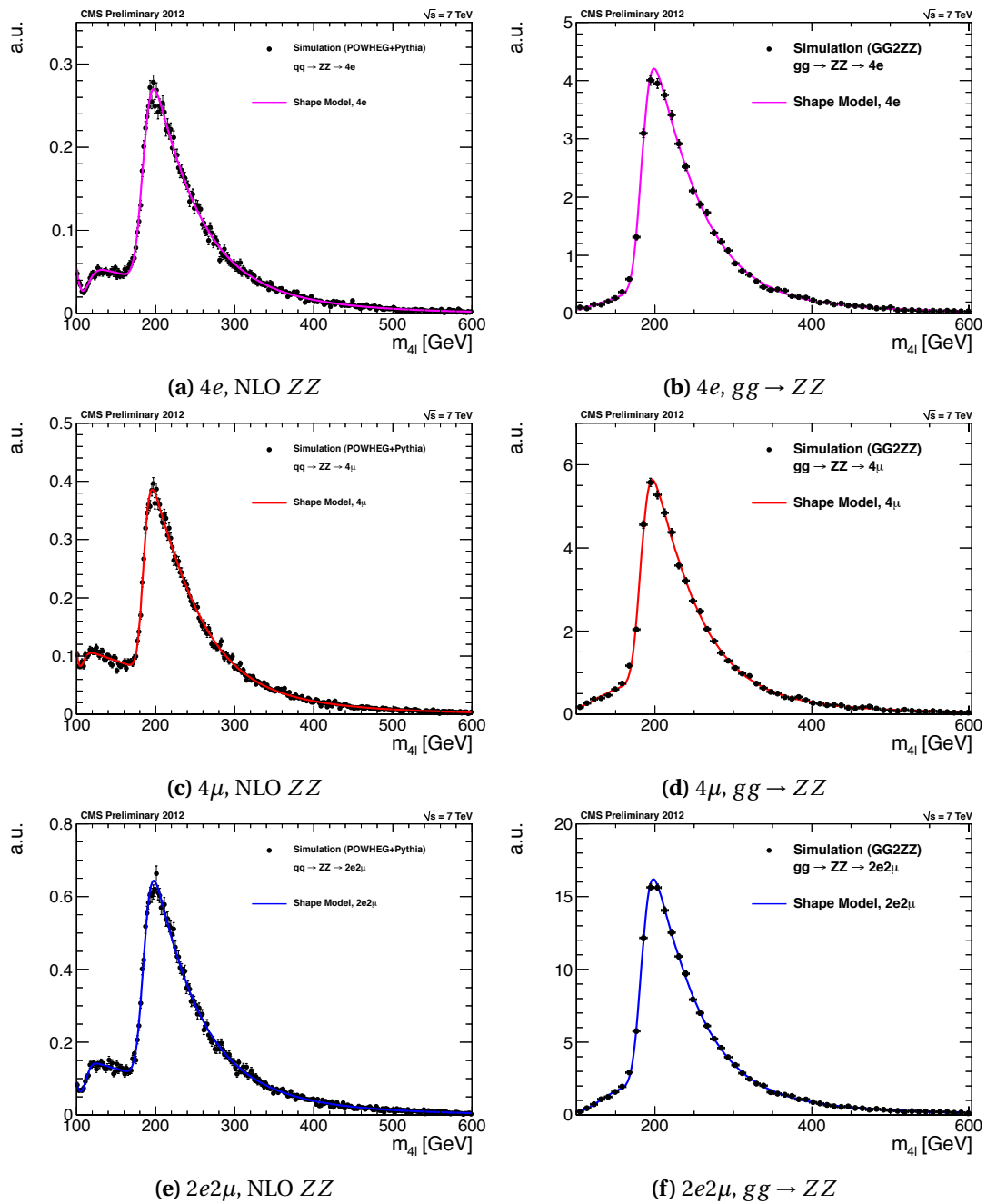


Figure 11.2: Probability density functions describing the NLO ZZ (left) and gg \rightarrow ZZ (right) background shape for 4e, 4 μ , and 2e2 μ final states at centre of mass energy of 7 TeV.

11.2 ZZ^(*) Background Model Uncertainties

In general, there are multiple sources of uncertainties of irreducible background model having major provenance in QCD scale and PDF uncertainties.

We did not find any systematic uncertainties that would considerably distort the $ZZ \rightarrow 4\ell$ invariant mass distributions in ranges corresponding to the Higgs boson width. Thus, all uncertainties we are discussing are included as normalization uncertainties, whose absolute value may depend on the Higgs boson mass hypothesis m_H being tested in the search.

11.2.1 Theoretical Uncertainties

Event Yield Uncertainties as a Function of $m_{4\ell}$

PDF+ α_s and QCD scale uncertainties for $pp \rightarrow ZZ \rightarrow 4\ell$ at NLO and $gg \rightarrow ZZ \rightarrow 4\ell$ are evaluated using MCFM [112]. We use the $2e2\mu$ final state and fiducial cuts for leptons similar to those in the analysis:

- $m_{ee} > 12$ GeV, $m_{\mu\mu} > 12$ GeV,
- $p_T > 7$ GeV and $|\eta| < 2.5$ for electrons,
- $p_T > 5$ GeV and $|\eta| < 2.4$ for muons.

In addition, the minimal jet-lepton and lepton-lepton ΔR_{min} -distance was set to zero. The cross-sections inclusive in number of jets were calculated at NLO and uncertainties evaluated, both, for 7 and 8 TeV.

According to Ref. [61], the PDF+ α_s and QCD scale uncertainties are treated as uncorrelated. Contrary, uncertainties between 7 and 8 TeV are assumed to be 100% correlated.

To evaluate the PDF+ α_s systematics, we use the PDF4LHC prescription [113]. Using three sets of PDFs, CT10 [114], MSTW08 [115], NNPDF [116], uncertainties were obtained as the envelope of $m_{4\ell}$ -dependent upper and lower values. The results are summarized in Figs. 11.3 and parametrized for both, 7 and 8 TeV as follows:

$$ZZ \text{ at NLO : } \kappa(m_{4\ell}) = 1 + 0.0035\sqrt{(m_{4\ell} - 30)} \quad (11.9)$$

$$gg \rightarrow ZZ : \kappa(m_{4\ell}) = 1 + 0.0066\sqrt{(m_{4\ell} - 10)} \quad (11.10)$$

For estimation of QCD scale systematic errors, we calculate variations in the differential cross-section $d\sigma/dm_{4\ell}$ changing the renormalization and factorization scales by a factor of two up and down from their default setting $\mu_R = \mu_F = m_Z$. Again, four-lepton mass dependent QCD

scale systematic uncertainties can be taken as envelope around obtained values. The results for 7 and 8 TeV are visualized in Fig. 11.4 and parametrized with:

$$\text{ZZ at NLO : } \kappa(m_{4\ell}) = 1.00 + 0.01\sqrt{(m_{4\ell} - 20)/13} \quad (11.11)$$

$$\text{gg} \rightarrow \text{ZZ} : \kappa(m_{4\ell}) = 1.04 + 0.10\sqrt{(m_{4\ell} + 40)/40} \quad (11.12)$$

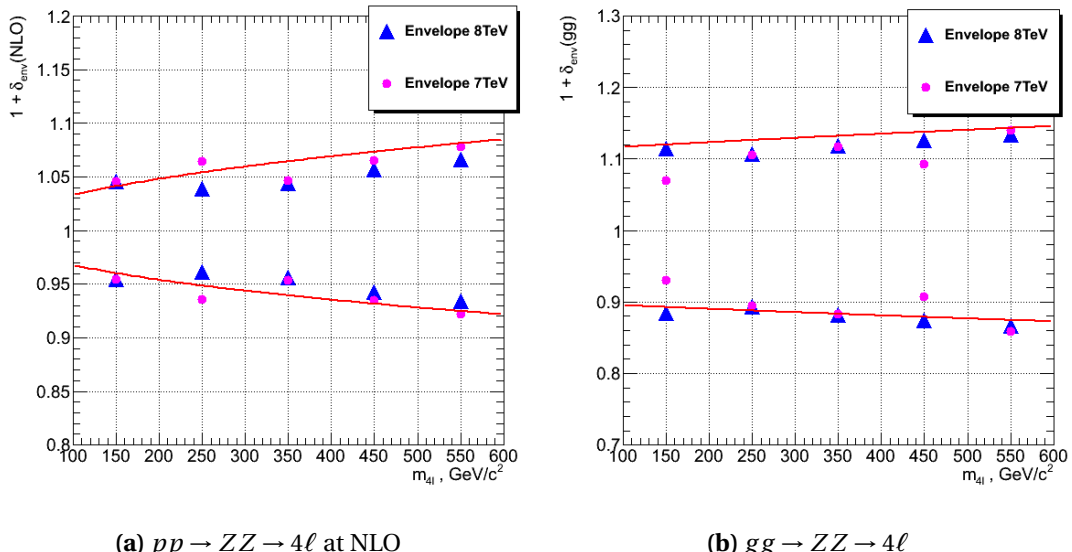


Figure 11.3: PDF+ α_s uncertainties for $pp \rightarrow ZZ \rightarrow 4\ell$ at NLO and $gg \rightarrow ZZ \rightarrow 4\ell$ processes. The points represent evaluated uncertainties. The curves $\kappa(m_{4\ell})$ are obtained by fitting and are to be used in the statistical analysis. These errors are driven by two independent nuisance parameters pdf_{qqbar} for $pp \rightarrow ZZ \rightarrow 4\ell$ at NLO and pdf_{gg} for $gg \rightarrow ZZ \rightarrow 4\ell$.

Shape uncertainties

The shape uncertainties in $m_{4\ell}$ distribution require the knowledge of correlations between possible event yield variations at different $m_{4\ell}$ points. For simplicity, we assume conservative 100% correlations between errors over the entire $m_{4\ell}$ mass range.

For a given hypothesis of Higgs boson mass m_H , the signal is a localized peak in the $m_{4\ell}$ distribution. Large variations in signal shape in the narrow regions under the Higgs boson peak are not expected. This is confirmed by looking at the local shape changes due to QCD scale and PDF variations. This holds true even for the high Higgs boson mass hypothesis where natural width of the boson is quite broad.

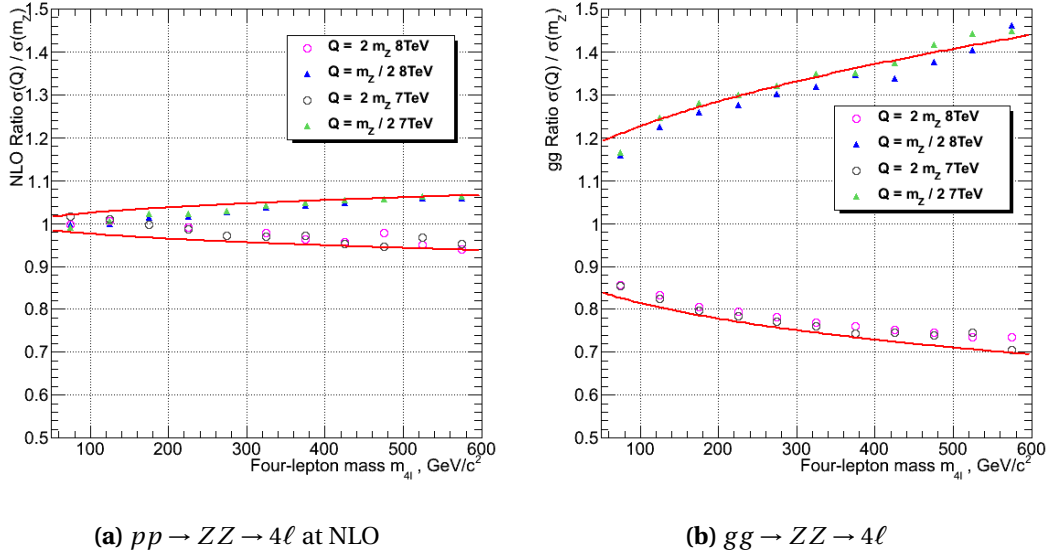


Figure 11.4: QCD scale uncertainties for $pp \rightarrow ZZ \rightarrow 4\ell$ at NLO and $gg \rightarrow ZZ \rightarrow 4\ell$ processes. The points represent evaluated uncertainties. The curves $\kappa(m_{4\ell})$ are obtained by fitting and are to be used in the statistical analysis. These errors are driven by two independent nuisance parameters $QCDscale_VV$ for $pp \rightarrow ZZ \rightarrow 4\ell$ at NLO and $QCDscale_ggVV$ for $gg \rightarrow ZZ \rightarrow 4\ell$.

Results

Finally, we present estimates for $ZZ^{(*)}$ irreducible background yields and uncertainties. The number of events $ZZ^{(*)} \rightarrow 4\ell$ in the signal region is calculated from MC simulation using Eq. (11.1) for an integrated luminosity of 5.05 fb^{-1} at 7 TeV and 12.21 fb^{-1} at 8 TeV. The calculation is performed in the full mass range, with the baseline and high-mass selections and is shown in Table 11.1 for the $q\bar{q}$ annihilation and for the gluon-gluon fusion separately.

Chapter 11: Irreducible Background Modelling and Uncertainties

Table 11.1: Number of ZZ background events and relative uncertainties in the signal region estimated from Monte Carlo simulation, for the baseline and high-mass event selections and for the full mass range and the un-blinded region. Results are for the 7 and 8 TeV analysis.

Baseline			
	channel	7 TeV	8 TeV
$q\bar{q}$	$N^{ZZ \rightarrow 4e}$	14.4 ± 1.2	10.91 ± 0.92
	$N^{ZZ \rightarrow 4\mu}$	21.9 ± 1.8	17.03 ± 1.43
	$N^{ZZ \rightarrow 2e2\mu}$	34.7 ± 2.9	27.53 ± 2.3
gg	$N^{ZZ \rightarrow 4e}$	0.93 ± 0.41	0.9 ± 0.39
	$N^{ZZ \rightarrow 4\mu}$	1.3 ± 0.56	1.52 ± 0.66
	$N^{ZZ \rightarrow 2e2\mu}$	2.22 ± 0.96	2.55 ± 1.11
High-mass			
$q\bar{q}$	$N^{ZZ \rightarrow 4e}$	11.94 ± 0.92	7.22 ± 1.0
	$N^{ZZ \rightarrow 4\mu}$	17.08 ± 1.43	10.69 ± 1.4
	$N^{ZZ \rightarrow 2e2\mu}$	29.06 ± 2.3	17.5 ± 2.3
gg	$N^{ZZ \rightarrow 4e}$	0.85 ± 0.26	0.64 ± 0.22
	$N^{ZZ \rightarrow 4\mu}$	1.18 ± 0.37	0.89 ± 0.30
	$N^{ZZ \rightarrow 2e2\mu}$	2.07 ± 0.63	1.56 ± 0.52

12 Kinematic Discriminant

After having claimed the observation of a new resonance, the existence of a new particle, it becomes crucial to measure its quantum numbers, its mass and couplings to SM fields as accurately as possible. Measuring masses, coupling constants and quantum numbers at a hadron collider is difficult, though many techniques for doing so were put forward recently. Such a technique used for instance for the measurement of the top mass at the Tevatron collider is the “matrix element method”, where one performs a likelihood fit on a per-event basis. Since more information about the event is used, more efficient separation of signal and background is accomplished and a higher accuracy of the top quark mass measurement is achieved. The idea that matrix elements, or multivariate per-event-likelihoods, can guide us in maximizing the amount of information that can be extracted from a given event is appealing, but it has not been widely used in hadron collider physics besides the top mass measurement. In this chapter we bring a matrix element method, so-called MELA, which is used to build per-event a single kinematic discriminant KD that will be used in complement to the four-lepton mass to characterize the events.

12.1 Methodology

Multiple extensive studies of the kinematics of the Higgs decay to ZZ final state have been performed in application to the Higgs boson properties measurements [119, 120, 121, 122, 121, 123, 124, 125, 126, 127, 128, 129, 130]. Recently a complete set of angular observables was introduced [128] which in addition to properties discrimination, may also help reject the background. The signal-to-background probability is created using analytical or empirical multi-dimension likelihood for an event to be signal or background. The analytical parametrizations of signal and background are taken from Refs. [128] and [130]. In what follows, we introduce the methodology in more detail with the analytical Matrix Element Likelihood Analysis (MELA) approach.

The angular distribution in the production and decay chain $ab \rightarrow X \rightarrow ZZ \rightarrow 4\ell$ is illustrated in Fig. 12.1 and can be expressed as a function of three helicity angles θ_1 , θ_2 , and Φ , and

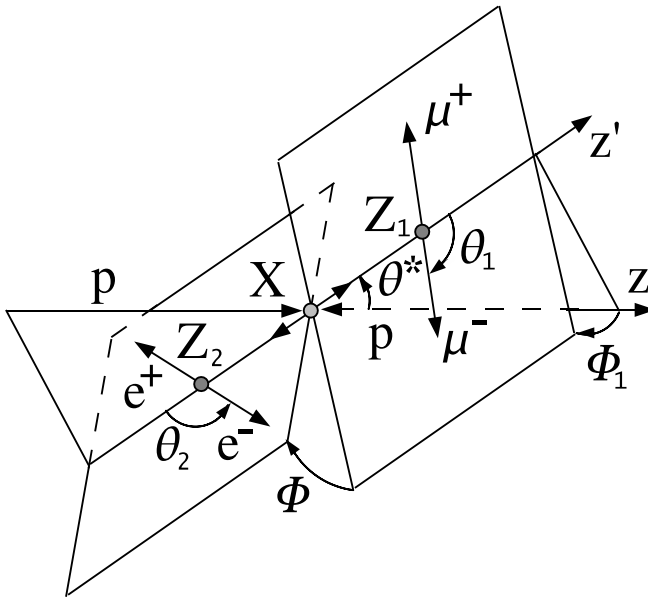


Figure 12.1: A particle X production and decay $ab \rightarrow X \rightarrow Z_1 Z_2 \rightarrow 4\ell$ with the two production angles θ^* and Φ_1 shown in the X rest frame and three decay angles θ_1 , θ_2 , and Φ shown in the P_i rest frames [128].

two production angles θ^* and Φ_1 . The full production and decay kinematics of a $ab \rightarrow X \rightarrow Z_1 Z_2 \rightarrow 4\ell$ process can be described with the following 12 observables that reflect all degrees of freedom with four lepton momenta:

- three resonance masses (including the off-shell cases): $m_{4\ell}, m_1, m_2$;
- five production and decay angles defined in Fig. 12.1 as $\vec{\Omega} = \{\theta^*, \Phi_1, \theta_1, \theta_2, \Phi\}$;
- longitudinal boost of the resonance, expressed as rapidity Y ;
- transverse momentum of the resonance p_T and its azimuthal angle;
- one arbitrary azimuthal angle Φ^* reflecting the overall orientation of the system.

In 2011, the baseline analysis of the $H \rightarrow ZZ \rightarrow 4\ell$ channel employed cuts on the two $Z^{(*)}$ invariant masses m_1 and m_2 with the shape-based fit of the $m_{4\ell}$ distribution, the so-called 1D fit. In the present analysis, we use additional information by constructing a KD from the seven observables composed from two $Z^{(*)}$ masses and five angles, i.e. $KD = F\{m_1, m_2, \theta^*, \Phi_1, \theta_1, \theta_2, \Phi\}$. Then, a 2D shape fit is performed with the two observables ($m_{4\ell}$, KD). In Figs. 12.2 and 12.3 we show discrimination power between signal and background for each individual observable. The KD combines this power in a single observable using full correlation of all input observables in the most optimal way. These observables are coming from well-understood electro-weak quantum mechanics of the processes of either Higgs or continuum ZZ production. It is very interesting that, as long as SM Higgs boson is considered, the seven observables

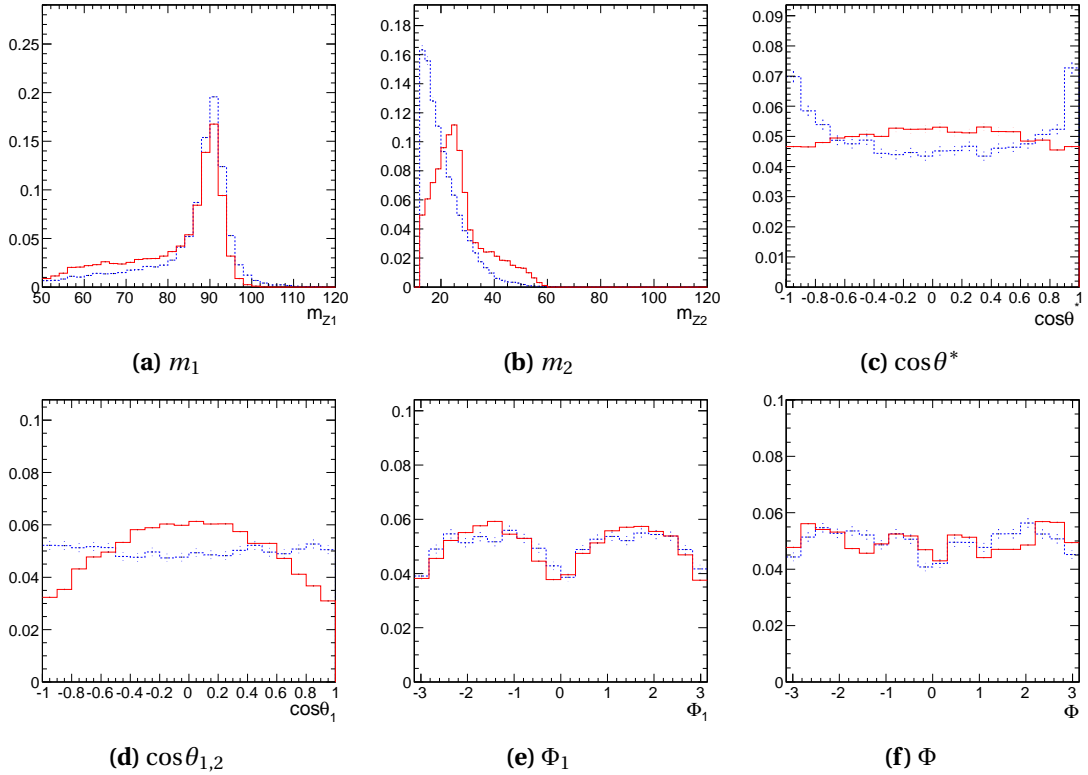


Figure 12.2: Kinematic distributions of Higgs signal events with $m_H = 120$ GeV (solid red) and background ZZ events (dashed blue) in the range $100 < m_{4\ell} < 135$ GeV.

are independent from the Higgs production mechanism. The same seven observables are also the key input to measuring the new boson properties, such as spin and CP quantum numbers, now, when the new boson has been discovered.

The distributions of Y and p_T are different for processes dominated by gluon fusion (signal) and $q\bar{q}$ production (background), due to larger longitudinal boost of the $q\bar{q}$ system and larger Initial State Radiation (QCD ISR) in gluon fusion. However, these observables are fully driven by QCD effects which are not fully validated yet. Therefore, they are not used in the present analysis.

12.2 Construction of MELA Discriminant

Construction of the kinematic discriminant (KD) in the MELA approach relies on probability for an event with a set of observables $(m_{4\ell}, m_1, m_2, \vec{\Omega})$ to come either from signal or background

$$\mathcal{P}_{\text{sig}}(m_1, m_2, \vec{\Omega} | m_{4\ell}) \quad (12.1)$$

$$\mathcal{P}_{\text{bkg}}(m_1, m_2, \vec{\Omega} | m_{4\ell}). \quad (12.2)$$

Chapter 12: Kinematic Discriminant

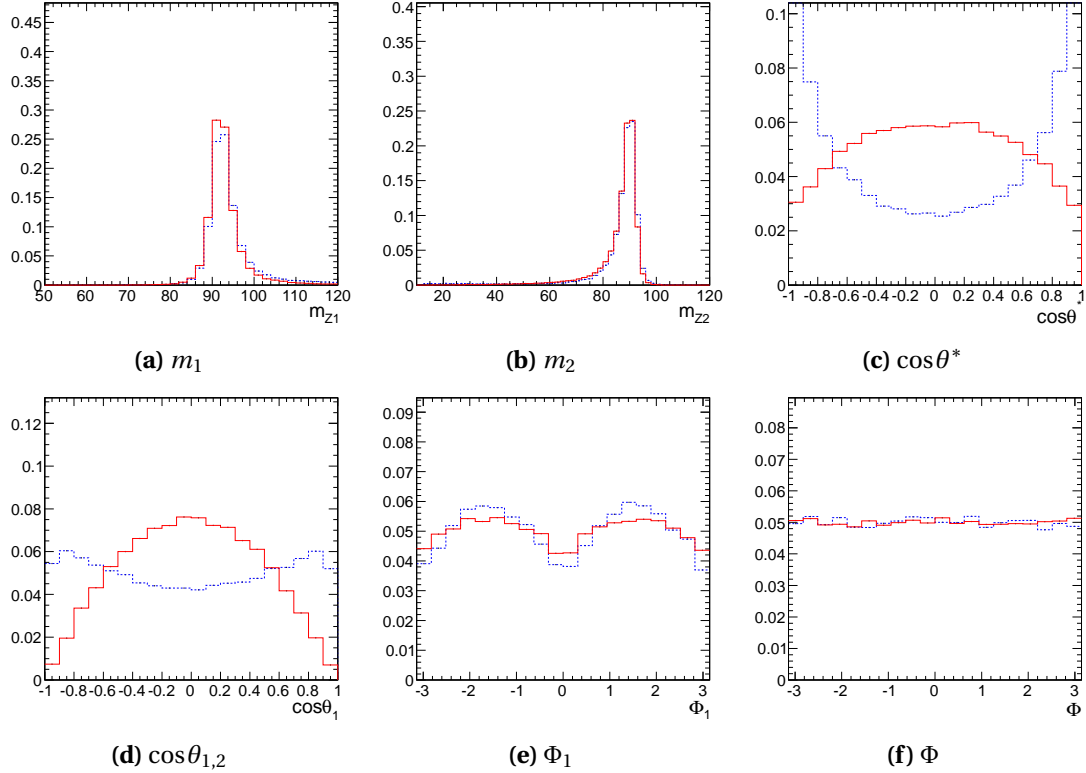


Figure 12.3: Distribution of Higgs signal events with $m_H = 400$ GeV (solid red) and background ZZ events (dashed blue) in the range $300 < m_{4\ell} < 500$ GeV.

The probabilities are normalized with respect to the seven observables and $m_{4\ell}$ is treated as a conditional parameter. These probabilities are calculated analytically in Ref. [128] for signal and in Ref. [130] for continuum ZZ background. Then the discriminant is constructed as follows

$$\text{KD} = \frac{\mathcal{P}_{\text{sig}}}{\mathcal{P}_{\text{sig}} + \mathcal{P}_{\text{bkg}}} = \left[1 + \frac{\mathcal{P}_{\text{bkg}}(m_1, m_2, \vec{\Omega} | m_{4\ell})}{\mathcal{P}_{\text{sig}}(m_1, m_2, \vec{\Omega} | m_{4\ell})} \right]^{-1} \quad (12.3)$$

There are several considerations in the above construction. In the above construction, the discriminant is continuously distributed between 0 and 1, with signal being pushed towards 1 and background towards 0 values. The parameterization of signal as a function of $m_{4\ell}$ instead of m_H allows continuous selection of the data-sample independent of the m_H hypothesis. To remove unnecessary correlation of KD with $m_{4\ell}$ and to ensure robustness of the fit implementation, both signal and background probabilities are normalized at any given value of $m_{4\ell}$. Parameterization is performed for ideal distributions without any detector effects which is an optimal approach having in mind that detector acceptance effects are identical for signal and background and would tend to cancel in the ratio in Eq. (12.3). Also statistically, the above

12.2. Construction of MELA Discriminant

construction of the KD is the most optimal given the input under consideration. All the input to the KD construction can be carefully controlled, and certain observables can be integrated out or included depending on the level of confidence in the input.

The signal and irreducible background ideal probability density functions can both be calculated analytically. The projections of signal probability density function derived in Ref. [131] are shown on top of SM Higgs events, generated at leading order through gluon-gluon fusion, in Fig. 12.4. The background probability density function was calculated in Ref. [130] including only diagrams where the intermediate state is a pair of Z bosons. Only recently, $Z\gamma^* \rightarrow 4\ell$ and $Z \rightarrow 4\ell$ processes are included to extend the validity to low $m_{4\ell}$ range where these contribution dominate. To overcome this disadvantage in the analysis performed for ICHEP2012 [82], a simplified parameterization was used for events below the $2m_Z$ kinematic threshold while the analytic PDF mentioned above was used above threshold, fixing both Z masses to 91.2 GeV. The present strategy is to use the coherent ZZ parameterization and the same eight inputs for all values of $m_{4\ell}$. Figure 12.5 shows projections of the irreducible background PDF on top of leading order Madgraph simulated events.

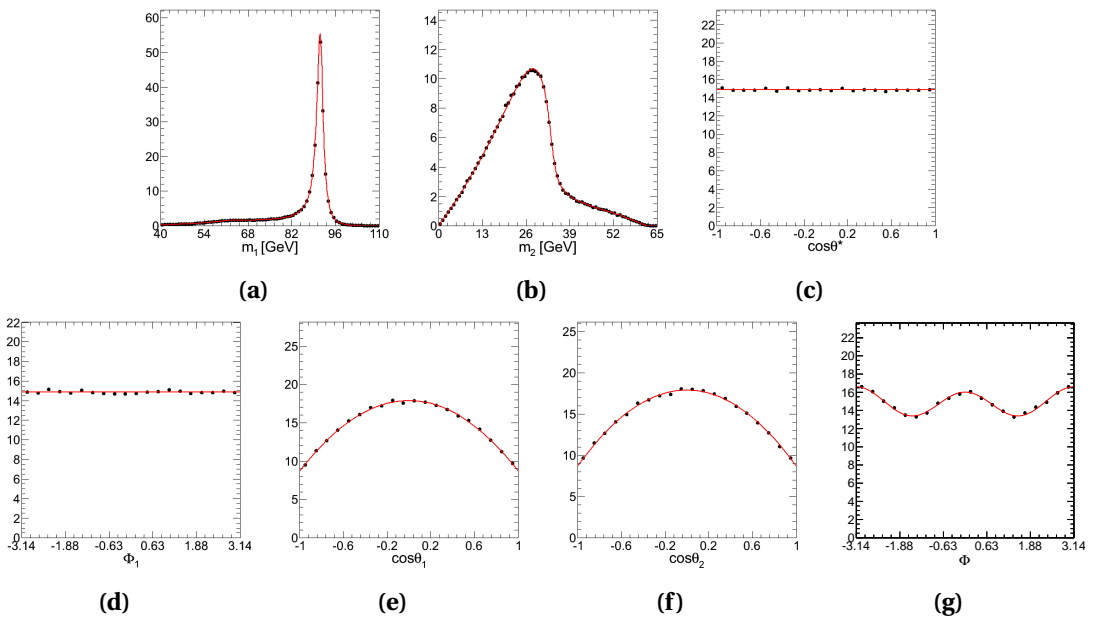


Figure 12.4: Projections of SM Higgs PDF Data on top of leading order ideal JHUGen MC events.

Figure 12.6 shows the resulting MELA KD distributions for signal and background in three different mass ranges. Good agreement is found between data and background simulation and a considerable separation between signal and background is evident.

Chapter 12: Kinematic Discriminant

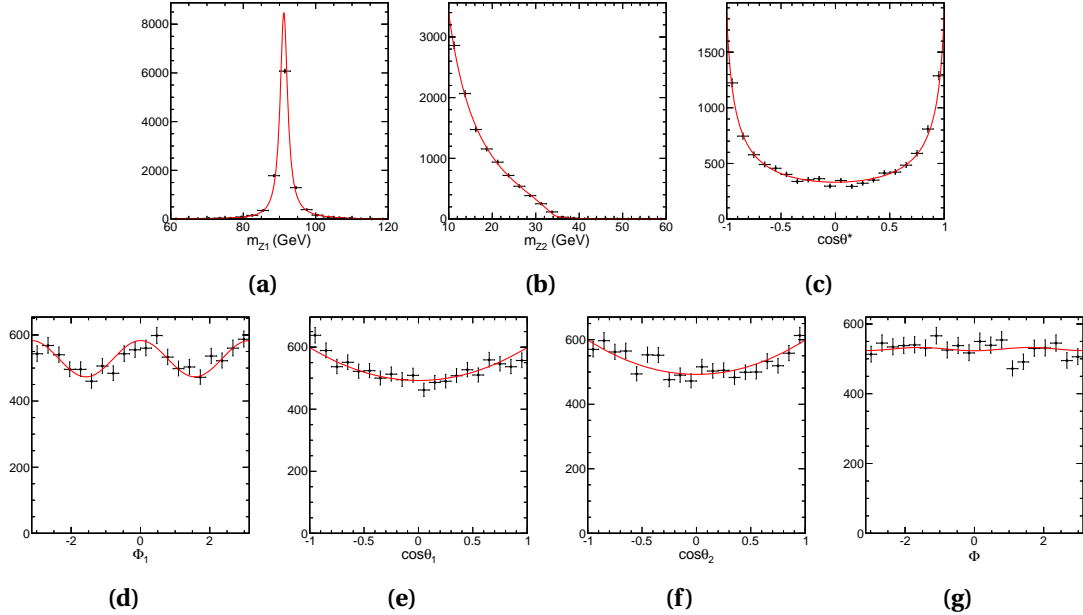


Figure 12.5: Projections of ZZ continuum PDF. Data is leading order ideal Madgraph MC events which includes both $ZZ \rightarrow 4\ell$ and $Z\gamma^* \rightarrow 4\ell$ processes.

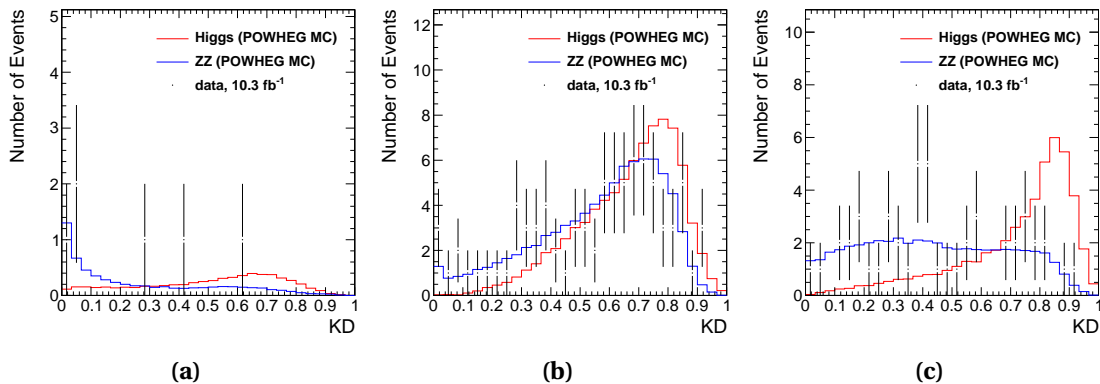


Figure 12.6: The KD distributions for signal and background in three mass ranges: $140 < m_{4\ell} < 160 \text{ GeV}$ (a), $200 < m_{4\ell} < 300 \text{ GeV}$ (b), and $250 < m_{4\ell} < 450 \text{ GeV}$ (c). The signal (red solid histogram) is shown for $m_H = 150, 250$, and 350 GeV , respectively. The ZZ continuum background is shown as blue solid histogram. The top plot also shows $Z + X$ background estimated from data control region.

12.3 Parametrization of MELA Discriminant

The MELA parameterization is performed using the ideal distributions without detector effects in Eq. (12.3), and the resulting observable KD is a single number for each event candidate. This observable is then parameterized using MC samples with full CMS simulation and with data-to-MC corrections applied for the quantum mechanical processes that we model well, such as signal and ZZ background. We use data control samples for instrumental and reducible background, such as $Z + X$. It is important to note that we use only invariant masses and angles in the sequential process with ZZ system production and decay, which is under good control from basic quantum mechanics and electroweak couplings. The KD observable viewed as single number, is as simple as the di-lepton invariant mass for example. It is also more reliable than transverse momentum of the objects, which in turn depend on QCD effects in the production.

The interference between identical leptons in $e^+ e^- e^+ e^-$ and $\mu^+ \mu^- \mu^+ \mu^-$ final state affects the KD distributions. This effect is relevant at low masses, below the ZZ threshold, where at least one of the Z bosons is off-shell increasing the phase-space for interference. The background simulation of continuum ZZ background already includes interference effects while the signal POWHEG+Pythia simulation of $H \rightarrow ZZ$ signal does not. In the later case we use Prophecy event generator to quantify the effect. As can be seen in Fig. 12.7, this effect is visible only at the low mass and essentially disappears at around $m_H = 160$ GeV. Using a linear fit of the ratio we perform a mass-dependent re-scaling to MC simulation when parameterizing the KD distribution for signal.

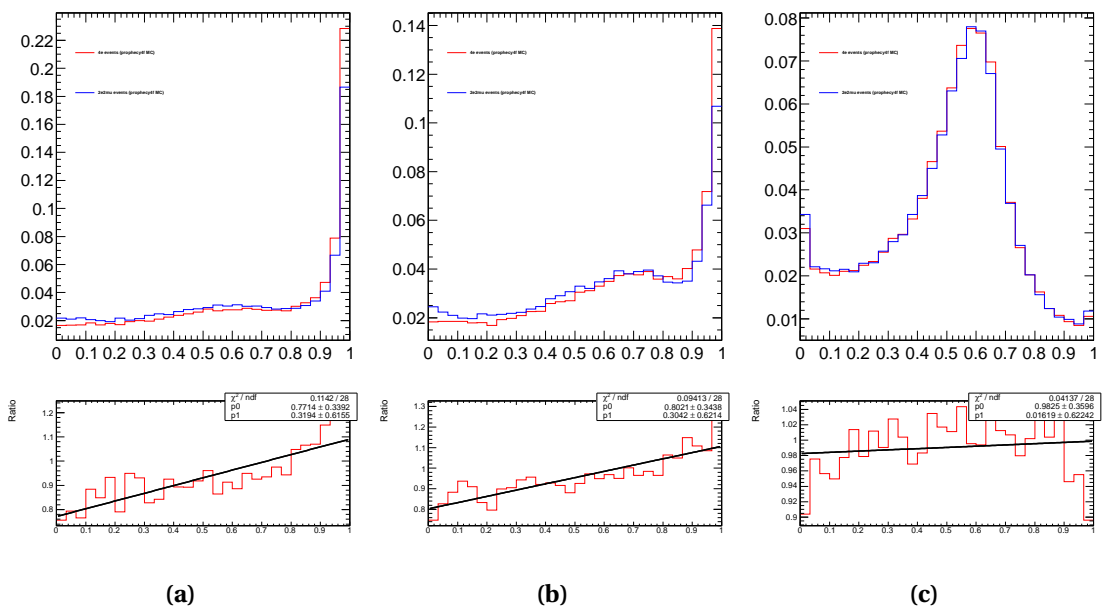


Figure 12.7: Distribution of signal MELA KD with and without interference effects and the ratio. Several m_H hypotheses are shown: (a) 120, (b) 125 and (c) 160 GeV.

Chapter 12: Kinematic Discriminant

Due to kinematic dependence on the mass, the KD is highly correlated with the value of the $m_{4\ell}$. This correlation must be included for any further analysis of the data which uses KD. The dominant background in full mass range is $q\bar{q} \rightarrow ZZ$. The secondary contribution comes from $Z + X$ background below $2m_Z$ threshold, and $gg \rightarrow ZZ$ background above the threshold. The ideal angular and mass distributions for the signal, $q\bar{q} \rightarrow ZZ$ and $gg \rightarrow ZZ$ background, come from basic quantum mechanics given the EWK couplings and are modelled well by MC.

The mis-modelling of lepton efficiency and resolutions may change the KD distribution. By making extreme variations, we estimate that those have very small effects on KD distributions. This is because, as opposed to $m_{4\ell}$, there is no distinct peak and smearing of broad distribution is a small effect. Figure 12.8a shows the effect on the KD shape due to extreme variation of MC efficiency by changing the tag-and-probe per-lepton scale factors from those obtained from data to flat ones which is normally a variation larger than the errors. Figure 12.8b shows an example of the shape variation due to extreme resolution variation in MC for the $H \rightarrow ZZ \rightarrow 4e$ channel. Since these detector related effects are somewhat smaller than statistical effects, we ignore them in systematic uncertainties for the KD.

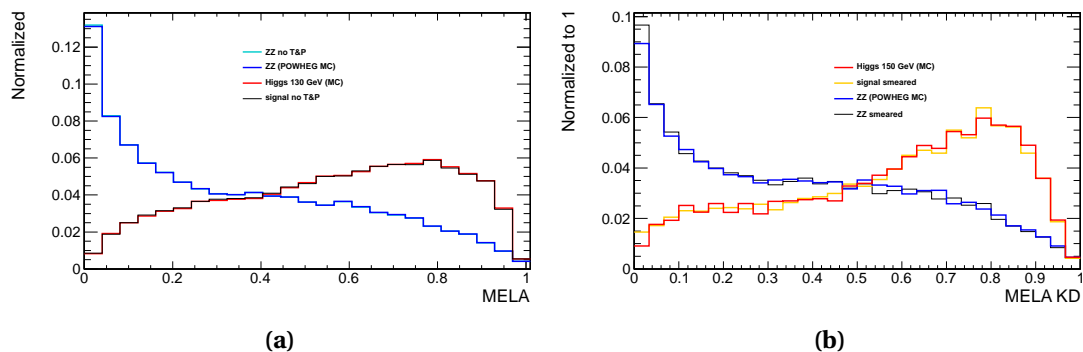


Figure 12.8: Distribution of the MELA KD for ZZ background and Higgs signal in MC, for events below $2m_Z$ threshold. For both signal and background two very close distributions are shown: (a) with and without the tag-and-probe corrections for data-MC differences; (b) with and without smearing of electron energy resolution, which is equal to uncertainty on this resolution. Only $H \rightarrow ZZ \rightarrow 4e$ channel is considered here.

In order to check the effect of background parametrization to KD we show in Fig. 12.9 the comparison of the KD distributions in several $m_{4\ell}$ slices below threshold for data control sample for $Z + X$ background, MC control sample for $Z + X$ background, and for MC POWHEG simulation of $q\bar{q} \rightarrow ZZ$ background. We observe a good agreement between the $Z + X$ background parameterization in data and simulation. This gives us confidence in the $Z + X$ background estimation. Another thing we see is that the data-driven $Z + X$ background distributions and continuum $q\bar{q} \rightarrow ZZ$ distribution are in good agreement. Therefore, a joint background parameterization can be used, and potential differences can be treated as systematic uncertainty. To include systematics in the analysis, we create alternative KD distributions according to the linear fit slope and its error by re-scaling the distributions

12.4. MELA for Spin-Parity Properties Measurements

according to that slope (with error on the slope added), as shown in Fig. 12.9. The shape of the KD changes to some extent as a function of $m_{4\ell}$, but its main feature remains, background is pushed towards zero and signal towards one.

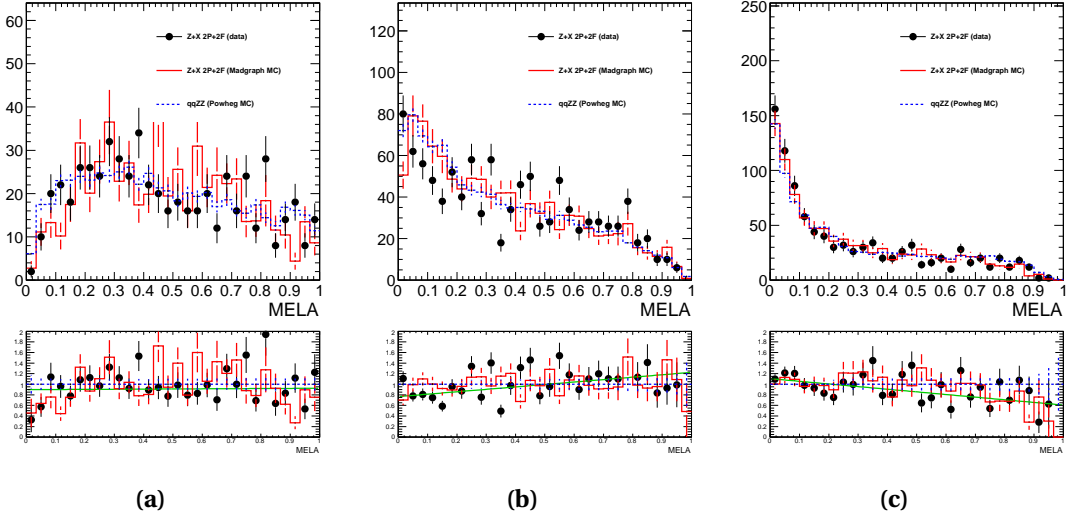


Figure 12.9: Parameterization of background MELA KD in $m_{4\ell}$ ranges: (a) [100,120], (b) [120,140], (c) [140,160] GeV. Points(red solid histogram) show data(MC) control sample for $Z + X$ background, blue dashed histogram shows MC POWHEG simulation of ZZ background. Bottom plots show the ratio between the $Z + X$ and ZZ background distributions.

12.4 MELA for Spin-Parity Properties Measurements

The new boson has been observed at the LHC, and now the focus of the analysis moves from the search to the measurements of its properties. It is crucial to determine the spin and parity quantum numbers of the new particle and its couplings to SM fields with great accuracy. These studies have been presented in Ref. [128, 131] and, internally to CMS in Ref. [132]. For this analysis, we profit from a simplified version of that approach using the MELA methodology in Sec. 12.1, where the signal-to-background probability ratio is replaced by the probability ratio for two signal hypotheses in the following way:

$$\mathcal{D}_{J^P} = \frac{\mathcal{P}_{SM}}{\mathcal{P}_{SM} + \mathcal{P}_{J^P}} = \left[1 + \frac{\mathcal{P}_{J^P}(m_1, m_2, \vec{\Omega} | m_{4\ell})}{\mathcal{P}_{SM}(m_1, m_2, \vec{\Omega} | m_{4\ell})} \right]^{-1}. \quad (12.4)$$

The $\vec{\Omega}$ in the above expression represents five angles describing production and decay kinematics of the boson in its frame, \mathcal{P}_{SM} is the probability distribution for the SM Higgs boson hypothesis, and \mathcal{P}_{J^P} is the probability for an alternative model. These probabilities are calculated analytically in Ref. [128].

In this analysis we consider two spin-parity alternative models, one is the pure pseudo-scalar

state $J^P = 0^-$ and the other is the spin-two state with the minimal graviton-like coupling to the bosons with $J^P = 2^+$. The most general decay amplitude for a spin-zero boson can be defined as

$$A = v^{-1} \epsilon_1^{*\mu} \epsilon_2^{*\nu} \left(a_1 g_{\mu\nu} m_H^2 + a_2 q_\mu q_\nu + a_3 \epsilon_{\mu\nu\alpha\beta} q_1^\alpha q_2^\beta \right) = A_1 + A_2 + A_3, \quad (12.5)$$

where ϵ_i are the Z boson polarization vectors, q_i are their momenta, and $q = q_1 + q_2$. The A_1 amplitude dominates in the SM Higgs boson decay, while the $J^P = 0^-$ state decay is expected to be dominated by the A_3 . The \mathcal{D}_{0^-} discriminant is therefore optimal for discrimination between the $|A_1|^2$ and $|A_3|^2$ amplitudes. We find their potential interference to have negligible effect on the discriminant distribution or the overall yield of events. We define the parameter $f_{a3} = |A_3|^2 / (|A_1|^2 + |A_3|^2)$, where we neglect the $|A_2|^2$ contribution. This parameter allows us to provide consistency tests of the $f_{a3} = 0$ and $f_{a3} = 1$ scenarios, as well as consider contribution of both amplitudes in the decay. The f_{a3} parameter is not a parameter which defines the mixture of parity-even and parity-odd states, because this would require model-dependent interpretation of the f_{a3} measurement. For the SM, f_{a3} is expected to be zero.

To illustrate the power of this approach, we use a narrow resonance at 125 GeV with scalar ($J^P = 0^+$) and pseudo-scalar ($J^P = 0^-$) Higgs hypothesis. The alternative hypotheses sample is produced with the generator from Ref. [128], the so-called JHU generator. The seven observables $\{m_1, m_2, \vec{\Omega}\}$, discussed in Sec. 12.1, are different for resonances with different quantum numbers, as shown in Fig. 12.10 and Fig. 12.11 with samples generated according to the $J^P = 0^+$ and $J^P = 0^-$ hypotheses.

Figure 12.12(left) shows distributions of the kinematic discriminant \mathcal{D}_{0^-} for scalar to pseudoscalar discrimination, the so-called “*pseudoMELA*”. These are shown for the reconstructed four-lepton invariant mass in the range [120 – 130] GeV, for signal and background. The right-hand side of the same figure shows distributions of the discriminant \mathcal{D}_{2^+} which is optimized for separation of SM Higgs boson and graviton-like minimal couplings hypothesis $J^P = 2^+$, the so-called “*graviMELA*”. For illustration we show in Fig. 12.13, the distribution of the angles after the reconstruction, acceptance and full analysis selection for pseudoscalar, graviton, scalar signal, and background, in the $m_{4\ell}$ region $120 < m_{4\ell} < 130$ GeV.

Separating SM background events from signal events is essential to achieve the best discrimination power. In an ideal case, the fit should include the three observables: $m_{4\ell}$, KD and alternative hypothesis discriminant. Due to statistical limitation of the current simulated samples, this approach has not been used for the present analysis. Instead, a statistically equivalent approach, that allows for a simpler 2D analysis, has been developed. The kinematic discriminant for signal to background separation is replaced by the \mathcal{D}_{J^P} which discriminates the two signal hypotheses. The $m_{4\ell}$ PDF is combined with the kinematic probability of the angular and mass distributions from the KD calculation into a single discriminant, so-called

12.4. MELA for Spin-Parity Properties Measurements

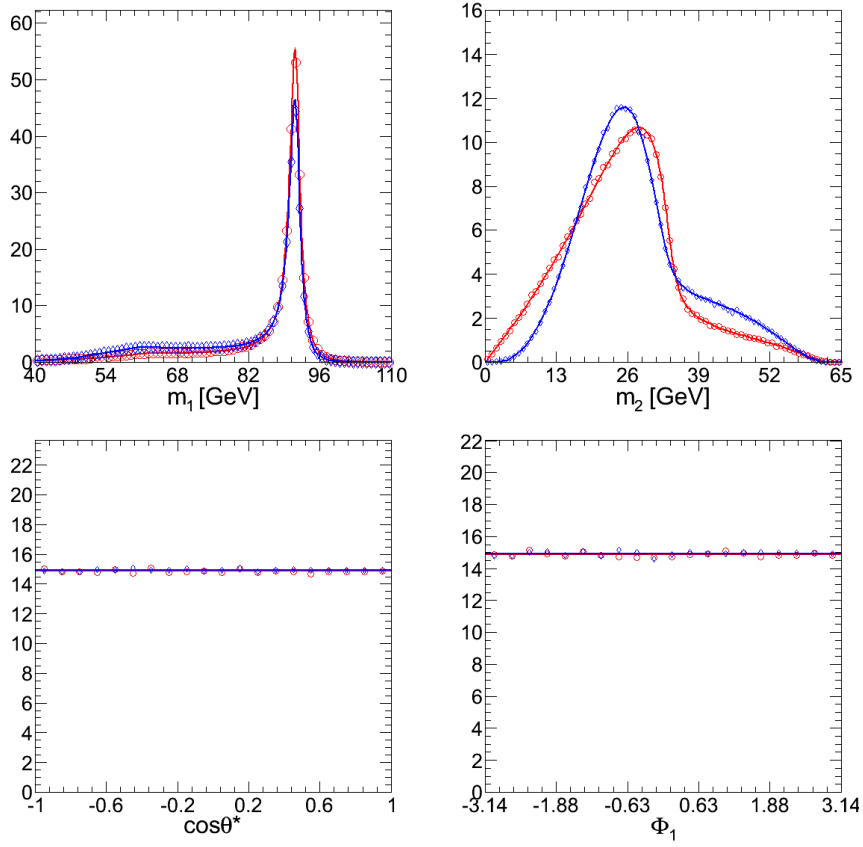


Figure 12.10: Distribution of the observables m_1 , m_2 (top row), $\cos\theta^*$, and Φ_1 (bottom row), generated for $m_X = 125$ GeV with leading order JHU generator events and projections of the ideal angular distributions. Two resonance hypotheses are shown: $J^P = 0^+$ (red) and 0^- (blue).

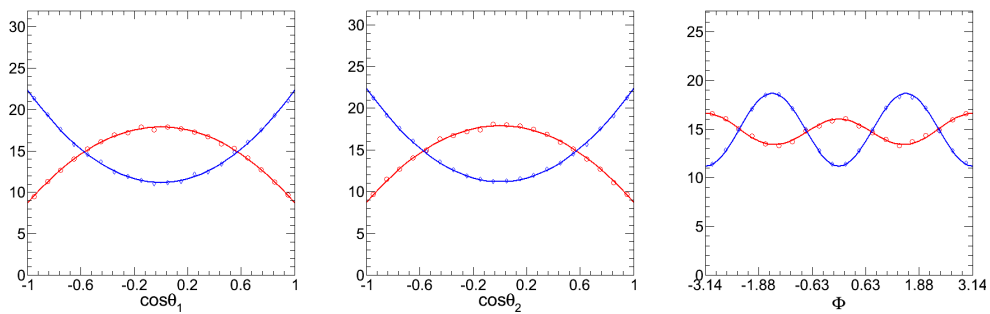


Figure 12.11: Distribution of the observables $\cos\theta_1$, $\cos\theta_2$, and Φ generated for $m_X = 125$ GeV with leading order JHU generator events and projections of the ideal angular distributions. Two resonance hypotheses are shown: $J^P = 0^+$ (red) and 0^- (blue).

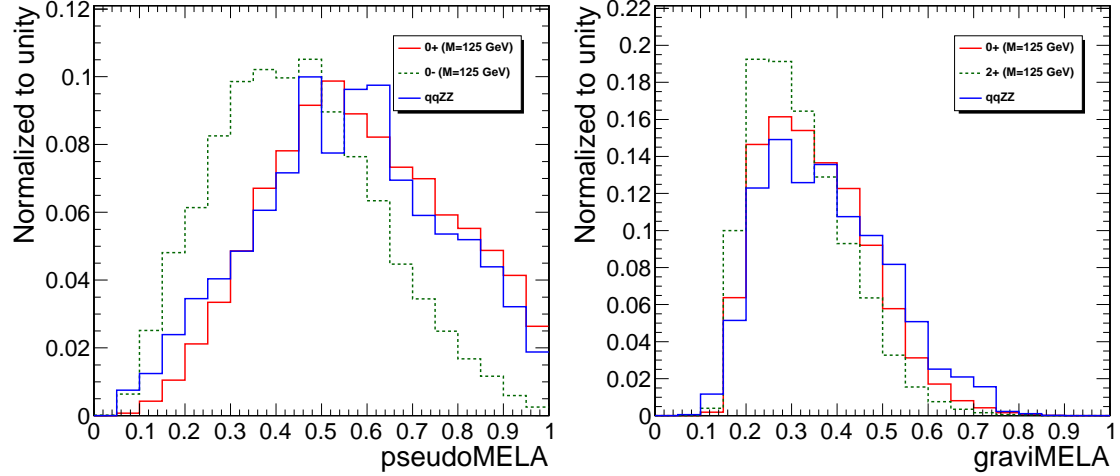


Figure 12.12: Distributions of the \mathcal{D}_{0^-} (pseudoMELA) discriminant (for scalar-to-pseudoscalar separation, left) and \mathcal{D}_{2^+} (graviMELA) discriminant (for scalar-to-spin-two separation, right). The distributions are shown for mass around 125 GeV and for signal (0^+ red, 0^- green, 2^+ KK graviton magenta) and background (blue).

Super MELA Discriminant (“superMELA”),

$$SMD = \frac{\mathcal{P}_{\text{sig}}}{\mathcal{P}_{\text{sig}} + \mathcal{P}_{\text{bkg}}} = \left[1 + \frac{\mathcal{P}_{\text{bkg}}(m_1, m_2, \vec{\Omega} | m_{4\ell}) \times \mathcal{P}_{\text{bkg}}(m_{4\ell})}{\mathcal{P}_{\text{sig}}(m_1, m_2, \vec{\Omega} | m_{4\ell}) \times \mathcal{P}_{\text{sig}}(m_{4\ell})} \right]^{-1}, \quad (12.6)$$

where probabilities \mathcal{P} also include the $m_{4\ell}$ parameterizations. From the statistical point of view, the analysis of the SMD discriminant is equivalent to the 2D analysis of the $m_{4\ell}$ and KD distributions. Finally, the spin-parity hypothesis analysis is performed as a 2D analysis of the $(\mathcal{D}_{\text{bkg}}, \mathcal{D}_{J^P})$ distributions with correlations of observables included in parameterizations.

Figure 12.14 shows the SMD distributions for two signal hypotheses of mass 125 GeV and the irreducible background in case of $4e$ final state. We observe that both signal hypothesis peak at one while background tends to peak at zero. To demonstrate the signal to background discrimination power brought by the SMD, the ROC curves for SMD and KD after all selections and in an invariant mass window of $105 < m_{4\ell} < 140$ GeV are shown in Fig. 12.15. The obvious gain in background rejection power of the SMD variable is expected since $m_{4\ell}$, the single most powerful discriminant for background, is incorporated into the discriminant.

12.4. MELA for Spin-Parity Properties Measurements

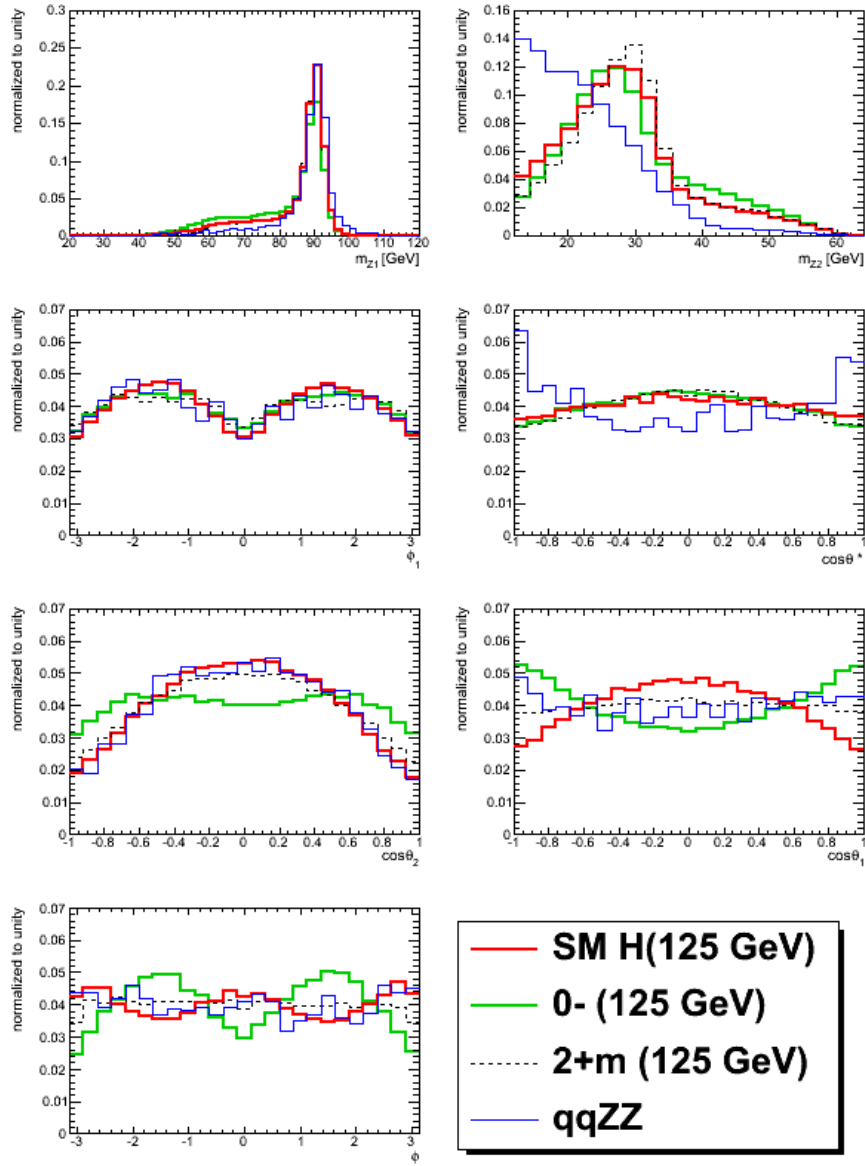


Figure 12.13: Distribution of angles and dilepton masses in the region $120 < m_{4\ell} < 130$ for different spin hypothesis (pseudoscalar and minimal-couplings graviton) compared with SM signal and $qqZZ$ background.

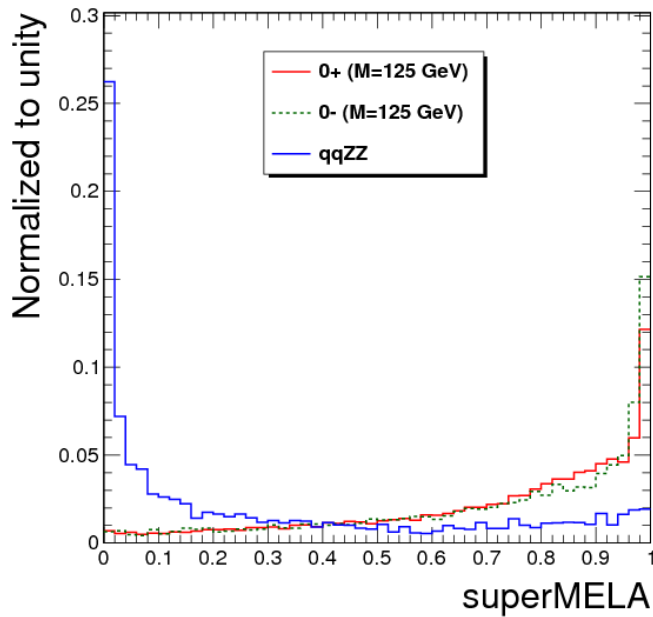


Figure 12.14: Distribution of SMD for 125 GeV SM Higgs and irreducible background events in the range $105 < m_{4\ell} < 140$ GeV for the $4e$ channel.

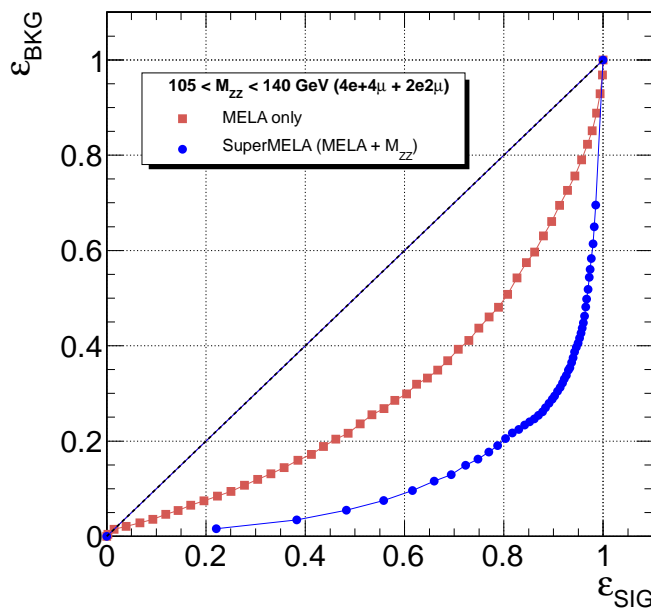


Figure 12.15: ROC curve using MELA (red square markers) or SMD (blue dots)

13 Statistical Analysis

After having discussed event selection in Ch. 8, signal parametrization in Ch. 9 and backgrounds description in Ch. 10 and 11, we are now ready to go for the final analysis results by making a proper statistical interpretation.

For the 2012 analysis we have chosen to profit from additional knowledge based on full kinematic information available in the Higgs boson event. Therefore, the two-dimensional distribution of four-lepton mass ($m_{4\ell}$) and kinematic discriminant (KD) described in chapter 12 is used to evaluate the exclusion limits and the significance of excesses. In addition to kinematic discriminant we also introduce an advanced analysis technique using mass resolutions assessed on the per-event basis. This is done via three-dimensional distributions explained in Sec. 13.2.

After finding the boson it is of extreme importance to measure its properties. For this purpose we use the approach with kinematic discriminant prepared for discriminating between various spin and parity hypothesis. Methodology for this measurement is described in Sec. 13.3.

13.1 Methodology of using 2D Distributions

Besides four-lepton invariant mass, we make use of the full kinematic information from the Higgs boson decay by combining them into two-dimensional distribution used for hypothesis testing, i.e. to obtain significance of excesses in terms of p-value and exclusion limits.

Based on event final state ($4\mu, 4e, 2e2\mu$) and LHC centre of mass energy (7 and 8 TeV) we split selected events into six categories and form unbinned distributions ($m_{4\ell}, \text{KD}$). These events are then used to test the null (only *background*) and the alternative (*background + signal*) hypothesis for 183 Higgs boson masses in range from 110 to 600 GeV. The mass steps are not uniform, i.e. they were chosen considering both, expected width (Γ) and the $m_{4\ell}$ resolution as described in Ref. [104]. For each mass point, we perform A simultaneous maximum likelihood fit of the six ($m_{4\ell}, \text{KD}$) distributions is then performed on each mass point as discussed in Ref. [104]. In reporting limits on Higgs boson cross-section, we adopt the modified frequentest

construction CL_s [133, 134, 104].

The 2D probability distribution function $\mathcal{P}(m_{4\ell}, \text{KD})$ for signal and background is constructed as

$$\mathcal{P}_{\text{sig}}(m_{4\ell}, \text{KD}) = \mathcal{P}_{\text{sig}}^{\text{1D}}(m_{4\ell}) \times \mathcal{T}_{\text{sig}}(m_{4\ell}, \text{KD}) \quad (13.1)$$

$$\mathcal{P}_{\text{bkg}}(m_{4\ell}, \text{KD}) = \mathcal{P}_{\text{bkg}}^{\text{1D}}(m_{4\ell}) \times \mathcal{T}_{\text{bkg}}(m_{4\ell}, \text{KD}) \quad (13.2)$$

where $\mathcal{P}_{\text{sig}}^{\text{1D}}(m_{4\ell})$ and $\mathcal{P}_{\text{bkg}}^{\text{1D}}(m_{4\ell})$ are the analytical functions used for 1D fits. Parametrization of distribution $\mathcal{P}_{\text{bkg}}^{\text{1D}}(m_{4\ell})$ for background is obtained using empirical functions from simulation in case of ZZ and from control regions in case of $Z + X$ background as discussed in Ch. 10 and 11. Higgs signal distribution after reconstruction is described with relativistic Breit-Wigner convoluted with a two-sided Crystal-Ball function [135] as discussed in Ch. 9. The 2D distributions $\mathcal{T}_{\text{sig}}(m_{4\ell}, \text{KD})$ and $\mathcal{T}_{\text{bkg}}(m_{4\ell}, \text{KD})$ are simple 2D histogram templates normalized in KD direction at any given value of $m_{4\ell}$. In this way we ensure that projections of the functions in Eqs. (13.1) and (13.2) to $m_{4\ell}$ axis are identical to analytical distributions $\mathcal{P}_{\text{sig}}^{\text{1D}}(m_{4\ell})$ and $\mathcal{P}_{\text{bkg}}^{\text{1D}}(m_{4\ell})$. These template distributions are created from simulation and are shown in Figs. 13.1 and 13.2 for low and high mass ranges, respectively.

Different electron and muon p_T thresholds and efficiencies effect kinematics of Higgs boson decay in the low mass range. Therefore, we have to separate KD distributions for each decay channel. At high masses, low transverse momentum thresholds do not affect kinematics and we join template distributions for all final states. In addition, 7 and 8 TeV samples are combined since kinematics is the same in both cases. Due to limited statistics in the background MC samples available, Background samples lack statistics giving rise to bins which are purely populated, or even unpopulated at high mass tails of the $m_{4\ell}$ distribution. This is solved by averaging over the range of 3×3 bins for $m_{4\ell} < 180$ GeV, 5×5 for $180 < m_{4\ell} < 300$ GeV and 7×7 for $m_{4\ell} > 300$ GeV. In addition to averaging, there is an overall protection to ensure that no bin has a zero probability.

Both $q\bar{q} \rightarrow ZZ$ and $Z + X$ background can be described by the same templates as previously shown. Systematic errors cover any small potential difference and is taken to be 100% correlated between different final states and run periods.

13.1. Methodology of using 2D Distributions

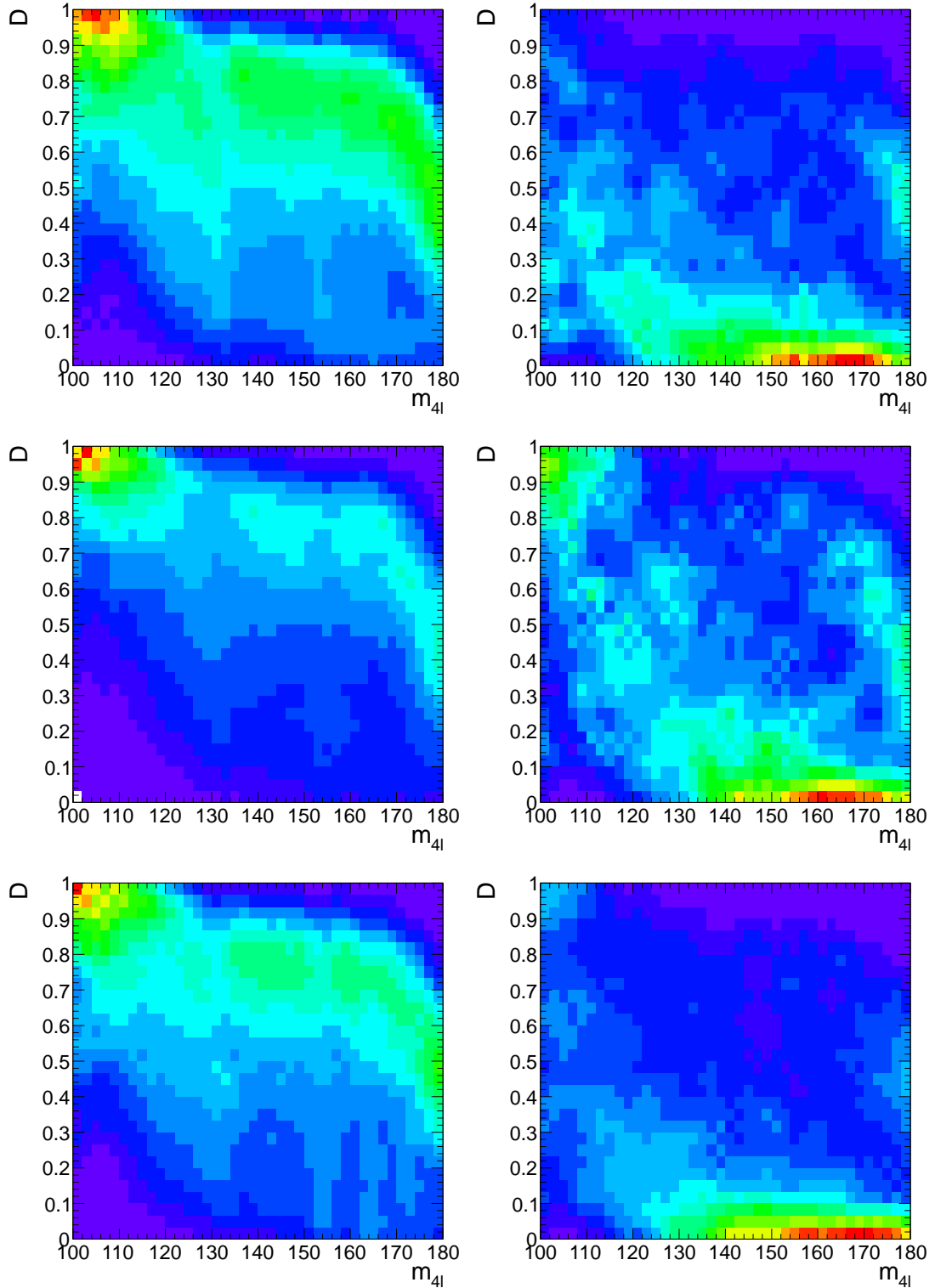


Figure 13.1: Parameterization signal and $q\bar{q} \rightarrow ZZ$ background template distributions $\mathcal{T}_{\text{sig}}(m_{4\ell}, \text{KD})$ (left) and $\mathcal{T}_{\text{bkg}}(m_{4\ell}, \text{KD})$ (right) from Eqs. (13.1) and (13.2) in three channels: $2e2\mu$ (top), $4e$ (middle), and 4μ (bottom).

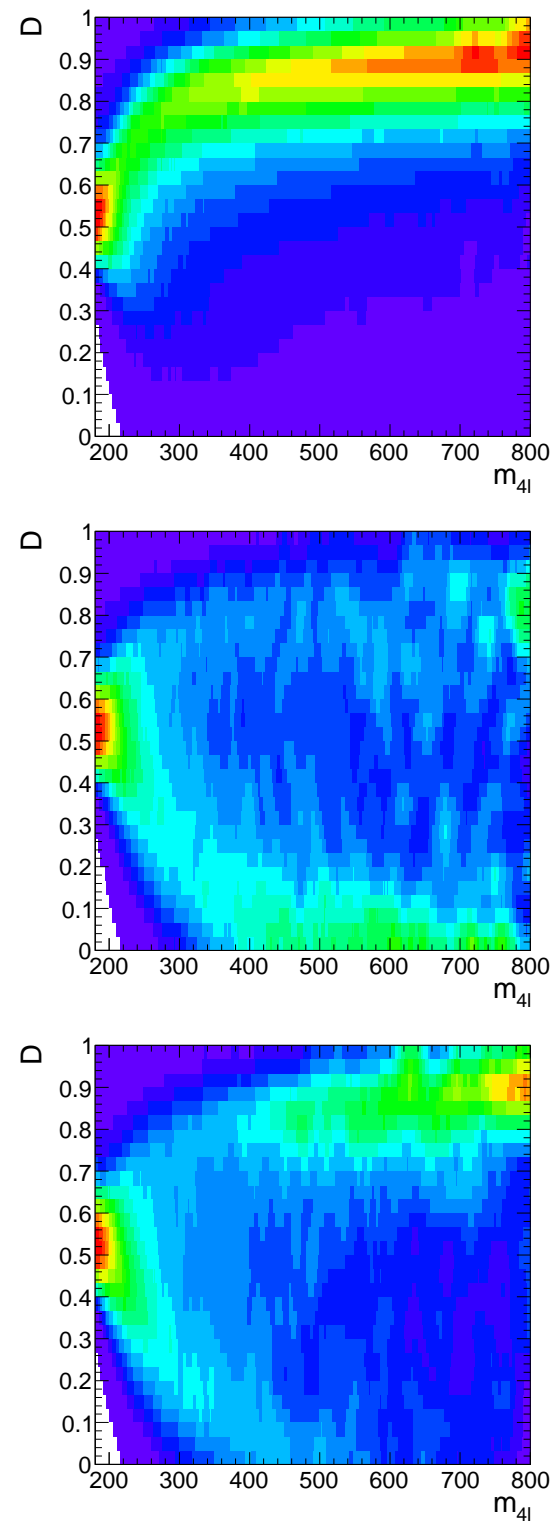


Figure 13.2: Parameterization of template distributions $\mathcal{T}(m_{4\ell}, \text{KD})$ for signal (top), $q\bar{q} \rightarrow ZZ$ background (middle), and $gg \rightarrow ZZ$ background (bottom).

13.2 Methodology of using 3D Distributions

Including knowledge of per-event four lepton invariant mass errors (EBE) brings additional knowledge and therefore is useful for the statistical treatment of selected events. However, the gain in sensitivity by including per-event mass errors is not expected to be as much as in $H \rightarrow \gamma\gamma$ search, where events with better $m_{\gamma\gamma}$ resolution have smaller backgrounds. In the case of the $H \rightarrow ZZ^{(*)} \rightarrow 4\ell$ analysis, the $m_{4\ell}$ error observable does not help in improving the signal-to-background discrimination. The whole gain comes solely from the proper accounting for the signal mass resolutions for individual events.

To construct the 3D probability distribution we proceed in two steps similar to construction of 2D PDF. First, we construct 2D conditional PDF for mass error versus four lepton invariant mass

$$\mathcal{P}_{\text{sig}}(m_{4\ell}, EBE) = \mathcal{P}_{\text{sig}}^{\text{1D}}(m_{4\ell}) \times \mathcal{P}_{\text{sig}}(EBE|m_{4\ell}) \quad (13.3)$$

$$\mathcal{P}_{\text{bkg}}(m_{4\ell}, EBE) = \mathcal{P}_{\text{bkg}}^{\text{1D}}(m_{4\ell}) \times \mathcal{P}_{\text{bkg}}(EBE|m_{4\ell}) \quad (13.4)$$

where the width (σ) of the Crystal Ball for signal is replaced with mass error for each event.

Then we include the kinematic discriminant and construct a 3D PDF as follows

$$\mathcal{P}_{\text{sig}}(m_{4\ell}, EBE, KD) = \mathcal{P}_{\text{sig}}^{\text{1D}}(m_{4\ell}) \times \mathcal{P}_{\text{sig}}(EBE|m_{4\ell}) \times \mathcal{P}_{\text{sig}}(KD|m_{4\ell}) \quad (13.5)$$

$$\mathcal{P}_{\text{bkg}}(m_{4\ell}, EBE, KD) = \mathcal{P}_{\text{bkg}}^{\text{1D}}(m_{4\ell}) \times \mathcal{P}_{\text{bkg}}(EBE|m_{4\ell}) \times \mathcal{P}_{\text{bkg}}(KD|m_{4\ell}) \quad (13.6)$$

This construction is based on the assumption that there is no correlation between mass error and KD which was validated by looking at the distributions of mass error versus KD. Figure 13.3 illustrates in case of $4e$ final state that there is no correlation between mass error and KD in both, signal and ZZ background samples.

An additional test to check for potential bias due to unaccounted correlation naturally built in those samples a study was performed with fully simulated Monte Carlo samples. It has been shown that there is no bias and that the error of the mass measurement are correctly calculated [106].

To check improvement on the performance for the various scenarios 4 sets of data cards were created:

- 1D: $m_{4\ell}$
- 2D: $m_{4\ell}$ vs. KD
- 2D: $m_{4\ell}$ vs. EBE
- 3D: $m_{4\ell}$ vs. KD vs. EBE.

Chapter 13: Statistical Analysis

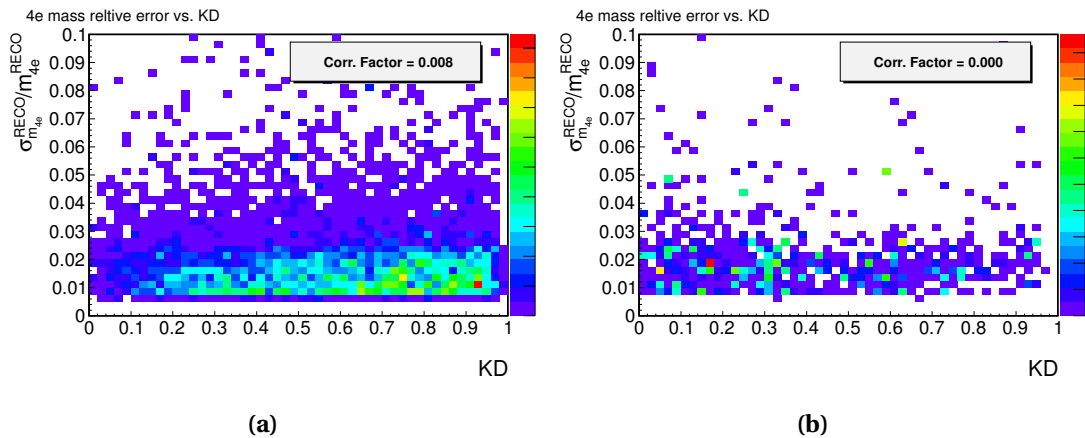


Figure 13.3: 4-lepton mass error versus KD distributions (points) in 4e final state for 125 GeV Higgs signal (left) and ZZ (right) simulated samples. The correlation factors are displayed on the figures as well.

For the study, the ICHEP2012 8 TeV data (5.3fb^{-1}) was used after rescaling the integrated luminosity to 20fb^{-1} . Then, we generate 20 000 toy experiments from the 3D data cards with $m_H = 125\text{ GeV}$ and SM signal strength. Statistical analysis are performed on these toys and for 4 sets data cards separately.

The fitted mass and its uncertainty of each toy are shown in the Fig. 13.4 (top). One can expect on average the uncertainty of mass measurement is improved by 7% when using mass errors. Figure 13.4 (bottom) shows the scatter distribution of two measured mass errors from 2D ($m_{4\ell}$ vs. KD) and 3D fits. One can see that the measured mass errors are smaller (more accurate) with 3D fitting.

Figure 13.5 (left) shows the distributions of significance of the 4 sets of data cards based on the above toys. By including per-event mass error, the expected significance can be improved by 3%. Figure 13.5 (right) shows the best fitted signal strength, on which there is no improvement as RMS is almost the same for all four methods of fitting.

13.2. Methodology of using 3D Distributions

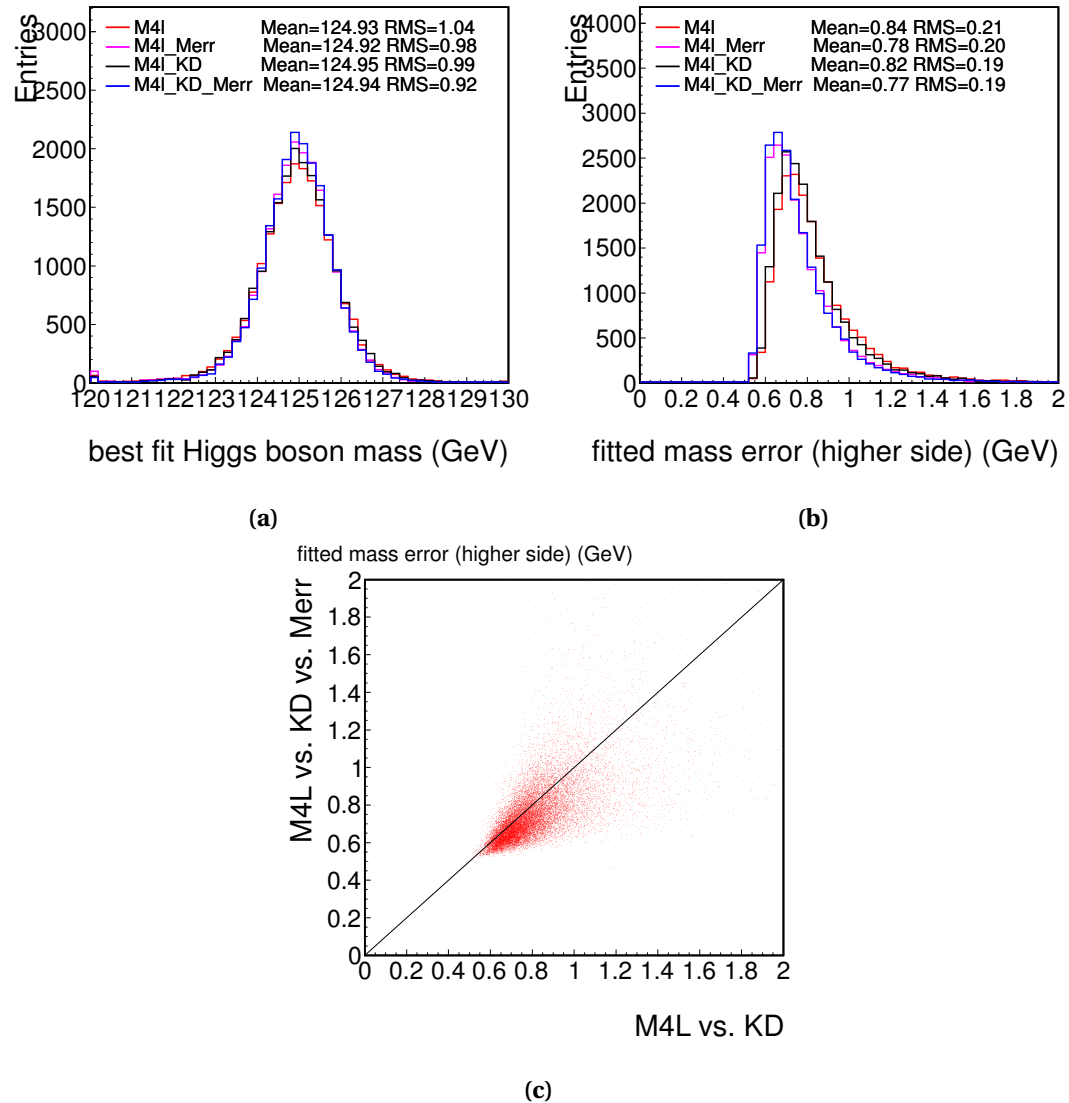


Figure 13.4: Expected distribution of fitted mass (top left) and its uncertainty (top right) from 4 sets of data cards for 20fb^{-1} 8 TeV data. In bottom, it's the scatter distribution of two measured mass errors from 2D ($m_{4\ell}$ vs. KD) and 3D fittings.

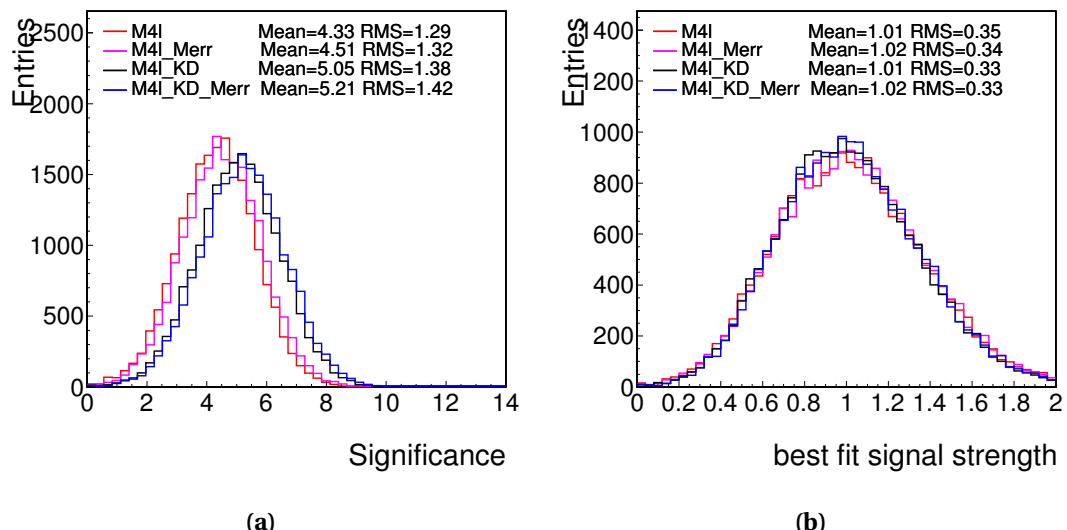


Figure 13.5: Expected significances (left) and signal strength (right) from 4 sets of data cards for 20fb^{-1} 8 TeV data.

13.3 Methodology for Spin and Parity Measurements

To distinguish between spin and parity hypothesis, for example 0^+ and 0^- , we build the (SMD, pseudoMELA) 2D template distribution, instead of the 2D (MELA, $m_{4\ell}$) from section 13.1. The SMD and pseudoMELA are described in Sec. 12.4. For SMD computation, a fixed mass value $m_H = 125$ GeV has been chosen to parametrize the P_{sig} in Eq. 12.6. Figure 13.6 shows the standard 2D templates using as input for the calculation the SM qqZZ background, a SM Higgs with $m_H = 125$ GeV and a pseudoscalar Higgs with $m_H = 125$ GeV, for the three decay channels separately. Then, the likelihood ratio $2\ln(\mathcal{L}_1/\mathcal{L}_2)$ with the likelihood \mathcal{L} evaluated for the two models is used with the signal strength (μ) in the fit left free to float as nuisance parameter.

The systematic uncertainties included in the nominal analysis are incorporated in the hypothesis separation analysis as well. To include uncertainty from lepton scale and resolution on the mass distribution of the signal, alternative SMD templates with $m_{4\ell}$ scaled and smeared are created, as in Fig. 13.7. During the likelihood calculation in statistical analysis, a morphing between the nominal and alternative templates is applied. The uncertainty on the shape of the template for the Z+X background is applied in a similar fashion. The template for the Z+X is obtained from data in the Z+X control region. Similar to the nominal analysis, we use the shape of the qqZZ template as a shape systematic. This can be justified from Fig. 13.8, where we see that the shapes of \mathcal{D}_{0^-} (pseudoMELA) and SMD for $Z + X$ background could be well modelled by the $q\bar{q} \rightarrow ZZ$ only. This covers conservatively uncertainties on the shape of both SMD and \mathcal{D}_{0^-} (pseudoMELA) for the Z+X background, uncertainties that could be due both to differences between control and signal region and to limited statistics in the control region.

The interference of identical leptons in the final state ($4e$ and 4μ) is not included in fully simulated samples. In addition, the alternative spin-parity signal simulation is available for 125 GeV but not for 126 GeV Higgs boson mass hypothesis. Both effects are accounted for by applying re-weighting procedure of the (SMD, \mathcal{D}_{0^-}) templates obtained from full simulation using the ratio of expectation from generator-based simulation with interference at 126 GeV. These correction factors and expected change in the distributions are shown in Fig. 13.9, where we see that the correction to the spin-zero samples is stable.

Chapter 13: Statistical Analysis

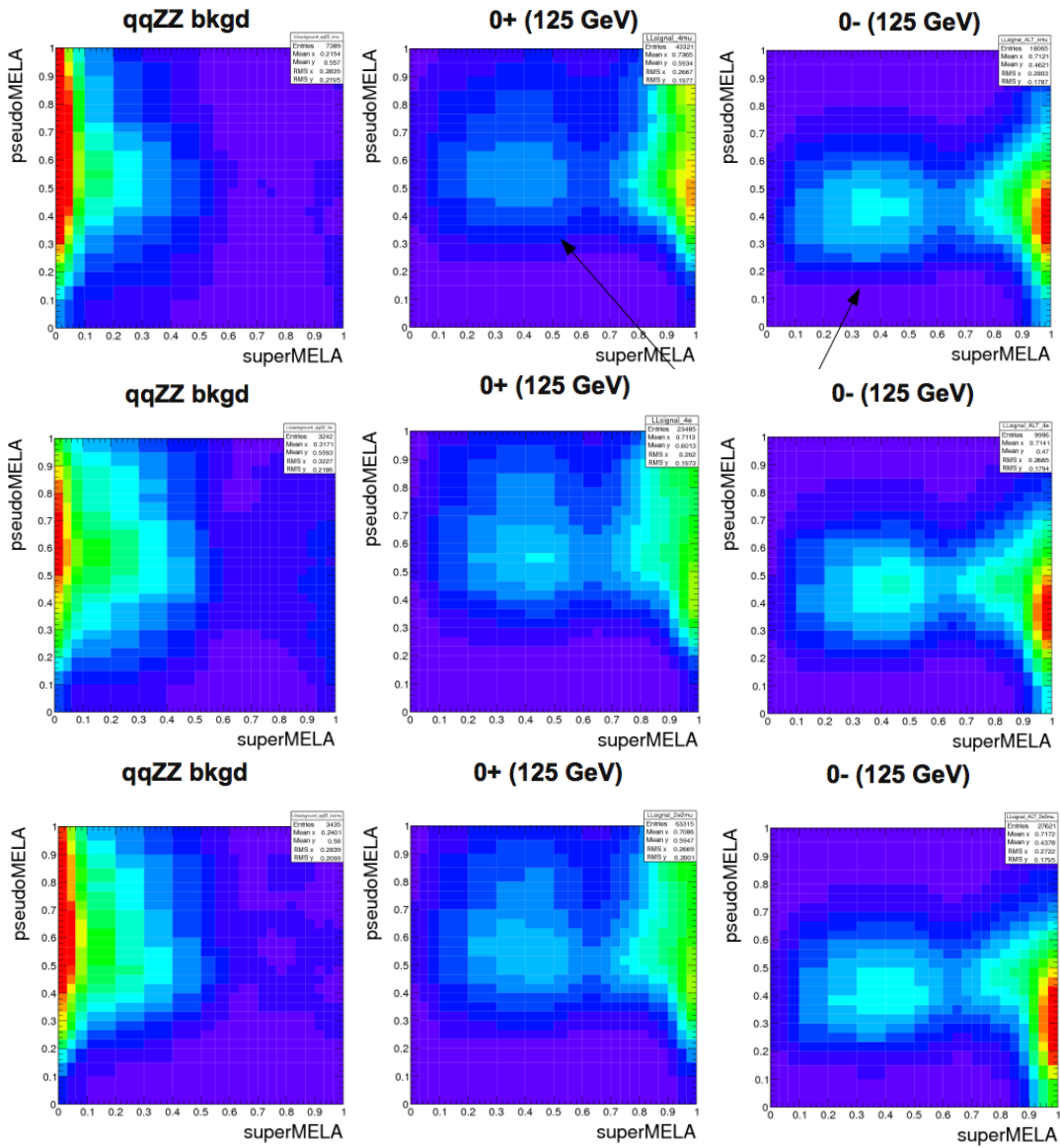


Figure 13.6: Two-dimensional templates (SMD, pseudoMELA) used for the spin and CP property measurement. The templates are presented separately for the 4μ (top row), $4e$ (middle row) and $2e2\mu$ (bottom row), respectively. In each row, the left-hand side plot shows the template for the simulation of the SM qqZZ background, while the central plot refers to the SM Higgs ($m_H = 125$ GeV) and the right-hand side plot to a pseudoscalar Higgs ($m_H = 125$ GeV). All templates are produced from 8 TeV MC with a cut $105 < m_{4\ell} < 140$ GeV.

13.3. Methodology for Spin and Parity Measurements

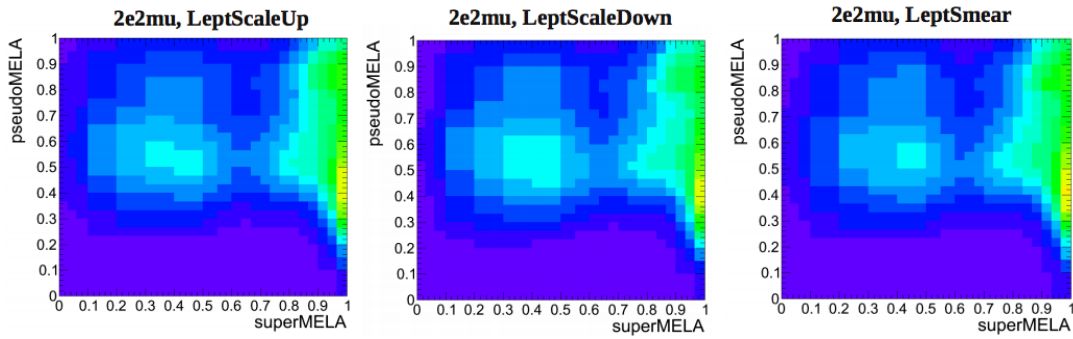


Figure 13.7: Alternative (SMD, \mathcal{D}_{0-}) 2D templates used as shape systematics for the signal in the $2e2\mu$ channel. Left: lepton scale shifted up by one sigma; Center: lepton scale shifted down by one sigma; Right: lepton energy smeared up by resolution. All templates are shown with a cut $105 < m_{4\ell} < 140$ GeV.

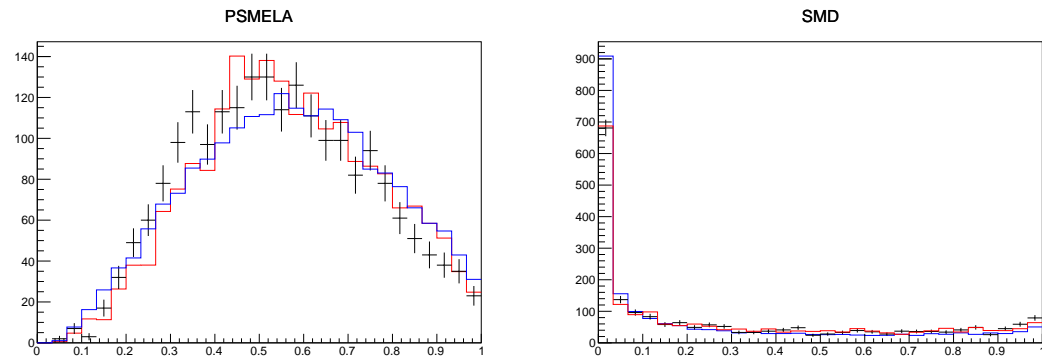


Figure 13.8: Distribution of \mathcal{D}_{0-} (left) and SMD (right) for $Z + X$ background in the control sample for data (black points), MC (red histogram) and for $q\bar{q} \rightarrow ZZ$ MC (blue solid histogram). The plot is presented for the mass range $105 < m_{4\ell} < 140$ GeV.

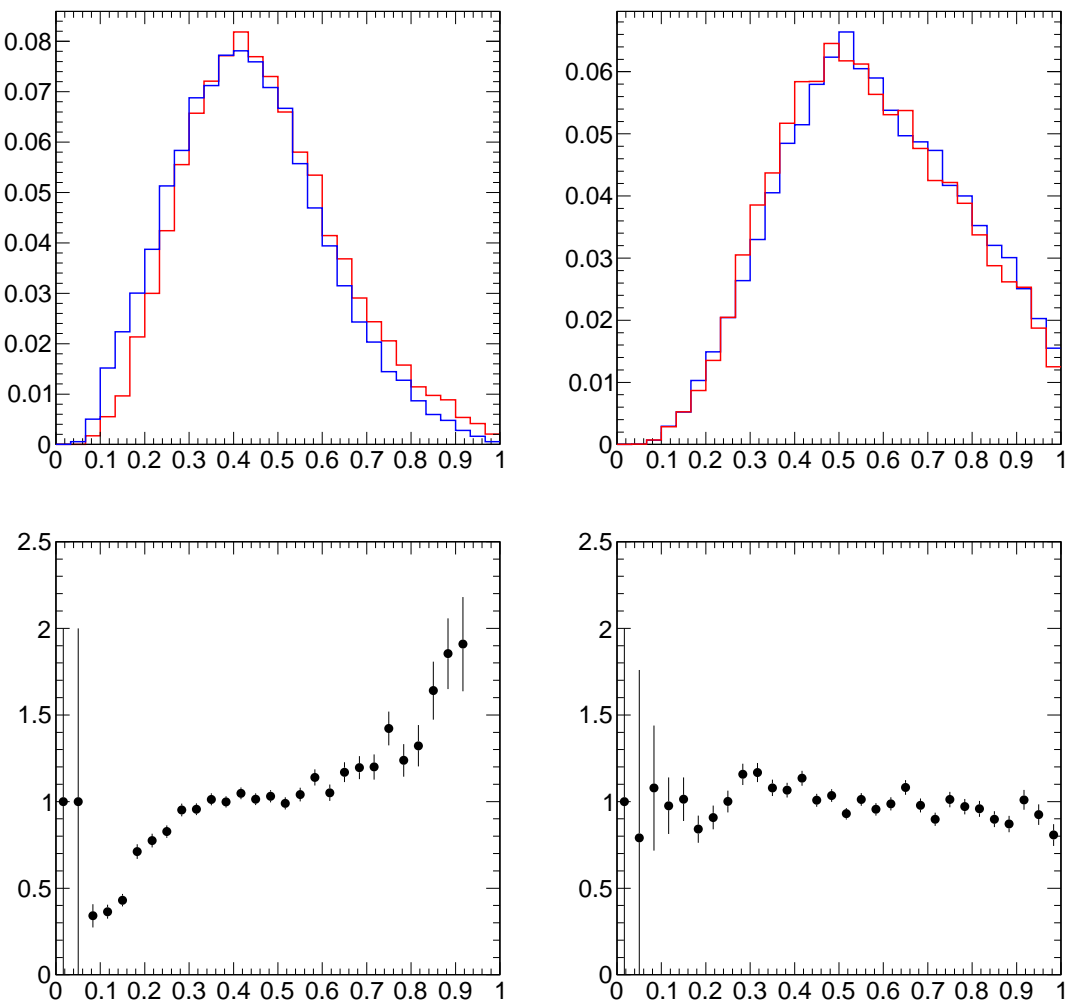


Figure 13.9: Top: Distribution of \mathcal{D}_{0^-} for 0^- (left) and 0^+ (right) samples before (blue) and after (red) effects of interference and mass change from 125 to 126 GeV are included. Bottom: re-weighting correction to the 0^- (left) and 0^+ (right) distributions of \mathcal{D}_{0^-} , in the 4μ channel.

Bingo! Part V

14 Final Results

In previous chapters we have defined all the tools and ingredients needed to bring final results.

The relevant event distributions and yields of the event selection together with the discussion on sources of uncertainties is presented in Sec. 14.1.

We discuss final results of the search for the Higgs boson by setting up exclusion limits in Sec. 14.2 and significance of local excesses of events in Sec. 14.3.

Since a new boson has been discovered it is crucial to measure its properties: invariant mass, and than spin-parity quantum numbers. The results of these measurements are discussed in Sec. 14.4 and Sec. 14.5.

14.1 Summary of Selection and Systematic Uncertainties

14.1.1 Event Yields

The number of candidates observed in 2011 and 2012 data, as well as the estimated background in the signal region, are reported in tables 14.1 and 14.2 for the Higgs phase space selection in 2011 and 2012 data, respectively. In Tab. 14.3 we show integrated yealds over whole data taking period.

Chapter 14: Final Results

Table 14.1: The number of event candidates observed in 2011 data for 5.05 fb^{-1} , compared to the mean expected background and signal rates for each final state for $100 < m_{4\ell} < 1000 \text{ GeV}$. For the Z + X background, the estimations are based on data.

Channel	$4e$	4μ	$2e2\mu$
ZZ background	15.06 ± 1.71	22.58 ± 2.23	35.66 ± 3.64
Z + X	$1.99^{+1.79}_{-1.19}$	$0.9^{+0.63}_{-0.45}$	$2.89^{+2.6}_{-1.44}$
All background expected	$17.05^{+2.47}_{-2.08}$	$23.48^{+2.32}_{-2.28}$	$38.54^{+4.47}_{-3.91}$
$m_H = 125 \text{ GeV}$	0.62 ± 0.09	1.12 ± 0.12	1.45 ± 0.17
$m_H = 126 \text{ GeV}$	0.69 ± 0.10	1.23 ± 0.13	1.62 ± 0.19
$m_H = 200 \text{ GeV}$	4.05 ± 0.47	5.75 ± 0.58	9.67 ± 1.01
$m_H = 350 \text{ GeV}$	2.35 ± 0.29	3.21 ± 0.34	5.57 ± 0.61
$m_H = 500 \text{ GeV}$	0.80 ± 0.10	1.07 ± 0.12	1.87 ± 0.21
Observed	14	20	43

Table 14.2: The number of event candidates observed in 2012 data 12.21 fb^{-1} , compared to the mean expected background and signal rates for each final state for $100 < m_{4\ell} < 1000 \text{ GeV}$. For the Z + X background, the estimations are based on data.

Channel	$4e$	4μ	$2e2\mu$
ZZ background	37.95 ± 4.60	60.14 ± 6.67	95.48 ± 10.61
Z + X	$5.66^{+5.09}_{-3.96}$	$1.99^{+1.59}_{-1.19}$	$7.26^{+7.26}_{-5.08}$
All background expected	$43.61^{+6.86}_{-6.07}$	$62.13^{+6.86}_{-6.78}$	$102.74^{+12.86}_{-11.77}$
$m_H = 125 \text{ GeV}$	1.80 ± 0.29	3.49 ± 0.41	4.49 ± 0.57
$m_H = 126 \text{ GeV}$	1.99 ± 0.32	3.81 ± 0.45	4.96 ± 0.63
$m_H = 200 \text{ GeV}$	11.49 ± 1.44	17.33 ± 1.97	28.79 ± 3.28
$m_H = 350 \text{ GeV}$	7.15 ± 0.91	10.42 ± 1.21	17.61 ± 2.05
$m_H = 500 \text{ GeV}$	2.54 ± 0.33	3.67 ± 0.43	6.19 ± 0.73
Observed	45	75	119

14.1. Summary of Selection and Systematic Uncertainties

Table 14.3: The number of event candidates observed, compared to the mean expected background and signal rates for each final state. For the Z + X background, the estimations are based on data. The results are given integrated over the full mass measurement range for the Higgs boson search from 100 to 1000 GeV and for 2011 and 2012 data combined.

Channel	4e	4 μ	2e2 μ
ZZ background	53.01 ± 6.31	82.73 ± 8.90	131.14 ± 14.25
Z + X	$7.64^{+6.88}_{-5.15}$	$2.88^{+2.22}_{-1.64}$	$10.14^{+9.85}_{-6.52}$
All background expected	$60.65^{+9.33}_{-8.15}$	$85.61^{+9.18}_{-9.05}$	$141.28^{+17.33}_{-15.68}$
$m_H = 125$ GeV	2.42 ± 0.38	4.61 ± 0.53	5.95 ± 0.74
$m_H = 126$ GeV	2.68 ± 0.42	5.05 ± 0.58	6.58 ± 0.82
$m_H = 200$ GeV	15.54 ± 1.91	23.08 ± 2.55	38.46 ± 4.29
$m_H = 350$ GeV	9.50 ± 1.19	13.63 ± 1.54	23.18 ± 2.65
$m_H = 500$ GeV	3.34 ± 0.43	4.73 ± 0.55	8.06 ± 0.94
Observed	59	95	162

14.1.2 Event Distributions

The reconstructed four-lepton invariant mass distribution is shown in Figure 14.1 for the full dataset, where different mass ranges, including the mass below 100 GeV (not used for analysis). These distributions are also shown in Figs. 14.2 and 14.3 but splitted by channel, and for 7 and 8 TeV data separately.

The reconstructed di-lepton invariant mass and MELA KD distributions are shown in Figure 14.4.

The SM background distributions are obtained combining the rate normalization from data-driven methods and knowledge on shapes taken from the MC samples.

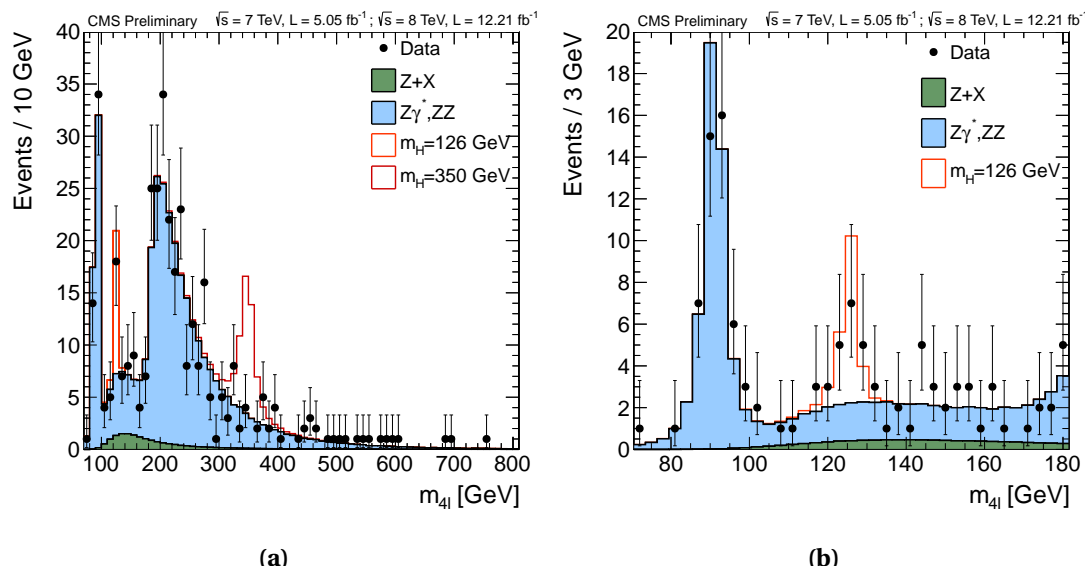


Figure 14.1: Distribution of the four-lepton reconstructed mass. Region $m_{4\ell} < 100$ GeV is shown but not used in analysis. The sample correspond to an integrated luminosity of $\mathcal{L} = 5.05 \text{ fb}^{-1}$ of 2011 data and $\mathcal{L} = 12.21 \text{ fb}^{-1}$ of 2012 data.

The correlation between the four-lepton reconstructed mass and KD, or the reconstructed mass of the second or first lepton pair are shown in Figs. 14.5.

14.1. Summary of Selection and Systematic Uncertainties

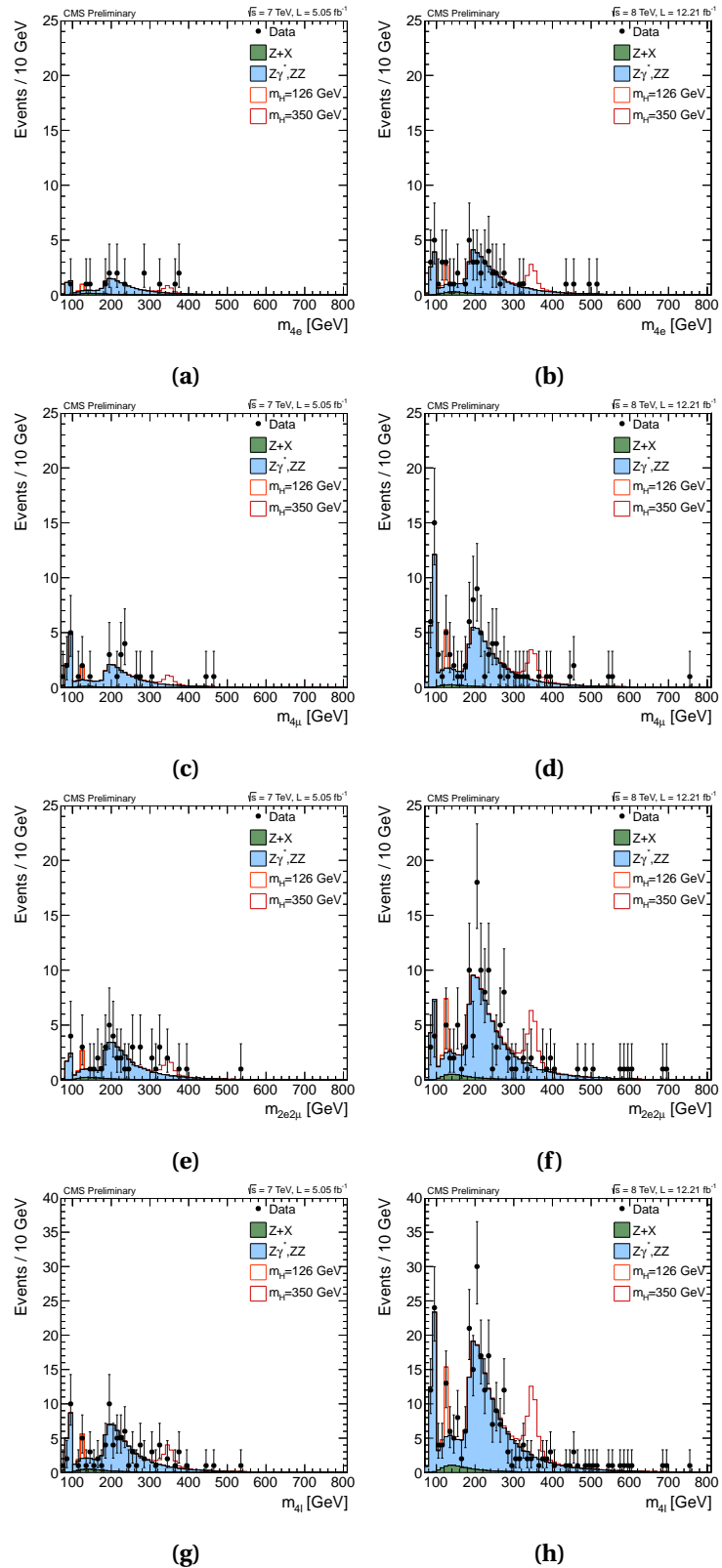


Figure 14.2: Distribution of the four-lepton reconstructed mass in several sub-channels: $4e$ (top), 4μ (middle top), $2e2\mu$ (middle bottom), for all channels combined (bottom) and for 7 TeV (left) and 8 TeV (right).

Chapter 14: Final Results

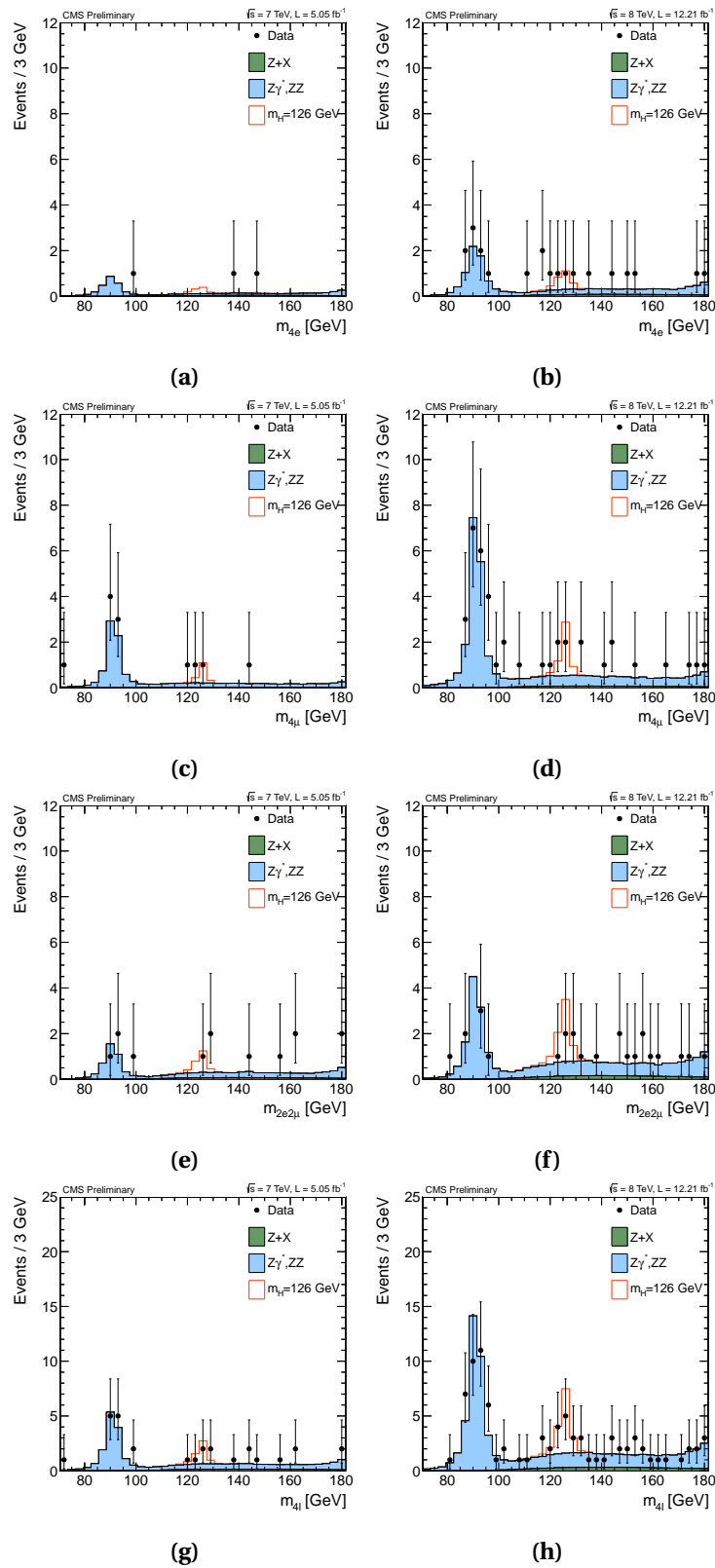


Figure 14.3: Distribution of the four-lepton reconstructed mass in the low-mass range in several sub-channels: $4e$ (top), 4μ (middle top), $2e2\mu$ (middle bottom), for all channels combined (bottom) and for 7 TeV (left) and 8 TeV (right).

14.1. Summary of Selection and Systematic Uncertainties

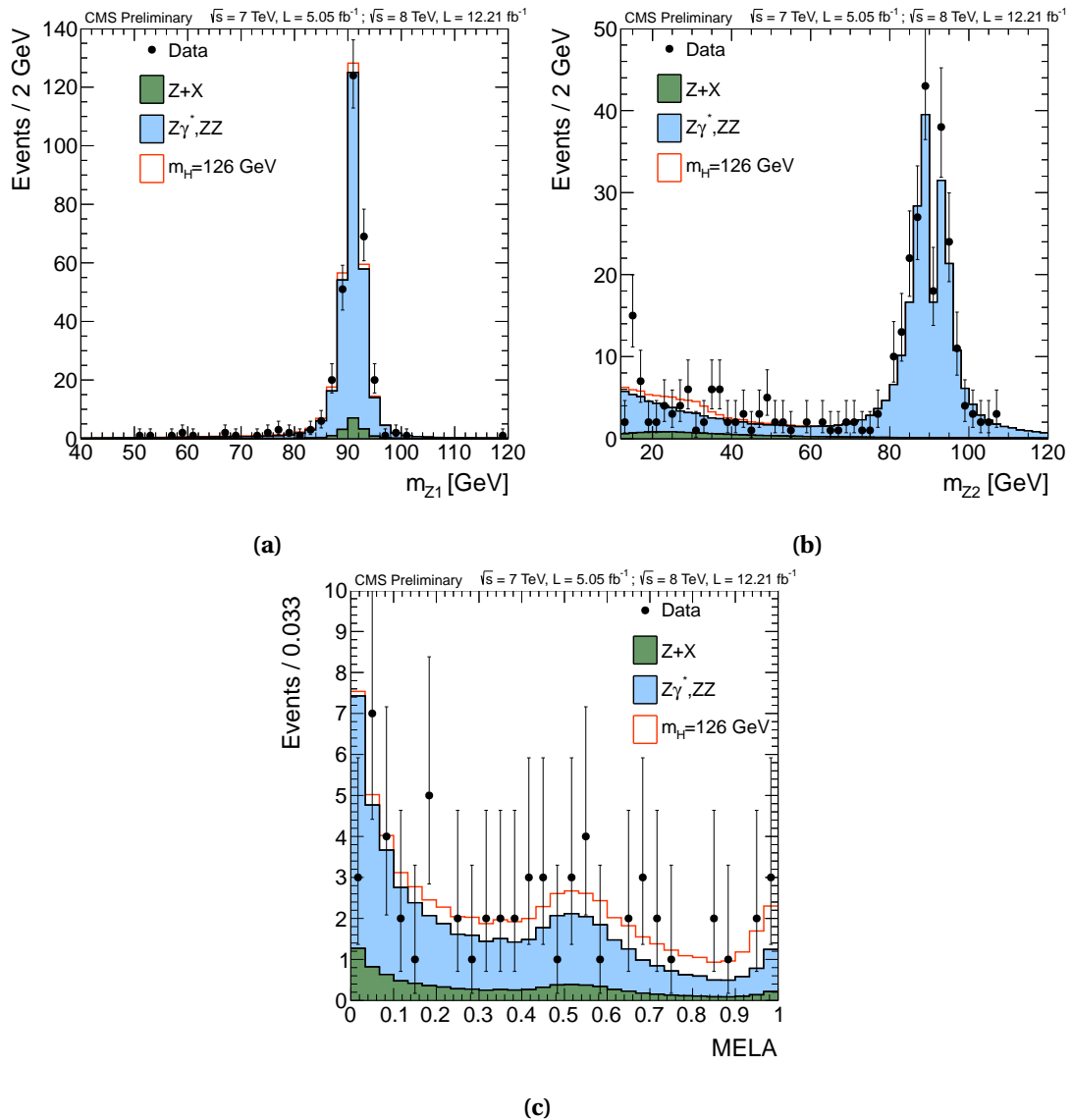


Figure 14.4: Distribution of Z_1 (top left) and Z_2 (top right) invariant mass, MELA KD in the mass range (100-180 GeV) on the bottom. The samples correspond to an integrated luminosity of $\mathcal{L} = 5.05 \text{ fb}^{-1}$ for the 7 TeV data, and 12.21 fb^{-1} for the 8 TeV data.

Chapter 14: Final Results

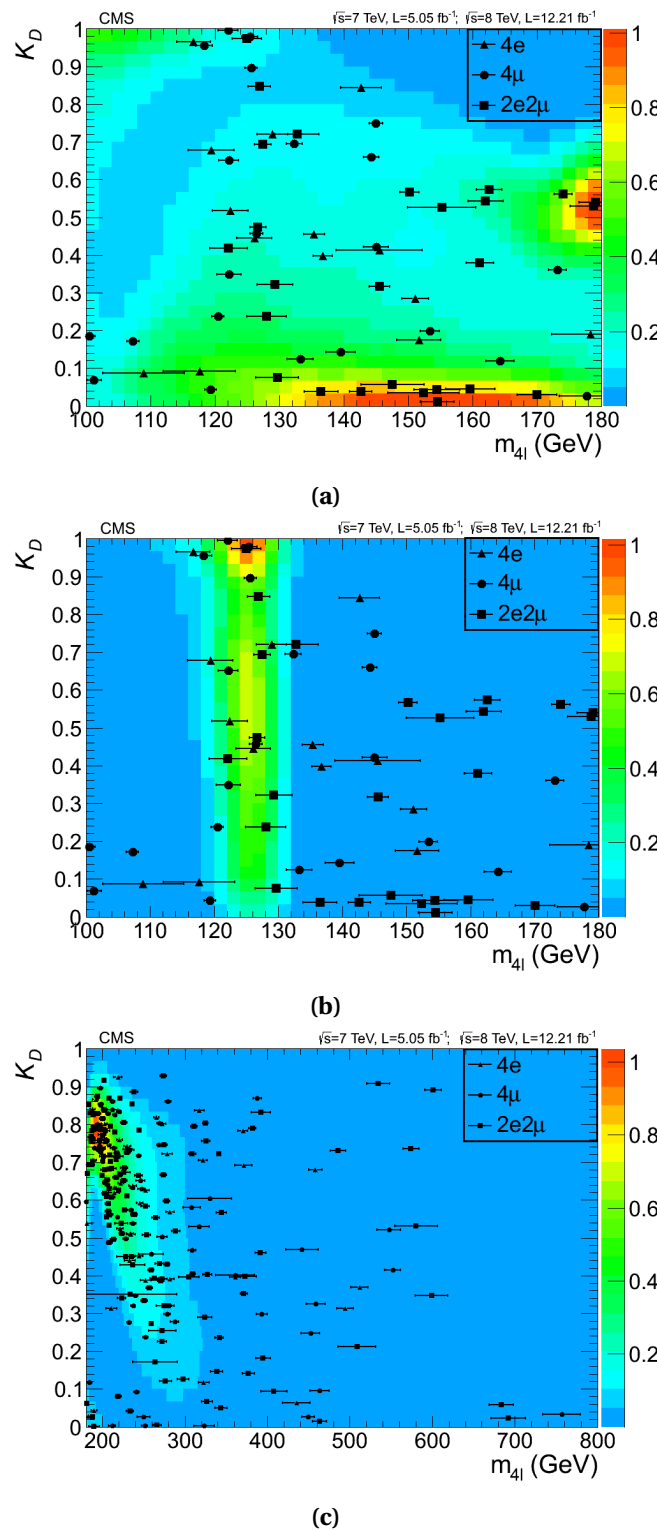


Figure 14.5: Distribution of the MELA KD versus the four-lepton reconstructed mass $m_{4\ell}$ for 2011 and 2012 data combined. Circles are 4μ events, triangles $4e$ events and squares $2e2\mu$ events. Per-event errors is attached to each event. Top plot: low-mass range with contours for background expectation. Middle plot: low-mass range with contours for signal expectation with $m_H = 126$ GeV. Bottom plot: high-mass range with contours for background expectation.

14.1. Summary of Selection and Systematic Uncertainties

Event Distributions of Spin and Parity Kinematic Discriminant

In Fig. 14.6 distributions of SMD (superMELA, top), \mathcal{D}_{0^-} (pseudoMELA, left), and \mathcal{D}_{2^+} (graviMELA, right) are shown. There is a clear excess of signal visible near SMD=1. The signal-enhanced plot of \mathcal{D}_{0^-} shows some preference for the SM-like distribution of events. The \mathcal{D}_{2^+} distribution provided relatively weak separation between the two hypotheses with the present statistics.

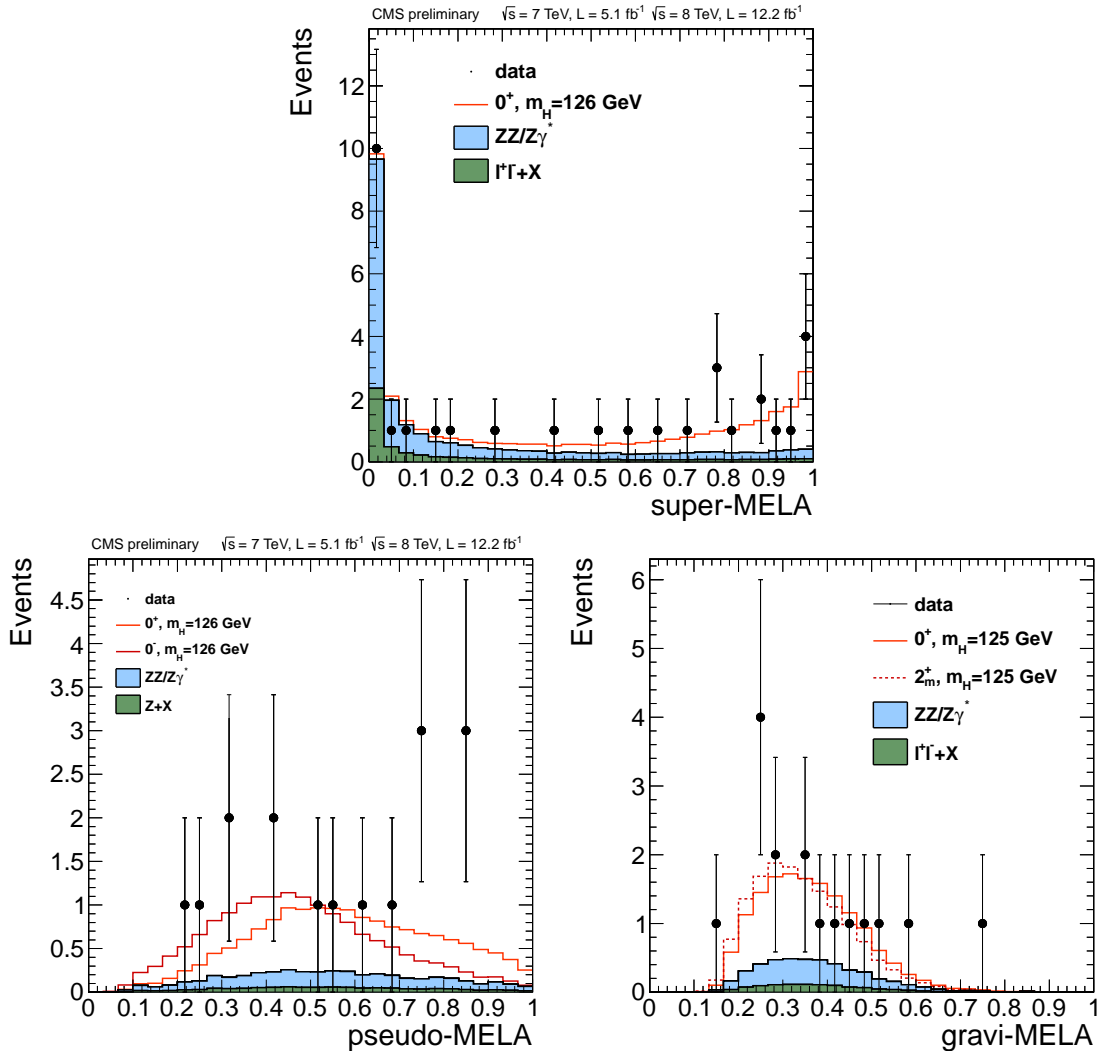


Figure 14.6: Distributions of SMD (superMELA, top), \mathcal{D}_{0^-} (pseudoMELA, left), and \mathcal{D}_{2^+} (graviMELA, right) for data, expected signal for two hypotheses and expected background. A cut $SMD > 0.5$ is applied when \mathcal{D}_{0^-} and \mathcal{D}_{2^+} are shown, to suppress background.

14.1.3 Systematic Uncertainties

The summary of systematic uncertainties for the analysis parts on 2011 and 2012 collected data is provided in the Tab. 14.4, 14.5, 14.6, 14.7. All systematic uncertainties, but uncertainty on luminosity, are 100% correlated between 7 and 8 TeV samples. Log-normal uncertainty on $Z + \text{jets}$ normalization is correlated between 7 and 8 TeV samples, but it is uncorrelated between different final states (i.e. it is correlated for $4e$ 7 TeV and $4e$ 8 TeV, but it is not correlated for example for $4e$ and 4μ). Uncertainties affecting muons and electrons are correlated to any other channel that contains those objects and are given combined and per event. Uncertainties on MELA template shapes are introduced through alternative shapes which are representing 1 sigma errors.

Table 14.4: Simulated samples for 7 TeV: Summary of the magnitude of theoretical and phenomenological systematic uncertainties in percent for $H \rightarrow ZZ \rightarrow 4\ell$ and $ZZ \rightarrow 4\ell$. Errors are common to all 4ℓ channels. Last three lines are parametric uncertainties on the shape of the HZZ4L signal Crystal Ball (mean, sigma and tail parameter).

Source of uncertainties	Process						
	ggH	VBF	WH	ZH	ttH	ZZ	ggZZ
gg partonic luminosity	7.5-10				0-10		10
$qq/q\bar{q}$ partonic luminosity		2.2-4.7	0-4.5	0-5.0		5	
QCD scale uncert. for $gg \rightarrow H$	8.7-10						
QCD scale uncert. for VBF qqH		0-1.5					
QCD scale uncert. for VH			0-0.75	0-1.3			
QCD scale uncert. for ttH					0-8.3		
4ℓ -acceptance for $gg \rightarrow H$	negl.	negl.	negl.	negl.	negl.		
Uncertainty on $BR(H \rightarrow 4\ell)$	2	2	2	2	2		
QCD scale uncert. for $ZZ(\text{NLO})$					2.6-6.7		
QCD scale uncert. for $gg \rightarrow ZZ$						24-44	
CB mean, parametric			0.4				
CB sigma, parametric			20				
CB tail parameter, parametric			5.0				

14.1. Summary of Selection and Systematic Uncertainties

Table 14.5: Simulated samples for 8 TeV: Summary of the magnitude of theoretical and phenomenological systematic uncertainties in percent for $H \rightarrow ZZ \rightarrow 4\ell$ and $ZZ \rightarrow 4\ell$. Errors are common to all 4ℓ channels. Last three lines are parametric uncertainties on the shape of the HZZ4L signal Crystal Ball (related to scale and resolution uncertainties mean, sigma, and tail parameter).

Source of uncertainties	Process						
	ggH	VBF	WH	ZH	ttH	ZZ	ggZZ
gg partonic luminosity	7.2-9.2				0-9.8		10
$q\bar{q}/q\bar{q}$ partonic luminosity		1.2-1.8	0-4.5	0-5.0		5	
QCD scale uncert. for $gg \rightarrow H$	5.5-7.9						
QCD scale uncert. for VBF $q\bar{q}H$		0.1-0.2					
QCD scale uncert. for VH			0-0.6	0-1.5			
QCD scale uncert. for ttH					0-8.8		
4ℓ -acceptance for $gg \rightarrow H$	negl.	negl.	negl.	negl.	negl.		
Uncertainty on $BR(H \rightarrow 4\ell)$	2	2	2	2	2		
QCD scale uncert. for $ZZ(\text{NLO})$					2.6-6.7		
QCD scale uncert. for $gg \rightarrow ZZ$						24-44	
CB mean, parametric			0.4				
CB sigma, parametric			20				
CB tail parameter, parametric			5.0				

Table 14.6: 7 and 8 TeV samples: Summary of the magnitude of instrumental systematic uncertainties in percent for $H \rightarrow ZZ \rightarrow 4\ell$ and $ZZ \rightarrow 4\ell$. The instrumental systematic uncertainties for all five Higgs boson production mechanisms are assumed to be same, similarly on $ZZ \rightarrow 4\ell$ (NLO) and $gg \rightarrow ZZ \rightarrow 4\ell$.

Source of uncertainties	Error for different processes					
	$H \rightarrow ZZ \rightarrow 4\ell$		$ZZ/ggZZ \rightarrow 4\ell$			
	$4e$	4μ	$2e2\mu$	$4e$	4μ	$2e2\mu$
Luminosity					2.2 (5 for 8 TeV)	
Trigger					negl.	
electron reco/ID/isolation (4e)					6.2-11	
muon reco/ID/isolation (4mu)					1.9	

Table 14.7: 7 and 8 TeV samples: Summary of the magnitude of systematic uncertainties (asymmetric) in percent for the reducible 4ℓ backgrounds (for 8 TeV in parenthesis). There are two methods for the reducible background estimate. The uncertainties we quote here are the combination from the two methods.

$4e$	4μ	$2e2\mu$
-40,+90 (-30,+90)	-40,+60 (-40,+80)	-50,+60 (-30,+100)

14.2 Exclusion Limits

In this section we present results for exclusion limits obtained in the $H \rightarrow ZZ^{(*)} \rightarrow 4\ell$ analysis for which, as mentioned earlier, we used a modified frequentist method (CL_s). The full definition of the method, as well as prescription adopted in both, ATLAS and CMS collaborations is described in Ref. [104]. It has become customary to express null results of SM-like Higgs searches as a limit on *signal strength modifier* (μ) used to change the SM Higgs boson cross-section of all production mechanisms by exactly the same scale μ as described by

$$\mu = \frac{\sigma}{\sigma_{SM}} \quad (14.1)$$

In Fig. 14.7 the expected limits obtained with a fit of the $(m_{4\ell}, \text{KD})$ distribution are shown. From Fig. 14.7 we conclude that a SM-Higgs boson can be excluded at 95% confidence level in mass regions [113, 116] GeV and [129, 720] GeV, while expected exclusion interval was [118, 670] GeV. The expected sensitivity is reached everywhere being well within 2σ band, except for the narrow mass interval around 125 GeV. In this region the excess of events is observed, visible also in four lepton invariant mass distribution plots (see Sec. 14.1.2). In the next section (14.3) we quantify the excess testing the background-only hypothesis, usually expressed in terms of *p-value*.

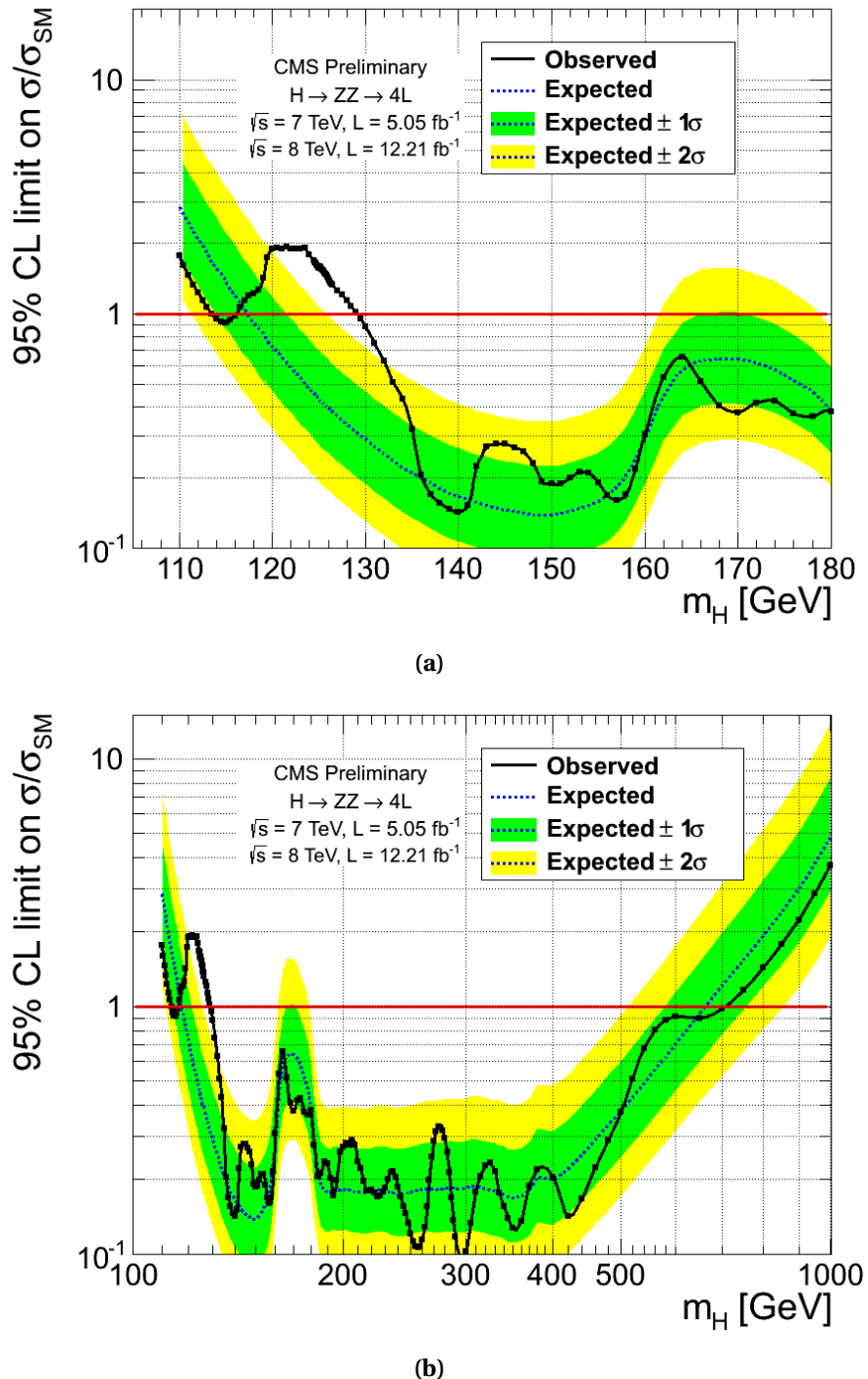


Figure 14.7: Observed and expected 95% CL upper limit on the ratio of the production cross-section to the SM expectation with the 2D fit. 2011 and 2012 data-samples are used. The 68% and 95% ranges of expectation for the background-only model are also shown with green and yellow bands, respectively. Top plot: lower mass range only, bottom plot: full mass range.

14.3 Significance of Excesses

The presence of a signal is quantified by the background-only p -value, i.e. the probability for the background to fluctuate and give excess of events as large or larger than observed one. The full definition of the method, as well as prescription adopted in both, ATLAS and CMS collaborations is described in Ref. [104].

In Fig. 14.8 we show the significance of the local fluctuation with respect to the Standard Model expectation. These significances are shown separately for 7 and 8 TeV data in Fig. 14.9 and for the comparison between 1D ($m_{4\ell}$) and 2D ($m_{4\ell}$, KD) fits in Fig. 14.10. Maximum significance of excess is reached using 2D fits (Fig. 14.10a) with the value of 4.5 standard deviations, thus letting us to claim an observation of a new mass resonant state with invariant mass around 126 GeV.

In the next section we will address the mass measurement using per-event errors to get the best possible precision out of the collected data.

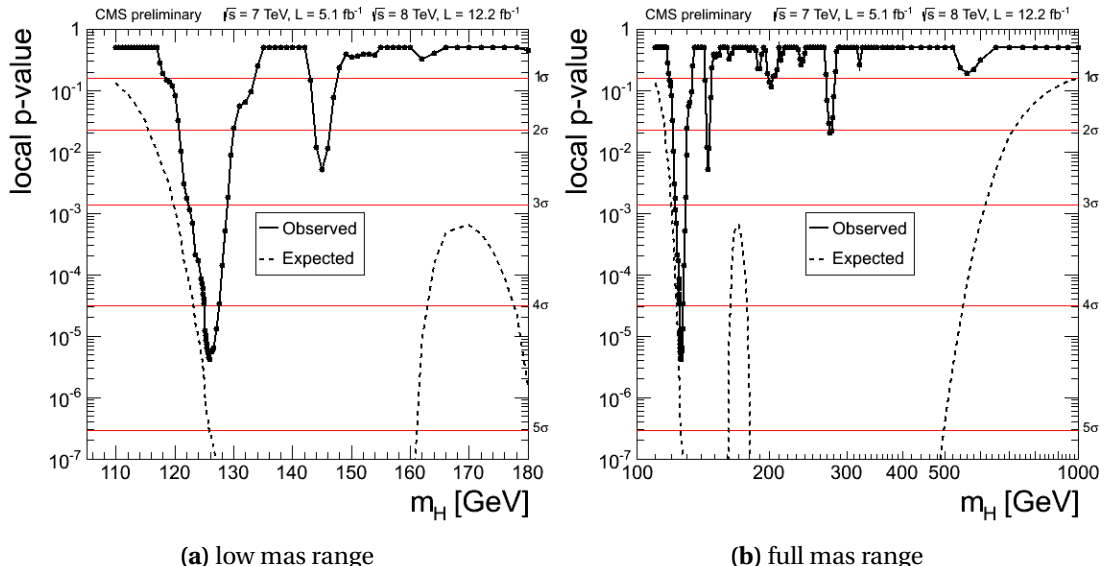


Figure 14.8: Significance of the local fluctuations with respect to the Standard Model expectation as a function of the Higgs boson mass for an integrated luminosity of 5.05 fb^{-1} at 7 TeV and 12.21 fb^{-1} at 8 TeV. Dashed line shows mean expected significance of the SM Higgs signal for a given mass hypothesis.

14.3. Significance of Excesses

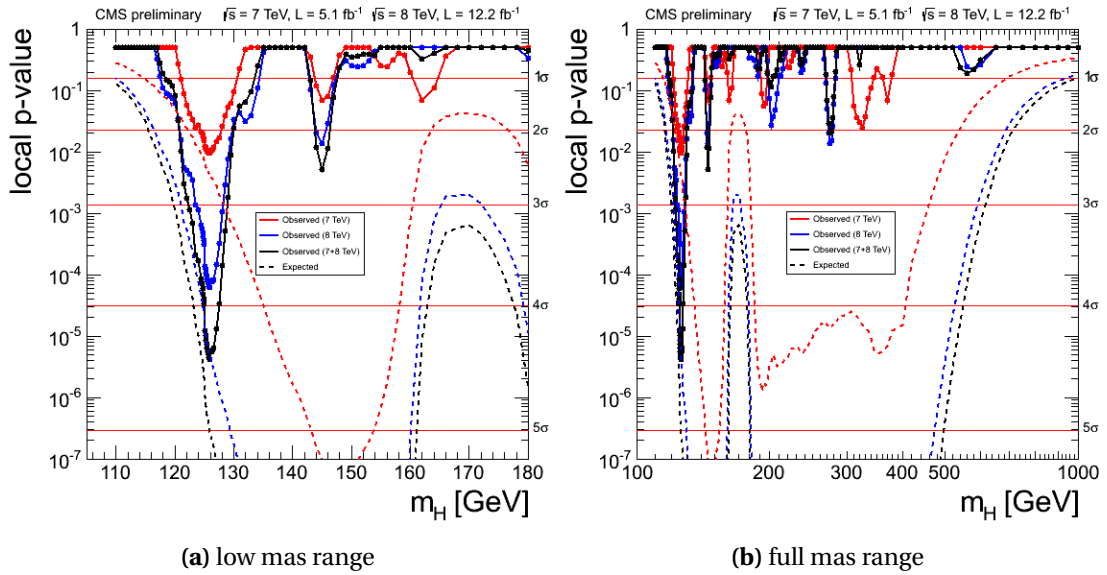


Figure 14.9: Significance of the local fluctuations with respect to the Standard Model expectation as a function of the Higgs boson mass for an integrated luminosity of 5.05 fb^{-1} at 7 TeV (red), 12.21 fb^{-1} at 8 TeV (blue) and the full dataset combined (black). Dashed line shows mean expected significance of the SM Higgs signal for a given mass hypothesis.

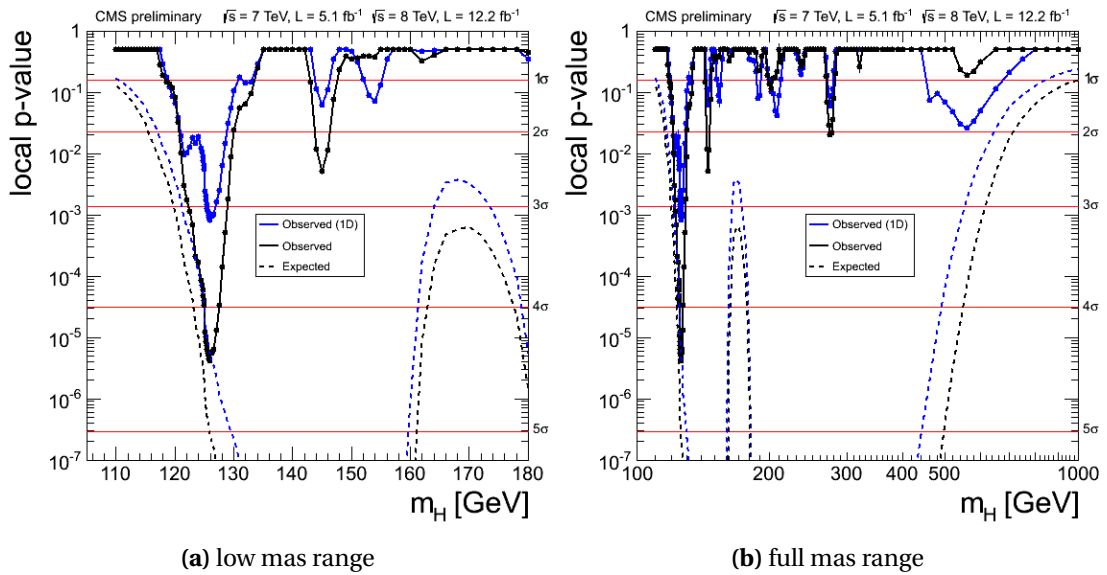
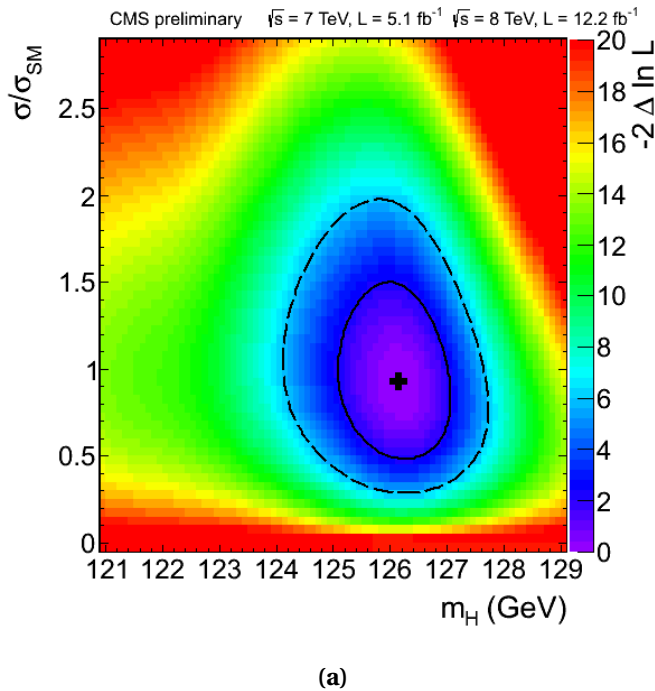


Figure 14.10: Significance of the local fluctuations with respect to the standard model expectation as a function of the Higgs boson mass for an integrated luminosity of 5.05 fb^{-1} at 7 TeV and 12.21 fb^{-1} at 8 TeV with a 1D (blue) and 2D (black) analysis. Dashed line shows mean expected significance of the SM Higgs signal for a given mass hypothesis.

14.4 Mass Measurement

With HCP2012 data set, we perform the likelihood scan in the mass versus signal strength space shown in Fig. 14.11. Results with per-event mass error are shown. Solid ellipses are 68% CL contours, for two degrees of freedom with $-2\Delta \ln \mathcal{L} = 2.3$. Without using per-event mass error, $m_H = 126.2^{+1.01}_{-1.09}$ GeV, while with per-event mass error, it gives $m_H = 126.2^{+0.87}_{-0.98}$ GeV. Including per-event mass error gives 10% improvement with current data we have. The signal strength μ , relative to the expectation for the standard model Higgs boson, is measured to be $\mu = 0.80^{+0.35}_{-0.28}$ at 126.2 GeV.



(a)

Figure 14.11: 3D test statistics $-2\ln Q$ vs Higgs boson mass m_H hypothesis and signal strength σ/σ_{SM} . The cross indicates the best-fit values. The solid and dashed contours show the 68% and 95% C.L. ranges, respectively. In this combination, the relative signal strengths for the various final states are constrained by the expectations for the SM Higgs boson.

With likelihood scan over mass, i.e. profiling signal strength, the results with and without systematic uncertainties are shown in Fig. 14.12 for 3D test statistic. With per-event mass error, the best estimate of Higgs mass is $126.2^{+0.58}_{-0.63}$ GeV, which is $\sim 6\%$ more precise than the one without per-event mass error ($126.2^{+0.65}_{-0.68}$) GeV.

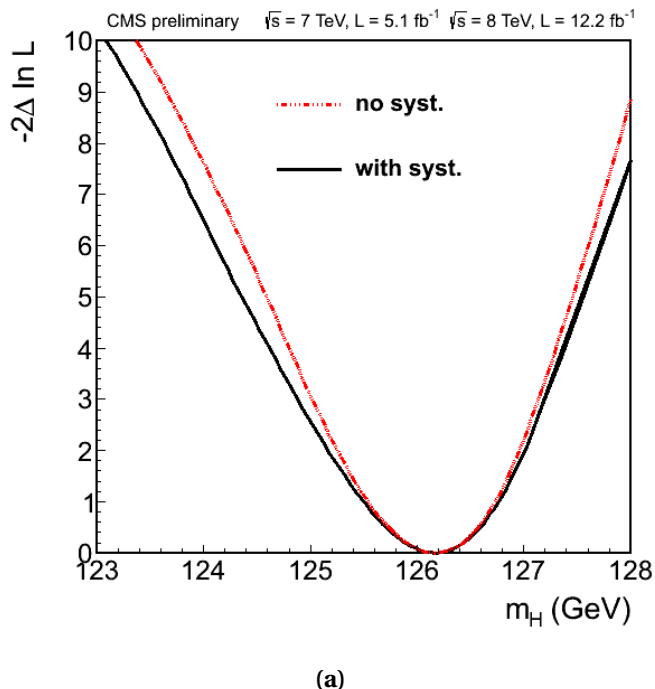


Figure 14.12: 1D test statistics $q(m_H)$ scan vs hypothesized Higgs boson mass m_H , obtained from the 3D test statistics profiling the minimum of the signal strengths, with and without systematics.

14.5 Spin and Parity Measurements

The methodology for spin-parity measurements has been discussed in Sec. 13.3. With a data integrated luminosity of 5.05 fb^{-1} at 7 TeV and 12.21 fb^{-1} at 8 TeV and for a boson with mass $m_H = 126 \text{ GeV}$ we expect signal significance of 4.6σ and the average hypothesis separation significance of 1.93σ . In any particular experiment separation from either 0^+ or 0^- hypothesis may vary depending on statistical distribution of events. The expected signal separation from toy experiments for each signal hypothesis along with observation in data are shown in Fig. 14.13. The distribution of log-likelihood ratio $q = -2\ln(\mathcal{L}_0^-/\mathcal{L}_{\text{SM}})$ is shown with generated samples of background and signal of two types (SM 0^+ and 0^-) for $m_H = 126 \text{ GeV}$. Here the likelihoods \mathcal{L} are calculated with the signal rates allowed to float independently for each signal type. The nuisance parameters are treated as independent as well. The expected distributions are generated with signal cross-section equal to that of the SM, which is consistent with observation. The observed value of q indicates that the hypothesis of $J^P = 0^-$ quantum numbers is inconsistent with observation within 2.4σ , while the SM assignment is consistent within 0.5σ . Using the CL_s criterion, the probability for $J^P = 0^-$ hypothesis is 2.4%.

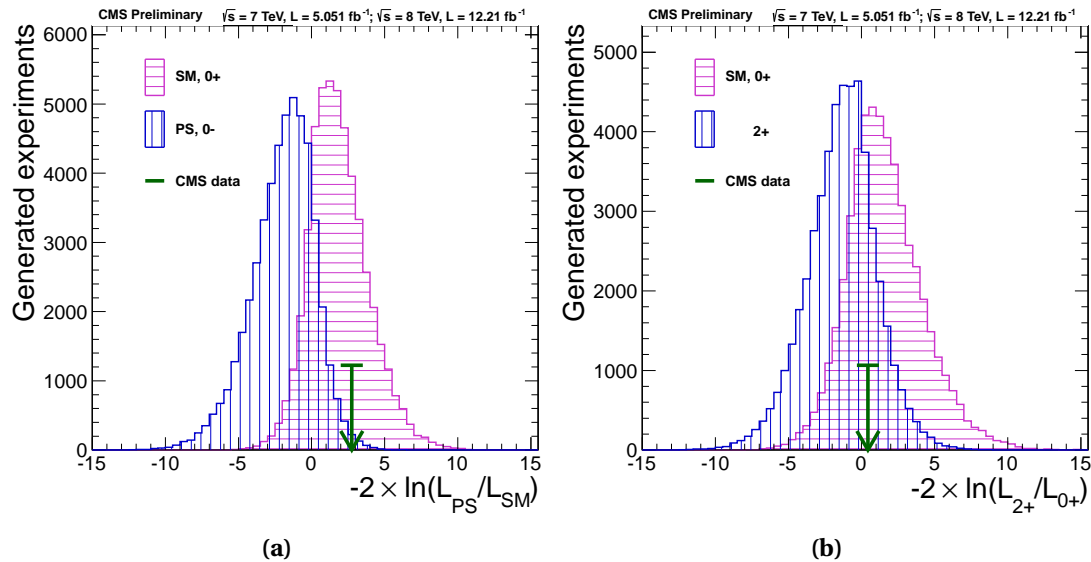


Figure 14.13: Distribution of $-2\ln(\mathcal{L}_1/\mathcal{L}_2)$ of toy experiments tossed according to a 0^+ signal hypothesis (magenta, horizontal hatches) and 0^- (a) or 2^+_{\min} (b) signal hypothesis (blue, vertical hatches) for $m_H = 126 \text{ GeV}$. The yields used in the generation of the pseudo-experiments are those expected with 5.05 fb^{-1} at 7 TeV and 12.21 fb^{-1} at 8 TeV of data. The arrow indicates observed value in data.

A consistency test of the parity-odd and parity-even hypothesis can be performed using the f_{a3} parameter, as discussed in Sec. 12.4. We can use \mathcal{D}_{0-} (pseudoMELA) to determine the parameter f_{a3} . To measure the value of f_{a3} , one can approximate the (SMD, \mathcal{D}_{0-}) probability density function by taking a mixture of the probability density functions generated for the 0^+

and 0^- states, ignoring the interference terms. This approximation is justified in Fig. 14.14 where the approximated distribution of \mathcal{D}_{0^-} (dashed purple line) and distribution from a fully simulated mixed parity state (green) are shown. Likelihood scans in 2 dimensions can then be used to constrain f_{a3} . Figure 14.15 shows the result of such a scan which corresponds to the value of $f_{a3} = 0.00^{+0.31}_{-0.00}$.

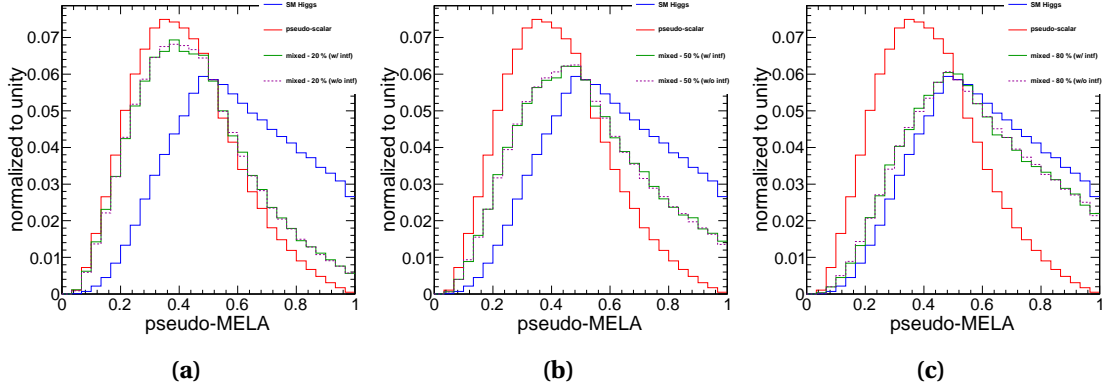


Figure 14.14: Distribution of \mathcal{D}_{0^-} (pseudoMELA) for several choice models, SM Higgs ($f_{a3} = 0$) in blue, $f_{a3} = 1$ in red. In green and dashed purple are two different model for different fractions of f_{a3} generated, green is the fully simulated model while dashed purple shows an approximation in which the interference of the two amplitudes is neglected. The different plots show variable f_{a3} . The left is $f_{a3} = 0.8$, the middle is $f_{a3} = 0.5$, and the right is $f_{a3} = 0.2$.

With the current analysis, the separation between the two spin cases 0^+ and 2^+ (minimal couplings) is weaker because the distributions of the specific \mathcal{D}_{2^+} for the different 2^+ and 0^+ hypotheses are similar, as shown in Fig. 12.12. MC studies indicate that with a luminosity of 5.05 fb^{-1} at 7 TeV and 12.21 fb^{-1} at 8 TeV and for a boson with mass $m_H = 126 \text{ GeV}$ the hypothesis separation significance is 1.2σ . The expected signal separation tossing toy experiments for each signal hypothesis along with observation in data are shown in Fig. 14.13. With the current statistics both the spin hypotheses $J = 0^+$ and $J = 2$ (minimal couplings) are consistent with the observation, respectively inside 0.4 and 0.8σ .

Chapter 14: Final Results

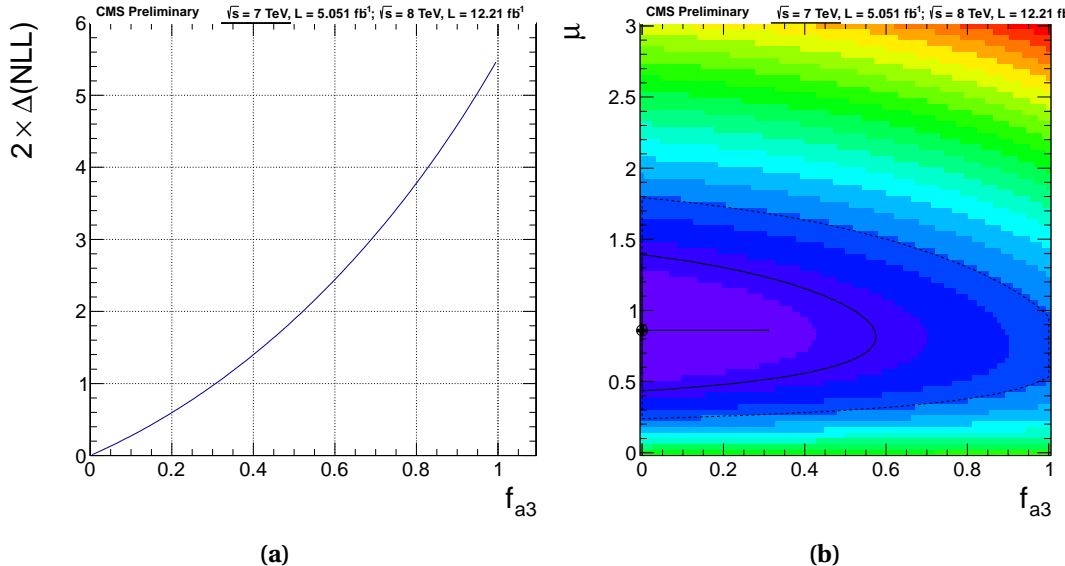


Figure 14.15: Distribution of $-2 \ln \mathcal{L}$ as a function of amplitude fraction f_{a3} (1D left) and with signal strength μ (2D right). The central point shows the minimum value of $-2 \ln \mathcal{L}$, the solid and dashed contours show 68% and 95% CL contours in two dimensions. The cross indicates the one-dimensional 68% CL intervals.

Conclusions

After two decades of design and construction, the LHC provided its first collision events in the end of 2009. The data recorded by the CMS experiment over the year 2010 allowed to understand the detector; simulations proved to give a very precise description of data. First measurements were made on variables that had not been previously measured, like the polarization of the W boson in proton-proton collisions. At this time, the analysis strategy was deployed and a set of discriminating observables defined always keeping in mind that the first analysis should be simple, robust and suitable for most Higgs boson mass hypothesis. Further on, the context of the LHC and CMS operations throughout 2010, 2011 and 2012 gave rhythm to the work presented in this thesis.

By summer 2011, the amount of collision data accumulated by CMS experiment was enough to exclude at 95% C.L. a broad range of Higgs boson masses allowed by the theory. A significant increase of the instantaneous luminosity gave rise to multiple interactions in a single bunch crossing—so-called pile-up. The pile-up effect study on lepton observables, particularly isolation was performed and a correction method, now used across many CMS analysis, deployed. The method uses the information of average energy density in the detector on per-event basis to correct and maintain the performance of isolation insusceptible to pile-up.

The low Higgs boson mass range which was not excluded by the summer 2011 conferences indicated that the search should profit from the full event information and that the phase space should be extended to better use the low transverse momentum leptons. A significant amount of work was done in this regard throughout 2012, e.g. introduction of kinematic discriminant, recovery of final state radiation, improvement of the leptons identification and the usage of isolation with particles. To better control the efficiency of lepton selection, the extensive study was performed using tag-and-probe method which uses dataset with Z bosons decaying into lepton pairs to provide efficiency measurement directly from collision data. These are then compared to efficiencies from simulation to obtain per lepton scale factors and selection uncertainties. A particular effort was made to extend the measurement down to electron transfer momentum of 7 GeV. It is worth to say that these are, together with muon measurements down to 5 GeV, the lowest thresholds ever controlled in the hadron colliders.

By summer 2012, there was enough data collected by CMS to announce the discovery of a new boson during the memorable CERN seminar on the 4th of July. After the discovery,

Chapter 14: Conclusions

the data taking period continued and the analysis was improved to increase the sensitivity and to allow for better discrimination of the spin-parity properties of the new boson. In this thesis, we use data collected up to September 2012 to confirm the observation of the new boson with 4.5σ significance in $H \rightarrow ZZ^{(*)} \rightarrow 4\ell$ channel only, and to make first measurement of the boson properties. The mass of the new boson is measured using per-event errors approach and is estimated to $m_H = 126.2^{+0.87}_{-0.98}$ GeV. Even though the amount of data is not enough to draw a definite conclusion on the spin and the parity properties of the new boson, nevertheless we can say that the hypothesis 0^+ of the Standard Model for the spin $J = 0$ and parity $P = +1$ quantum numbers is found to be consistent with the observation while the pseudoscalar hypothesis 0^- with a CL_s value of 2.4% is disfavoured. Since no other significant excess is found, and upper limits at 95% confidence level exclude the ranges 113–116 GeV and 129–720 GeV while the expected exclusion range for the Standard Model Higgs boson is 118–670 GeV.

Appendix Part

A ECAL Energy Measurement with Multivariate Regression

ECAL Energy Measurement using a Multivariate Regression

We use the GBRForest implementation of the regression algorithm using boosted decision trees. We train the boosted decision tree on the Drell-Yan Monte Carlo sample using the exact same variables that have been used for the $H \rightarrow \gamma\gamma$ analysis [74]. Different sets of input variables are used depending on whether the electron is detected in the barrel or the endcap of the electromagnetic calorimeter. The variables that are used for both the barrel and the endcap are the following:

- SCRawEnergy: the uncorrected energy of the supercluster,
- scEta: η coordinate of the supercluster
- scPhi: ϕ coordinate of the supercluster
- R9: ratio of the energy in the 3-by-3 grid of crystals around the seed crystal to the uncorrected energy of the supercluster,
- etawidth: width of the supercluster in the η direction,
- phiwidth: width of the supercluster in the ϕ direction,
- NClusters: the number of clusters forming the supercluster,
- HoE: ratio of hadronic energy to electromagnetic energy,
- rho: measure of the energy density of the pileup in the event,
- vertices: number of reconstructed primary vertices,
- EtaSeed: η coordinate of the seed cluster,
- PhiSeed: ϕ coordinate of the seed cluster,

Chapter A: ECAL Energy Measurement with Multivariate Regression

- ESeed: energy of the seed cluster,
- E3x3Seed: energy in the 3-by-3 grid of crystals around the seed crystal,
- E5x5Seed: energy in the 5-by-5 grid of crystals around the seed crystal,
- $\sigma_{i\eta i\eta}$
- $\sigma_{i\phi i\phi}$
- $\sigma_{i\eta i\phi}$
- EMaxSeed: energy of the highest energy crystal,
- E2ndSeed: energy of the second highest energy crystal,
- ETopSeed: energy of the adjacent crystal above the highest energy crystal,
- EBottomSeed: energy of the adjacent crystal below the highest energy crystal,
- ELeftSeed: energy of the adjacent crystal to the left of the highest energy crystal,
- ERightSeed: energy of the adjacent crystal to the right of the highest energy crystal,
- E2x5MaxSeed,
- E2x5TopSeed,
- E2x5BottomSeed,
- E2x5LeftSeed,
- E2x5RightSeed,
- pt: transverse momentum of the electron computed using the standard combination of the ECAL energy measurement and the track momentum measurement.

In addition, the following variables which indicate the proximity of the electron to gaps between modules and supermodules are used for electrons in the barrel:

- IEtaSeed: the index of the seed crystal in the η coordinate,
- IPhiSeed: the index of the seed crystal in the ϕ coordinate,
- IEtaSeed mod 5,
- IPhiSeed mod 2,
- $(|IEtaSeed| \leq 25) \times (IEtaSeed \bmod 25) +$
 $(|IEtaSeed| > 25) \times ((IEtaSeed - 25 \times |IEtaSeed| / IEtaSeed) \bmod 20)$,

-
- IPhiSeed mod 20,
 - EtaCrySeed: the η of the seed crystal in local coordinates,
 - PhiCrySeed: the η of the seed crystal in local coordinates.

For endcap electrons, we additionally include the ratio of the energy measured in the preshower to the energy of the supercluster.

B Tag-and-probe Measurements

Chapter B: Tag-and-probe Measurements

Table B.1: Reconstruction, Identification, Isolation and IP efficiencies and scale factors for single electrons, measured with the Tag-and-Probe technique on data. All measurements are obtained using Z decays in 2012 data.

p_T range (GeV)	η range	Data Eff.	MC Eff.	Scale factor (\pm sys. \pm stat.)
7 - 10	0 - 1.566	0.669	0.7712	$0.8670^{+0.117}_{-0.117} \pm 0.043$
10-15	0 - 0.8	0.845	0.8514	$0.9926^{+0.002}_{-0.002} \pm 0.013$
15-20	0 - 0.8	0.887	0.8873	$0.9999^{+0.015}_{-0.015} \pm 0.004$
20-30	0 - 0.8	0.871	0.8830	$0.9868^{+0.010}_{-0.010} \pm 0.002$
30-40	0 - 0.8	0.930	0.9389	$0.9900^{+0.006}_{-0.006} \pm 0.001$
40-50	0 - 0.8	0.950	0.9563	$0.9937^{+0.001}_{-0.001} \pm 0.000$
>50	0 - 0.8	0.956	0.9628	$0.9934^{+0.004}_{-0.004} \pm 0.001$
10-15	0.8 - 1.4442	0.845	0.8514	$0.9926^{+0.002}_{-0.002} \pm 0.013$
15-20	0.8 - 1.4442	0.887	0.8873	$0.9999^{+0.015}_{-0.015} \pm 0.004$
20-30	0.8 - 1.4442	0.870	0.8827	$0.9856^{+0.007}_{-0.007} \pm 0.004$
30-40	0.8 - 1.4442	0.927	0.9370	$0.9891^{+0.004}_{-0.004} \pm 0.001$
40-50	0.8 - 1.4442	0.947	0.9542	$0.9921^{+0.002}_{-0.002} \pm 0.001$
>50	0.8 - 1.4442	0.953	0.9591	$0.9941^{+0.003}_{-0.003} \pm 0.001$
7 - 10	1.4442 - 1.566	0.626	0.8998	$0.8347^{+0.053}_{-0.053} \pm 0.108$
10-15	1.4442 - 1.566	0.872	0.8545	$1.0100^{+0.033}_{-0.033} \pm 0.022$
15-20	1.4442 - 1.566	0.897	0.9072	$0.9966^{+0.021}_{-0.021} \pm 0.011$
20-30	1.4442 - 1.566	0.850	0.9511	$0.9944^{+0.025}_{-0.025} \pm 0.003$
30-40	1.4442 - 1.566	0.897	0.9530	$0.9884^{+0.002}_{-0.002} \pm 0.003$
40-50	1.4442 - 1.566	0.943	0.6237	$0.9913^{+0.003}_{-0.003} \pm 0.003$
>50	1.4442 - 1.566	0.941	0.7676	$0.9878^{+0.015}_{-0.015} \pm 0.003$
7 - 10	1.566 - 2.5	0.562	0.6237	$0.9011^{+0.080}_{-0.080} \pm 0.108$
10-15	1.566 - 2	0.773	0.7676	$1.0065^{+0.040}_{-0.040} \pm 0.022$
15-20	1.566 - 2	0.842	0.8532	$0.9874^{+0.003}_{-0.003} \pm 0.011$
20-30	1.566 - 2	0.819	0.8315	$0.9855^{+0.014}_{-0.014} \pm 0.002$
30-40	1.566 - 2	0.859	0.8816	$0.9740^{+0.024}_{-0.024} \pm 0.002$
40-50	1.566 - 2	0.883	0.8886	$0.9933^{+0.013}_{-0.013} \pm 0.001$
>50	1.566 - 2	0.887	0.9037	$0.9818^{+0.006}_{-0.006} \pm 0.002$
10-15	2 - 2.5	0.773	0.7676	$1.0065^{+0.040}_{-0.040} \pm 0.022$
15-20	2 - 2.5	0.842	0.8532	$0.9874^{+0.003}_{-0.003} \pm 0.011$
20-30	2 - 2.5	0.797	0.8102	$0.9832^{+0.019}_{-0.019} \pm 0.002$
30-40	2 - 2.5	0.832	0.8597	$0.9683^{+0.012}_{-0.012} \pm 0.002$
40-50	2 - 2.5	0.857	0.8679	$0.9871^{+0.025}_{-0.025} \pm 0.002$
>50	2 - 2.5	0.862	0.8829	$0.9758^{+0.006}_{-0.006} \pm 0.002$

Table B.2: Identification, Isolation and IP efficiencies for single electrons, measured with the Tag and Probe technique on data, and data/MC discrepancy obtained applying the method on MC. All measurements are obtained using Z decays in 2011 data.

p_T range (GeV)	η range	Data Eff.	MC Eff.	Scale factor (\pm sys. \pm stat.)
7-10	0 - 1.4442	0.730	0.748	$0.976^{+0.019}_{-0.032} \pm 0.060$
10-15	0 - 0.8	0.814	0.805	$1.012^{+0.022}_{-0.038} \pm 0.015$
15-20	0 - 0.8	0.850	0.840	$1.012^{+0.022}_{-0.038} \pm 0.007$
20-30	0 - 0.8	0.905	0.916	$0.989^{+0.017}_{-0.029} \pm 0.002$
30-40	0 - 0.8	0.950	0.954	$0.996^{+0.010}_{-0.010} \pm 0.001$
40-50	0 - 0.8	0.966	0.969	$0.997^{+0.010}_{-0.010} \pm 0.000$
>50	0 - 0.8	0.972	0.972	$1.000^{+0.011}_{-0.012} \pm 0.001$
10-15	0.8 - 1.4442	0.830	0.848	$0.970^{+0.018}_{-0.030} \pm 0.014$
15-20	0.8 - 1.4442	0.868	0.858	$1.011^{+0.010}_{-0.010} \pm 0.007$
20-30	0.8 - 1.4442	0.905	0.917	$0.987^{+0.022}_{-0.039} \pm 0.002$
30-40	0.8 - 1.4442	0.945	0.948	$0.997^{+0.010}_{-0.010} \pm 0.001$
40-50	0.8 - 1.4442	0.949	0.958	$0.991^{+0.010}_{-0.010} \pm 0.001$
>50	0.8 - 1.4442	0.949	0.965	$0.984^{+0.011}_{-0.014} \pm 0.001$
>7	1.4442 - 1.566	0.852	0.863	$0.987^{+0.049}_{-0.084} \pm 0.003$
7-10	1.566 - 2.5	0.708	0.698	$1.015^{+0.021}_{-0.036} \pm 0.048$
10-15	1.566 - 2	0.804	0.817	$0.975^{+0.026}_{-0.047} \pm 0.021$
15-20	1.566 - 2	0.859	0.843	$1.019^{+0.010}_{-0.010} \pm 0.006$
20-30	1.566 - 2	0.926	0.916	$1.011^{+0.014}_{-0.022} \pm 0.002$
30-40	1.566 - 2	0.922	0.938	$0.983^{+0.013}_{-0.020} \pm 0.000$
40-50	1.566 - 2	0.923	0.941	$0.980^{+0.010}_{-0.010} \pm 0.001$
>50	1.566 - 2	0.938	0.952	$0.985^{+0.011}_{-0.013} \pm 0.000$
10-15	2 - 2.5	0.814	0.809	$0.997^{+0.010}_{-0.012} \pm 0.021$
15-20	2 - 2.5	0.834	0.838	$0.995^{+0.010}_{-0.010} \pm 0.006$
20-30	2 - 2.5	0.898	0.919	$0.978^{+0.011}_{-0.014} \pm 0.003$
30-40	2 - 2.5	0.899	0.916	$0.982^{+0.010}_{-0.010} \pm 0.002$
40-50	2 - 2.5	0.931	0.914	$1.018^{+0.010}_{-0.010} \pm 0.002$
>50	2 - 2.5	0.931	0.925	$1.006^{+0.013}_{-0.020} \pm 0.000$

Chapter B: Tag-and-probe Measurements

Table B.3: Efficiency for the requirement on the significance of the 3d impact parameter, measured using the tag-and-probe method for muons with $p_T < 20$ GeV and reconstructed as tracks in the inner tracker.

Region		Efficiencies for 2011 [%]			Efficiencies for 2012 [%]		
$ \eta $ range	p_T range	data	sim.	ratio \pm stat.	data	sim.	ratio \pm stat.
+0.0, +1.2	5.0, 7.5	97.4	97.8	0.996 \pm 0.007	100.0	96.1	1.041 \pm 0.020
+0.0, +1.2	7.5, 10.0	98.2	99.3	0.989 \pm 0.004	97.3	97.9	0.994 \pm 0.029
+0.0, +1.2	10.0, 15.0	99.4	99.2	1.002 \pm 0.005	95.8	98.9	0.969 \pm 0.037
+0.0, +1.2	15.0, 20.0	100.0	99.9	1.001 \pm 0.004	100.0	99.9	1.001 \pm 0.013
+1.2, +2.4	5.0, 7.5	99.1	99.3	0.998 \pm 0.013	98.6	98.5	1.001 \pm 0.015
+1.2, +2.4	7.5, 10.0	99.0	99.6	0.993 \pm 0.008	93.6	98.8	0.947 \pm 0.056
+1.2, +2.4	10.0, 15.0	97.4	99.7	0.977 \pm 0.011	100.0	99.3	1.007 \pm 0.043
+1.2, +2.4	15.0, 20.0	100.0	99.8	1.002 \pm 0.001	100.0	100.0	1.000 \pm 0.001

Table B.4: Efficiency for the requirement on the significance of the 3d impact parameter, measured using the tag-and-probe method for muons with $p_T > 20$ GeV and reconstructed as tracks in the inner tracker.

Region η range	Efficiencies for 2011A [%]			Efficiencies for 2011B [%]			Efficiencies for 2012 [%]		
	data	sim.	ratio \pm stat.	data	sim.	ratio \pm stat.	data	sim.	ratio \pm stat.
-2.4, -2.1	99.5	99.6	0.999 \pm 0.001	98.4	99.6	0.988 \pm 0.003	98.8	99.2	0.995 \pm 0.003
-2.1, -1.6	99.5	99.8	0.997 \pm 0.001	98.2	99.8	0.984 \pm 0.001	99.2	99.5	0.997 \pm 0.002
-1.6, -1.2	99.9	99.9	1.000 \pm 0.001	98.9	99.9	0.990 \pm 0.001	99.8	99.8	1.001 \pm 0.001
-1.2, -0.9	99.8	99.9	1.000 \pm 0.001	99.6	99.9	0.998 \pm 0.001	99.7	99.8	0.999 \pm 0.001
-0.9, -0.6	99.8	99.9	0.999 \pm 0.001	99.8	99.9	0.999 \pm 0.001	99.7	99.8	1.000 \pm 0.001
-0.6, -0.3	99.8	99.9	0.999 \pm 0.001	99.8	99.9	0.999 \pm 0.001	99.7	99.8	1.000 \pm 0.001
-0.3, -0.2	99.4	99.5	0.999 \pm 0.001	99.4	99.5	0.998 \pm 0.001	99.0	99.0	1.000 \pm 0.002
-0.2, +0.2	99.9	99.9	0.999 \pm 0.001	99.8	99.9	0.999 \pm 0.001	99.7	99.7	1.000 \pm 0.001
+0.2, +0.3	99.3	99.4	0.999 \pm 0.001	99.2	99.4	0.998 \pm 0.001	98.6	99.1	0.995 \pm 0.002
+0.3, +0.6	99.8	99.9	0.998 \pm 0.001	99.9	99.9	1.000 \pm 0.001	99.9	99.8	1.001 \pm 0.001
+0.6, +0.9	99.8	99.9	0.999 \pm 0.001	99.7	99.9	0.998 \pm 0.001	99.6	99.8	0.998 \pm 0.001
+0.9, +1.2	99.7	99.8	0.998 \pm 0.001	99.6	99.8	0.998 \pm 0.001	99.7	99.7	1.000 \pm 0.001
+1.2, +1.6	99.7	99.8	0.999 \pm 0.001	98.8	99.8	0.990 \pm 0.001	99.9	99.6	1.003 \pm 0.001
+1.6, +2.1	99.5	99.7	0.998 \pm 0.001	98.2	99.7	0.985 \pm 0.001	99.2	99.5	0.996 \pm 0.002
+2.1, +2.4	99.3	99.4	0.999 \pm 0.001	97.7	99.4	0.983 \pm 0.003	98.7	99.2	0.995 \pm 0.003

Table B.5: Efficiency for the requirement on the significance of the 3d impact parameter, measured using the tag-and-probe method for muons with $p_T < 20$ GeV and passing the Particle Flow identification.

Region		Efficiencies for 2011 [%]			Efficiencies for 2012 [%]		
$ \eta $ range	p_T range	data	sim.	ratio \pm stat.	data	sim.	ratio \pm stat.
+0.0, +1.2	5.0, 10.0	99.2	99.5	0.997 \pm 0.009	95.6	100.0	0.956 \pm 0.028
+0.0, +1.2	10.0, 15.0	99.5	99.6	0.999 \pm 0.002	98.4	99.3	0.991 \pm 0.007
+0.0, +1.2	15.0, 20.0	99.6	99.5	1.001 \pm 0.001	99.4	99.7	0.996 \pm 0.002
+1.2, +2.4	5.0, 10.0	97.6	99.0	0.986 \pm 0.005	98.2	98.0	1.002 \pm 0.014
+1.2, +2.4	10.0, 15.0	99.1	99.2	0.998 \pm 0.001	98.7	99.5	0.992 \pm 0.004
+1.2, +2.4	15.0, 20.0	98.9	99.3	0.996 \pm 0.001	98.7	99.5	0.992 \pm 0.001

Table B.6: Efficiency for the requirement on the significance of the 3d impact parameter, measured using the tag-and-probe method for muons with $p_T > 20$ GeV and passing the Particle Flow identification.

Region η range	Efficiencies for 2011 [%]			Efficiencies for 2012 [%]		
	data	sim.	ratio \pm stat.	data	sim.	ratio \pm stat.
-2.4, -2.1	98.9	99.1	0.998 \pm 0.001	99.1	99.3	0.998 \pm 0.001
-2.1, -1.6	99.3	99.5	0.998 \pm 0.001	99.1	99.5	0.996 \pm 0.001
-1.6, -1.2	99.5	99.6	0.999 \pm 0.001	99.4	99.6	0.998 \pm 0.001
-1.2, -0.9	99.6	99.6	1.000 \pm 0.001	99.5	99.7	0.998 \pm 0.001
-0.9, -0.6	99.7	99.6	1.000 \pm 0.001	99.6	99.6	0.999 \pm 0.001
-0.6, -0.3	99.7	99.6	1.001 \pm 0.001	99.6	99.6	1.000 \pm 0.001
-0.3, -0.2	99.7	99.6	1.001 \pm 0.001	99.8	99.7	1.001 \pm 0.001
-0.2, +0.2	99.7	99.6	1.001 \pm 0.001	99.7	99.7	0.999 \pm 0.001
+0.2, +0.3	99.7	99.6	1.001 \pm 0.001	99.6	99.7	0.999 \pm 0.001
+0.3, +0.6	99.7	99.6	1.000 \pm 0.001	99.6	99.7	1.000 \pm 0.001
+0.6, +0.9	99.6	99.6	1.000 \pm 0.001	99.6	99.6	0.999 \pm 0.001
+0.9, +1.2	99.6	99.6	1.000 \pm 0.001	99.5	99.6	0.999 \pm 0.001
+1.2, +1.6	99.5	99.6	0.999 \pm 0.001	99.4	99.7	0.997 \pm 0.001
+1.6, +2.1	99.2	99.5	0.996 \pm 0.001	99.2	99.5	0.997 \pm 0.001
+2.1, +2.4	98.7	99.1	0.996 \pm 0.001	98.8	99.3	0.995 \pm 0.001

Table B.7: Isolation efficiency measured using the tag-and-probe method for muons with $p_T < 20$ GeV and passing the Particle Flow identification and the 3d impact parameter requirements.

Region $ \eta $ range	p_T range	Efficiencies for 2011 [%]			Efficiencies for 2012 [%]		
		data	sim.	ratio \pm stat.	data	sim.	ratio \pm stat.
+0.0, +1.2	5.0, 10.0	87.7	89.7	0.978 \pm 0.020	86.0	88.4	0.973 \pm 0.064
+0.0, +1.2	10.0, 15.0	93.0	93.5	0.995 \pm 0.005	91.0	91.4	0.996 \pm 0.019
+0.0, +1.2	15.0, 20.0	95.2	95.0	1.002 \pm 0.002	93.2	94.7	0.984 \pm 0.007
+1.2, +2.4	5.0, 10.0	88.7	88.7	1.001 \pm 0.008	92.0	86.2	1.068 \pm 0.022
+1.2, +2.4	10.0, 15.0	94.3	94.2	1.002 \pm 0.003	93.7	94.6	0.991 \pm 0.008
+1.2, +2.4	15.0, 20.0	96.8	96.7	1.001 \pm 0.002	97.0	96.9	1.001 \pm 0.005

Chapter B: Tag-and-probe Measurements

Table B.8: Isolation efficiency measured using the tag-and-probe method for muons with $p_T > 20$ GeV and passing the Particle Flow identification and the 3d impact parameter requirements.

Region η range	Efficiencies for 2011 [%]			Efficiencies for 2012 [%]		
	data	sim.	ratio \pm stat.	data	sim.	ratio \pm stat.
-2.4, -2.1	99.5	99.4	1.001 \pm 0.001	99.5	99.4	1.001 \pm 0.001
-2.1, -1.6	99.5	99.6	1.000 \pm 0.001	99.7	99.6	1.001 \pm 0.001
-1.6, -1.2	99.5	99.5	1.000 \pm 0.001	99.6	99.7	0.999 \pm 0.001
-1.2, -0.9	99.5	99.4	1.000 \pm 0.001	99.5	99.6	0.999 \pm 0.001
-0.9, -0.6	99.5	99.5	1.000 \pm 0.001	99.5	99.6	0.999 \pm 0.001
-0.6, -0.3	99.4	99.4	1.000 \pm 0.001	99.4	99.5	0.999 \pm 0.001
-0.3, -0.2	99.5	99.4	1.000 \pm 0.001	99.4	99.3	1.001 \pm 0.001
-0.2, +0.2	99.4	99.4	1.000 \pm 0.001	99.4	99.4	1.000 \pm 0.001
+0.2, +0.3	99.5	99.4	1.000 \pm 0.001	99.5	99.6	0.999 \pm 0.001
+0.3, +0.6	99.5	99.4	1.000 \pm 0.001	99.4	99.4	1.000 \pm 0.001
+0.6, +0.9	99.4	99.5	1.000 \pm 0.001	99.5	99.7	0.998 \pm 0.001
+0.9, +1.2	99.5	99.5	1.000 \pm 0.001	99.6	99.4	1.001 \pm 0.001
+1.2, +1.6	99.5	99.5	1.000 \pm 0.001	99.5	99.6	0.999 \pm 0.001
+1.6, +2.1	99.5	99.5	0.999 \pm 0.001	99.5	99.6	1.000 \pm 0.001
+2.1, +2.4	99.3	99.4	0.999 \pm 0.001	99.6	99.4	1.002 \pm 0.001

Table B.9: Muon trigger efficiency measured using the tag-and-probe method for muons with $p_T > 20$ GeV and passing the full offline selection, for the Run2011A period.

Region η range	Efficiencies for Mu17 leg [%]			Efficiencies for Mu8 leg [%]		
	data	sim.	ratio \pm stat.	data	sim.	ratio \pm stat.
-2.4, -2.1	88.2	91.1	0.969 \pm 0.002	90.5	91.5	0.989 \pm 0.002
-2.1, -1.6	92.1	94.3	0.977 \pm 0.001	92.8	94.4	0.983 \pm 0.001
-1.6, -1.2	96.0	97.1	0.990 \pm 0.001	96.2	97.1	0.991 \pm 0.001
-1.2, -0.9	96.2	97.5	0.986 \pm 0.001	96.4	97.6	0.988 \pm 0.001
-0.9, -0.6	96.0	97.6	0.983 \pm 0.001	96.1	97.6	0.984 \pm 0.001
-0.6, -0.3	97.9	98.8	0.991 \pm 0.001	98.0	98.8	0.992 \pm 0.001
-0.3, -0.2	87.9	91.6	0.959 \pm 0.002	88.1	91.7	0.961 \pm 0.002
-0.2, +0.2	97.4	98.3	0.991 \pm 0.001	97.5	98.3	0.991 \pm 0.001
+0.2, +0.3	87.3	90.6	0.963 \pm 0.002	87.4	90.7	0.964 \pm 0.002
+0.3, +0.6	97.5	98.7	0.988 \pm 0.001	97.6	98.7	0.988 \pm 0.001
+0.6, +0.9	96.2	97.3	0.989 \pm 0.001	96.3	97.4	0.990 \pm 0.001
+0.9, +1.2	96.1	97.4	0.986 \pm 0.001	96.3	97.6	0.987 \pm 0.001
+1.2, +1.6	95.5	96.7	0.988 \pm 0.001	95.8	96.8	0.989 \pm 0.001
+1.6, +2.1	92.6	93.2	0.993 \pm 0.001	93.3	93.4	1.000 \pm 0.001
+2.1, +2.4	88.5	89.9	0.984 \pm 0.002	90.6	90.5	1.001 \pm 0.002

Table B.10: Muon trigger efficiency measured using the tag-and-probe method for muons with $p_T > 20$ GeV and passing the full offline selection, for the Run2011B period.

Region η range	Efficiencies for Mu17 leg [%]			Efficiencies for Mu8 leg [%]		
	data	sim.	ratio \pm stat.	data	sim.	ratio \pm stat.
-2.4, -2.1	84.8	91.1	0.931 \pm 0.003	87.3	91.5	0.954 \pm 0.003
-2.1, -1.6	89.7	94.3	0.951 \pm 0.001	90.4	94.4	0.958 \pm 0.001
-1.6, -1.2	95.2	97.1	0.980 \pm 0.001	95.4	97.1	0.982 \pm 0.001
-1.2, -0.9	95.6	97.5	0.980 \pm 0.002	95.8	97.6	0.982 \pm 0.001
-0.9, -0.6	95.8	97.6	0.981 \pm 0.001	95.9	97.6	0.982 \pm 0.001
-0.6, -0.3	97.5	98.8	0.987 \pm 0.001	97.6	98.8	0.987 \pm 0.001
-0.3, -0.2	86.8	91.6	0.947 \pm 0.003	86.8	91.7	0.947 \pm 0.003
-0.2, +0.2	97.0	98.3	0.986 \pm 0.001	97.0	98.3	0.986 \pm 0.001
+0.2, +0.3	87.0	90.6	0.960 \pm 0.003	87.0	90.7	0.960 \pm 0.003
+0.3, +0.6	97.3	98.7	0.986 \pm 0.001	97.3	98.7	0.986 \pm 0.001
+0.6, +0.9	96.0	97.3	0.986 \pm 0.001	96.1	97.4	0.987 \pm 0.001
+0.9, +1.2	95.4	97.4	0.979 \pm 0.001	95.6	97.6	0.980 \pm 0.003
+1.2, +1.6	94.7	96.7	0.979 \pm 0.001	95.0	96.8	0.981 \pm 0.001
+1.6, +2.1	90.6	93.2	0.972 \pm 0.001	91.5	93.4	0.980 \pm 0.002
+2.1, +2.4	84.2	89.9	0.936 \pm 0.003	86.6	90.5	0.957 \pm 0.003

Table B.11: Muon trigger efficiency measured using the tag-and-probe method for muons with $p_T > 20$ GeV and passing the full offline selection, for the 2012 running period.

Region η range	Efficiencies for Mu17 leg [%]			Efficiencies for Mu8 leg [%]		
	data	sim.	ratio \pm stat.	data	sim.	ratio \pm stat.
-2.4, -2.1	89.4	90.7	0.985 \pm 0.004	94.2	93.9	1.003 \pm 0.003
-2.1, -1.6	89.3	91.9	0.972 \pm 0.003	94.1	95.2	0.988 \pm 0.002
-1.6, -1.2	91.6	92.7	0.987 \pm 0.002	97.9	98.2	0.996 \pm 0.001
-1.2, -0.9	93.1	94.8	0.982 \pm 0.002	97.7	98.5	0.993 \pm 0.001
-0.9, -0.6	95.8	97.4	0.984 \pm 0.002	97.3	98.5	0.988 \pm 0.001
-0.6, -0.3	97.9	98.5	0.994 \pm 0.001	98.9	99.4	0.996 \pm 0.001
-0.3, -0.2	85.8	91.6	0.936 \pm 0.005	88.2	93.2	0.946 \pm 0.004
-0.2, +0.2	96.8	97.7	0.990 \pm 0.001	98.0	98.6	0.994 \pm 0.001
+0.2, +0.3	86.3	89.7	0.962 \pm 0.005	88.5	91.4	0.968 \pm 0.005
+0.3, +0.6	97.9	98.7	0.992 \pm 0.001	98.9	99.4	0.995 \pm 0.001
+0.6, +0.9	96.5	97.2	0.993 \pm 0.001	97.8	98.2	0.995 \pm 0.001
+0.9, +1.2	93.1	94.2	0.988 \pm 0.002	97.8	98.1	0.998 \pm 0.001
+1.2, +1.6	90.2	93.0	0.970 \pm 0.003	97.0	97.8	0.991 \pm 0.001
+1.6, +2.1	92.9	93.2	0.997 \pm 0.002	96.5	96.4	1.001 \pm 0.002
+2.1, +2.4	89.6	90.7	0.988 \pm 0.004	94.0	93.8	1.002 \pm 0.003

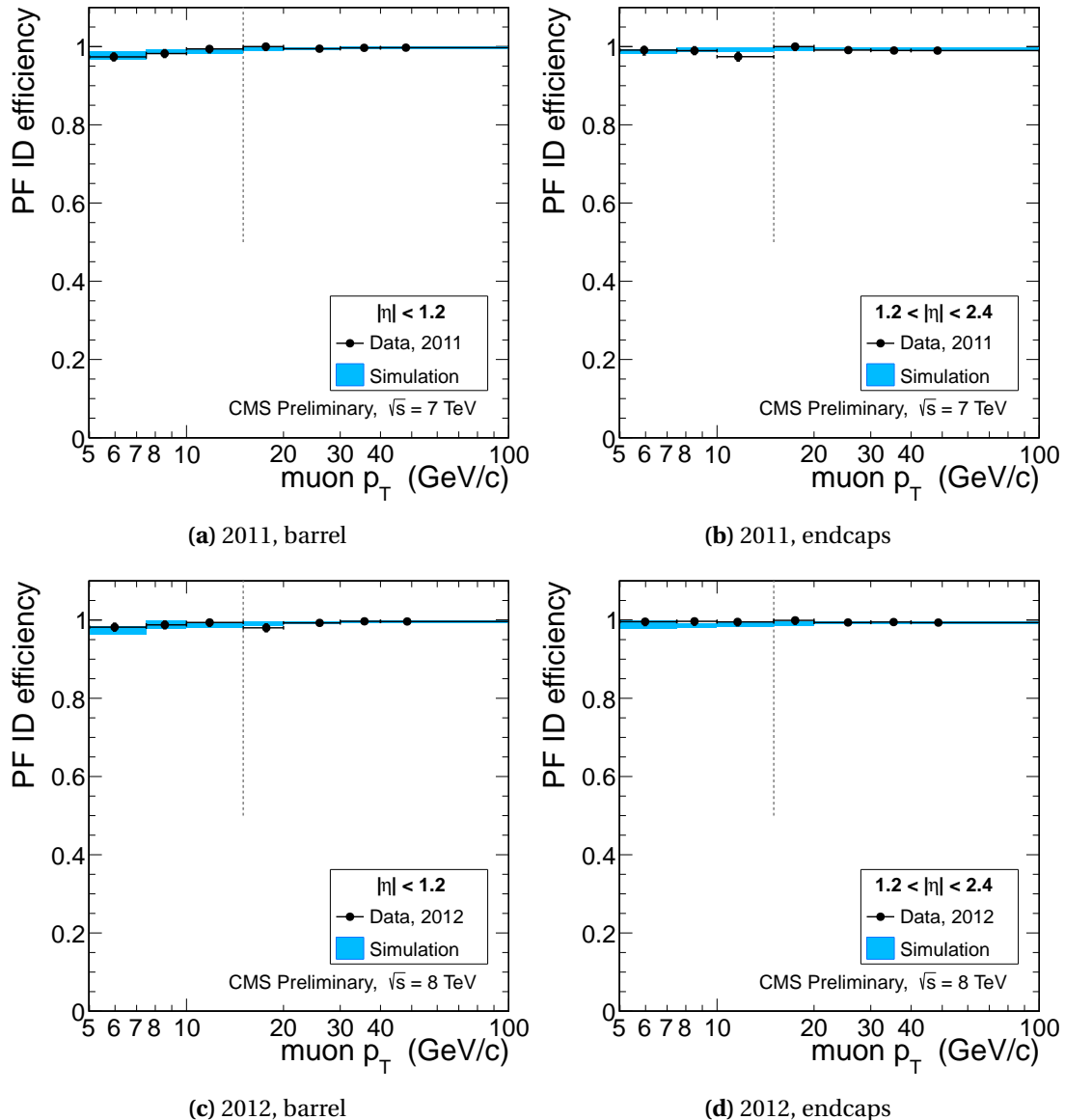


Figure B.1: Muon reconstruction and identification efficiency for Particle Flow muons, measured with the tag-and-probe method on 2011 data (top) and 2012 data (bottom) as function of muon p_T , in the barrel (left) and endcaps (right).

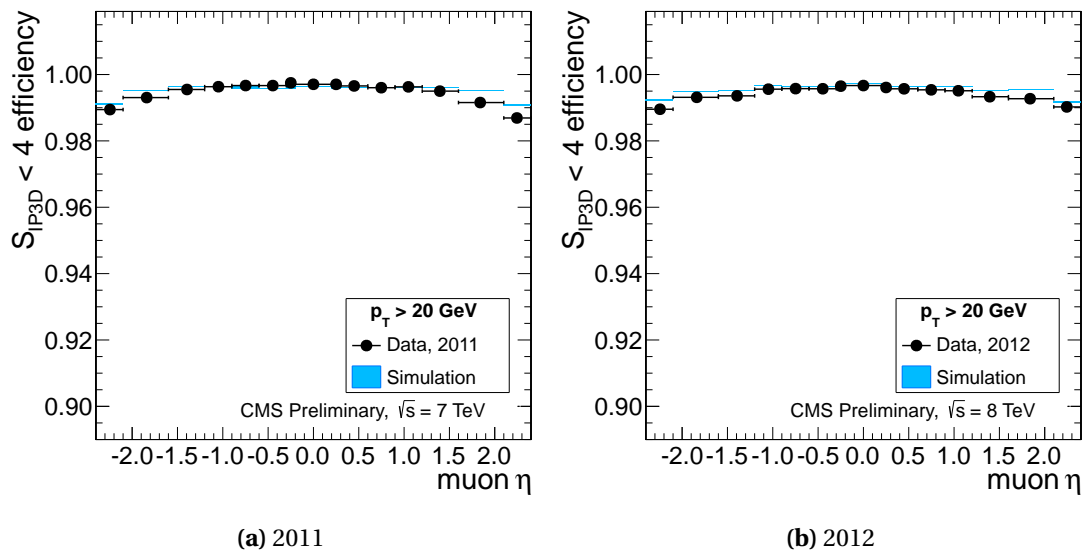


Figure B.2: Efficiency for the requirement on the 3D impact parameter significance $|S_{\text{IP3D}}| < 4$, as function of muon pseudorapidity, for 2011 data (left) and 2012 data (right). Muons with $p_T > 20 \text{ GeV}$ and satisfying the Particle Flow identification requirements are used.

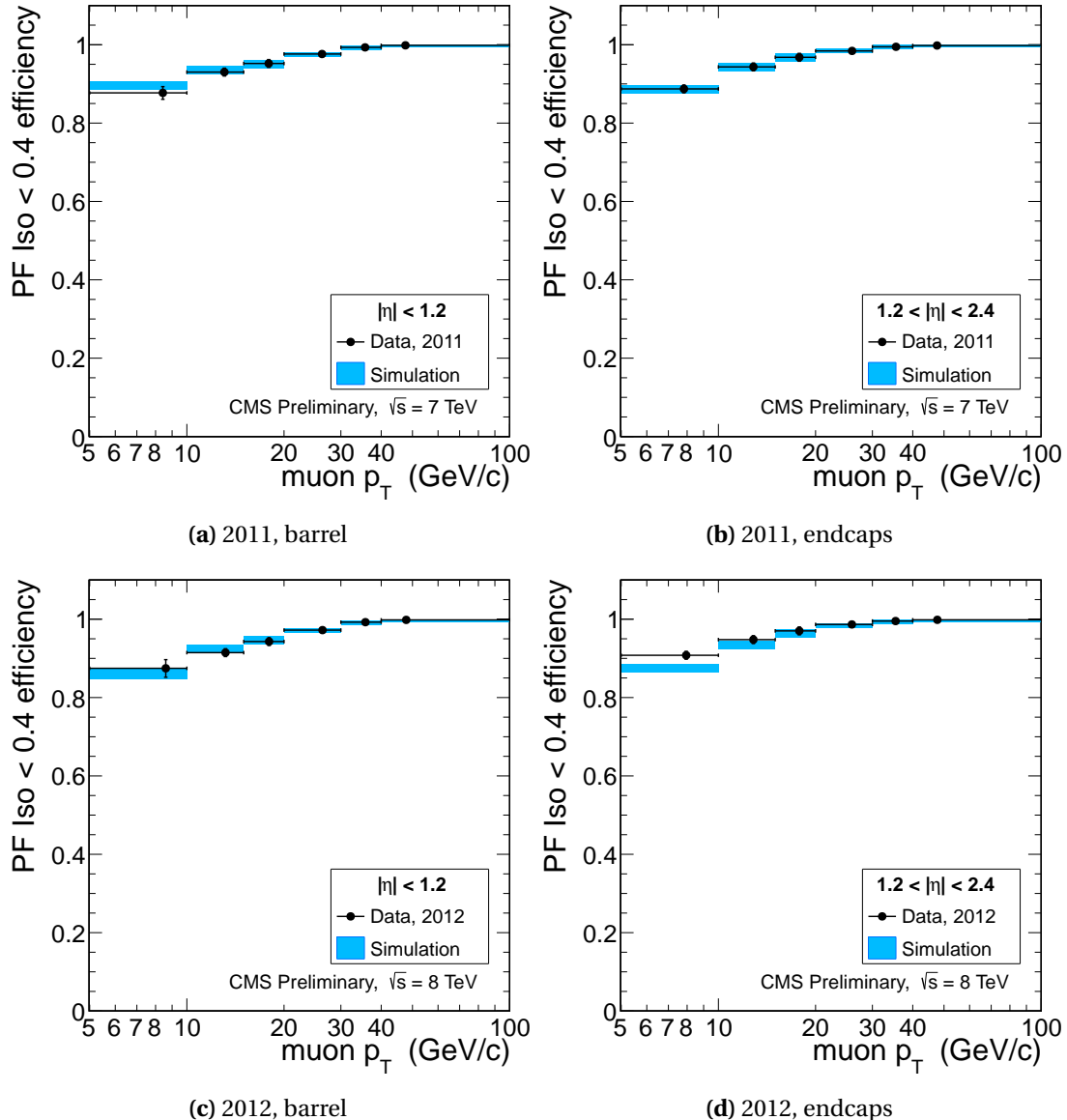


Figure B.3: Muon isolation efficiency for Particle Flow muons passing the impact parameter requirements, measured with the tag-and-probe method on 2011 data (top) and 2012 data (bottom) as function of muon p_T , in the barrel (left) and endcaps (right). FIXME plots of 2012 to be updated with more data.

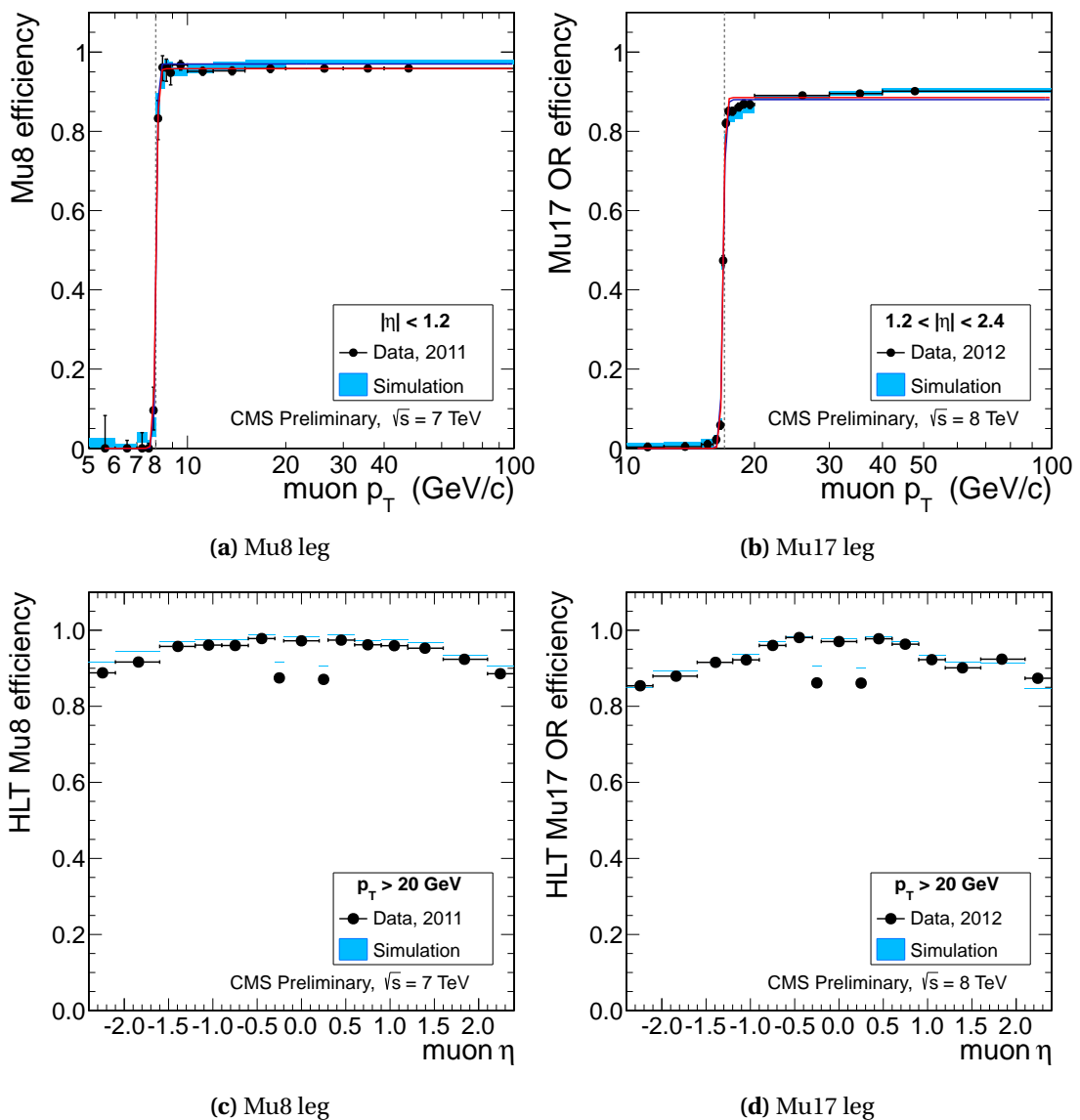


Figure B.4: Muon HLT Trigger efficiency for the Mu8 leg (on the left), the Mu17 leg (right), as a function of the muon p_T (top), of the muon η (bottom). Muons are asked to pass ID, Isolation and SIP requirements of the analysis.

Bibliography

- [1] Serguei Chatrchyan et al. Observation of a new boson at a mass of 125 GeV with the CMS experiment at the LHC. *Phys.Lett.*, B716:30–61, 2012.
- [2] E. Fermi. Trends to a Theory of beta Radiation. (In Italian). *Nuovo Cim.*, 11:1–19, 1934.
- [3] S.L. Glashow. Partial Symmetries of Weak Interactions. *Nucl.Phys.*, 22:579–588, 1961.
- [4] Steven Weinberg. A model of leptons. *Physical Review Letters*, 19(21):1264–1266, 1967.
- [5] Abdus Salam. Elementary particle theory. *Almquist & Wisksells*, page 367, 1968.
- [6] F. Englert and R. Brout. Broken Symmetry and the Mass of Gauge Vector Mesons. *Phys.Rev.Lett.*, 13:321–322, 1964.
- [7] T.W.B. Kibble. Symmetry breaking in nonAbelian gauge theories. *Phys.Rev.*, 155:1554–1561, 1967.
- [8] G.S. Guralnik, C.R. Hagen, and T.W.B. Kibble. Global Conservation Laws and Massless Particles. *Phys.Rev.Lett.*, 13:585–587, 1964.
- [9] Peter W. Higgs. Broken symmetries, massless particles and gauge fields. *Phys.Lett.*, 12:132–133, 1964.
- [10] Peter W. Higgs. Broken Symmetries and the Masses of Gauge Bosons. *Phys.Rev.Lett.*, 13:508–509, 1964.
- [11] Peter W. Higgs. Spontaneous Symmetry Breakdown without Massless Bosons. *Phys.Rev.*, 145:1156–1163, 1966.
- [12] Search for the fermiophobic model Higgs boson decaying into two photons. 2012.
- [13] G. Ridolfi. Search for the higgs boson: theoretical perspectives.
- [14] Precision electroweak measurements and constraints on the Standard Model. 2010.
- [15] R. Barate et al. Search for the standard model Higgs boson at LEP. *Phys.Lett.*, B565:61–75, 2003.

Bibliography

- [16] T. Aaltonen et al. Combined CDF and D0 Upper Limits on Standard Model Higgs Boson Production with up to 8.2 fb^{-1} of Data. 2011. *Temporary entry*.
- [17] M. Baak, M. Goebel, J. Haller, A. Hoecker, D. Kennedy, K. Mönig, M. Schott, and J. Stelzer. Updated status of the global electroweak fit and constraints on new physics. *The European Physical Journal C*, 72:1–35, 2012.
- [18] Search for higgs boson in vh production with h to bb. 2011.
- [19] Search for the standard model higgs boson produced in association with a vector boson and decaying to a b-quark pair using up to 4.7 fb^{-1} of pp collision data at $\sqrt{s} = 7 \text{ tev}$ with the atlas detector at the lhc. Technical Report ATLAS-CONF-2012-015, CERN, Geneva, Mar 2012.
- [20] Combined CDF and D0 Search for Standard Model Higgs Boson Production with up to 10.0 fb^{-1} of Data. 2012.
- [21] Yves Baconnieri, Giorgio Brianti, P Lebrun, A G Mathewson, R Perin, and Yves Baconnieri. *LHC: the Large Hadron Collider accelerator project. oai:cds.cern.ch:257706*. CERN, Geneva, 1993.
- [22] The Large Hadron Collider: Conceptual design. 1995.
- [23] Lyndon Evans and Philip Bryant. Lhc machine. *Journal of Instrumentation*, 3(08):S08001, 2008.
- [24] European Organization for Nuclear Research. CMS Collaboration. *Compact Muon Solenoid Technical Proposal*. CERN/LHCC. CERN, 1994.
- [25] The CMS Collaboration. The cms experiment at the cern lhc. *Journal of Instrumentation*, 3(08):S08004, 2008.
- [26] Electromagnetic calorimeter calibration with 7 tev data. 2010.
- [27] Yong Yang. Commissioning, performance and calibration of crystals of the electromagnetic calorimeter of cms. Technical Report CMS-CR-2010-270, CERN, Geneva, Nov 2010.
- [28] Ecal 2010 performance results. Jun 2011.
- [29] Petar Adzic, Reyes Alemany-Fernandez, and Almeida et al. Energy resolution of the barrel of the cms electromagnetic calorimeter. oai:cds.cern.ch:1009081. Technical Report CMS-NOTE-2006-148, CERN, Geneva, Nov 2006.
- [30] Emilio Meschi, T Monteiro, Christopher Seez, and Pratibha Vikas. Electron reconstruction in the cms electromagnetic calorimeter. oai:cds.cern.ch:687345. Technical Report CMS-NOTE-2001-034, CERN, Geneva, Jun 2001.

- [31] P. Meridiani *et al.* Position resolution at the 2006 ecal test beam. Technical Report CMS Detector Note DN-2007/011, CERN, Geneva, 2007.
- [32] Vardan Khachatryan *et al.* Observation of Long-Range Near-Side Angular Correlations in Proton-Proton Collisions at the LHC. *JHEP*, 1009:091, 2010.
- [33] (ed.) Sphicas, P. CMS: The TriDAS project. Technical design report, Vol. 2: Data acquisition and high-level trigger. 2002.
- [34] S. Baffioni *et al.* Electron reconstruction in CMS. *Eur. Phys. J.*, C49:1099–1116, 2007.
- [35] S. et al. Chatrchyan. Search for the standard model higgs boson in the decay channel $h \rightarrow zz \rightarrow 4l$ in pp collisions at $\sqrt{s} = 7$ tev. *Phys. Rev. Lett.*, 108:111804, Mar 2012.
- [36] Marlow, D. talk at the CMS GWM. <https://indico.cern.ch/getFile.py/access?contribId=2&resId=0&materialId> 2011.
- [37] Pierini, M. talk at the joint pvt/po meeting. <https://twiki.cern.ch/twiki/bin/viewauth/CMS/PdwgMain>, 2011.
- [38] Torbjorn Sjöstrand, Stephen Mrenna, and Peter Z. Skands. PYTHIA 6.4 Physics and Manual. *JHEP*, 05:026, 2006.
- [39] Johan Alwall *et al.* MadGraph/MadEvent v4: The New Web Generation. *JHEP*, 09:028, 2007.
- [40] Stefano Frixione, Paolo Nason, and Carlo Oleari. Matching NLO QCD computations with Parton Shower simulations: the POWHEG method. *JHEP*, 11:070, 2007.
- [41] T. Binoth, N. Kauer, and P. Mertsch. Gluon-induced QCD corrections to $pp \rightarrow ZZ \rightarrow \ell\bar{\ell}\ell'\bar{\ell}'$. In *Proceedings of the XVI Int. Workshop on Deep-Inelastic Scattering and Related Topics (DIS'07)*, 2008.
- [42] LHC Higgs Cross Section Working Group. Handbook of LHC Higgs Cross Sections: 1. Inclusive Observables. CERN Report CERN-2011-002, 2011.
- [43] Charalampos Anastasiou, Radja Boughezal, and Frank Petriello. Mixed QCD-electroweak corrections to Higgs boson production in gluon fusion. *JHEP*, 04:003, 2009.
- [44] Daniel de Florian and Massimiliano Grazzini. Higgs production through gluon fusion: updated cross sections at the Tevatron and the LHC. *Phys. Lett. B*, 674:291, 2009.
- [45] S. Dawson. Radiative corrections to Higgs boson production. *Nucl. Phys. B*, 359:283, 1991.
- [46] M. Spira *et al.* Higgs boson production at the LHC. *Nucl. Phys. B*, 453:17, 1995.

Bibliography

- [47] Robert V. Harlander and William B. Kilgore. Next-to-next-to-leading order Higgs production at hadron colliders. *Phys. Rev. Lett.*, 88:201801, 2002.
- [48] Charalampos Anastasiou and Kirill Melnikov. Higgs boson production at hadron colliders in NNLO QCD. *Nucl. Phys. B*, 646:220, 2002.
- [49] V. Ravindran, J. Smith, and W. L. van Neerven. NNLO corrections to the total cross section for Higgs boson production in hadron-hadron collisions. *Nucl. Phys. B*, 665:325, 2003.
- [50] Stefano Catani et al. Soft-gluon resummation for Higgs boson production at hadron colliders. *JHEP*, 07:028, 2003.
- [51] Stefano Actis et al. NLO Electroweak Corrections to Higgs Boson Production at Hadron Colliders. *Phys. Lett. B*, 670:12, 2008.
- [52] M. Ciccolini, Ansgar Denner, and S. Dittmaier. Strong and electroweak corrections to the production of Higgs + 2-jets via weak interactions at the LHC. *Phys. Rev. Lett.*, 99:161803, 2007.
- [53] M. Ciccolini, Ansgar Denner, and S. Dittmaier. Electroweak and QCD corrections to Higgs production via vector-boson fusion at the LHC. *Phys. Rev. D*, 77:013002, 2008.
- [54] T. Figy, C. Oleari, and D. Zeppenfeld. Next-to-leading order jet distributions for Higgs boson production via weak-boson fusion. *Phys. Rev. D*, 68:073005, 2003.
- [55] K. Arnold et al. VBFNLO: A parton level Monte Carlo for processes with electroweak bosons. *Comput. Phys. Commun.*, 180:1661, 2009.
- [56] Paolo Bolzoni et al. Higgs production via vector-boson fusion at NNLO in QCD. *Phys. Rev. Lett.*, 105:011801, 2010.
- [57] A. Bredenstein et al. Precise predictions for the Higgs-boson decay $H \rightarrow WW/ZZ \rightarrow 4$ leptons. *Phys. Rev. D*, 74:013004, 2006.
- [58] A. Bredenstein et al. Radiative corrections to the semileptonic and hadronic Higgs-boson decays $H \rightarrow WW / ZZ \rightarrow 4$ fermions. *JHEP*, 02:080, 2007.
- [59] A. Djouadi, J. Kalinowski, and M. Spira. HDECAY: A program for Higgs boson decays in the standard model and its supersymmetric extension. *Comput. Phys. Commun.*, 108:56, 1998.
- [60] Stefano Actis et al. NNLO Computational Techniques: the Cases $H \rightarrow \gamma\gamma$ and $H \rightarrow gg$. *Nucl. Phys. B*, 811:182, 2009.
- [61] ATLAS and CMS Collaborations. LHC Higgs Combination Working Group report. *ATL-PHYS-PUB-2011-11, CMS NOTE-2011/005*, 2011.

- [62] Giuseppe Bozzi, Stefano Catani, Daniel de Florian, and Massimiliano Grazzini. Transverse-momentum resummation and the spectrum of the Higgs boson at the LHC. *Nucl. Phys. B*, 737:73, 2006.
- [63] S. Baffioni et al. Search strategy for the higgs boson in the $zz^{(*)}$ decay channel at $\sqrt{s} = 10\text{ tev}$ with the cms experiment'. *CMS AN*, 2010/237, 2010.
- [64] M Cacciari, S Frixione, M.L. Mangano, P. Nason, and G. Ridolfi. Updated predictions for the total production crosssections of top and of heavier quark pairs at the tevatron and at the lhc.
- [65] S. Baffioni et al. Electron reconstruction in cms. *CMS Note*, 2006/040, 2006.
- [66] S. Baffioni et al. Electron reconstruction in cms. *CMS Analysis Note*, 2009/164, 2009.
- [67] CMS Collaboration. Electron reconstruction and identification at $\sqrt{s} = 7\text{ tev}$. *CMS Physics Analysis Summary*, CMS-PAS-EGM-10-004, 2010.
- [68] CMS Collaboration. Electron commissioning results at at $\sqrt{s} = 7\text{ tev}$. *CMS Detector Performance Summaries*, 2011/003, 2011.
- [69] Particle-flow event reconstruction in cms and performance for jets, taus, and e_t^{miss} . *CMS PAS*, PFT-09/001, 2009.
- [70] M. Pioppi. Electron pre-identification in the particle flow framework. *CMS Note*, 2008/032, 2008.
- [71] W. et al. Adam. Track reconstruction in the cms tracker. *CMS Note*, 2006/041, 2006.
- [72] W. et al. Adam. Reconstruction of electrons with the gaussian-sum filter in the cms tracker at the lhc. *CMS Note*, 2005/001, 2005.
- [73] S. Baffioni et al. Electron charge determination commissioning from 7 tev data. *CMS AN*, 2010/468, 2010.
- [74] A. Benaglia et al. Search for a standard model higgs boson decaying into two photons in 2012 data. *CMS AN*, 2012/160, 2012.
- [75] Y. Chen et al. Electron energy reconstruction using a multivariate regression. *CMS AN*, 2012/327, 2012.
- [76] R. Paramatti. Private communication, an in preparation. 2.
- [77] Arie Bodek and Jiyeon Han. Improved Rochester misalignment and muon scale corrections extracted for 2011A, 2011B CMS data. *CMS AN*, 2012/298, 2012.
- [78] e/g POG. Electron selection criteria in 2012. *CMS AN*, 2012/201, 2012.
- [79]

Bibliography

- [80] Y. Freund. Boosting a weak learning algorithm by majority. *Information and Computation*, 121(2):256 – 285, 1995.
- [81] J. Friedman, T. Hastie, and R. Tibshirani. Additive logistic regression: a statistical view of boosting (with discussion and a rejoinder by the authors). *The annals of statistics*, 28(2):337–407, 2000.
- [82] N. Amapane et al. Search for the standard model higgs boson in the decay channel $h \rightarrow zz \rightarrow 4\ell$ in pp collisions. *CMS Analysis Note*, AN-12-141, 2012.
- [83] CMS Collaboration. Muo-10-004: Performance of CMS muon reconstruction in pp collision events at $\sqrt{s} = 7$ TeV. Technical report, 2010. In preparation to *JINST*.
- [84] R. Frühwirth. Application of Kalman filtering to track and vertex fitting. *Nucl. Instrum. Meth. A*, 262:444, 1987.
- [85] Serguei Chatrchyan et al. Performance of CMS muon reconstruction in cosmic-ray events. *JINST*, 5:T03022, 2010.
- [86] CMS Collaboration. Cms physics technical design report, volume i: Detector performance and software. *CERN/LHCC*, 2006-001, 2006.
- [87] CMS Collaboration. Measurement of tracking efficiency. *CMS Physics Analysis Summary*, CMS-PAS-TRK-10-002, 2010.
- [88] CMS Collaboration. Particle-flow event reconstruction in cms and performance for jets, taus, and missing e_T . *CMS Physics Analysis Summary*, CMS-PAS-PFT-09-001, 2009.
- [89] CMS Collaboration. Commissioning of the particle-flow event reconstruction with leptons from j/psi and w decays at 7 tev. *CMS Physics Analysis Summary*, CMS-PAS-PFT-10-003, 2010.
- [90] Matteo Cacciari and Gavin P. Salam. Pileup subtraction using jet areas. *Phys. Lett.*, B659:119–126, 2008.
- [91] Matteo Cacciari, Gavin P. Salam, and Gregory Soyez. The Catchment Area of Jets. *JHEP*, 04:005, 2008.
- [92] Particle-flow event reconstruction in cms and performance for jets, taus, and met. Apr 2009.
- [93] Commissioning of the particle-flow event reconstruction with the first lhc collisions recorded in the cms detector.
- [94] Commissioning of the particle-flow reconstruction in minimum-bias and jet events from pp collisions at 7 tev. 2010.
- [95] G. Daskalakis et al. Measuring electron efficiencies at cms with early data. *CMS Analysis Note*, 2007/019, 2007.

- [96] S. Baffioni et al. Electron efficiency measurement from 7 tev data. *CMS AN*, 2010/471, 2010.
- [97] CMS. Electron VBF Selection. <https://twiki.cern.ch/twiki/bin/viewauth/CMS/VbtfEleID2011>, 2011.
- [98] K. Nakamura et al. (Particle Data Group). The review of particle physics. *J. Phys. G*, 37:075021, 2010.
- [99] CMS. Electron reconstruction efficiency measurement for 2011. <https://twiki.cern.ch/twiki/bin/view/CMS/EgCommissioningAndPhysicsDeliverables>, 2011.
- [100] CMS collaboration. Tag-and-probe systematic errors. 2011.
- [101] CMS Collaboration. Trk-10-001: Description and performance of the CMS track and primary vertex reconstruction. In preparation, 2011.
- [102] S. Baffioni et al. Discovery potential for the SM Higgs boson in the $H \rightarrow ZZ^{(*)} \rightarrow e^+e^-e^+e^-$ decay channel. *J. Phys.*, G34:N23–N46, 2007.
- [103] S. Baffioni et al. Search strategy for the higgs boson in the zz decay channel with the cms experiment. *CMS AN*, 2008/050, 2008.
- [104] ATLAS and CMS Collaborations, LHC Higgs Combination Group. Procedure for the lhc higgs boson search combination in summer 2011. ATL-PHYS-PUB/CMS NOTE 2011-11, 2011/005, 2011.
- [105] P. Avery, M. Chen, A. Drozdetskiy, A. Korytov, G. Mitselmakher, M. Snowball. A complete model of the four-lepton invariant mass distributions for $H \rightarrow ZZ \rightarrow 4l$ and $ZZ \rightarrow 4l$ events. *CMS Analysis Note*, 2011-202.
- [106] N. Amapane et al. Search for the standard model higgs boson in the decay channel $h \rightarrow zz \rightarrow 4l$ in pp collisions. *CMS AN*, 2012/367, 2012.
- [107] Stefano Goria, Giampiero Passarino, and Dario Rosco. The Higgs Boson Lineshape. *Nucl.Phys.*, B864:530–579, 2012.
- [108] LHC Higgs Cross Section Working Group web page.
- [109] Giampiero Passarino. Higgs Interference Effects in $gg \rightarrow ZZ$ and their Uncertainty. *JHEP*, 1208:146, 2012.
- [110] LHC Higgs Cross Section Working Group, S. Dittmaier, C. Mariotti, G. Passarino, and R. Tanaka (Eds.). Handbook of LHC Higgs cross sections: 1. Inclusive observables. *CERN-2011-002*, CERN, Geneva, 2011, All the numbers can be obtained at <https://twiki.cern.ch/twiki/bin/view/LHCPhysics/CrossSections>.
- [111] Higgs Branching ratio errors.

Bibliography

- [112] Ciaran Williams John Campbell, Keith Ellis. Mcfm - monte carlo for femtobarn processes. 2011.
- [113] S. Alekhin et al. The PDF4LHC working group interim report. 2011.
- [114] H. L. Lai, M. Guzzi, J. Huston, Z. Li, P. M. Nadolsky, J. Pumplin and C. P. Yuan. New parton distributions for collider physics. *Phys.Rev.*, D(82):074024, 2010.
- [115] A. D. Martin, W. J. Stirling, R. S. Thorne and G. Watt. Parton distributions for the LHC. *Eur. Phys. J.*, C(63):189, 2009.
- [116] R. D. Ball, L. Del Debbio, S. Forte, A. Guffanti, J. I. Latorre, J. Rojo and M. Ubiali. A first unbiased global NLO determination of parton distributions and their uncertainties. *Nucl. Phys.*, B(838):136, 2010.
- [117] G. Bozzi, S. Catani, D. de Florian, and M. Grazzini. The q_T spectrum of the Higgs boson at the LHC in QCD perturbation theory. *Phys. Lett.*, B(564):65, 2003.
- [118] Observation of z to 4l production in pp collisions at 7 tev. 2012.
- [119] A. Soni and R.M. Xu. Probing CP violation via Higgs decays to four leptons. *Phys.Rev.*, D48:5259–5263, 1993.
- [120] Vernon D. Barger, King-man Cheung, A. Djouadi, Bernd A. Kniehl, and P.M. Zerwas. Higgs bosons: Intermediate mass range at e+ e- colliders. *Phys.Rev.*, D49:79–90, 1994.
- [121] S.Y. Choi, 2 Miller, D.J., M.M. Muhlleitner, and P.M. Zerwas. Identifying the Higgs spin and parity in decays to Z pairs. *Phys.Lett.*, B553:61–71, 2003.
- [122] B.C. Allanach, K. Odagiri, M.J. Palmer, Michael Andrew Parker, A. Sabetfakhri, et al. Exploring small extra dimensions at the large hadron collider. *JHEP*, 0212:039, 2002.
- [123] C.P. Buszello, I. Fleck, P. Marquard, and J.J. van der Bij. Prospective analysis of spin- and CP-sensitive variables in $H \rightarrow ZZ \rightarrow l(1)^+ l(1)^- l(2)^+ l(2)^-$ at the LHC. *Eur.Phys.J.*, C32:209–219, 2004.
- [124] Rohini M. Godbole, 2 Miller, D.J., and M. Margarete Muhlleitner. Aspects of CP violation in the H ZZ coupling at the LHC. *JHEP*, 0712:031, 2007.
- [125] Wai-Yee Keung, Ian Low, and Jing Shu. Landau-Yang Theorem and Decays of a Z' Boson into Two Z Bosons. *Phys.Rev.Lett.*, 101:091802, 2008.
- [126] Oleg Antipin and Amarjit Soni. Towards establishing the spin of warped gravitons. *JHEP*, 0810:018, 2008.
- [127] Kaoru Hagiwara, Qiang Li, and Kentarou Mawatari. Jet angular correlation in vector-boson fusion processes at hadron colliders. *JHEP*, 0907:101, 2009.

- [128] Yanyan Gao, Andrei V. Gritsan, Zijin Guo, Kirill Melnikov, Markus Schulze, et al. Spin determination of single-produced resonances at hadron colliders. *Phys.Rev.*, D81:075022, 2010.
- [129] A. De Rujula, Joseph Lykken, Maurizio Pierini, Christopher Rogan, and Maria Spiropulu. Higgs look-alikes at the LHC. *Phys.Rev.*, D82:013003, 2010.
- [130] James S. Gainer, Kunal Kumar, Ian Low, and Roberto Vega-Morales. Improving the sensitivity of Higgs boson searches in the golden channel. *JHEP*, 1111:027, 2011.
- [131] Sara Bolognesi, Yanyan Gao, Andrei V. Gritsan, Kirill Melnikov, Markus Schulze, Nhan V. Tran, and Andrew Whitbeck. On the spin and parity of a single-produced resonance at the LHC. *Submitted to Phys.Rev.*, 2012.
- [132] Alessio Bonato, Andrei Gritsan, Zijin Guo, Nhan Tran, and andrew Whitbeck. Angular Analysis of Resonances $pp \rightarrow X \rightarrow ZZ$. *CMS Analysis Note*, 2010-351.
- [133] Thomas Junk. Confidence level computation for combining searches with small statistics. *Nucl. Instrum. Meth. A*, 434:435, 1999.
- [134] A.L. Read. Modified frequentist analysis of search results (the CL_s method). Technical Report CERN-OPEN-2000-005, CERN, 2000.
- [135] M. Oreglia. *A study of the reactions psi-prime → gamma gamma psi*. PhD thesis, Stanford University, 1980. SLAC-0236.

Roko Pleština

Curriculum Vitae

WORK EXPERIENCE

- FESB, University of Split, Croatia**
LLR - École Polytechnique, Palaiseau, France
Ph.D. Student - Teaching Assistant
- SINCE 2008–2013
- Research within project "Search for the Higgs boson and new physics with CMS detector" under supervision of Ivica Puljak (FESB) and Yves Sirois(LLR)
 - Delivered lectures within Physics Department at FESB

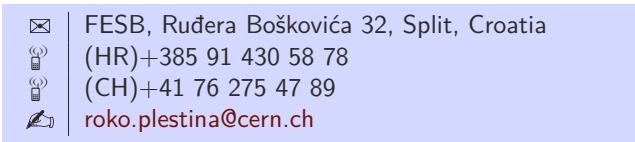
- CMS collaboration, CERN, Geneva, Switzerland**
- Measurement of efficiency of electron selection using *tag-and-probe* method
 - Optimization of the event selection for Higgs boson search in $H \rightarrow ZZ \rightarrow 4\ell$ channel
 - Study on "effective area" pile-up subtraction method
 - Efficiency study of electron/photon/tau level-1 trigger algorithms for the upgrade Phase 2
 - Data quality monitoring for proton-proton collisions
- SINCE 2009.

EDUCATION

- 2013 Ph. D. Degree
LLR - École Polytechnique
Palaiseau, France
Thesis title: "Evidence for Standard Model Higgs boson like particle decaying into four leptons with CMS detector"
 Defended on 21st February 2013. before jury composed by:
 J-C. Brient, P. Bloch, A-I. Etienne, A. Djouadi, I. Puljak
 and Y. Sirois
- 2008 M. Sc. Degree
Faculty of Science
University of Zagreb
Thesis title: "Potential of CMS detector for Higgs boson search in decay channel $H \rightarrow ZZ^ \rightarrow 4e$ "*
 M. Sc. Degree obtained with excellent grades
 Ranked among 10% of best students at Physics Department

FURTHER EDUCATION

- 2009 *CERN School of Computing*
 Göttingen, Germany
- 2009 *Trans European School of High Energy Physics*
 Zakopane, Poland
- 2007 *CERN Summer Student Programme*
 CERN-Geneva, Switzerland



SCHOLARSHIPS, AWARDS AND RECOGNITION

Nominated for the best young scientist award from Croatian Ministry of Science, Education and Sports	2012
Scholarship from French Government	2009
CERN Summer Student Programme	2007
Scholarship from Croatian Ministry of Science and Technology	2000
I. place at the national geography competition	1997
Excellent grades from teaching surveys	2012

ORGANIZATION AND PARTICIPATION TO SCIENTIFIC CONFERENCES

2012	<i>ICHEP</i> , Melbourne, Australia (<i>poster</i>)
2012	<i>LHC days in Split</i> , Split (<i>organization, poster</i>)
2012	<i>Higgs Hunting</i> , Orsay, France
2011	<i>Higgs Hunting</i> , Orsay, France
2011	7 th scientific meeting of Croatian Physical Society, Primosten, Croatia (<i>talk</i>)
2010	<i>LHC days in Split</i> , Split, Croatia (<i>organization</i>)
2010	<i>Higgs Hunting</i> , Orsay, France
2009	6 th scientific meeting of Croatian Physical Society, Primosten, Croatia (<i>poster</i>)
2008	4lepton workshop, Paris, France
2008	<i>Physics at LHC</i> , Split, Croatia (<i>organization</i>)
2004	<i>Matter under extreme conditions</i> , Brijuni, Croatia

SKILLS AND COMPETENCES

Computing

OPERATING SYSTEMS	Linux, Windows
PROGRAMMING	C, C++, Python, Bash
SCIENTIFIC TOOLS	Root, CMSSW, GRID
OFFICE TOOLS	L <small>A</small> T <small>E</small> X, MS Office, OpenOffice

Languages

ENGLISH	written/spoken
FRENCH	written/spoken
SPANISH	written/spoken
ITALIAN	written/spoken
CROATIAN	mother tongue

MEMBERSHIPS

CMS collaboration, CERN - Geneva
Croatian Physical Society

POPULARIZATION OF SCIENCE

Organization of *Festival of Science*, Split, Croatia 2012
Public lecture *The Large Hadron Collider at CERN*, Festival of Science, Split, Croatia, 2012
Lecture *The Geomagnetism*, professional seminar for geography teachers, Split, Croatia, 2010
Public lecture *The Elementary Particle Physics*, professional seminar for geography teachers, Split, Croatia 2010

REFERENCES

Ivica Puljak, FESB, University of Split, Croatia
Ivica.Puljak@cern.ch, (+385)21.30.58.85
Yves Sirois, LLR, École Polytechnique, Palaiseau, France
Yves.Sirois@cern.ch, (+33) 1.69.33.55.66
Alexandre Zabi, LLR, École Polytechnique, Palaiseau, France
Alexandre.Zabi@cern.ch, (+41) 76.487.07.37

OTHER ACTIVITIES

- project "Get to know Croatia - astronomy", won the contest from Croatian Ministry of Tourism for new tourism products (2011.)
- involved in project of writing handbook of physics for elementary and high school students (since 2010)

PERSONAL DATA

DATE OF BIRTH	3 rd March 1982, Split, Croatia
NATIONALITY	Croatian
SEX	male
FAMILY	married to Jelena Vukajlovic P. PhD student, Switzerland son Roger Carlo (3)